# Unleashing the Power of Organic Corrosion Inhibitors in Aircraft Coating Design

Zhao, J.

**DOI**
10.4233/uuid:0db2a247-5404-453f-bfc4-e8320bbde2a9

**Publication date**
2025

**Document Version**
Final published version

**Citation (APA)**
Zhao, J. (2025). *Unleashing the Power of Organic Corrosion Inhibitors in Aircraft Coating Design*. [Dissertation (TU Delft), Delft University of Technology]. https://doi.org/10.4233/uuid:0db2a247-5404-453f-bfc4-e8320bbde2a9

# Unleashing the Power of Organic Corrosion Inhibitors in Aircraft Coating Design

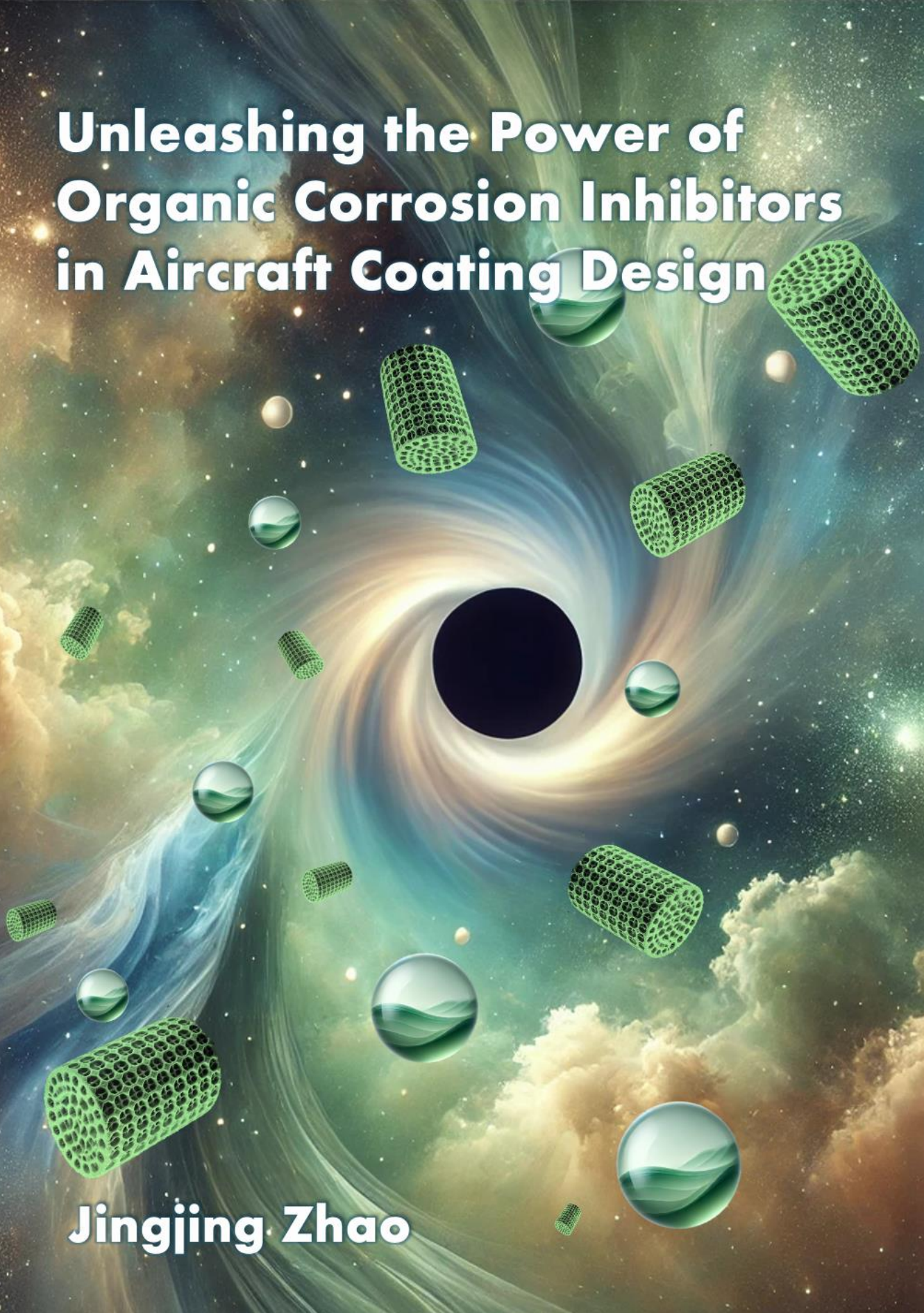

Jingjing Zhao

# Unleashing the Power of Organic Corrosion Inhibitors in Aircraft Coating Design

**Jingjing ZHAO**

# Unleashing the Power of Organic Corrosion Inhibitors in Aircraft Coating Design

Dissertation

for the purpose of obtaining the degree of doctor
at Delft University of Technology
by the authority of the Rector Magnificus, Prof.dr.ir. T.H.J.J. van der Hagen
chair of the Board for Doctorates
to be defended publicly on
Friday 21 February 2025 at 10:00
by

**Jingjing ZHAO**

Master of Science in Biochemical Engineering
Tianjin university, China
born in Tianjin, China

**This dissertation has been approved by the promotors.**

**Composition of the doctoral committee:**

| | |
|---|---|
| Rector Magnificus | Chairperson |
| Dr. S.J. Garcia Espallargas | Delft University of Technology, promotor |
| Prof.dr.ir. J. R. van Ommen | Delft University of Technology, promotor |

**Independent members:**

| | |
|---|---|
| Prof.dr.ir. R. Benedictus | Delft University of Technology |
| Prof.dr. M. G. Olivier | University of Mons, Belgium |
| Prof.dr. I. de Graeve | Vrije University Brussel, Belgium |
| Dr. J. G. Buijnsters | Delft University of Technology |
| Prof. C. A. Dransfeld | Delft University of Technology, reserve member |

**Other members:**

| | |
|---|---|
| Dr. M. Jordan | Airbus Operations GmbH, Germany |

The research in this thesis was carried out in the Department of Aerospace Structures and Materials, Faculty of Aerospace Engineering.



Keywords: Organic inhibitors, Coatings, AA2024-T3, Optics, Electrochemistry

Printed in ProefschriftMaken



ISBN: 978-94-6510-452-2

# Summary

The main objective of this dissertation is to demonstrate two strategies for incorporating highly efficient organic corrosion inhibitors into aerospace coatings and to establish fundamental guidelines for designing such coatings. Each chapter tackles important scientific and industrial challenges related to corrosion, organic inhibitors, and coating systems, using newly developed inhibitor-loading strategies, lab-scale operando optics, electrochemistry, spectroscopic and surface techniques, and industrial techniques.

**Chapter 1** introduces the field of anticorrosion aerospace coatings, the protection mechanisms used by organic corrosion inhibitors, and a range of strategies to integrate these inhibitors into coatings, from nano/microcarriers to the here introduced use of gas-phase deposition onto organic particles. This literature overview emphasizes the limited information available on: (i) inhibitor layer stability as function of its interaction with the surface and environment, and (ii) strategies to load high amounts of organic corrosion inhibitors in coatings ensuring full inhibitor availability for long-term and cyclic protection. The chapter concludes by outlining the research objectives and dividing the thesis into three sections.

*Section 1* **(Chapter 2)** introduces the potential of the state-of-the-art diatom technology at the start of this thesis in the context of model aircraft coatings and highly demanding industrial testing: i.e. using natural silica microcarriers (fossilized diatom exoskeletons or diatomite or diatomaceous earth or DE) for loading inorganic and organic corrosion inhibitors. To this aim, we used a previously established inhibitor loading strategy for diatomite, load lab-scale model aircraft primers with these carriers and assess their corrosion behavior through salt fog spray tests and droplet tests. These accelerated tests simulate to some extent harsh environmental conditions encountered by aircraft and are commonly used to screen anticorrosive coatings and to progress towards higher technology readiness levels (TRLs). The results indicate that, with the state-of-the-art technology, $Ce(NO_3)_3$ loaded diatomite outperforms in protection the one offered by diatomite loaded with two organic inhibitors. However, the results also demonstrate that the synergy between diatomite carriers with two organic inhibitors and between diatomite with $Ce(NO_3)_3$ and 2,5-dimercapto-1,3,4-thiadiazole (HDMTD) are very efficient strategies with room for improvement but good potential to reduce the use of rare earth based inhibitors and other critical raw materials in corrosion protection.

*Section 2* (**Chapters 3, 4 and 5**) delves into the fundamental understanding of the protection mechanisms of selected organic inhibitors (HDMTD and KDMTD) and technological improvements to allow their efficient loading in diatomite carriers.

**Chapter 3** compares the behavior of diatomite particles loaded with two chemically comparable inhibitor salts (i.e., HDMTD and KDMTD) in coatings, emphasizing the relevance of inhibitor acidity and ionic state over concentration. While HDMTD demonstrates higher intrinsic protection in solution, its performance in epoxy coatings is reduced by side reactions with the epoxy-amine binder. In contrast, KDMTD, due to its ionic state, offers advantages such as high-

water solubility and lower reactivity with the polymer matrix than HDMTD. Both inhibitors were incorporated into coatings using diatom exoskeletons as microcarriers. Results indicate that loading of both inhibitors in diatomite microcarriers is possible but that this strategy does not fully limit epoxy-amine diffusion into the carriers. As a consequence, HDMTD reacts relatively more with the matrix than KDMTD, hence leading to faster and more abundant inhibitor release in the case of KDMTD. Optical analysis showed that this higher release is also related to 'coating sweating' in the case of KDMTD due to its high hygroscopic character. Operando reflected microscopy of damaged coatings allowed analyzing the exposed metal at a defect as well as the coating activity around the damage. The results show, for the HDMTD-diatomite samples, very low levels of degradation (limited to minimal IM dealloying) at all pH conditions tested (pH 5, 7, 10) despite slower and lower inhibitor release even after wet-dry cycles. Interestingly, KDMTD-diatomite samples showed comparable inhibiting efficiency when acid pHs were used (pH 5) but relatively higher degradation at pH 7 and 10 despite higher inhibitor amounts were released. The work highlights the importance of optimizing inhibitor structure and ionic state over release concentration to enhance corrosion protection but also hints at the potential use of KDMTD provided the pH is acidic and the loading challenges for hygroscopic inhibitors are solved.

**Chapter 4** addresses some challenges identified in Chapter 3 for the use of KDMTD and investigates if diatomite surface modification can affect loading and release of KDMTD into diatomite and how it can protect it from the matrix and humidity to decrease 'coating sweating', two aspects limiting the use of this highly water-soluble inhibitor. To this aim, three trichlorosilanes with varying alkyl chain lengths (C4, C8, C18) were used to modify the surface of *Aulacoseira*-type diatomite (DE) prior to KDMTD loading. Results show an optimal chain length at C8 with 3.5 times higher inhibitor adsorption and 35% more release (i.e. 70-75% of the loaded inhibitor) than without surface modification. When incorporated into organic coatings, the C8-modified DE-KDMTD particles also showed better dispersion in epoxy-amine matrices, with minimal resin infusion into the diatomite shells, making around 35% more inhibitor available for release based on release studies from coatings. In contrast with the results showed in Chapter 3, operando reflected microscopy reveals good protection at damaged sites when using KDMTD at pH7 provided C8-modified diatomite is used, even though local corrosion is not completely eliminated. At pH 5, excellent protection from corrosion with no detectable degradation signs is observed. Re-exposure tests show that coatings with C8-modified DE particles maintain well their protective efficiency during the studied immersion and re-immersion conditions. These findings show that surface modification of diatomite enables more effective loading of KDMTD, minimizes negative interactions with the coating matrix, and improves sustained protection at damaged sites by enhancing inhibitor release even though the sweating problem is not fully solved.

**Chapter 5** deepens into the fundamental mechanisms behind the high levels of corrosion protection observed for AA2024-T3 in presence of HDMTD, highlights the role of small NaCl concentrations as a factor to improve corrosion inhibitor efficiency and introduces the concept of inhibiting layer stability as a largely unexplored factor responsible for efficient corrosion protection. To this aim, AA2024-T3, with or without 1mM HDMTD, was exposed to varying NaCl concentrations (0 to 0.5 M) and re-immersed into un-inhibited NaCl solutions. Analysis at the macroscopic level using reflected microscopy and electrochemical noise as well as local analysis at intermetallic (IM) level using Raman microscopy and XPS allowed studying the effect

of the immersion conditions on the chemical state of the corrosion inhibitor as function of the IM metallurgy (composition) and its relation to local protection. Results show that HDMTD at low concentrations effectively inhibits corrosion, even in NaCl-rich electrolytes. HDMTD adsorption increases with the reduction of aluminum (hydro)oxide, particularly at higher NaCl levels, and is more concentrated at the S-phase, even if present on the whole surface. The type of interaction varies with NaCl concentration, with more stable chemisorption dominating at low NaCl levels. The stability of inhibiting layers is confirmed during re-exposure to NaCl solutions without inhibitors, especially in samples where layers formed in the presence of small amounts of NaCl, hence leading to more stable and protective layers. These findings offer new insights into the protective mechanism of HDMTD as a corrosion inhibitor for AA2024-T3. The observed compositional variations of HDMTD on the metal surface as function of metallurgy, along with the influence of NaCl and acidity in forming stable inhibiting layers, pave the way for developing more stable inhibiting layers.

*Section 3* (**Chapters 6 and 7**) presents a novel strategy, based on gas-deposition of nanolayers onto HDMTD microparticles in a fluidized bed, aiming at reducing the reactivity of HDMTD with the polymer matrix while maximizing the amounts of HMDTD added to the coating.

**Chapter 6** introduces and validates this new strategy by depositing a $TiO_x$ nanolayer on HDMTD microparticles and incorporating these into epoxy-amine matrices applied onto aerospace-grade aluminum alloy AA2024-T3. Operando reflected microscopy, thermal analysis, and inhibitor release tests indicate that a 20 nm nanolayer significantly enhances particle dispersion and reduces the interaction between HDMTD and the epoxy-amine matrix. Local operando reflected microscopy, combined with electrochemical potential noise and release tests, demonstrates that the gas-phase deposited nanolayer not only improves dispersion but also enhances inhibitor release and provides effective long-term protection at damaged sites exposed to wet-wash-dry cycles. The findings also emphasize the importance of sufficient inhibitor release during the initial immersion to ensure both initial protection and the formation of stable inhibiting layers during re-immersion that can be further maintained by extra release of low inhibitor concentrations.

**Chapter 7** moves to a higher Technology Readiness Level to study the potential of this new strategy in a lab-scale aircraft model primer. Aircraft primers are prepared using 3%, 6%, and 10% pigment volume concentration (PVC) of $TiO_x$ nanolayer-coated HDMTD microparticles (HDMTD/$TiO_x$) in 25% PVC coatings applied to AA2024-T3 substrates. Corrosion protection at damaged sites is evaluated using operando reflected microscopy during 24h immersion in 0.5M NaCl solution, a 7-day droplet test, and a 1000-hour neutral salt fog spray (NSS) test. The results indicate high levels of protection in all three tests for all coatings. However, the nanolayer-protected inhibitor pigments were behind some blistering during the NSS test. Among the coatings, the 6% PVC HDMTD/$TiO_x$ coating (4.3 wt% inhibitors, similar to the coatings in Chapter 2) provided the best balance between strong protection at damaged sites and minimized blistering. The study suggests that, for the tests performed, high levels of protection at scribes is possible with relatively low organic corrosion inhibitor amounts in the coating provided side reactions are prevented. The findings highlight the potential of this new strategy as well as the room for development to reduce blistering and increase corrosion protection durability, considering the versatility in the chemistry and layer properties of the nanolayers and the range of available corrosion inhibitor chemistries.

Overall, the findings and the two loading strategies (diatomite carriers and gas-phase deposition of nanolayers) studied and discussed in this dissertation offer new insights to overcome long-standing challenges in the design of anticorrosion aerospace coating using organic inhibitors.

In summary, the following critical aspects identified for the study case in this thesis (AA2024-T3, HDMTD inhibiting salts) may have universal value and should be considered in anticorrosion coating design with organic inhibitors:

(i) Besides the concentration of inhibitors in the coating, factors such as acidity, the ionic state of inhibitors (**Chapter 3**), and the presence of oxide destabilizing ions in the electrolyte (such as $Cl^-$) (**Chapter 5**) play a crucial role in the inhibition mechanisms, efficiency and inhibiting layer stability provided by organic inhibitors.

(ii) Isolating the organic inhibitors in organic coating matrices can effectively improve the dispersion of inhibitor particles in the coating, reduce the unwanted side reactions, and enable sufficient inhibitor release. This approach, is demonstrated by both the diatomite surface modification (**Chapter 4**) and the gas-phase deposition of a nanolayer on the inhibitor microparticles (**Chapters 6 and 7**), significantly enhancing corrosion inhibition.

(iii) Rapid and sufficient inhibitor release during the initial immersion is essential to prevent the rapid dealloying of IMs and to establish stable inhibiting layers. Sustained release is important yet not essential to maintain the stability during re-immersion. (**Chapters 4 and 6**).

In addition, this dissertation highlights certain room for improvement in the two strategies explored to fully unravel their potential in order to reach a higher TRL and final implementation.

(i) **Diatomite carriers strategy**: Diatomite particles effectively disperse inhibitor pigments and prevent unwanted reactions with the coating matrix through surface modification. This modification also enhances inhibitor loading and sustained protection at damaged sites. However, challenges remain. For example: (i) significant internal volume in diatomite remains unfilled, research into alternative surface modification methods, such as selective modification, is needed to enable sufficient inhibitor loading inside the particles; (ii) only one inhibitor and surface modification condition were studied, indicating the need for broader exploration of different inhibitors and surface modification chemistries; (iii) the observed synergy with dual inhibitors suggests potential for reducing dependance on rare earth inhibitors, though further investigation is needed to understand the underlying mechanisms and best combinations.

(ii) **Gas-phase deposition of nanolayers strategy**: This novel approach, which involves depositing very thin nanolayers on inhibitor particles, was found very promising in improving the dispersion of inhibitors within the coating and reducing interactions with the epoxy-amine matrix, thus providing sustained corrosion protection. Further optimization could focus on: (i) impact of nanolayer thickness, its composition, and uniformity on the effectiveness of corrosion protection; (ii) exploring the relationship between corrosion inhibitor chemistry and nanolayer formation and type and its impact on corrosion inhibition to enhance the versatility of this approach; (iii) improving the overall properties of the coating, including

adhesion and mechanical strength, to ensure long-term durability; and (iv) optimizing the gas-phase deposition process to achieve consistency, scalability, and cost-effectiveness in practical applications.

# Samenvatting

Het hoofddoel van dit proefschrift is om twee strategieën te demonstreren voor het integreren van zeer efficiënte organische corrosieremmers in lucht- en ruimtevaartcoatings en om fundamentele richtlijnen vast te stellen voor het ontwerpen van dergelijke coatings. Elk hoofdstuk behandelt belangrijke wetenschappelijke en industriële uitdagingen met betrekking tot corrosie, organische remmers en coatingsystemen, waarbij gebruik wordt gemaakt van nieuw ontwikkelde strategieën voor remmerlading, laboratoriumschaal operando optica, elektrochemie, spectroscopische en oppervlaktetechnieken, en industriële technieken.

**Hoofdstuk 1** introduceert het gebied van anticorrosieve lucht- en ruimtevaartcoatings, de beschermingsmechanismen die worden gebruikt door organische corrosieremmers, en een reeks strategieën om deze remmers in coatings te integreren, variërend van nano/microdragers tot het hier geïntroduceerde gebruik van gasfase-afzetting op organische deeltjes. Dit literatuuroverzicht benadrukt de beperkte beschikbare informatie over: (i) de stabiliteit van de remmerlaag als functie van de interactie met het oppervlak en de omgeving, en (ii) strategieën om grote hoeveelheden organische corrosieremmers in coatings te laden, waarbij volledige beschikbaarheid van de remmer voor langdurige en cyclische bescherming wordt gegarandeerd. Het hoofdstuk besluit met het schetsen van de onderzoeksdoelstellingen en het verdelen van het proefschrift in drie secties.

*Sectie 1* (**Hoofdstuk 2**) introduceert het potentieel van de meest geavanceerde diatomeeëntechnologie aan het begin van dit proefschrift in de context van modelcoatings voor vliegtuigen en zeer veeleisende industriële tests: namelijk het gebruik van natuurlijke silicium microdragers (gefossiliseerde diatomeeënskeletten of diatomiet of kiezelgoer of DE) voor het laden van anorganische en organische corrosieremmers. Daartoe gebruikten we een eerder vastgestelde remmerladingsstrategie voor diatomiet, laadden we laboratoriumschaal modelprimers met deze dragers en beoordeelden we hun corrosiegedrag door middel van zoutnevelspuittests en druppeltests. Deze versnelde tests simuleren tot op zekere hoogte barre omgevingsomstandigheden waarmee vliegtuigen worden geconfronteerd en worden algemeen gebruikt om anticorrosieve coatings te screenen en om vooruitgang te boeken naar hogere Technology Readiness Levels (TRL's). De resultaten geven aan dat met de state-of-the-art technologie $Ce(NO_3)_3$ geladen diatomiet betere bescherming biedt dan diatomiet geladen met twee organische remmers. De resultaten tonen echter ook aan dat de synergie tussen diatomietdragers met twee organische remmers en tussen diatomiet met $Ce(NO_3)_3$ en 2,5-dimercapto-1,3,4-thiadiazool (HDMTD) zeer efficiënte strategieën zijn met ruimte voor verbetering, maar met goed potentieel om het gebruik van zeldzame aardmetalen en andere kritieke grondstoffen in corrosiebescherming te verminderen.

*Sectie 2* (**Hoofdstukken 3, 4 en 5**) gaat dieper in op het fundamentele begrip van de beschermingsmechanismen van geselecteerde organische remmers (HDMTD en KDMTD) en technologische verbeteringen om hun efficiënte lading in diatomietdragers mogelijk te maken.

**Hoofdstuk 3** vergelijkt het gedrag van diatomietdeeltjes geladen met twee chemisch vergelijkbare remmerzouten (d.w.z. HDMTD en KDMTD) in coatings, waarbij de nadruk ligt op het belang van remmerzuurgraad en ionische toestand boven concentratie. Terwijl HDMTD hogere intrinsieke bescherming in oplossing vertoont, wordt de prestatie in epoxycoatings verminderd door nevenreacties met het epoxy-amidebindmiddel. KDMTD biedt daarentegen, vanwege zijn ionische toestand, voordelen zoals hoge wateroplosbaarheid en lagere reactiviteit met de polymeermatrix dan HDMTD. Beide remmers werden in coatings opgenomen met behulp van diatomeeënskeletten als microdragers. De resultaten geven aan dat het laden van beide remmers in diatomiet microdragers mogelijk is, maar dat deze strategie de epoxy-aminediffusie in de dragers niet volledig beperkt. Als gevolg hiervan reageert HDMTD relatief meer met de matrix dan KDMTD, wat leidt tot snellere en grotere remmerafgifte in het geval van KDMTD. Optische analyse toonde aan dat deze hogere afgifte ook verband houdt met 'coating sweating' in het geval van KDMTD vanwege zijn sterk hygroscopisch karakter. Operando reflectie microscopie van beschadigde coatings maakte het mogelijk om het blootgestelde metaal bij een defect te analyseren, evenals de coatingactiviteit rond de schade. De resultaten tonen aan dat de HDMTD-diatomietmonsters zeer lage niveaus van degradatie vertonen (beperkt tot minimale IM ontleding) onder alle geteste pH-condities (pH 5, 7, 10) ondanks langzamere en lagere remmerafgifte, zelfs na nat-droog cycli. Interessant is dat KDMTD-diatomietmonsters een vergelijkbare inhiberende efficiëntie vertoonden bij gebruik van zure pH-waarden (pH 5), maar relatief hogere degradatie bij pH 7 en 10, ondanks dat grotere hoeveelheden remmer werden afgegeven. Het werk benadrukt het belang van het optimaliseren van de structuur en ionische toestand van de remmer boven de afgifteconcentratie om corrosiebescherming te verbeteren, maar wijst ook op het potentieel van KDMTD, mits de pH zuur is en de uitdagingen met betrekking tot belading voor hygroscopische remmers worden opgelost.

**Hoofdstuk 4** behandelt enkele uitdagingen die in Hoofdstuk 3 zijn geïdentificeerd voor het gebruik van KDMTD en onderzoekt of oppervlakteaanpassing van diatomiet invloed kan hebben op de lading en afgiftevan KDMTD in diatomiet, en hoe dit het kan beschermen tegen de matrix en vochtigheid om 'coating sweating' te verminderen, twee aspecten die het gebruik van deze zeer in water oplosbare remmer beperken. Hiervoor werden drie trichloorsilanen met verschillende alkylketenlengtes (C4, C8, C18) gebruikt om het oppervlak van Aulacoseira-type diatomiet (DE) te modificeren voorafgaand aan de lading met KDMTD. De resultaten tonen aan dat een optimale ketenlengte bij C8 resulteert in 3,5 keer hogere remmeradsorptie en 35% meer afgifte (d.w.z. 70-75% van de geladen remmer) dan zonder oppervlakteaanpassing. Wanneer opgenomen in organische coatings, vertoonden de C8-gemodificeerde DE-KDMTD-deeltjes ook een betere dispersie in epoxy-amidematrices, met minimale harsinfusie in de diatomietskeletten, waardoor ongeveer 35% meer remmer beschikbaar was voor afgiftevolgens afgiftestudies van coatings. In tegenstelling tot de resultaten in Hoofdstuk 3, onthult operando reflectiemicroscopie een goede bescherming op beschadigde plekken bij gebruik van KDMTD bij pH 7, mits C8-gemodificeerde diatomiet wordt gebruikt, hoewel lokale corrosie niet volledig wordt geëlimineerd. Bij pH 5 wordt uitstekende bescherming tegen corrosie waargenomen zonder detecteerbare tekenen van degradatie. Herbelichtingstests tonen aan dat coatings met C8-gemodificeerde DE-deeltjes hun

beschermende efficiëntie goed behouden tijdens de bestudeerde onderdompeling en her-onderdompeling. Deze bevindingen tonen aan dat oppervlakteaanpassing van diatomiet een effectievere lading van KDMTD mogelijk maakt, negatieve interacties met de coatingmatrix minimaliseert, en de voortdurende bescherming op beschadigde plekken verbetert door de remmerafgifte te vergroten, hoewel het zweten van de coating niet volledig is opgelost.

**Hoofdstuk 5** verdiept zich in de fundamentele mechanismen achter de hoge niveaus van corrosiebescherming die zijn waargenomen voor AA2024-T3 in aanwezigheid van HDMTD, benadrukt de rol van kleine NaCl-concentraties als een factor om de efficiëntie van corrosieremmers te verbeteren, en introduceert het concept van de stabiliteit van de remmende laag als een grotendeels onontdekte factor die verantwoordelijk is voor effectieve corrosiebescherming. Daartoe werd AA2024-T3, met of zonder 1mM HDMTD, blootgesteld aan variërende NaCl-concentraties (0 tot 0,5 M) en herondergedompeld in niet-geremde NaCl-oplossingen. Analyse op macroscopisch niveau met behulp van reflectiemicroscopie en elektrochemische ruis, evenals lokale analyse op intermetallisch (IM) niveau met behulp van Raman-microscopie en XPS, maakte het mogelijk om het effect van de onderdompelingsomstandigheden op de chemische toestand van de corrosieremmer te bestuderen als functie van de IM-metallurgie (samenstelling) en de relatie met lokale bescherming. De resultaten tonen aan dat HDMTD bij lage concentraties effectief corrosie remt, zelfs in NaCl-rijke elektrolyten. De adsorptie van HDMTD neemt toe met de reductie van aluminium(hydro)oxide, vooral bij hogere NaCl-niveaus, en is meer geconcentreerd in de S-fase, zelfs als het op het hele oppervlak aanwezig is. Het type interactie varieert met de NaCl-concentratie, waarbij meer stabiele chemisorptie de overhand heeft bij lage NaCl-niveaus. De stabiliteit van remmende lagen wordt bevestigd tijdens herblootstelling aan NaCl-oplossingen zonder remmers, vooral in monsters waar lagen zijn gevormd in aanwezigheid van kleine hoeveelheden NaCl, wat leidt tot stabielere en beschermende lagen. Deze bevindingen bieden nieuwe inzichten in het beschermingsmechanisme van HDMTD als corrosieremmer voor AA2024-T3. De waargenomen samenstellingsvariaties van HDMTD op het metaaloppervlak als functie van metallurgie, samen met de invloed van NaCl en zuurgraad bij het vormen van stabiele remmende lagen, openen de weg naar de ontwikkeling van stabielere remmende lagen.

*Sectie 3* (**Hoofdstukken 6 en 7**) presenteert een nieuwe strategie, gebaseerd op gasdepositie van nanolagen op HDMTD-microdeeltjes in een gefluïdiseerd-bedreactor, met als doel de reactiviteit van HDMTD met de polymeermatrix te verminderen terwijl de hoeveelheden HMDTD in de coating worden gemaximaliseerd.

**Hoofdstuk 6** introduceert en valideert deze nieuwe strategie door een $TiO_x$-nanolaag op HDMTD-microdeeltjes te deponeren en deze te incorporeren in epoxy-amidematrices die worden aangebracht op lucht- en ruimtevaartkwaliteit aluminiumlegering AA2024-T3. Operando reflectiemicroscopie, thermische analyse en remmerafgiftetests geven aan dat een 20 nm nanolaag de deeltjesdispersie aanzienlijk verbetert en de interactie tussen HDMTD en de epoxy-amidematrix vermindert. Lokale operando reflectiemicroscopie, gecombineerd met elektrochemische potentiaalruis en afgiftetests, toont aan dat de gasfase-gedeponeerde nanolaag niet alleen de dispersie verbetert, maar ook de remmerafgifte bevordert en effectieve langdurige bescherming biedt op beschadigde plekken die worden blootgesteld aan natte-was-droog cycli. De bevindingen benadrukken ook het belang van voldoende remmerafgifte tijdens de initiële onderdompeling om zowel initiële bescherming te garanderen als de vorming van stabiele

remmende lagen tijdens her-onderdompeling, die verder kunnen worden onderhouden door extra afgiftevan lage remmerconcentraties.

**Hoofdstuk 7** gaat naar een hoger Technology Readiness Level om het potentieel van deze nieuwe strategie te bestuderen in een laboratoriumschaal vliegtuigmodelprimer. Vliegtuigprimers worden bereid met 3%, 6% en 10% pigmentvolumeconcentratie (PVC) van $TiO_x$-nanolaag-gecoate HDMTD-microdeeltjes (HDMTD/TiOx) in 25% PVC-coatings die worden aangebracht op AA2024-T3-substraten. Corrosiebescherming op beschadigde plekken wordt geëvalueerd met behulp van operando reflectiemicroscopie tijdens 24 uur onderdompeling in 0,5M NaCl-oplossing, een 7-daagse druppeltest en een 1000-uur neutrale zoutnevelspuittest (NSS). De resultaten wijzen op hoge niveaus van bescherming in alle drie de tests voor alle coatings. De nanolaag-beschermde remmerpigmenten veroorzaakten echter enige blaasvorming tijdens de NSS-test. Van de coatings bood de 6% PVC HDMTD/$TiO_x$-coating (4,3 gewichtsprocent remmers, vergelijkbaar met de coatings in Hoofdstuk 2) de beste balans tussen sterke bescherming op beschadigde plekken en minimale blaasvorming. De studie suggereert dat, voor de uitgevoerde tests, hoge niveaus van bescherming op krassen mogelijk zijn met relatief lage hoeveelheden organische corrosieremmers in de coating, mits nevenreacties worden voorkomen. De bevindingen benadrukken het potentieel van deze nieuwe strategie, evenals de ruimte voor verdere ontwikkeling om blaasvorming te verminderen en de duurzaamheid van corrosiebescherming te vergroten, rekening houdend met de veelzijdigheid in de chemie en laag-eigenschappen van de nanolagen en het brede scala aan beschikbare corrosieremmerchemie.

Over het geheel genomen bieden de bevindingen en de twee beladingsstrategieën (diatomietdragers en gasfaseafzetting van nanolagen) die in dit proefschrift zijn bestudeerd en besproken, nieuwe inzichten om langdurige uitdagingen in het ontwerp van anticorrosieve lucht- en ruimtevaartcoatings met organische remmers te overwinnen.

Samenvattend kunnen de volgende kritische aspecten, geïdentificeerd voor de casestudy in dit proefschrift (AA2024-T3, HDMTD-remmerzouten), universele waarde hebben en moeten ze worden overwogen bij het ontwerp van anticorrosieve coatings met organische remmers:

(i) Naast de concentratie van remmers in de coating spelen factoren zoals zuurgraad, de ionische toestand van remmers (**Hoofdstuk 3**) en de aanwezigheid van oxide-destabiliserende ionen in de elektrolyt (zoals $Cl^-$) (**Hoofdstuk 5**) een cruciale rol in de remmingsmechanismen, efficiëntie en stabiliteit van de remmende laag die door organische remmers wordt geboden.

(ii) Het isoleren van de organische remmers in organische coatingmatrices kan de dispersie van remmerdeeltjes in de coating effectief verbeteren, ongewenste nevenreacties verminderen en voldoende remmerafgifte mogelijk maken. Deze aanpak, gedemonstreerd door zowel de oppervlakteaanpassing van diatomiet (**Hoofdstuk 4**) als de gasfaseafzetting van een nanolaag op de remmer-microdeeltjes (**Hoofdstukken 6 en 7**), verbetert de corrosieremming aanzienlijk.

(iii) Snelle en voldoende remmerafgifte tijdens de initiële onderdompeling is essentieel om snelle ontleding van intermetallische deeltjes (IM's) te voorkomen en stabiele remmende lagen te vestigen. Aanhoudende afgifteis belangrijk, maar niet essentieel, om de stabiliteit tijdens her-onderdompeling te behouden (**Hoofdstukken 4 en 6**).

Daarnaast wijst dit proefschrift op bepaalde verbeteringsmogelijkheden in de twee onderzochte strategieën om hun potentieel volledig te benutten om zo een hoger TRL (Technology Readiness Level) en uiteindelijke implementatie te bereiken.

(i) **Strategie met diatomietdragers**: Diatomietdeeltjes verspreiden effectief remmerpigmenten en voorkomen ongewenste reacties met de coatingmatrix door oppervlakteaanpassing. Deze aanpassing verbetert ook de remmerlading en de voortdurende bescherming op beschadigde plekken. Er blijven echter uitdagingen bestaan. Bijvoorbeeld: (i) een significant intern volume in diatomiet blijft ongevuld, onderzoek naar alternatieve methoden voor oppervlakteaanpassing, zoals selectieve aanpassing, is nodig om voldoende remmerlading in de deeltjes mogelijk te maken; (ii) er werd slechts één remmer en oppervlakteaanpassingsconditie bestudeerd, wat wijst op de noodzaak van een bredere verkenning van verschillende remmers en oppervlakteaanpassingstechnieken; (iii) de waargenomen synergie met dubbele remmers suggereert potentieel om de afhankelijkheid van zeldzame aardmetalen te verminderen, hoewel verder onderzoek nodig is om de onderliggende mechanismen en beste combinaties te begrijpen.

(ii) **Strategie met gasfaseafzetting van nanolagen**: Deze nieuwe benadering, waarbij zeer dunne nanolagen op remmerdeeltjes worden afgezet, bleek veelbelovend te zijn bij het verbeteren van de dispersie van remmers in de coating en het verminderen van interacties met de epoxy-amidematrix, waardoor langdurige corrosiebescherming wordt geboden. Verdere optimalisatie zou zich kunnen richten op: (i) de impact van de dikte van de nanolaag, de samenstelling ervan en de uniformiteit op de effectiviteit van corrosiebescherming; (ii) het verkennen van de relatie tussen de chemie van corrosieremmers en de vorming en het type nanolaag en de impact ervan op corrosieremming om de veelzijdigheid van deze benadering te vergroten; (iii) het verbeteren van de algehele eigenschappen van de coating, waaronder hechting en mechanische sterkte, om langdurige duurzaamheid te waarborgen; en (iv) het optimaliseren van het gasfaseafzettingsproces om consistentie, schaalbaarheid en kosteneffectiviteit in praktische toepassingen te bereiken.

# 总结

本论文的主要目标是验证两种将高效有机缓蚀剂应用于航空航天涂层的策略，并建立设计此类涂层的基本准则。每一章都探讨了与腐蚀、有机缓蚀剂和涂层系统相关的重要科学和工业挑战，采用了新开发的缓蚀剂负载策略、实验室规模的原位光学技术、电化学、光谱和表面技术以及工业技术。

第一章介绍了防腐航空航天涂层领域、有机缓蚀剂的保护机制以及将这些缓蚀剂整合到涂层中的一系列策略，从纳米/微载体到本文引入的气相沉积到有机颗粒上的方法。文献综述强调了以下两个方面的信息：(i) 缓蚀剂层稳定性作为其与表面和环境相互作用的重要因素，以及 (ii) 在涂层中负载大量有机缓蚀剂的策略，以确保缓蚀剂在长期和循环保护中的完全可用性。本章最后概述了研究目标，并将论文分为三个部分。

第一部分（第二章）在论文开头介绍了在模型飞机涂层和高要求的工业测试背景下，使用天然二氧化硅微载体负载无机和有机缓蚀剂。为此，我们采用了之前建立的硅藻土缓蚀剂负载策略，将这些载体负载到实验室规模的模型飞机底漆中，并通过盐雾喷涂测试和滴液测试评估其耐腐蚀性能。这些加速测试在一定程度上模拟了飞机遇到的恶劣环境条件，通常用于筛选防腐涂层并提高技术成熟度等级（TRL）。结果表明，$Ce(NO_3)_3$ 负载的硅藻土在保护性能上优于负载两种有机缓蚀剂的硅藻土。然而，负载两种有机缓蚀剂的硅藻土载体与使用 $Ce(NO_3)_3$ 和 2,5-二巯基-1,3,4-噻二唑（HDMTD）的硅藻土之间的协同作用是非常有效的策略，虽然仍有改进空间，但在减少稀土基缓蚀剂和其他关键原材料在防腐中的使用方面具有良好的潜力。

第二部分（第三、四、五章）深入探讨了所选有机缓蚀剂（HDMTD 和 KDMTD）的保护机制，以及为了实现其在硅藻土载体中的有效负载所做的技术改进。

第三章比较了两种化学结构相似的缓蚀剂盐（即 HDMTD 和 KDMTD）负载的硅藻土颗粒在涂层中的行为，强调了缓蚀剂酸度和离子状态相对于浓度的重要性。虽然 HDMTD 在溶液中表现出较高的保护作用，但由于与环氧胺的副反应，其在环氧涂层中的性能有所降低。相比之下，由于其离子状态，KDMTD 具有高水溶性和与聚合物反应活性较低等优点。两种缓蚀剂均采用硅藻外壳作为微载体被纳入涂层。结果表明，缓蚀剂的硅藻土载体的负载并不能完全限制环氧胺进入载体。因此，HDMTD 与涂层的反应相对比 KDMTD 更强烈，因此 KDMTD 的释放速度更快、释放量更大。光学分析显示，这种更高的释放量还与 KDMTD 在“涂层出汗”现象有关，这归因于其高度吸湿的特性。涂层的原位反射显微镜能够分析划痕处的暴露金属以及周围的涂层活动。结果显示，对于 HDMTD-硅藻土样品，在所有测试的 pH 条件下（pH 5, 7, 10）退化水平极低（仅限于 IM 的溶解），即使在湿干循环后，缓蚀剂的释放也较慢且较少。有趣的是，当使用酸性 pH 值（pH 5）时，KDMTD-硅藻土样品显示出相当的抑制效率，但在 pH 7 和 10 时，尽管释放的缓蚀剂量较高，但退化相对更严重。本章工作强调了优化缓蚀剂结构和离子状态的重要性，而不是单纯依赖释放浓度，以增强防腐保护，并暗示了 KDMTD 在酸性 pH 条件下和解决吸湿性缓蚀剂加载挑战的前提下的潜在用途。

第四章解决了第三章中提出的一些与 KDMTD 使用相关的挑战，并探讨了硅藻土表面改性是否会影响 KDMTD 在硅藻土中的负载和释放，以及如何保护它免受涂层和湿气的影响，以减少“涂层出汗”现象，这是限制这种高水溶性抑制剂使用的两个方面。为此，使用了三种具有不同烷基链长度（C4、C8、C18）的三氯硅烷对 Aulacoseira 硅藻土（DE）进行了改性，然后再进行 KDMTD 的负载。结果显示，C8 链长度为最佳，吸附量提高了 3.5 倍，释放量提高了 35%（即释放了所加载抑

制剂的 70-75%），与未改性表面相比。在有机涂层中，C8 改性的 DE-KDMTD 颗粒在环氧胺基树脂基质中也表现出更好的分散性，树脂渗入硅藻土颗粒的情况极少，使得根据涂层的释放研究，大约 35%更多的抑制剂可以释放出来。与第三章的结果相比，反射显微镜显示，使用 C8 改性硅藻土的 KDMTD 在 pH 7 时在受损部位提供了良好的保护，尽管局部腐蚀未完全消除。在 pH 5 时，观察到极好的防腐保护，且无可检测的退化迹象。再浸没测试显示，含有 C8 改性 DE 颗粒的涂层在所研究的浸泡和再浸泡条件下很好地保持了其保护效率。这些发现表明，尽管“涂层出汗”问题尚未完全解决硅藻土的表面改性能够更有效地负载 KDMTD，最小化与涂层基质的负面相互作用，并通过增强抑制剂释放，改善在受损部位的持续保护。

第五章深入探讨了在 HDMTD 存在下观察到的 AA2024-T3 合金高防腐保护的基本机制，强调了少量 NaCl 浓度作为提高腐蚀抑制剂效率的因素，并引入了抑制层稳定性这一在防腐保护中尚未深入研究的因素。为此，AA2024-T3 合金样品在有或没有 1mM HDMTD 的情况下，暴露于不同浓度的 NaCl 溶液（0 到 0.5M）中，并重新浸入未添加抑制剂的 NaCl 溶液中。通过反射显微镜和电化学噪声的宏观分析，以及通过拉曼显微镜和 XPS 的局部金属间相（IM）水平分析，研究了浸泡条件对抑制剂化学状态的影响及其与局部防护的关系。结果显示，即使在富含 NaCl 的电解质中，低浓度的 HDMTD 也能有效抑制腐蚀。随着铝（氢）氧化物的减少，HDMTD 的吸附量增加，尤其是在较高的 NaCl 水平下，并且更多地集中在 S 相上，尽管它存在于整个表面上。不同 NaCl 浓度下的相互作用类型不同，低 NaCl 水平下以更稳定的化学吸附为主。在没有抑制剂的 NaCl 溶液中重新暴露时，尤其是在含少量 NaCl 的条件下形成的抑制层样品中，抑制层的稳定性得到了确认，从而形成了更稳定和保护性更强的层。这些发现为 HDMTD 作为 AA2024-T3 合金腐蚀抑制剂的保护机制提供了新的见解。随着金属表面 HDMTD 的成分变化，以及 NaCl 和酸度在形成稳定抑制层中的作用的影响，这些发现为开发更稳定的抑制层铺平了道路。

第三部分（第六和七章）提出了一种新颖的策略，基于在流化床中对 HDMTD 微粒进行气相沉积纳米层，以减少 HDMTD 与聚合物基质的反应性，同时最大化 HDMTD 在涂层中的添加量。

第六章介绍并验证了这一新策略，通过在 HDMTD 微粒上沉积 $TiO_x$ 纳米层，并将其掺入应用于航空级铝合金 AA2024-T3 的环氧胺基树脂基质中。操作中的反射显微镜、热分析和抑制剂释放测试表明，20 纳米厚的纳米层显著改善了颗粒的分散性，并减少了 HDMTD 与环氧胺基树脂基质的相互作用。局部操作中的反射显微镜结合电化学电位噪声和释放测试证明，气相沉积的纳米层不仅改善了分散性，还增强了抑制剂的释放，并在暴露于湿洗干燥循环的受损部位提供了有效的长期保护。研究结果还强调了在初始浸泡过程中释放足够的抑制剂的重要性，以确保初始保护和在再浸泡过程中形成稳定的抑制层，这些层可以通过低浓度抑制剂的额外释放进一步维持。

第七章进入了更高的技术就绪等级，研究了这一新策略在实验室规模飞机模型底漆中的潜力。使用 3%、6%和 10%颜料体积分数（PVC）的 $TiO_x$ 纳米层涂覆的 HDMTD 微粒（HDMTD/$TiO_x$）在 25% PVC 涂层中制备飞机底漆，并将其应用于 AA2024-T3 基板。使用操作中的反射显微镜在 0.5M NaCl 溶液中浸泡 24 小时、7 天滴液测试和 1000 小时中性盐雾喷射（NSS）测试评估了受损部位的防腐保护。结果表明，所有涂层在这三种测试中均表现出高水平的防护。然而，纳米层保护的抑制剂颜料在 NSS 测试中引起了一些起泡现象。在所有涂层中，6% PVC 的 HDMTD/$TiO_x$ 涂层（抑制剂含量为 4.3 wt%，类似于第 2 章中的涂层）在受损部位的强防护性和最小化起泡现象之间提供了最佳平衡。研究表明，在所进行的测试中，较低有机腐蚀抑制剂含量的涂层在避免副反应的前提下，仍能在划痕处提供较高水平的保护。研究结果突出了这一新策略的潜力，以及减少起泡和提高耐腐蚀保护持久性的开发空间，同时考虑到纳米层的化学性质和层特性以及可用腐蚀抑制剂化学品的多样性。

总体而言，本论文研究和讨论的两种负载策略（硅藻土载体和气相沉积纳米层）为克服在使用有机抑制剂设计航空防腐涂层中长期存在的挑战提供了新的见解。本论文的研究案例（AA2024-T3合金、HDMTD抑制盐）中识别出的以下关键方面可能具有普遍价值，应在设计含有机抑制剂的防腐涂层时予以考虑：

(i) 除了涂层中抑制剂的浓度外，诸如酸度、抑制剂的离子状态（第三章）以及电解质中存在的不稳定氧化物的离子（如 $Cl^-$）（第五章）等因素，在有机抑制剂提供的抑制机制、效率和抑制层稳定性中起着关键作用。

(ii) 将有机抑制剂隔离在有机涂层基质中，可以有效改善抑制剂颗粒在涂层中的分散，减少不必要的副反应，并确保足够的抑制剂释放。这种方法通过硅藻土表面改性（第四章）和在抑制剂微粒上气相沉积纳米层（第六和七章）得到了证明，显著增强了防腐效果。

(iii) 在初始浸泡过程中，快速且足够的抑制剂释放对于防止金属间相（IMs）的快速脱合金化并建立稳定的抑制层至关重要。虽然持续释放也很重要，但在再浸泡过程中保持稳定性并非必不可少（第四和六章）。

此外，论文还强调了两种策略的改进空间，以充分发挥其潜力并达到更高的技术就绪水平（TRL）和最终的实际应用：

(i) 硅藻土载体策略：硅藻土颗粒通过表面改性有效分散了抑制剂颜料，并防止了与涂层基质的副反应。该改性还增强了抑制剂的负载和在受损部位的持续保护。然而，仍然存在一些挑战。例如：（i）硅藻土中显著的内部体积尚未填满，需要研究替代的表面改性方法，如选择性改性，以确保抑制剂能够充分填充颗粒内部；（ii）只研究了一种抑制剂和一种表面改性条件，表明需要更广泛地探索不同的抑制剂和表面改性化学；（iii）双抑制剂的协同效应表明可以减少对稀土抑制剂的依赖，尽管还需要进一步研究以了解其背后的机制和最佳组合。

(ii) 气相沉积纳米层策略：这一新颖的方法涉及在抑制剂颗粒上沉积非常薄的纳米层，在改善抑制剂在涂层中的分散性和减少与环氧胺基树脂基质的相互作用方面展现了很大潜力，从而提供了持续的防腐保护。进一步优化的方向可以集中在：（i）纳米层厚度、成分和均匀性对防腐效果的影响；（ii）探讨腐蚀抑制剂化学与纳米层的形成及类型之间的关系，以及其对防腐效果的影响，以增强该方法的多样性；（iii）改善涂层的整体性能，包括附着力和机械强度，以确保长期耐用性；以及（iv）优化气相沉积工艺，以实现一致性、可扩展性和实际应用中的成本效益。

# Contents

# Chapter 1
# Introduction

## 1.1 Background on anticorrosion aerospace coatings

For several decades, aluminum alloys (AAs) have been the primary structural materials in aircraft due to their excellent properties. The Cu-rich 2xxx series alloys (e.g. AA2024-T3, AA2219-T6) are favored for fuselage skin and frame parts because of their good strength-to-weight ratio and fatigue resistance. The Zn-rich 7xxx series alloys (e.g. AA7075-T6, AA7050) are used for a wide variety of structural parts due to their high strength. The Mg-Si-rich 6xxx series alloys (e.g. AA6061-T6, AA6063) are used for wing and fuselage structures due to their good mechanical properties.[1-3] Despite the widespread use of composite materials in recent years, high-strength aluminum alloys remain essential. [4, 5] Additionally, aluminum alloys are highly recyclable, aligning with the principles of sustainable development.[6, 7] Nevertheless, most aerospace aluminum alloys, particularly AA2024-T3 used in this thesis, are limited by their high corrosion sensitivity. In alloys from the 2xxx and 7xxx, the alloying elements providing enhanced mechanical properties are also responsible for localized corrosion.[8, 9]

Corrosion of metallic substrates not only leads to high costs but also has a massive impact on global $CO_2$ emissions. For instance, the cost of corrosion is estimated to be equivalent to 3-4% of the global GDP. Additionally, the $CO_2$ emission from the steel production to replace corroded steel is estimated to account for 4.1-9.1% of the total emissions by 2030 for the European Union and U.S. [10]

Even though depending on the application the protective coating system can consist of 2 up to 6 layers with different functions, the most common corrosion protection system for aircraft includes up to three layers: a pretreatment layer, a primer, and a topcoat (in specific areas), as illustrated in Figure 1.1.[11, 12] The first layer is a thin pretreatment layer. Traditionally, this has been a chromium (VI) anodizing layer (CAA) or chromium (VI) conversion coating, but it is currently replaced with either chromium (III) conversion coating or an anodizing layer using tartaric-sulfuric acid (TSA) and boric-sulfuric acid (BSA). [13,14] The primer layer, which varies in thickness from 5 to 200 µm in aerospace applications, consists of an organic resin matrix, typically epoxy-amine, loaded with corrosion inhibitor and other active and non-active pigments up to 25-35% pigment volume concentration (PVC). The primer primary function is to provide

active corrosion protection. This implies that, when the coating is damaged and exposed to moisture, soluble corrosion inhibitors will dissolve and diffuse to the damage site to interact with the AA substrate in various manners to prevent corrosion attack. [15, 16] Finally, the topcoat, typically polyurethane based, acts as a barrier against mechanical damage and degrading environmental factors such as UV, moisture and chemicals. [17]

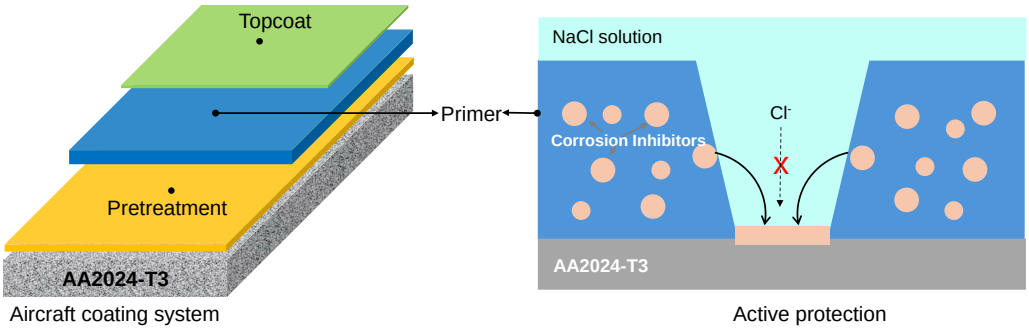


Figure 1.1 Schematic illustration of an aircraft coating system (left). Right image represents a primer anticorrosive coating layer with embedded corrosion inhibitors. The inhibitors are released to the damage site to create a protective layer at the metal surface.

When dealing with the primer layer, chromium (VI)-based compounds have been for decades the most effective and preferred corrosion inhibitors.[18] However, hexavalent Cr compounds are known to be carcinogenic and genotoxic[19] and are banned in 2024 by the EU REACH regulation. [20] Significant efforts have been made for decades to find suitable corrosion inhibitors alternative to Cr(VI) that match the effectiveness of chromate in organic coatings.[18, 21, 22] However, matching high efficient protection levels at all pHs, environmental conditions, applications, and using existing polymeric matrices (e.g. epoxy-amine) has proven a significant challenge despite the broad range of inhibitors proposed.[23]

One of the largest categories of corrosion inhibitors explored for AA2024-T3 are inorganic and hybrid inhibitor salts based on rare-earths (e.g. $La^{3+}$, $Ce^{3+}$ and $Pr^{3+}$) and lithium.[24, 25, 29] The two groups rely on different mechanisms to protect the underlying alloy structures. Rare-earth ions react with the $OH^-$ produced at the cathodic sites hence forming protective oxide/hydroxide deposits that inhibit the cathodic oxygen reduction reaction. The combination of rare earth ions with organic compounds, such as in the cases of cerium dibutyl phosphate ($[Ce(dbp)_3]$), cerium diphenyl phosphate $[Ce(dpp)_3]$, and cerium-diethyldithiocarbamate (Ce-DEDTC), leads to even more interesting results as they suppress both anodic and cathodic reactions and provide enhanced inhibition. [26-28] However, the depositions formed by either rare earth salts or complexes remain less stable than $Cr_2O_3$ in acidic environments[29] requiring additional research to understand how to optimize their release and improve their stability.[30] Lithium salts offer protection of alloys after an exothermic reaction dissolving the aluminum top surface and forming hybrid protective bilayer films consisting of a dense bottom layer and a top porous layer formed by Li/Al layered double

hydroxide structures. [31-33] Despite their efficacy, the stability of these layers [31, 33, 34] and the increasing cost of lithium in competition with batteries and biomedical applications also pose significant challenges for industrial use.[35] Additionally, the extraction and production of rare-earth elements and lithium poses challenges, magnified by their geopolitical value reflected in their enlisting as critical raw materials (CRMs) by all major regional powers as the European Union, China and the USA. These challenges call for the continued search for novel strategies (e.g. self-healing coatings able to close damages to recover barrier properties[36] ) and corrosion inhibitors (e.g. organic inhibitors) to protect aircraft and other engineering structures with sustainable and environmentally friendly solutions.

## 1.2 Organic inhibitors

Organic inhibitors have also received growing attention because of their high efficiency, production versatility and accessibility, relatively low toxicity of many compounds, and multi-metal protection character (i.e. low-substrate selectivity). One notable advantage of organic inhibitors is that, for the same inhibition levels, they generally add less weight compared to inorganic ones. [37-39] Moreover, a mechanistic difference with inorganic inhibitors, is that the inhibition provided by organic inhibitors is mostly due to the adsorption (physisorption and/or chemisorption) of inhibitor molecules on the metallic surface leading to, in the best case scenario, an insoluble protective layer. [40, 41] In other words, organic inhibitors mostly have a generalist inhibition effect acting on both anodic and cathodic sites despite some local preferences as discussed in this thesis.

It has been well established that heteroatoms (N, S, O and P) are crucial for the corrosion inhibition properties of organic inhibitors on metallic surfaces such as copper, iron, and aluminum alloys.[42-44] Among them, the most widely explored compounds are azole derivatives,[45, 46] mercapto compounds, [47, 48] quinoline, [49, 50] amide and carbonyl derivatives, [51] drugs and dyes and a growing amount of natural extracts. [44, 52-54] The polar groups (e.g., $-NO_2$, $-NH_2$, -SH, -OH, $-OCH_3$, and $-CH_3$) and unsaturated bonds (double and triple) in these organic compounds can serve as the adsorption centers using the lone pair or $\pi$ electrons.[55]

The corrosion inhibition properties of heterocyclic compounds on metals involve both physical and chemical adsorption, as illustrated in Figure 1.2. [56] Physical adsorption occurs through the electrostatic attraction between charged organic inhibitors and the charged metal surface. Chemisorption involves the vacant orbital of the metal atom at the surface interacting with the lone pair electrons of heteroatoms in the organic inhibitor. Such an interaction results in the formation of strong chemical bonds between the nonionic organic corrosion inhibitor molecules and the metal surface. The adsorption process can be influenced by factors such as the chemical structure, the concentration of the inhibitors, the surface charge distribution of the metals, and the environment (ions, pH, temperature, UV, etc).[57, 58] Furthermore, the inhibition efficiency of organic corrosion inhibitors usually depends on the adsorption strength, the metal surface coverage efficiency (homogeneity and local vs global character) and the formation of monomolecular or multimolecular layers. [54, 59, 60]

Due to the structural complexity and various synthesis possibilities of organic inhibitors, a deeper understanding of their inhibition mechanisms is essential. [61, 62] Density functional theory (DFT) calculations combined with electrochemical tests as electrochemical impedance spectroscopy (EIS) and potentiodynamic polarization tests (PP) have been used as primary tools to provide atomic level insights into the inhibition mechanism, such as the effect of molecular structure and ions on the adsorption on Al-atoms, and corrosion inhibition efficiency values. [63, 64] However, the direct experimental observation of the presence of such thin organic layers on metals requires other advanced and less commonly available analytical methods such as XPS and ToF-SIMS. [41, 65] Additionally, investigations into the stability of these inhibitor layers are rare, both at the laboratory research scale and at the industrial level. It has been widely observed that the inhibited metal substrate will eventually corrode, but the underlying reasons are not well understood. Therefore, investigating the stability of the inhibitor layers is essential. [15]

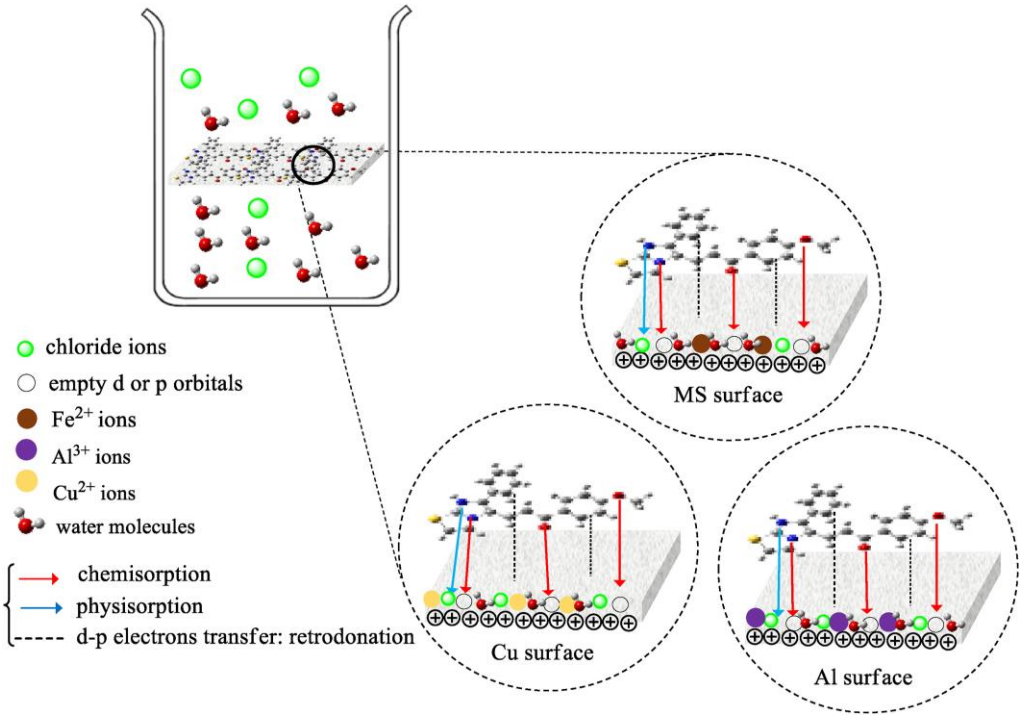


Figure 1.2 Schematic illustration of organic inhibitor molecules adsorbing on different metal surfaces. The chloride ions are adsorbed on the metal surfaces (Fe, Al and Cu) and attract the protonated organic inhibitor molecules via physisorption. Chemisorption occurs due to the sharing of lone pair electrons on heteroatoms and p-electrons of aromatic ring with the vacant d or p-orbitals of metals. Reprinted from [56] with permission from Elsevier.

# 1.3 Organic inhibitors in primers relevant for aircraft

### *1.3.1 Coating binder–organic corrosion inhibitor challenges*

Organic primers used in aircraft typically use two-component cross-link epoxy-amine/polyester resins as the main organic component. Epoxy-amine primer technology is generally preferred for its versatility, good adhesion to metal substrates, effective corrosion resistance, and the ability to balance chemical resistance, flexibility, impact resistance, and hardness to meet aerospace industry standards. The precise choice of epoxy resins (typically a mixture of different resins) and curing agents depends on the desired coating properties and is generally proprietary. Most epoxy resins are formulated with amine through an addition reaction that opens the ring and forms a crosslinked network, as shown in Figure 1.3.[66] [67] The primer formulation also includes fillers/pigments, active pigments (i.e., corrosion inhibitors), solvents, and additives.

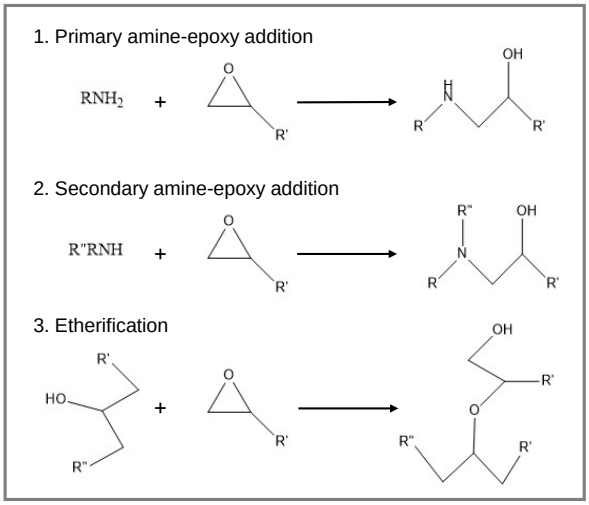


Figure 1.3 Epoxy-amine curing reaction

One of the factors that can interfere with the cross-linking process of the epoxy-amine are other organic molecules present in the formulation, including any organic corrosion inhibitor added as pigment. As a result of these reactions, coating properties mentioned above are significantly affected while inhibition potential of good inhibitors in solution typically drops when in the coating due to inhibitor fixation and deactivation. In particular, epoxy groups and amines are very reactive between them but also with other functional groups such as carboxylic acids and thiols typically present in highly efficient organic inhibitors like diethyldithiocarbamate (DEDTC),[68] 2,5-dimercapto-1,3,4-thiadiazole (DMTD)[69] and hydroxyl-terminated poly(amine-ester)[70].

On the other hand, the resistance to degradation of organic coatings decreases over time due to environmental factors. When highly soluble hydrophilic inhibitors are unevenly distributed in the coating, low cross-linked hydrophilic regions can form. Environmental stress and moisture exposure cause these hydrophilic and low crosslinking regions to expand and intercommunicate through the entire coating thickness, creating a percolating network. This pathway allows rapid water uptake and diffusion of low Mw species and salts and leads to under-film delamination, blistering, local corrosion and, eventually, coating failure as depicted in Figure 1.4.[71-73] Moreover, the process is accompanied with local pH variations, which could cause further delamination. [74-76] This blistering phenomenon is a common negative side effect of using highly soluble corrosion inhibitors aggravated by uneven dispersion.

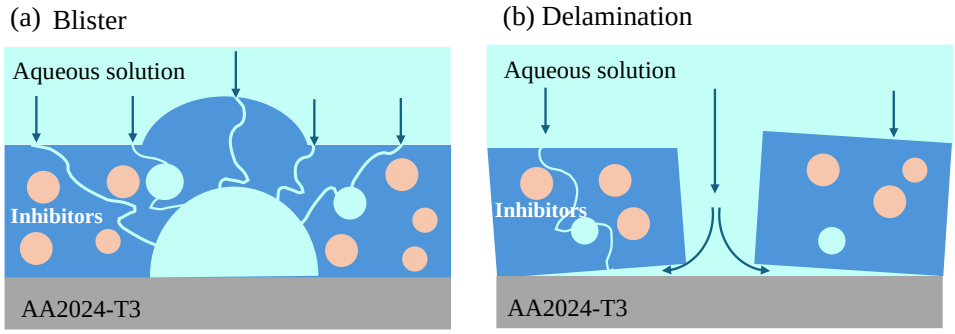


Figure 1.4 Water uptake and corrosion inhibitors dissolution in the coating leading to (a) blister and (b) delamination.

### *1.3.2 Reducing unwanted interactions: from nano to micro carriers*

As discussed above, incorporating organic inhibitors into the organic coating matrix significantly hinders their inhibitory activity and negatively affects the coating properties. Encapsulation using nano/microcarriers is the most common strategy to avoid such negative effects, as it protects the highly reactive inhibitors from interacting with the polymer matrix. This allows the inhibitors to be released and in many cases prevents the coating from rapid failure through blistering.[15, 77-79] Besides isolation, some of the carriers allowed inhibitor release through dissolution in water accelerated or induced by triggers as pH changes, [80, 81, 82] ion exchange, [83-85] and mechanical stress from scratching, cutting, or pressing. [86,87] Figure 1.5 summarizes the most important and successful nano and microcarriers reported in literature as carriers of inorganic and organic inhibitors.

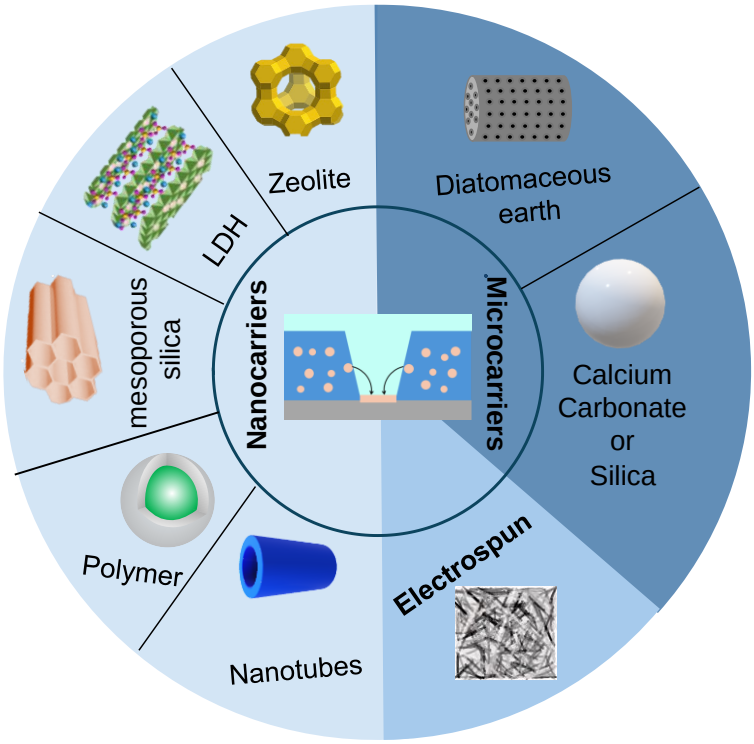


Figure 1.5 Nano/microcarriers for corrosion inhibitors

The biggest advantage of nanocarriers, including nanotubes[86], nanofibers[87], zeolites[79], conductive nanoparticles (e.g., polyaniline and polypyrrole)[88], mesoporous silica[89, 90], layered double hydroxide (LDH) [83-85] and other polymeric nanocapsules[91], is their versatility and good dispersion below the critical pigment volume concentration. For example, 2-Mercaptobenzothiazole (MBT) has been encapsulated in carriers as different as silica nanocapsules, halloysite nanotubes, and ion-exchange clay.[82, 92, 93] However, the relatively low loading capacity of inhibitors in nanocarriers and the relatively low CPVC of nanoparticles in coatings limits the use of the nanocarriers and their efficiency for long term protection at relatively large damages (e.g. >100 µm wide). [94-96]

To overcome the loading and dispersion limitations of nanocarriers and based on the fundamental principles of highly efficient Cr(VI) primers using micron sized particles, more recent research has highlighted the potential of microcarriers such as $CaCO_3$ [80] synthesized or natural silica microparticles (diatomaceous earth) [97-99] or the use of macroscopic interconnected electrospun nanonetworks[100]. Synthesized calcium carbonate porous microparticles (1µm diameter) were used to load different inhibitors, cerium nitrate, salicylaldoxime and 2,5-dimercapto-1, 3, 4-thiadiazole (DMTD). [80] These particles are sensitive to acidic pH which, makes them soluble and allows for an increased inhibitor release. The reported results showed higher levels of barrier performance and protection for intact coatings when the $CaCO_3$ was loaded with inorganic

inhibitor, $Ce(NO_3)_3$ , than with organic inhibitor DMTD. [80] In our previous works [97, 98] we introduced the use of natural silica microparticles from fossilized diatom exoskeletons (diatomaceous earth (DE)) as a versatile and economic route to load inhibitors as $Ce(NO_3)_3$ and DMTD (Figure 1.6). While both coatings showed excellent barrier protection, at large damages (1mm wide, 350 µm deep) sites, the coatings with $Ce(NO_3)_3$ loaded in DE particles showed excellent inhibition, while the coatings loaded with DMTD-DE showed good initial protection lost at relatively long immersion times (<10 days). Interestingly, the use of DE loaded with DMTD allowed decreasing the use of Ce-loaded DE by half (0.5Ce-DE/0.5MTD-DE) and still protect for 30 days immersion, hence pinpointing at interesting synergetic behaviors but also the difficulty to load directly organic inhibitors in DE carriers. Moreover, the loading method used allowed only 2% of the available internal volume of DE particles to be filled with inhibitors, suggesting low inhibition might be related to insufficient loading and release. [97, 98]

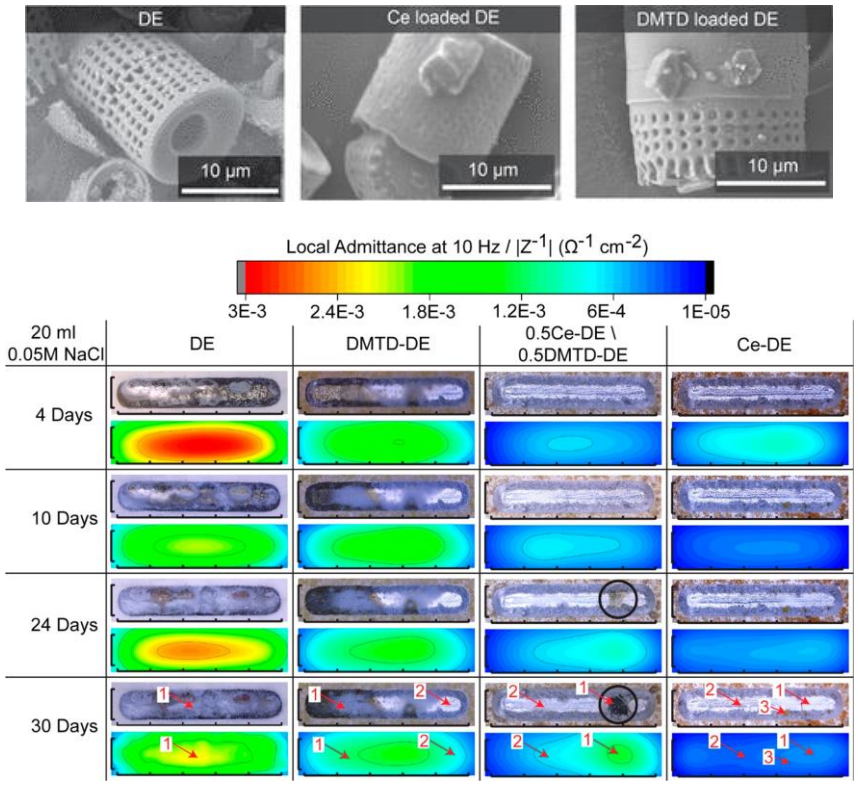


Figure 1.6 Optical images and local EIS maps of large scratches (1mm wide by 350 um depth) performed on epoxy coatings containing diatomaceous earth loaded with Ce and DMTD inhibitors applied to AA2024-T3. [97, 98]

### *1.3.3 Gas-deposition techniques to create thin oxide layers: an unexplored route to protect corrosion inhibitors*

Gas-phase deposition techniques, including physical vapor deposition (PVD), chemical vapor deposition (CVD), atomic layer deposition (ALD), and molecular layer deposition (MLD) are typically used to create homogeneous thin films on flat, porous, and regular substrates, primarily for electronic devices.[101, 102] Recently, gas-phase deposition in a fluidized bed reactor allowed extending the concept of thin film deposition from flat large surfaces to microparticles considering applications in pharmaceutical, catalysis and energy.[103-105] The deposition process can involve either continuous exposure of substrates to precursors, as in CVD, or, as illustrated in Figure 1.7, sequential exposures of particles to precursors and co-reactants, separated by purging steps and repeated for varying cycles to deposit nanofilms, a method known as ALD.[106] The sequential exposure in ALD allows for precise control over film thickness and composition. For instance, $Al_2O_3$, $TiO_2$, and $SiO_2$ have been successfully applied as nano-thin films on water soluble organic drug particles via atomic layer deposition in fluidized bed reactors to control drug particle dissolution rates in solution. [107-109] Nevertheless, these techniques have so far not been used to protect organic corrosion inhibitors and attracted our interest in the course of this project as an interesting strategy to maximize the amount of protected inhibitor embedded in coatings.

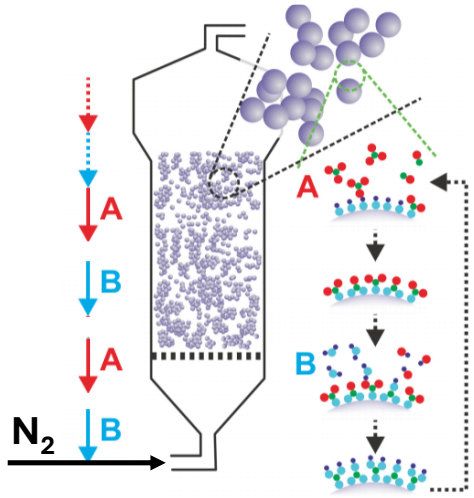


Figure 1.7 Gas-phase deposition of a thin film on particles in a fluidized bed reactor.[106]

Organic corrosion inhibitors share some similar properties with drug microparticles, such as moisture sensitivity (hygroscopicity, solubility) and adhesive and cohesive characteristics. Their higher hygroscopicity, irregular shapes, and broad particle size distributions pose challenges for deposition due to reduced flow, agglomeration, and irregular layer growth. A preliminary attempt to use this technique on MBT corrosion inhibitor led to disappointing results [110] yet the lack of systematic approach and understanding on the causes of low performance leaves open space to further explore this route for corrosion inhibition as will be shown in this thesis.

## 1.4 Objective and Outline

The overall scientific objective of this thesis is to demonstrate two promising strategies to incorporate very efficient organic corrosion inhibitors in aerospace organic coatings. To do this it was necessary to (i) establish fundamental understanding on the inhibition mechanisms of the selected organic inhibitors for AA2024-T3 and their functioning when embedded in coatings as well as (ii) establishing the fundamental strategies that will allow embedding organic inhibitors in large amounts and with low coating-inhibitor reactivity to ensure long term and cyclic protection at large damages. To this aim, lab scale techniques based on operando optics and electrochemistry as well as industrial techniques were developed and implemented.

This thesis is structured into three main sections, as depicted in Figure 1.8.

In the *first section* (**Chapter 2)**, following this introduction, we evaluated the state-of-the-art technology using natural silica microcarriers (fossilized diatom exoskeletons or diatomite) to load inorganic and organic corrosion inhibitors. To this aim, we used the established loading strategy we presented in previous works, loaded lab-scale aircraft primers with these carriers, and studied their corrosion behaviour with a range of techniques. This allowed establishing a foundational understanding of the existing technology and its limitations. During this phase, it became clear the large room for improvement to allow an effective incorporation of organic corrosion inhibitors as good as 2,5-Dimercapto-1,3,4-thiadiazole (DMTD).

In the *second section* of the thesis the focus is on the in-depth fundamental understanding of the mechanisms that make the selected organic inhibitor (DMTD) a very interesting candidate for protection of AA2024-T3. To this aim we studied the advantages, boundaries and underlying mechanism for use of HDMTD and KDMTD in exoskeletons and in particular how the ionic state of the inhibitor is more relevant than the concentration (**Chapter 3**); We also explored strategies to increase the loading of KDMTD in diatomite to make this more soluble and less epoxy-amine reactive salt version of DMTD a viable option for corrosion protection. The focus was on the surface modification of diatomite layers and the stability of the inhibiting layers on the metal **(Chapter 4**). Subsequently, the inherently superior inhibition performance of HDMTD was uncovered, leading to an in-depth study on the inhibition mechanisms of HDMTD on bare AA2024-T3, with a particular focus on how small amounts of NaCl enhance corrosion protection (**Chapter 5**).

The *last section* of the thesis addresses a new strategy using gas-deposition in fluidized bed as an interesting strategy to embed organic inhibitors in reactive polymers as epoxy-amine networks in large amounts. The proof of concept of this idea is established and validated in **Chapter 6** with a strong focus on the concept of stability of inhibiting networks. Finally, **Chapter 7** demonstrates this new strategy in the context of a lab-scale aircraft model primer and compares it to the diatom exoskeleton system.

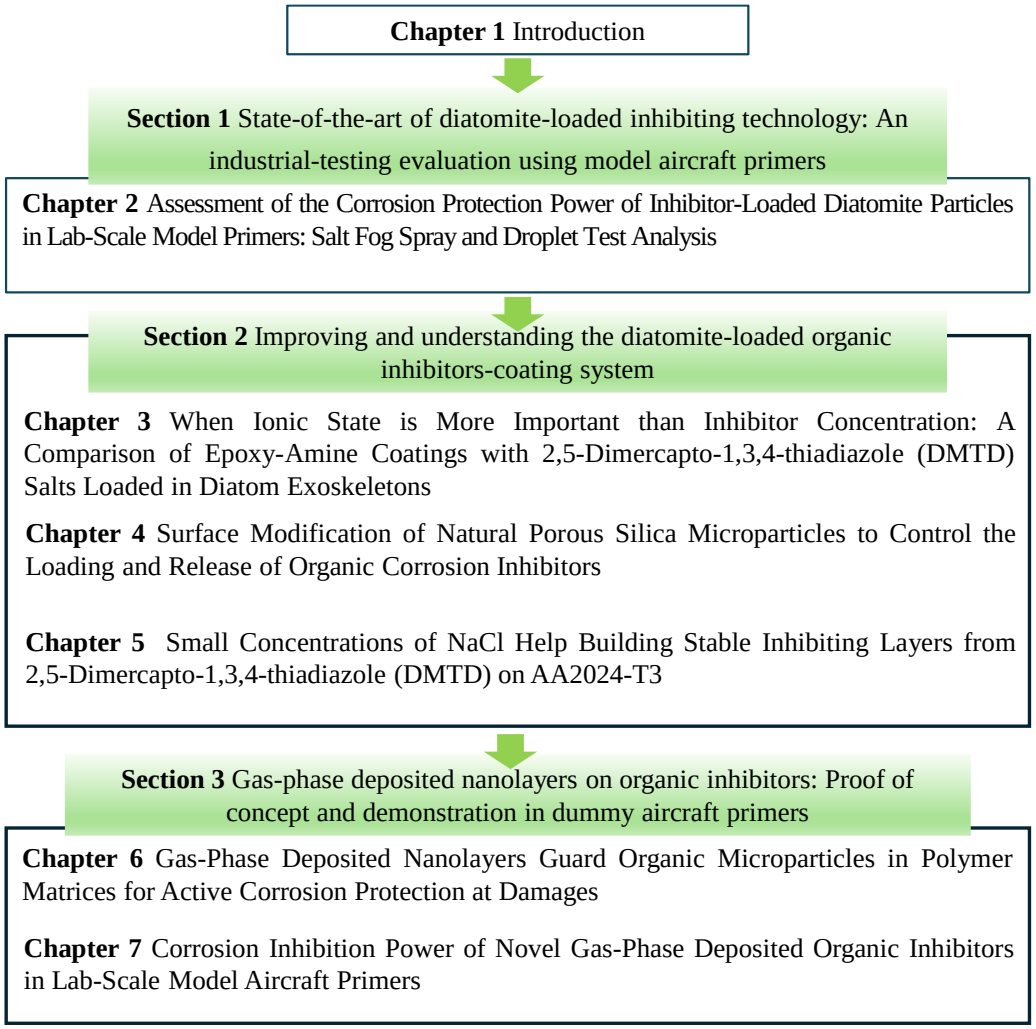


Figure 1.8 Thesis outline

## 1.5 References

(1) Nakai, M.; Eto, T. New aspect of development of high strength aluminum alloys for aerospace applications. *Materials Science and Engineering: A* **2000**, *285* (1-2), 62-68.
(2) Rambabu, P.; Eswara Prasad, N.; Kutumbarao, V.; Wanhill, R. Aluminium alloys for aerospace applications. *Aerospace materials and material technologies: volume 1: aerospace materials* **2017**, 29-52.
(3) Williams, J. C.; Starke Jr, E. A. Progress in structural materials for aerospace systems. *Acta materialia* **2003**, *51* (19), 5775-5799.
(4) Tiwary, A.; Kumar, R.; Chohan, J. S. A review on characteristics of composite and advanced materials used for aerospace applications. *Materials Today: Proceedings* **2022**, *51*, 865-870.
(5) Dursun, T.; Soutis, C. Recent developments in advanced aircraft aluminium alloys. *Materials & Design (1980-2015)* **2014**, *56*, 862-871.
(6) Li, S. S.; Yue, X.; Li, Q. Y.; Peng, H. L.; Dong, B. X.; Liu, T. S.; Yang, H. Y.; Fan, J.; Shu, S. L.; Qiu, F. Development and applications of aluminum alloys for aerospace industry. *Journal of Materials Research and Technology* **2023**.
(7) Bulei, C.; Kiss, I.; Alexa, V. Development of metal matrix composites using recycled secondary raw materials from aluminium wastes. *Materials Today: Proceedings* **2021**, *45*, 4143-4149.
(8) Benavides, S. Corrosion control in the aerospace industry. **2009**.
(9) Hughes, A. E.; Parvizi, R.; Forsyth, M. Microstructure and corrosion of AA2024. *Corrosion Reviews* **2015**, *33* (1-2), 1-30.
(10) Iannuzzi, M.; Frankel, G. The carbon footprint of steel corrosion. *npj Materials Degradation* **2022**, *6* (1), 101.
(11) Peltier, F.; Thierry, D. Review of Cr-Free Coatings for the Corrosion Protection of Aluminum Aerospace Alloys. *Coatings* **2022**, *12* (4). DOI: 10.3390/coatings12040518.
(12) Bierwagen, G. Next generation of aircraft coatings systems. *Journal of Coatings Technology* **2001**, *73* (915), 45-52.
(13) Zhao, J.; Xia, L.; Sehgal, A.; Lu, D.; McCreery, R.; Frankel, G. S. Effects of chromate and chromate conversion coatings on corrosion of aluminum alloy 2024-T3. *Surface and Coatings Technology* **2001**, *140* (1), 51-57.
(14) Paz Martínez-Viademonte, M.; Abrahami, S. T.; Hack, T.; Burchardt, M.; Terryn, H. A review on anodizing of aerospace aluminum alloys for corrosion protection. *Coatings* **2020**, *10* (11), 1106.
(15) Sinko, J. Challenges of chromate inhibitor pigments replacement in organic coatings. *Progress in organic coatings* **2001**, *42* (3-4), 267-282.
(16) Scholes, F.; Furman, S.; Hughes, A.; Nikpour, T.; Wright, N.; Curtis, P.; Macrae, C.; Intem, S.; Hill, A. Chromate leaching from inhibited primers: Part I. Characterisation of leaching. *Progress in Organic Coatings* **2006**, *56* (1), 23-32.
(17) Kunst, S. R.; Beltrami, L. V. R.; Cardoso, H. R. P.; Menezes, T. L.; de Fraga Malfatti, C. l. UV curing paint on hybrid films modified with plasticizer diisodecyl adipate applied on tinplate: the effects of curing temperature and the double layer. *Industrial & Engineering Chemistry Research* **2014**, *53* (49), 19216-19227.
(18) Gharbi, O.; Thomas, S.; Smith, C.; Birbilis, N. Chromate replacement: what does the future hold? *npj Materials Degradation* **2018**, *2* (1), 12.
(19) Henkler, F.; Brinkmann, J.; Luch, A. The role of oxidative stress in carcinogenesis induced by metals and xenobiotics. *Cancers* **2010**, *2* (2), 376-396.
(20) Peltier, F.; Thierry, D. Review of Cr-free coatings for the corrosion protection of aluminum aerospace alloys. *Coatings* **2022**, *12* (4), 518.
(21) Mitton, D. B.; Carangelo, A.; Acquesta, A.; Monetta, T.; Curioni, M.; Bellucci, F. Selected Cr (VI) replacement options for aluminum alloys: a literature survey. *Corrosion Reviews* **2017**, *35* (6), 365-381.
(22) Becker, M. Chromate-free chemical conversion coatings for aluminum alloys. *Corrosion Reviews* **2019**, *37* (4), 321-342.

(23) Ma, I. W.; Ammar, S.; Kumar, S. S.; Ramesh, K.; Ramesh, S. A concise review on corrosion inhibitors: types, mechanisms and electrochemical evaluation studies. *Journal of Coatings Technology and Research* **2022**, 1-28.
(24) Bethencourt, M.; Botana, F.; Calvino, J.; Marcos, M.; Rodriguez-Chacon, M. Lanthanide compounds as environmentally-friendly corrosion inhibitors of aluminium alloys: a review. *Corrosion Science* **1998**, *40* (11), 1803-1819.
(25) Matter, E.; Kozhukharov, S.; Machkova, M.; Kozhukharov, V. Comparison between the inhibition efficiencies of Ce (III) and Ce (IV) ammonium nitrates against corrosion of AA2024 aluminum alloy in solutions of low chloride concentration. *Corrosion Science* **2012**, *62*, 22-33.
(26) Ho, D.; Brack, N.; Scully, J.; Markley, T.; Forsyth, M.; Hinton, B. Cerium dibutylphosphate as a corrosion inhibitor for AA2024-T3 aluminum alloys. *Journal of the Electrochemical Society* **2006**, *153* (9), B392.
(27) Markley, T. A.; Hughes, A. E.; Ang, T. C.; Deacon, G. B.; Junk, P.; Forsyth, M. Influence of praseodymium: synergistic corrosion inhibition in mixed rare-earth diphenyl phosphate systems. *Electrochemical and Solid-State Letters* **2007**, *10* (12), C72.
(28) Mohammadi, I.; Shahrabi, T.; Mahdavian, M.; Izadi, M. Cerium/diethyldithiocarbamate complex as a novel corrosion inhibitive pigment for AA2024-T3. *Scientific reports* **2020**, *10* (1), 5043.
(29) Mendez, J. A. C.; Vong, Y. M.; Bueno, J. d. J. P. Cerium and other rare earth salts as corrosion inhibitors—A review. *Protection of Metals and Physical Chemistry of Surfaces* **2022**, *58* (4), 801-810.
(30) Mopon Jr, M.; Mol, A.; Garcia, S. J. Effect of delayed inhibitor supply on AA2024-T3 intermetallic activity: A local in situ analysis with reflected microscopy. *Corrosion Science* **2024**, *230*, 111910.
(31) Visser, P.; Liu, Y.; Zhou, X.; Hashimoto, T.; Thompson, G. E.; Lyon, S. B.; van der Ven, L. G.; Mol, A. J.; Terryn, H. A. The corrosion protection of AA2024-T3 aluminium alloy by leaching of lithium-containing salts from organic coatings. *Faraday Discussions* **2015**, *180*, 511-526.
(32) Visser, P.; Lutz, A.; Mol, J.; Terryn, H. Study of the formation of a protective layer in a defect from lithium-leaching organic coatings. *Progress in Organic Coatings* **2016**, *99*, 80-90.
(33) Li, Z.; Visser, P.; Hughes, A. E.; Homborg, A.; Gonzalez-Garcia, Y.; Mol, A. Review of the state of art of Li-based inhibitors and coating technology for the corrosion protection of aluminium alloys. *Surface and Coatings Technology* **2024**, 130441.
(34) Hughes, A.; Laird, J.; Ryan, C.; Visser, P.; Terryn, H.; Mol, A. Particle characterisation and depletion of Li2CO3 inhibitor in a polyurethane coating. *Coatings* **2017**, *7* (7), 106.
(35) Olivetti, E. A.; Ceder, G.; Gaustad, G. G.; Fu, X. Lithium-ion battery supply chain considerations: analysis of potential bottlenecks in critical metals. *Joule* **2017**, *1* (2), 229-243.
(36) Montano, V.; Vogel, W.; Smits, A.; Van Der Zwaag, S.; Garcia, S. J. From scratch closure to electrolyte barrier restoration in self-healing polyurethane coatings. *ACS Applied Polymer Materials* **2021**, *3* (5), 2802-2812.
(37) Xhanari, K.; Finšgar, M. Organic corrosion inhibitors for aluminum and its alloys in chloride and alkaline solutions: A review. *Arabian Journal of Chemistry* **2019**, *12* (8), 4646-4663.
(38) Goyal, M.; Kumar, S.; Bahadur, I.; Verma, C.; Ebenso, E. E. Organic corrosion inhibitors for industrial cleaning of ferrous and non-ferrous metals in acidic solutions: A review. *Journal of Molecular Liquids* **2018**, *256*, 565-573.
(39) Serdaroğlu, G.; Kaya, S. Organic and inorganic corrosion inhibitors: a comparison. *Organic corrosion inhibitors: synthesis, characterization, mechanism, and applications* **2021**, 59-73.
(40) Donahue, F. M.; Nobe, K. Theory of organic corrosion inhibitors: adsorption and linear free energy relationships. *Journal of the Electrochemical Society* **1965**, *112* (9), 886.
(41) Kuznetsov, Y. I. Organic corrosion inhibitors: Where are we now? Part I. Adsorption. *International Journal of Corrosion and Scale Inhibition* **2015**, *4* (4), 284-310.
(42) Quraishi, M. A.; Chauhan, D. S.; Saji, V. S. *Heterocyclic organic corrosion inhibitors: principles and applications*; Elsevier, 2020.
(43) Verma, D. K.; Dewangan, Y.; Dewangan, A. K.; Asatkar, A. Heteroatom-based compounds as sustainable corrosion inhibitors: an overview. *Journal of Bio-and Tribo-Corrosion* **2021**, *7* (1), 15.
(44) Quraishi, M. A.; Chauhan, D. S.; Saji, V. S. Heterocyclic biomolecules as green corrosion inhibitors. *Journal of Molecular Liquids* **2021**, *341*, 117265.

(45) Edraki, M.; Sheydaei, M.; Zaarei, D. A brief review of the performance of azole-type organic corrosion inhibitors. *Chemical Review and Letters* **2022**, *6* (1), 79-85.
(46) Ergun, Ü.; Emregül, K. C. Azole compounds as corrosion inhibitors: part I. *Journal of materials engineering and performance* **2014**, *23*, 213-221.
(47) Mahdavian, M.; Ashhari, S. Mercapto functional azole compounds as organic corrosion inhibitors in a polyester-melamine coating. *Progress in Organic Coatings* **2010**, *68* (4), 259-264.
(48) Vernack, E.; Costa, D.; Tingaut, P.; Marcus, P. DFT studies of 2-mercaptobenzothiazole and 2-mercaptobenzimidazole as corrosion inhibitors for copper. *Corrosion Science* **2020**, *174*, 108840.
(49) Lavanya, K.; Saranya, J.; Chitra, S. Recent reviews on quinoline derivatives as corrosion inhibitors. *Corrosion Reviews* **2018**, *36* (4), 365-371.
(50) Ebenso, E. E.; Obot, I. B.; Murulana, L. Quinoline and its derivatives as effective corrosion inhibitors for mild steel in acidic medium. *International Journal of Electrochemical Science* **2010**, *5* (11), 1574-1586.
(51) Erami, R. S.; Amirnasr, M.; Meghdadi, S.; Talebian, M.; Farrokhpour, H.; Raeissi, K. Carboxamide derivatives as new corrosion inhibitors for mild steel protection in hydrochloric acid solution. *Corrosion Science* **2019**, *151*, 190-197.
(52) Popoola, L. T. Progress on pharmaceutical drugs, plant extracts and ionic liquids as corrosion inhibitors. *Heliyon* **2019**, *5* (2).
(53) Abdallah, M. Antibacterial drugs as corrosion inhibitors for corrosion of aluminium in hydrochloric solution. *Corrosion Science* **2004**, *46* (8), 1981-1996.
(54) Popoola, L. T. Organic green corrosion inhibitors (OGCIs): a critical review. *Corrosion Reviews* **2019**, *37* (2), 71-102.
(55) Verma, C.; Olasunkanmi, L.; Ebenso, E. E.; Quraishi, M. Substituents effect on corrosion inhibition performance of organic compounds in aggressive ionic solutions: a review. *Journal of Molecular Liquids* **2018**, *251*, 100-118.
(56) Ech-chihbi, E.; Salim, R.; Ouakki, M.; Koudad, M.; Guo, L.; Azam, M.; Benchat, N.; Rais, Z.; Taleb, M. Corrosion resistance assessment of copper, mild steel, and aluminum alloy 2024-T3 in acidic solution by a novel imidazothiazole derivative. *Materials Today Sustainability* **2023**, *24*, 100524.
(57) Hackerman, N.; Makrides, A. Action of polar organic inhibitors in acid dissolution of metals. *Industrial & Engineering Chemistry* **1954**, *46* (3), 523-527.
(58) Guo, L.; Qi, C.; Zheng, X.; Zhang, R.; Shen, X.; Kaya, S. Toward understanding the adsorption mechanism of large size organic corrosion inhibitors on an Fe (110) surface using the DFTB method. *RSC advances* **2017**, *7* (46), 29042-29050.
(59) Ramachandran, S.; Tsai, B.-L.; Blanco, M.; Chen, H.; Tang, Y.; Goddard, W. A. Self-assembled monolayer mechanism for corrosion inhibition of iron by imidazolines. *Langmuir* **1996**, *12* (26), 6419-6428.
(60) Costa, D.; Ribeiro, T.; Cornette, P.; Marcus, P. DFT modeling of corrosion inhibition by organic molecules: carboxylates as inhibitors of aluminum corrosion. *The Journal of Physical Chemistry C* **2016**, *120* (50), 28607-28616.
(61) Seebach, D. Organic synthesis—where now? *Angewandte Chemie International Edition in English* **1990**, *29* (11), 1320-1367.
(62) Ahmed, M. H. O.; Al-Amiery, A. A.; Al-Majedy, Y. K.; Kadhum, A. A. H.; Mohamad, A. B.; Gaaz, T. S. Synthesis and characterization of a novel organic corrosion inhibitor for mild steel in 1 M hydrochloric acid. *Results in physics* **2018**, *8*, 728-733.
(63) Fernine, Y.; Haldhar, R.; Arrousse, N.; Ebntouhami, M.; Taleb, A.; Kim, S.-C.; Taleb, M. Combined atomic-scale/DFT-theoretical simulations and corrosion protection study of AA2024-T3 in 3.5% NaCl by phenolphthalein derivatives: Surface characterization (FT-IR, FT-RAMAN, and SEM). *Journal of Electroanalytical Chemistry* **2023**, *943*, 117610.
(64) Wang, D.; Yang, D.; Zhang, D.; Li, K.; Gao, L.; Lin, T. Electrochemical and DFT studies of quinoline derivatives on corrosion inhibition of AA5052 aluminium alloy in NaCl solution. *Applied Surface Science* **2015**, *357*, 2176-2183.
(65) Lei, Y.; Zhiyong, L.; Weibin, Y.; Zixiao, W. Adsorption and characterization of an organic corrosion inhibitor for inhibiting carbon steel corrosion in chloride solution. *Current Analytical Chemistry* **2016**, *12* (2), 141-146.

(66) Verma, C.; Olasunkanmi, L. O.; Akpan, E. D.; Quraishi, M.; Dagdag, O.; El Gouri, M.; Sherif, E.-S. M.; Ebenso, E. E. Epoxy resins as anticorrosive polymeric materials: A review. *Reactive and Functional Polymers* **2020**, *156*, 104741.
(67) Kausar, A. Performance of corrosion protective epoxy blend-based nanocomposite coatings: a review. *Polymer-Plastics Technology and Materials* **2020**, *59* (6), 658-673.
(68) Williams, G.; Coleman, A. J.; McMurray, H. N. Inhibition of Aluminium Alloy AA2024-T3 pitting corrosion by copper complexing compounds. *Electrochimica Acta* **2010**, *55* (20), 5947-5958.
(69) Harvey, T.; Hardin, S.; Hughes, A.; Muster, T.; White, P.; Markley, T.; Corrigan, P.; Mardel, J.; Garcia, S.; Mol, J. The effect of inhibitor structure on the corrosion of AA2024 and AA7075. *Corrosion science* **2011**, *53* (6), 2184-2190.
(70) Du, S.; Chen, S.; Zhang, Z.; Ye, Z.; Mao, H.; Yang, H.; Lian, C.; Bao, C. Corrosion inhibition behavior of hydroxyl-terminated hyperbranched poly (amine-ester) for Q235 steel in HCl solution. *Materials Chemistry and Physics* **2022**, *292*, 126831.
(71) Nguyen, T.; Hubbard, J.; Pommersheim, J. Unified model for the degradation of organic coatings on steel in a neutral electrolyte. *Journal of Coatings Technology(USA)* **1996**, *68* (855), 45-56.
(72) de Lima-Neto, P.; de Araujo, A. P.; Araujo, W. S.; Correia, A. N. Study of the anticorrosive behaviour of epoxy binders containing non-toxic inorganic corrosion inhibitor pigments. *Progress in Organic Coatings* **2008**, *62* (3), 344-350.
(73) Galliano, F.; Landolt, D. Evaluation of corrosion protection properties of additives for waterborne epoxy coatings on steel. *Progress in organic coatings* **2002**, *44* (3), 217-225.
(74) Coughlin, R. Corrosion inhibitors. *Handbook of Coatings Additives, second ed., Marcel Dekker, New York* **2004**, 127-144.
(75) Blustein, G.; Romagnoli, R.; Jaén, J.; Di Sarli, A.; Del Amo, B. Zinc basic benzoate as eco-friendly steel corrosion inhibitor pigment for anticorrosive epoxy-coatings. *Colloids and Surfaces A: Physicochemical and Engineering Aspects* **2006**, *290* (1-3), 7-18.
(76) King, A.; Kannan, B.; Scully, J. Environmental degradation of a Mg-rich primer in selected field and laboratory environments: part 2—primer and topcoat. *Corrosion* **2014**, *70* (5), 536-557.
(77) Zahidah, K. A.; Kakooei, S.; Ismail, M. C.; Raja, P. B. Halloysite nanotubes as nanocontainer for smart coating application: A review. *Progress in Organic Coatings* **2017**, *111*, 175-185.
(78) Zheludkevich, M.; Tedim, J.; Ferreira, M. "Smart" coatings for active corrosion protection based on multi-functional micro and nanocontainers. *Electrochimica Acta* **2012**, *82*, 314-323.
(79) Zadeh, M. A.; Tedim, J.; Zheludkevich, M.; van Der Zwaag, S.; Garcia, S. J. Synergetic active corrosion protection of AA2024-T3 by 2D-anionic and 3D-cationic nanocontainers loaded with Ce and mercaptobenzothiazole. *Corrosion Science* **2018**, *135*, 35-45.
(80) Snihirova, D.; Lamaka, S. V.; Montemor, M. "SMART" protective ability of water based epoxy coatings loaded with CaCO3 microbeads impregnated with corrosion inhibitors applied on AA2024 substrates. *Electrochimica Acta* **2012**, *83*, 439-447.
(81) Zheludkevich, M. L.; Shchukin, D. G.; Yasakau, K. A.; Möhwald, H.; Ferreira, M. G. Anticorrosion coatings with self-healing effect based on nanocontainers impregnated with corrosion inhibitor. *Chemistry of Materials* **2007**, *19* (3), 402-411.
(82) Maia, F.; Tedim, J.; Lisenkov, A. D.; Salak, A. N.; Zheludkevich, M. L.; Ferreira, M. G. Silica nanocontainers for active corrosion protection. *Nanoscale* **2012**, *4* (4), 1287-1298.
(83) Zheludkevich, M.; Poznyak, S.; Rodrigues, L.; Raps, D.; Hack, T.; Dick, L.; Nunes, T.; Ferreira, M. Active protection coatings with layered double hydroxide nanocontainers of corrosion inhibitor. *Corrosion Science* **2010**, *52* (2), 602-611.
(84) Tedim, J.; Kuznetsova, A.; Salak, A.; Montemor, F.; Snihirova, D.; Pilz, M.; Zheludkevich, M.; Ferreira, M. Zn–Al layered double hydroxides as chloride nanotraps in active protective coatings. *Corrosion Science* **2012**, *55*, 1-4.
(85) Vieira, D. E.; Salak, A. N.; Ferreira, M. G.; Vieira, J. M.; Brett, C. M. Ce-substituted Mg-Al layered double hydroxides to prolong the corrosion protection lifetime of aluminium alloys. *Applied Surface Science* **2022**, *573*, 151527.
(86) Abdullayev, E.; Lvov, Y. Clay nanotubes for corrosion inhibitor encapsulation: release control with end stoppers. *Journal of Materials Chemistry* **2010**, *20* (32), 6681-6687.

(87) Yabuki, A.; Kanagaki, M.; Nishikawa, C.; Lee, J. H.; Fathona, I. W. Effective release of corrosion inhibitor by cellulose nanofibers and zeolite particles in self-healing coatings for corrosion protection. *Progress in Organic Coatings* **2021**, *154*, 106194.
(88) Yimyai, T.; Crespy, D.; Rohwerder, M. Corrosion‐Responsive Self‐Healing Coatings. *Advanced Materials* **2023**, *35* (47), 2300101.
(89) Manzano, M.; Vallet‐Regí, M. Mesoporous silica nanoparticles for drug delivery. *Advanced functional materials* **2020**, *30* (2), 1902634.
(90) Olivieri, F.; Castaldo, R.; Cocca, M.; Gentile, G.; Lavorgna, M. Mesoporous silica nanoparticles as carriers of active agents for smart anticorrosive organic coatings: a critical review. *Nanoscale* **2021**, *13* (20), 9091-9111.
(91) Kim, C.; Karayan, A. I.; Milla, J.; Hassan, M.; Castaneda, H. Smart coating embedded with pH-responsive nanocapsules containing a corrosion inhibiting agent. *ACS applied materials & interfaces* **2020**, *12* (5), 6451-6459.
(92) Poznyak, S.; Tedim, J.; Rodrigues, L.; Salak, A.; Zheludkevich, M.; Dick, L.; Ferreira, M. Novel inorganic host layered double hydroxides intercalated with guest organic inhibitors for anticorrosion applications. *ACS Applied Materials & Interfaces* **2009**, *1* (10), 2353-2362.
(93) Shchukin, D. G.; Lamaka, S.; Yasakau, K.; Zheludkevich, M.; Ferreira, M.; Möhwald, H. Active anticorrosion coatings with halloysite nanocontainers. *The Journal of Physical Chemistry C* **2008**, *112* (4), 958-964.
(94) Wei, H.; Wang, Y.; Guo, J.; Shen, N. Z.; Jiang, D.; Zhang, X.; Yan, X.; Zhu, J.; Wang, Q.; Shao, L. Advanced micro/nanocapsules for self-healing smart anticorrosion coatings. *Journal of Materials Chemistry A* **2015**, *3* (2), 469-480.
(95) Borisova, D.; Akçakayıran, D.; Schenderlein, M.; Möhwald, H.; Shchukin, D. G. Nanocontainer‐based anticorrosive coatings: effect of the container size on the self‐healing performance. *Advanced Functional Materials* **2013**, *23* (30), 3799-3812.
(96) Denissen, P. J.; Homborg, A. M.; Garcia, S. J. Requirements for corrosion inhibitor release from damaged primers for stable protection: A simulation and experimental approach using cerium loaded carriers. *Surface and Coatings Technology* **2022**, *430*, 127966.
(97) Denissen, P. J.; Garcia, S. J. Cerium-loaded algae exoskeletons for active corrosion protection of coated AA2024-T3. *Corrosion Science* **2017**, *128*, 164-175.
(98) Denissen, P. J.; Shkirskiy, V.; Volovitch, P.; Garcia, S. J. Corrosion inhibition at scribed locations in coated AA2024-T3 by cerium-and DMTD-loaded natural silica microparticles under continuous immersion and wet/dry cyclic exposure. *ACS applied materials & interfaces* **2020**, *12* (20), 23417-23431.
(99) Silva, T.; Marques, A. C.; Shakoor, A.; Montemor, M.; Taryba, M. Biopolyurethane Coatings with Silica-Titania Microspheres (Microscafs®) as Functional Filler for Corrosion Protection. *Available at SSRN 4855161*.
(100) Dieleman, C. D.; Denissen, P. J.; Garcia, S. J. Long‐Term Active Corrosion Protection of Damaged Coated‐AA2024‐T3 by Embedded Electrospun Inhibiting Nanonetworks. *Advanced Materials Interfaces* **2018**, *5* (12). DOI: 10.1002/admi.201800176.
(101) Knez, M.; Nielsch, K.; Niinistö, L. Synthesis and surface engineering of complex nanostructures by atomic layer deposition. *Advanced materials* **2007**, *19* (21), 3425-3438.
(102) Pedersen, H.; Leone, S.; Kordina, O.; Henry, A.; Nishizawa, S.-i.; Koshka, Y.; Janzén, E. Chloride-based CVD growth of silicon carbide for electronic applications. *Chemical reviews* **2012**, *112* (4), 2434-2453.
(103) Adhikari, S.; Selvaraj, S.; Kim, D. H. Progress in powder coating technology using atomic layer deposition. *Advanced Materials Interfaces* **2018**, *5* (16), 1800581.
(104) Van Ommen, J.; Goulas, A. Atomic layer deposition on particulate materials. *Materials Today Chemistry* **2019**, *14*, 100183.
(105) Skoog, S.; Elam, J.; Narayan, R. Atomic layer deposition: medical and biological applications. *International materials reviews* **2013**, *58* (2), 113-129.
(106) Valdesueiro, D.; Meesters, G. M.; Kreutzer, M. T.; Van Ommen, J. R. Gas-phase deposition of ultrathin aluminium oxide films on nanoparticles at ambient conditions. *Materials* **2015**, *8* (3), 1249-1263.

(107) Kääriäinen, T. O.; Kemell, M.; Vehkamäki, M.; Kääriäinen, M.-L.; Correia, A.; Santos, H. A.; Bimbo, L. M.; Hirvonen, J.; Hoppu, P.; George, S. M. Surface modification of acetaminophen particles by atomic layer deposition. *International Journal of Pharmaceutics* **2017**, *525* (1), 160-174.
(108) La Zara, D.; Zhang, F.; Sun, F.; Bailey, M. R.; Quayle, M. J.; Petersson, G.; Folestad, S.; van Ommen, J. R. Drug powders with tunable wettability by atomic and molecular layer deposition: From highly hydrophilic to superhydrophobic. *Applied Materials Today* **2021**, *22*, 100945.
(109) Moseson, D. E.; Benson, E. G.; Nguyen, H. T.; Wang, F.; Wang, M.; Zheng, K.; Narwankar, P. K.; Taylor, L. S. Atomic layer coating to inhibit surface crystallization of amorphous pharmaceutical powders. *ACS Applied Materials & Interfaces* **2022**, *14* (36), 40698-40710.
(110) Ding, Z. Smart release of corrosion inhibitors by a novel encapsulation method. **2016**.

# Chapter 2

## Assessment of the Corrosion Protection Power of Inhibitor-Loaded Diatomite Particles in Lab-Scale Model Primers: Salt Fog Spray and Droplet Test Analysis

*In recent years, innovative approaches have been explored to incorporate corrosion inhibitors into organic coatings without affecting their inhibition properties. One such promising approach is loading inhibitors into microcarriers such as natural porous silica microparticles (i.e., fossilized diatom exoskeletons or diatomite). In this chapter, we investigated loading both inorganic inhibitors and organic inhibitors into diatomite particles, incorporated these particles into lab-scale model epoxy-amine primers and applied them on AA2024-T3. The evaluation of the corrosion protection power of the diatomite-based state-of-the-art technology involves two key testing methodologies: salt fog spray tests and droplet tests. These tests, broadly used in industry, simulate some of the harsh environmental conditions encountered by aircraft during flight and therefore provide relevant information to help moving selected technologies to higher technology readiness levels (TRLs) and forms the basis for the further research and development in this thesis.*

# 2.1 Introduction

During the last decades, many inorganic inhibitors (e.g., Ce, Li salts) and organic inhibitors have been studied in solution and in organic primers for the corrosion protection of AA2024-T3. [1-3] Nevertheless, research in coatings, and especially when using organic inhibitors, has proven complex due to several formulation challenges related to unwanted interactions and reactions of the inhibitors with the polymeric coating matrix. Such reactions lead to negative effects on application properties such as viscosity and pot-life, but also to performance properties as they may affect (i) inhibitor release and efficiency and (ii) overall thermomechanical and adhesion properties. For most corrosion inhibitors alternative to traditional (CrVI-based) inorganic salts, the use of nano/microcarriers appears a necessary strategy to reduce negative interactions, thus allowing the use of the full potential of the inhibitors used. [4, 5]

In our previous works, we introduced the use of naturally-occurring nanoporous, hollow, amorphous silica microparticles (namely, fossilized diatom exoskeletons known as diatomite or Diatomaceous Earth, DE) as carriers for inorganic and organic inhibitors using $Ce(NO_3)_3$ and 2,5-dimercapto-1,3,4-thiadiazole (HDMTD) as model inhibitors. [6, 7] When using lab-scale continued immersion tests (i.e., immersed in 20 mL 0.05M NaCl solution for 30 days) the solvent-borne epoxy-amine coating with $Ce(NO_3)_3$ loaded in DE showed sustained corrosion protection of large scratches (i.e., 1mm wide, 350µm deep for 70µm coatings) for at least 30 days with only 3.7 wt% active inhibitors in the coating given by 10% diatomite PVC and 1.5% inhibitor volume. Despite the high levels of protection, only 15% of the DE volume was filled with inhibitors, hence suggesting the technology efficiency can be increased when better loading strategies are developed. Under the same testing circumstances, the HDMTD in DE coating was only able to provide short-term protection (for 4 days), suggesting insufficient release attributed to insufficient loading and/or negative side reactions between carrier and inhibitor. Furthermore, it was found that the use of 50% DE-HDMTD in combination with 50% DE-Ce particles showed a synergistic effect, leading to comparable corrosion protection as the DE-Ce system yet with 50% less DE-Ce particles. Besides this, short cyclic exposure (immersion-dry) showed excellent protection at damaged sites when using DE-Ce carriers. Despite the interesting results, the previous works on the diatomite technology as discussed above, usually employed relatively mild electrolyte concentrations in immersion to investigate corrosion inhibition mechanisms. To know better the state-of-the-art of the technology and move further in the TRL scale and get closer to potential industrial applications, other type of tests and primer matrices are needed.

In this work, three corrosion inhibitors ($Ce(NO_3)_3$, HDMTD, and the di-potassium salts of DMTD (namely KDMTD)) were selected, loaded in DE particles and embedded in a lab-scale model aircraft primer with other particle pigments before application on anodized and bare AA2024-T3 aerospace grade alloys. While Ce and HDMTD were introduced in earlier works, [6, 7] KDMTD was chosen due to its (i) higher water solubility and (ii) lower expected reactivity with the epoxy-amine matrix than HDMTD, in an attempt to increase the inhibition efficiency of the DMTD-loaded DE technology and to gain further insights on the mechanisms behind the apparent loss of

inhibition in the HDMTD-DE system. Systems combining different inhibitor-loaded DE particles were also tested in the search for further synergistic effects of cerium, HDMTD and KDMTD as hinted in our previous work.[7] To test the corrosion inhibition potential, the coatings were artificially damaged and examined with (i) neutral salt fog spray for up to 1000 hours as an accelerated test simulating month- to year- long exposure [8, 9] and (ii) droplet tests in closed environment for 7 days to accelerate and facilitate the screening of possible inhibitor solutions. [10, 11] The analysis of the exposure was then performed using optics, spectroscopic and SEM analysis. The results showed that inorganic inhibitors like $Ce(NO_3)_3$ performed better then organic inhibitors (i.e., HDMTD and KDMTD) when loading the inhibitors into diatomite. The stability of HDMTD on AA2024 and its interaction with the epoxy-amine binder need further study. Although KDMTD effectively inhibits corrosion, its hygroscopic nature leads to rapid depletion and coating failure. This highlights the need to better understand KDMTD behavior comparing with HDMTD and explore alternative loading strategies.

# 2.2 Experimental

*2.2.1 Materials*

Diatomaceous earth (called Diafil 525, diatomite, DE) was supplied by Profiltra Customized Solutions (The Netherlands, NL). Cerium nitrate hexahydrate ($Ce(NO_3)_3\ 6H_2O$), 2,5-dimercapto-1,3,4-thiadiazole (HDMTD>99%) and 2,5-dimercapto-1,3,4-thiadiazolate di-potassium salts (KDMTD >99%) corrosion inhibitors were purchased from Sigma-Aldrich. 3 mm thick bare and TSA (Tartaric-Sulfuric Acid anodizing) aluminum alloy 2024-T3 (AA2024-T3) panels were received from Airbus and used as substrate. The aircraft primer formulation consists of epoxy resin Beckopox 1 and 2, amine hardener Ancamine, solvents ethylmethyl ketone (MEK) and methylisobutyl ketone (MIBK), dispersion agent and wetting agent supplied by BYK, $TiO_2$ supplied by Sachtleben, blue pigment from BASF, and $BaSO_4$ pigments. Sodium chloride (NaCl, purity > 98%) and dimethylformamide (DMF, ≥99.9%) were acquired from VWR Chemicals and all aqueous solutions were prepared using Milipore® filtered water.

*2.2.2 DE loading with inhibitors*

Mixtures of 5 g of DE and 5 g inhibitor ($Ce(NO_3)_3\ 6H_2O$, HDMTD or KDMTD) were added to 10 mL dimethylformamide (DMF, ≥99.9%) and stirred with a shaking table at 320 rpm for 24h. The mixtures were then spread on a glass plate with the help of a 100 μm spiral bar coater. The thin layers of DE particles with inhibitor were then dried at 60 °C for 30 min, removed from the glass plate with a spatula and further dried as a powder at 60 °C for 24 h. The resulting powders (50/50 wt% DE/inhibitor) were finally stored in a desiccator until needed.

*2.2.3 Preparation of primers on aerospace grade aluminum alloys*

The 3mm thick bare and TSA AA2024-T3 metal sheets were cut into pieces of 100 x100 mm prior to surface cleaning and coating application. Prior to coating, the AA2024-T3 bare panels were cleaned using the following steps: (1) removal of the native oxide layer and surface roughness formation by Scotch Brite 3M; (2) degreasing with acetone; and (3) rinsing with distilled water and air drying. The TSA panels were used as received.

Different DE-inhibitor pigments were added to the standard coating binder formulation as listed in Table 2.1. Seven different coating compositions were prepared as listed in Table 2.2. The coatings formulation was given as a function of the total epoxy resin (phr=parts per hundred epoxy resin in weight). Briefly, two epoxy resins Beckopox1 and Beckopox2 by a mass ratio of 4.7:1 was mixed at 700 rpm for 2 min. Then, methyl ethyl ketone (MEK), methyl isobutyl ketone (MIBK), BYK dispersing agent and BYK wetting agent were weighted and transferred to the mixture under slow stirring at 700 rpm for 2 min to adjust the viscosity. The pigment particles $TiO_2$, $BaSO_4$ and blue pigment were added to the mixture sequentially and mixed at 2000 rpm for 2min of each. After mixing the pigments, the whole mixture was milled by 0.6 mm Zr beads at 3500 rpm for 1h until the particle size was below 20 μm. The base component was filtered by a 0.2 mm filter, mixed with Ancamine at 1000 rpm in a high-speed mixer for 1 min, and then left to pre-cure at room temperature for 15 min. At this moment the DE-loaded particles with inhibitors were added and the coating formulation mixed at 2000 rpm for 1min. (Note: We also

incorporated KDMTD and HDMTD directly into the coating formulation. However, the mixtures became highly viscous, resulting in unusable coatings.) Finally, the coating dispersion was applied onto the metal surfaces using a doctor blade with wet thickness of 150 μm. After a flash-off period of 30 min at room temperature the coatings were cured at 80 °C for 3h to achieve full crosslinking and solvent evaporation. The total PVC of the coating was 25% including 10% PVC of inhibitor-containing particles. The coatings were finally stored in a desiccator prior to further tests.

Table 2.1 Composition of the 25% PVC coatings

| **Composition** | **Density ($g/cm^3$)** | **Weight fraction (phr)** |
|---|---|---|
| Beckopox resin 1 | 1.07 | 83 |
| Beckopox resin 2 | 1.12 | 17 |
| Ethylmethyl ketone (MEK) | 0.805 | 12 |
| Methylisobutyl ketone (MIBK) | 0.8 | 46 |
| Dispersing agent | 1.08 | 8 |
| Wetting agent | 1.03 | 1 |
| $TiO_2$ | 4.1 | 47 |
| $BaSO_4$ | 4.5 | 42 |
| Blue pigment | 1.65 | 1 |
| DE-inhibitor pigment | 1.34 | 16 |
| Ancamine hardener | 1.01 | 45 |

Table 2.2 Coatings formulations as a function of Beckopox resin (phr=parts per hundred epoxy resin in weight). All DE-inhibitor particles contained 50 wt.% inhibitor.

| No. | Inhibitor pigments | DE inhibiting pigments (phr) | Dry weight Percent of inhibitor (wt%) | Inactive pigments (phr) | The rest of the common compositions (phr) | Coating thickness (µm) |
|---|---|---|---|---|---|---|
| 1 | DE | 16 | 0 | 90 | 154 | 65-75 |
| 2 | DE-$Ce(NO_3)_3$ | 16 | 4.3 | 90 | 154 | 65-75 |
| 3 | DE-HDMTD | 16 | 4.3 | 90 | 154 | 65-75 |
| 4 | DE-KDMTD | 16 | 4.3 | 90 | 154 | 65-75 |
| 5 | DE-$Ce(NO_3)_3$ and DE-HDMTD 1:1 mixture | 16 | 4.3 | 90 | 154 | 65-75 |
| 6 | DE-$Ce(NO_3)_3$ and DE-KDMTD 1:1 mixture | 16 | 4.3 | 90 | 154 | 65-75 |
| 7 | DE-KDMTD and DE-HDMTD 1:1 mixture | 16 | 4.3 | 90 | 154 | 65-75 |

*2.2.4 Droplet tests*

The coated bare AA2024-T3 samples were mechanically cut into 3x3 cm. No edge delamination was observed in any sample, hence confirming good adhesion for subsequent testing. Scribes of 1 mm wide, 20 mm long and 0.35 mm deep (i.e. approximately 0.28mm deep in the metal) were created on the coating surfaces by a Roland EGX-350 engraver equipped with a 1 mm diameter end mill. The scribed samples were then placed in closed boxes with wetted towels beneath the metal plates to keep the humidity. A droplet of 105µL 0.5M NaCl solution was then dropped on each scribe. The towels were wetted with distilled water every two days.

The samples were then monitored optically every day with the help of a Keyence VHX 1000 optical microscope during one week exposure. At the end of the exposure, the droplets on the scribes were collected with a pipette and the panels were dried and stored in a desiccator until further analysis. The concentration of the inhibitors in the collected droplets was measured with a PerkinElmer LAMBDA 35 UV/VIS spectrometer using the calibration curves made with $Ce(NO_3)_3$, HDMTD and KDMTD solutions as seen in support information Figure SI 2.1. The scribes were evaluated using a Keyence Laser Scanning Confocal microscope and JEOL SJM-

840 scanning electron microscope (SEM) coupled with energy dispersive X-ray spectroscopy (EDS) at 15kV.

During the droplet test, liquid droplets appeared on the intact coatings containing DE-KDMTD. To elucidate the origin of the droplets, the liquids were analyzed with a Renishaw inVia Confocal Raman spectrometer equipped with a laser source at 532 nm (laser power of 10%, 10 s exposure).

*2.2.5 Salt fog spray tests*

The 10 cm × 10 cm bare-AA2024-T3 and TSA coated panels (6 of each coating composition and substrate) were cross-scribed following the standard ISO 9227. To this aim, 1 mm wide, 60 mm long, and 0.35 mm deep crossed scratches were performed with the help of an engraver. The salt fog spray tests were conducted by exposing the scratched bare and TSA AA2024-T3 coated samples to a salt fog environment generated by spraying a 5 wt% aqueous NaCl solution at 35°C for 1000 hours in accordance with ISO 9227. Samples were removed at intervals of 0, 168, 336, 500, 750, and 1000 hours, then dried, photographed and evaluated. The corrosion performance was evaluated based on the following parameters: the appearance and growth of pits, corrosion products, and creepage from the scribes.

# 2.3 Results and discussion

*2.3.1 Droplet tests*

Figure 2.1 shows the optical micrographs of the 7-day droplet tests on 7 samples with different inhibitor pigments. They can be categorized into three groups: (i) coating without any inhibitors, namely DE; (ii) coatings with one type of inhibitor, namely DE-Ce, DE-KDMTD, DE-HDMTD; and (iii) coatings with two types of inhibitors, namely DE-Ce/DE-KDMTD, DE-Ce/DE-HDMTD, DE-HDMTD/DE-KDMTD.

As can be seen in Figure 2.1 no blistering was observed in this test while differences between the scribes are remarkable. Unsurprisingly, the coating without inhibitors (Figure 2.1a) shows the presence of a layer of dark corrosion products (aluminum (hydro)oxide and copper oxide), known as tarnishing, [12] at the scratch area under the droplet already in the first day of exposure. By 2 days of exposure, the corrosion process has further extended to the left side of the scratch, affecting the area outside the droplet. At 7 days of exposure, a thick layer of corrosion products covering almost all the scribe is clearly visible formed. The coatings with one inhibitor type, DE-Ce (Figure 2.1b) and DE-KDMTD (Figure 2.1c), show significant protection of the whole scribe even at 7 days exposure. No corrosion-related surface phenomena appeared under the droplet areas on these samples even though lines marking the edges of the droplets were clearly visible and attributed to local corrosion induced by the harsh splash zone environment rich in oxygen. Interestingly, yellowish products, typical color of DMTD solution and Ce and DMTD on AA2024 surfaces, appeared after 2 days of exposure on the right side of the scratch of the DE-KDMTD sample (see inset). This suggests KDMTD from the scratched coating leached out also from areas beyond the water droplet either by capillarity effect or by humidity induced water bridges between paint and metal scribe as those observed in any surface at high relative humidities known as molecular water layers, MWLs [13]. This observation hints at the unattended potential role of MWLs in inhibitor transport. The HDMTD-containing coating (DE-HDMTD, Figure 2.1d), on the other hand, shows a delay in the appearance of metallic surface degradation, with lesser presence of dark corrosion products, compared to the DE sample at 1 day but significantly lower protection than the Ce and KDMTD containing coatings. The lack of full protection over time suggests that HDMTD is either unstable on the AA2024-T3 surface or that there was insufficient inhibitor release. This result aligns with our previous work, [7] where coatings with DE-HDMTD showed initial protection during immersion in milder NaCl solutions (0.05M) which deteriorated at longer exposure times. Considering the comparable, if not higher, inhibitory power of HDMTD in solution, as well as its relatively high solubility, and the fact that the coatings have the same inhibitor loading, the results confirm the higher reactivity of HDMTD with epoxy-amine matrix limiting its release and protective power.

As in the single inhibitor systems, the combination of DE-Ce and DE-KDMTD (Figure 2.1e) shows comparable inhibition power to the individual systems (Figure 2.1b and 2.1c) at the area beneath the droplet. Besides this, less corrosion products are seen at the edges of the droplet and beyond the droplet itself at longer exposure times. This suggests a slight improvement in the

overall protection behavior compared to the individual inhibitors, and therefore some degree of inhibiting synergy indicating that one or the other inhibitor can be partially replaced without having a detrimental effect on the anticorrosion behavior based on this test.

When half of the DE-Ce particles in the well-protecting system in Figure 2.1b. is replaced by DE-HDMTD (Figure 2.1f), the inhibiting power drops compared to 100% DE-Ce particles based on optical inspection. This suggests that the amount of cerium released was apparently insufficient to offer effective damage inhibition or/and that the HDMTD acidity (pH drops to 5 in solution) induced a destabilization of the cerium hydroxide layers. A closer look at the scribes using confocal microscopy and SEM (Figure 2.2) reveals a non-uniform amount of oxide corrosion products in the case of the DE-HDMTD (pits in confocal and small deposits in SEM), yet lower than for the DE coating (significant amount of aluminum oxide deposits corresponding to significant pitting). In contrast, the coatings with DE-Ce/DE-HDMTD show significantly lower corrosion attack (pits decrease and bare metal area increases in confocal, and deposits decrease in SEM). In any case these results align with the optical observations in the droplet test and indicate the limited ability of HDMTD alone or in combination with Ce to effectively protect large scribes.

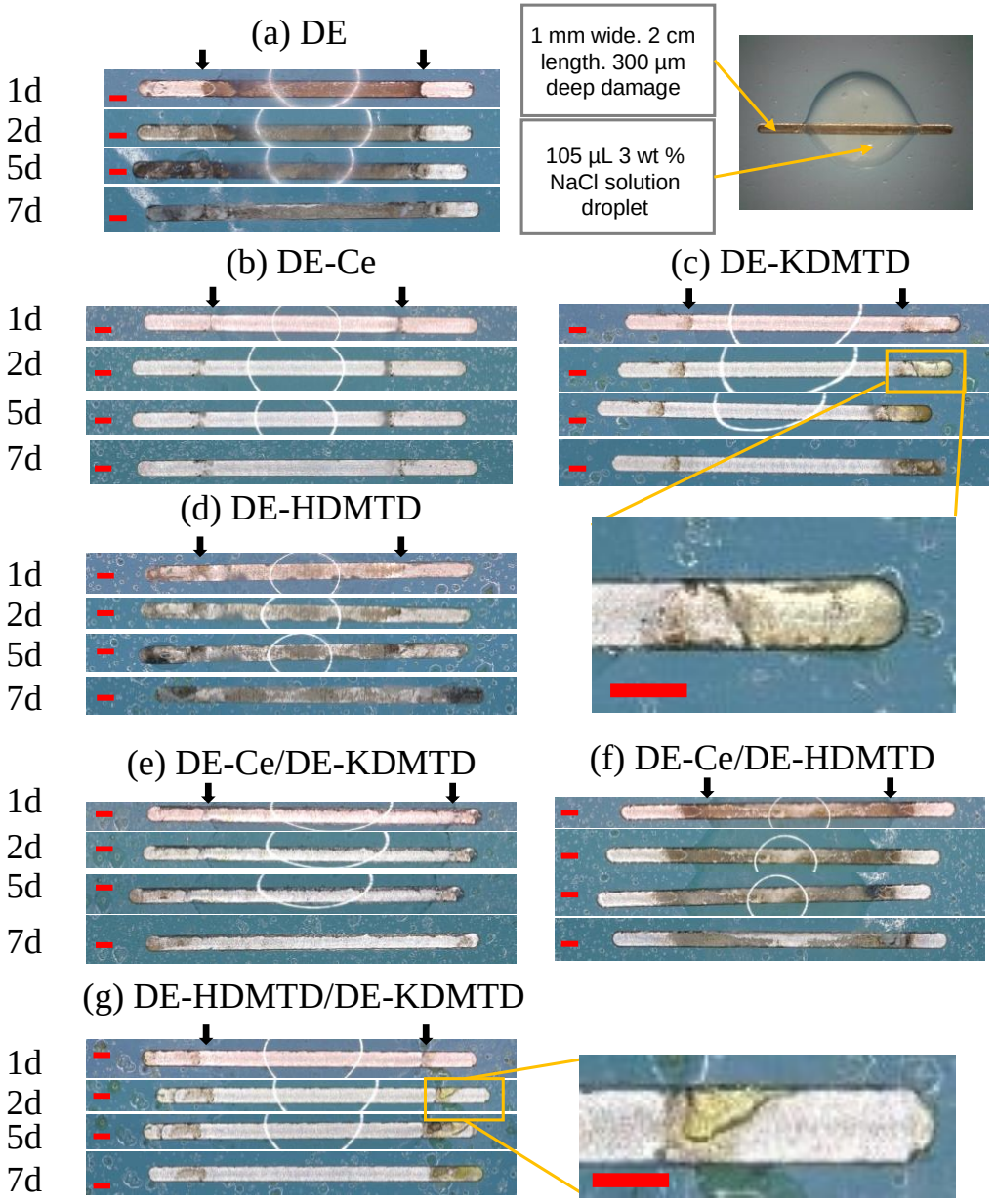


Figure 2.1 Optical images of seven scratched coatings exposed to the 105 µL, 3 wt % NaCl solution droplets, captured at intervals of 1 day, 2 days, 5 days, and 7 days. Red scale bar: 1 mm. Note: The white lines in the center of the scribes are a visual reflection effect induced by the curvature of the droplet. The edges of the droplet can be seen as dark lines at the left and right of the center of the scribe (marked by two black arrows). The small white circles on the coatings are water condensation droplets.

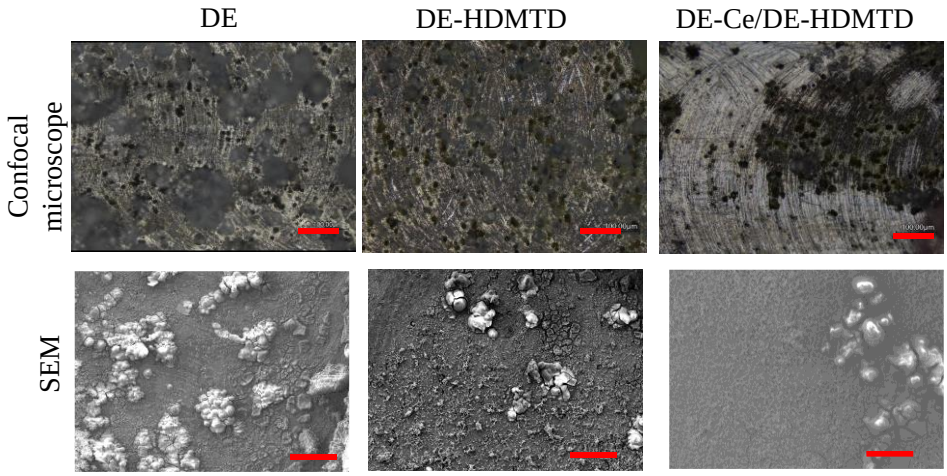


Figure 2.2 Confocal microscope and SEM analysis of the post-mortem coatings containing DE, DE-HDMTD and DE-Ce/DE-HDMTD pigments. Scale bar: 100 μm.

Interestingly, as seen in Figure 2.1g, when half of the particles DE-KDMTD are replaced by DE-HDMTD particles, the inhibition power is not affected and remains very high. This is evidenced by the yellowish products observed on the DE-HDMTD/DE-KDMTD sample (see inset in Figure 2.1g) and suggests that either the acidity induced by the HDMTD helps increasing the inhibiting power of KDMTD or/and, based on the low efficiency observed for the DE-HDMTD sample (Figure 2.1d), the DE-KDTMD coatings could contain less particle loading to obtain comparable levels of corrosion protection. All in all, as confirmed by the close-up confocal images in Figure 2.3 showing absence of pitting or oxide precipitates, the coatings containing DE-Ce or DE-KDMTD or combinations of DE-KDMTD with DE-Ce and DE-HDMTD lead to very high levels of protection at and around large scribes for at least 7 days exposure to the droplet test despite the relatively low amounts of active inhibitor used (4.3 wt.%).

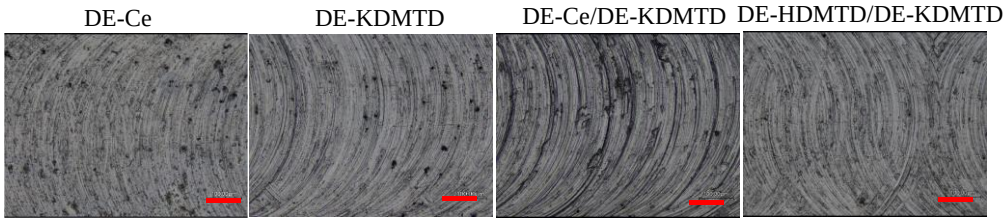


Figure 2.3 Confocal microscope of the post-mortem coatings containing DE-Ce, DE-KDMTD, DE-Ce/DE-KDMTD and DE-HDMTD/DE-KDMTD pigments. Scale bar: 100 μm.

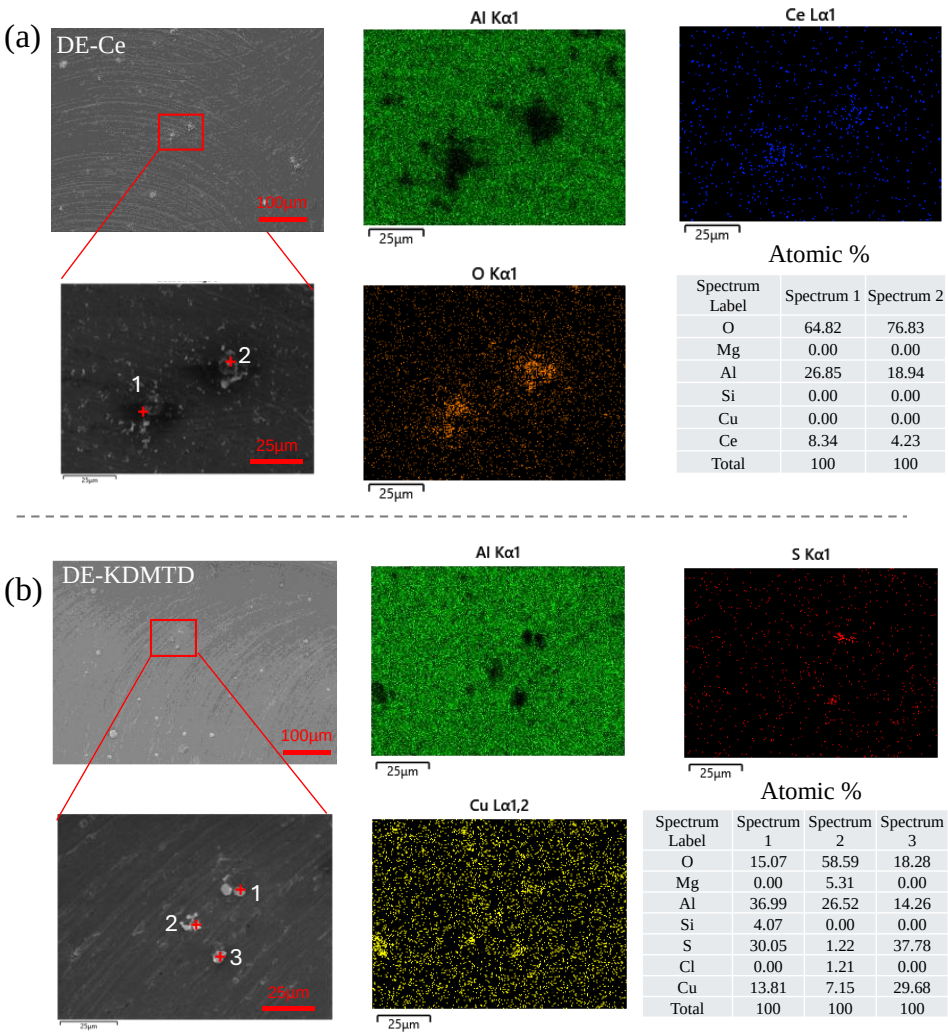


| Spectrum Label | Spectrum 1 | Spectrum 2 |
|---|---|---|
| O | 64.82 | 76.83 |
| Mg | 0.00 | 0.00 |
| Al | 26.85 | 18.94 |
| Si | 0.00 | 0.00 |
| Cu | 0.00 | 0.00 |
| Ce | 8.34 | 4.23 |
| Total | 100 | 100 |

| Spectrum Label | Spectrum 1 | Spectrum 2 | Spectrum 3 |
|---|---|---|---|
| O | 15.07 | 58.59 | 18.28 |
| Mg | 0.00 | 5.31 | 0.00 |
| Al | 36.99 | 26.52 | 14.26 |
| Si | 4.07 | 0.00 | 0.00 |
| S | 30.05 | 1.22 | 37.78 |
| Cl | 0.00 | 1.21 | 0.00 |
| Cu | 13.81 | 7.15 | 29.68 |
| Total | 100 | 100 | 100 |

Figure 2.4 SEM-EDS analysis of the scratches of the (a) DE-Ce and (b) DE-KDMTD coatings after 7 days exposure to droplet test.

To have a clearer view of the level and mechanism of protection provided by the good performing samples, a SEM-EDS analysis of the DE-Ce and DE-KDMTD was performed at the end of the 7 days exposure (Figure 2.4). In both samples, the AA2024 substrate appears largely intact, showing no signs of local corrosion such as trenching or pitting at intermetallic particles. Figure 2.4a reveals high amounts of cerium (>4 atomic %) and oxygen (64-74 at.%) at two clearly visible deposition sites, indicating the presence of cerium oxide/hydroxide in these areas as described elsewhere[1, 14] together with traces of Ce at different locations over the surface, hence confirming the release and preferentially local inhibition mechanism of cerium. Notably, the SEM-EDS analysis of the scratch on the DE-KDMTD coating in Figure 2.4b shows a significantly high

amount of sulfur (>30 atomic %) at locations 1 and 3. These locations also display high amounts of copper, suggesting the preferential deposition of KDMTD on the copper-rich intermetallic particles. This finding aligns with research indicating that heteroatom corrosion inhibitors can adsorb on copper to protect metal substrates [15] [16] and our recent work (**Chapter 3**) quantifying the state and amount of HDMTD as function of the local microstructure of AA2024-T3 with preferential deposition on Cu-rich IMs and around Cu-poor IMs. [17] However, the comparably high levels of corrosion protection achieved with the 50/50 DE-HDTMD/DE-KDMTD coating system and the presence of yellowish regions at the edge of the scratch, as seen in Figure 2.1c and 2.1g, suggest an excessive amount of KDMTD inhibitor was used leading to an "over-release" and the design rule suggestion that lower amounts of KDMTD (or DE-KDMTD particles) may be used still leading to good corrosion protection ad damage sites as measured by the droplet test.

In order to gain more insights on the inhibitor release relation to local protection, the droplets used in the droplet test were tested using UV-Vis (spectroscopy). To do so, the droplets collected after exposure were diluted 100 times before analysis to obtain spectra as shown in Figure 2.5. The inhibitor concentrations were then determined using the calibration curves in Figure SI 2.1. The coatings containing DE-Ce, DE-HDMTD, and DE-Ce/DE-HDMTD did not show absorbance peaks at 252 nm for $Ce^{3+}$ and 328 nm for HDMTD. This indicates the inhibitor concentrations in the droplets for these samples were below the detectable range of UV-Vis ($<10^{-5}$ M) because of low release or because the dilution to 100 was excessive for these samples, either way pointing at a release at least $<10^{-3}$M, sufficient to protect in the case of Ce salts as confirmed with the analysis above. In contrast, coatings with KDMTD released extremely high amounts of inhibitors into the droplets, with concentrations reaching up to 5 mM (and the half when 50% Ce-DE was used). These results align with previous observations from optical images and SEM-EDS analysis which, considering that protection of AA2024 for this inhibitor can be achieved at $10^{-4}$M [18], suggest that KDMTD was over-released.

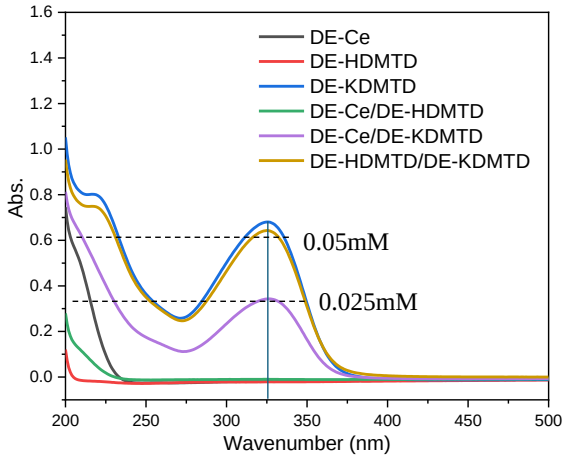


Figure 2.5 UV-Vis spectroscopy of the 100 times diluted droplets solutions of the six coating systems. Results confirm high release levels of KDMTD.

Although the DE-KDMTD-containing coatings demonstrated a high level of protection during droplet tests, the issue of over-release poses significant risks, such as blistering and delamination, potentially leading to coating failure, but also fast inhibitor depletion. The results also indicate that the direct loading of KDMTD into DE particles does not fully prevent this problem, even if it allows for better quality of films (Note: the films using HDMTD and KDMTD particles directly without DE led to non-usable coatings). As pointed out in Figure 2.1, and as expected, the intact areas of all coatings showed droplet condensation which in soluble inhibitors should increase release and protection. Nevertheless, when the samples were led to stabilize at room conditions (25 ºC and room humidity 50%) it was observed that the coatings with KDMTD presented liquid droplets on the surface, as shown in Figure 2.6a, for an intact DE-KDMTD coating exposed to ambient conditions for 1 day. This "sweating" phenomenon is attributed to the high hygroscopic value of KDMTD, also responsible for the high inhibitor over-release discussed above. To confirm this negative effect, Raman analysis was performed on the liquid droplets. Figure 2.6b allows comparing the Raman signals of KDMTD powder, Ancamine, KDMTD in water and the liquid droplets on the coated panels. As it can be seen, the droplets (green top curve) show signals that confirm the presence of KDMTD (-C-N, N-N, C-S-C) [19] and Ancamine ($-NH_2$, $-CH_2-CH_3$). This suggests that a high amount of KDMTD, along with unreacted Ancamine from the polymer binder, can leach out from the intact coating expectedly due to the hygroscopic character of KDMTD but also confirms the high levels of corrosion protection at damage sites being enhanced by the hygroscopic character of KDMTD.

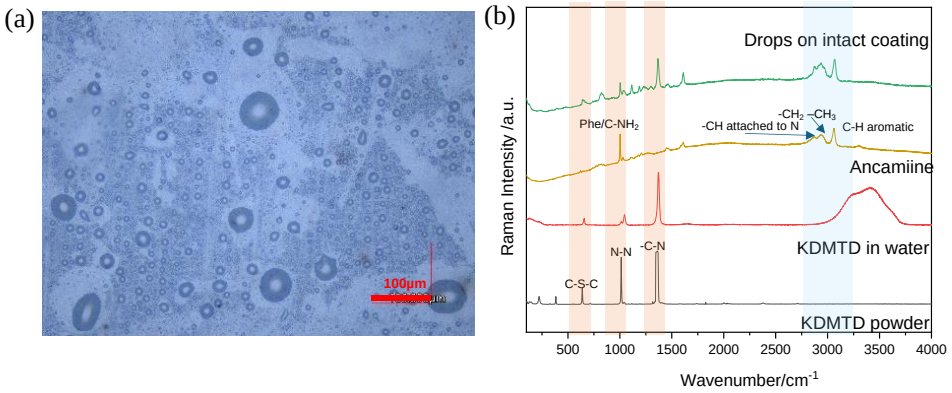


Figure 2.6 (a) Optical image of an intact coating containing DE-KDMTD pigments exposed to the room environment for 1 day; (b) Raman results for KDMTD powder, Ancamine, KDMTD in water, and the droplets observed on the surface. Results confirm these ‘exudates’ correspond to large amounts of KDMTD/Ancamine unreacted mixture.

### *2.3.2 Neutral salt fog spray (NSS) tests on bare and TSA AA2024-T3*

Figure 2.7 shows the salt fog spray test results for the seven coating systems applied on bare AA2024-T3. The optical images were assessed based on the following corrosion parameters: the appearance of white corrosion products (aluminum oxide), pitting corrosion (shown as holes at

intermetallic particles surrounded by white corrosion products), and creepage of corrosion below the coating originating from the edges of the scratches.

The red line in between photos in Figure 2.7 indicates the onset time at which white corrosion products appear at the scribe of each sample. Three coatings: DE, DE-KDMTD, and DE-Ce/DE-KDMTD exhibited an early appearance of white corrosion products occurring between 168 h and 336 h. The coatings DE-HDMTD and DE-Ce showed a delayed appearance of white corrosion products, with DE-HDMTD showing signs after 336 h and DE-Ce after 500 h.

Notably, DE-Ce/DE-HDMTD and DE-HDMTD/DE-KDMTD did not display white corrosion products within 1000 h of exposure to the neutral salt fog spray. These results highlight the synergistic effect of the inhibitor combination to prevent attack at scribes during NSS tests using 0.5M NaCl as opposed to the less effective protection of the coatings loaded with single DE-inhibitor particles as evaluated for this NSS evaluation parameter of 'white corrosion product'.

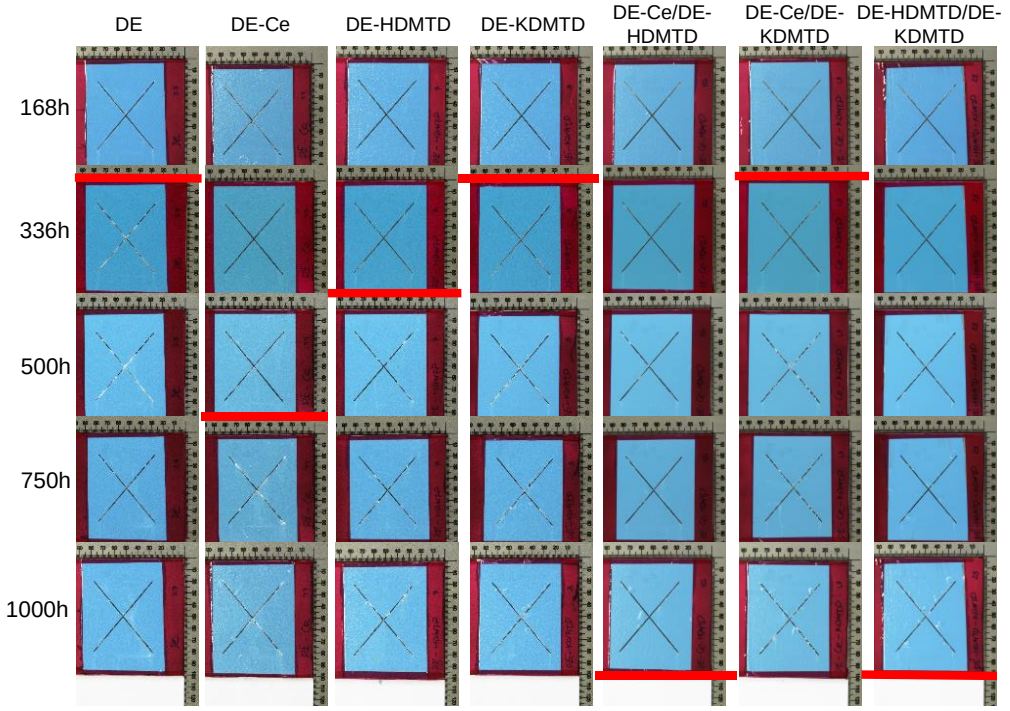


Figure 2.7 Salt fog spray tests results of the 7 coating systems on bare AA2024-T3. The red line marks the onset of white corrosion product appearance.

The pit presence and creepage were quantified at two specific times: at the onset of detection (336 h) and at the end of the test (1000 h). This allowed identifying the amount of pits and creepage as well as progression of the same in time. The detailed counting process for each sample can be found in Figure 2.8 for the case of DE-KDMTD (2.8a), DE-Ce (2.8b), DE-HDMTD (2.8c) and DE-Ce/DE-HDMTD (2.8d) coatings and in the supplementary information, Figure SI 2.2. The summarized results are presented in Figure 2.9.

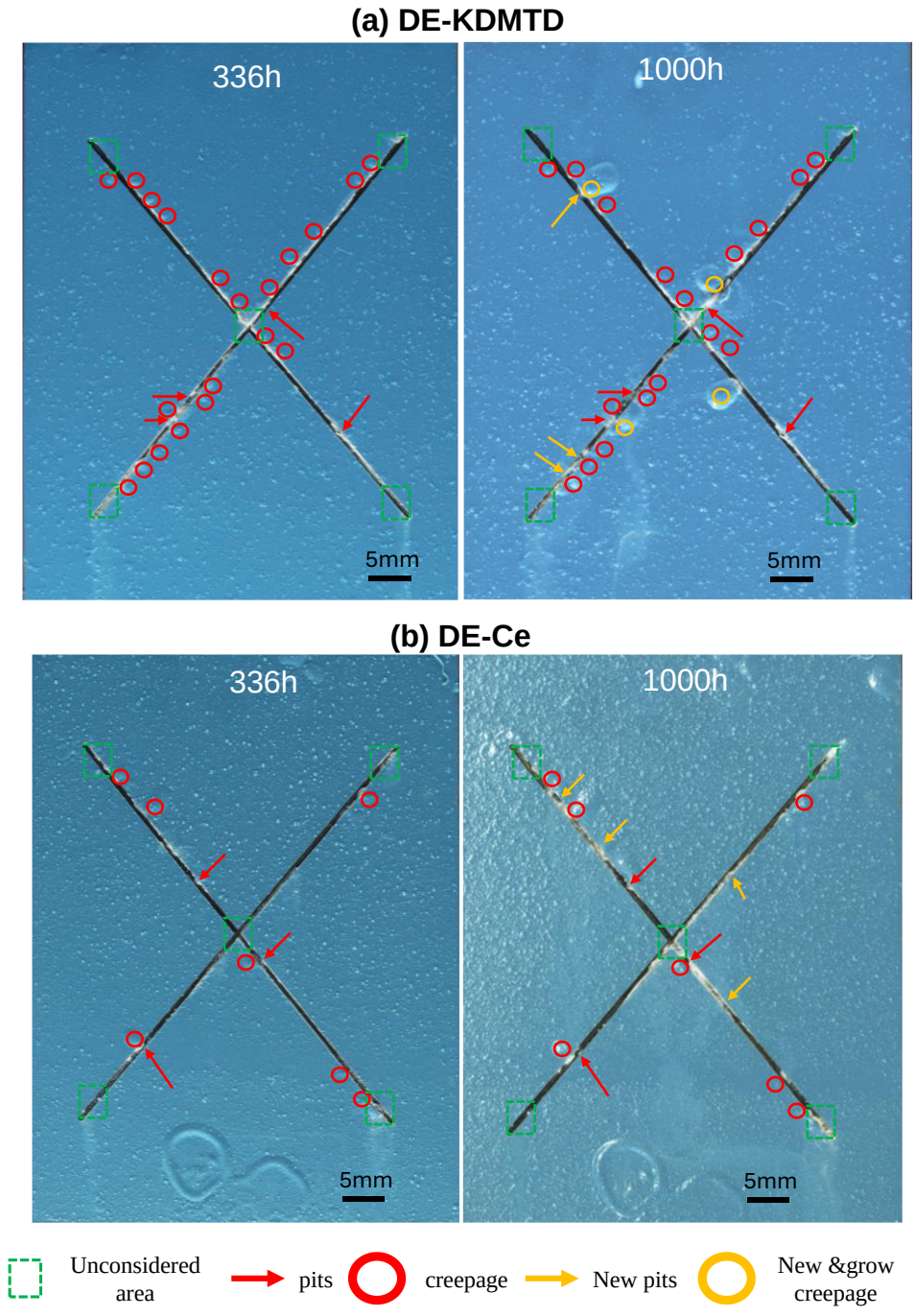


Figure 2.8-1 NSS results of (a) DE-KDMTD and (b) DE-Ce coatings.

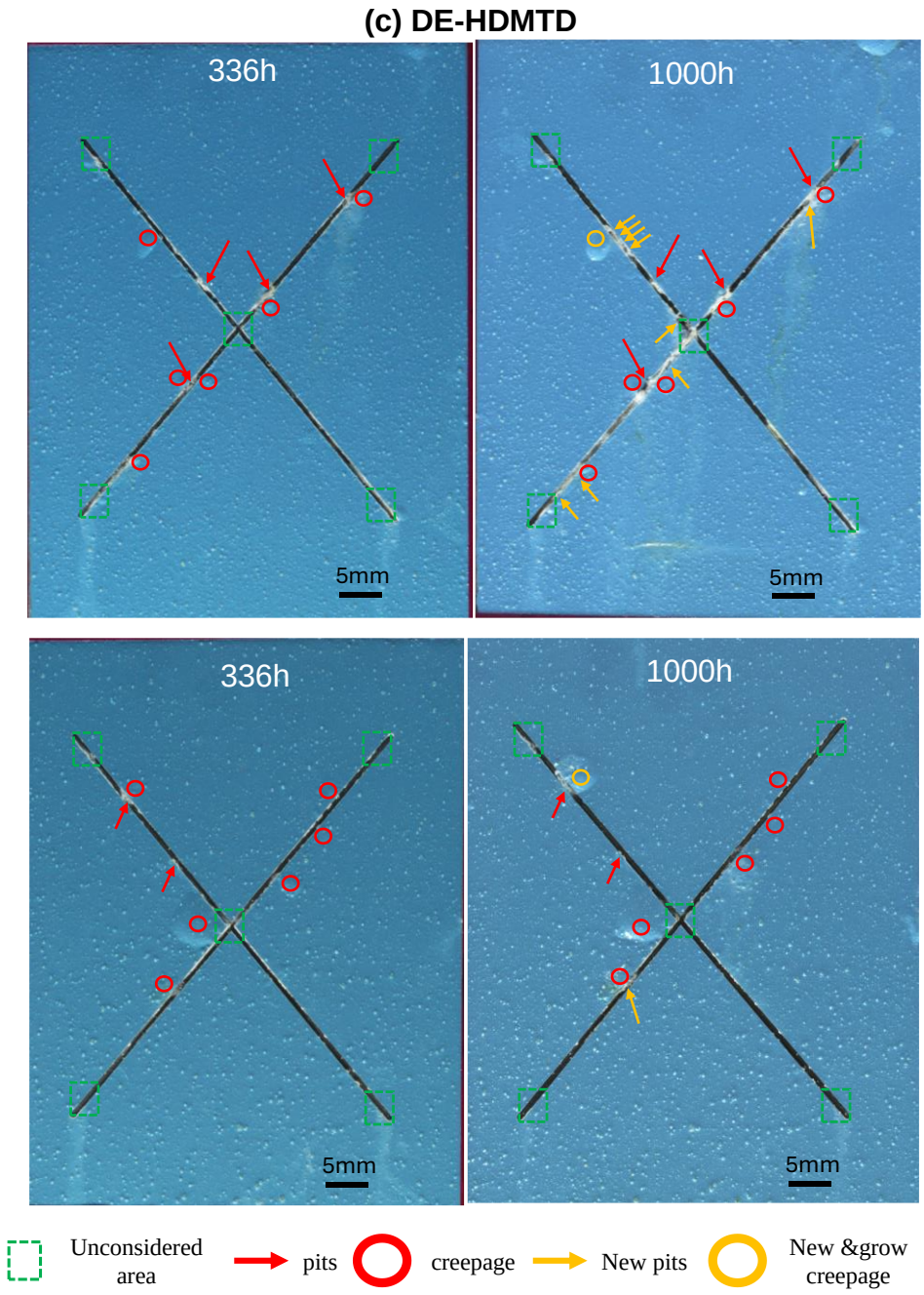


Figure 2.8-2 NSS results of (c) DE-HDMTD and (d) DE-Ce/DE-HDMTD coatings.

Firstly, all the coatings exhibited creepage at 336 h (as marked in Figure 2.8 and Figure SI 2.2 with a red circle), indicating that the pigments added to the primer negatively affected the coating wet-adhesion to bare AA2024-T3. Coatings containing KDMTD (Figure 2.8a) showed

significantly higher levels of creepage than the other samples at 336h (blue columns in Figure 2.9) followed by relatively high increase of creepage points from 336 to 1000 h. This is attributed to the hygroscopic nature of KDMTD and its related ability to release from the coating, as discussed in the previous section. The other coatings showed comparable creepage levels between them with no clear differences between DE (Figure SI 2.2a) and DE-loaded with Ce (Figure 2.8b) or HDMTD (Figure 2.8c) at 336h but also no significant creepage increase from 336h to 1000h. In line with this, lower creepage was observed in the KDMTD containing coatings when DE-KDMTD was partially replaced DE particles containing Ce or HDMTD (Figure SI 2.2b and 2.2c).

In terms of pitting, the coating without inhibitors (Figure SI 2.2a) exhibited a high number of pits at both 336 h (8 pits) and 1000 h (15 pits) with the mentioned reduced creepage. Among the three coatings with a single type of inhibitor pigment, the DE-Ce coating (Figure 2.8b) performed the best in pitting (2 locations growing to 8 at 1000h) and creepage (comparable to that of HDMTD). The DE-HDMTD coating (Figure 2.8c) showed comparable creepage to DE-Ce and a comparably low number of pits at 336 h that nevertheless grew when exposed to 1000h. Conversely, and in line with the high inhibitor release, leading to more creepage, the DE-KDMTD coating (Figure 2.8a) showed the lowest number of pits at both 336 h and 1000 h.

Interestingly, the combination of DE-Ce with DE-HDMTD (Figure 2.8d) resulted in the lowest number of pits and minimal creepage compared to the coatings with a single DE-inhibitor particle type. In contrast, the other combinations of DE-inhibitor carriers led to high levels of both pits and creepage in the case of DE-Ce/DE-KDMTD(Figure SI 2.2b) and low number of pits but high creepage in the case of DE-HDMTD/DE-KDMTD (Figure SI 2.2c), hence exposing the predominant role of a highly hygroscopic inhibitor in creepage while not being able to stop pitting progression when combined with an efficient inhibitor as Ce, probably due to a competition mechanism in NSS difficult to evaluate in this test, but also highlighting once more that better KDMTD coatings can be achieved using lower DE-KDMTD concentration since DE-HDMTD/DE-KDMTD showed better pitting and creepage behavior than the DE-KDMTD sample with half KDMTD content, in good agreement with the droplet test results.

Overall, and considering the three characteristic parameters used in the NSS analysis (white product, pitting, creepage), the best performing coatings to protect bare AA2024-T3 appear to be the DE-Ce/DE-HDMTD followed by DE-Ce and DE-HDMTD/DE-KDMTD.

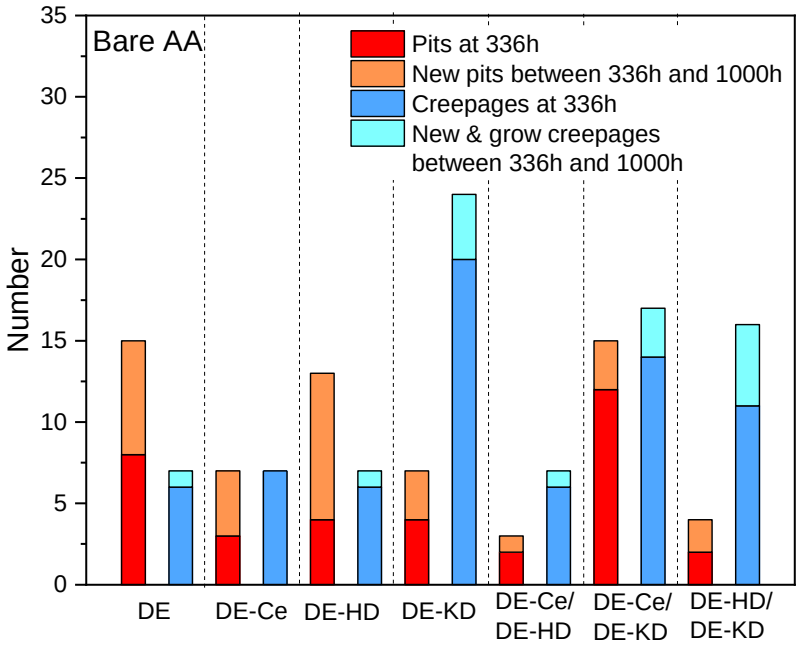


Figure 2.9 Pit and creepage count for DE-containing coatings applied on bare AA2024-T3 during exposure to NSS for 1000h.

Considering the results obtained in terms of protection of bare AA2024-T3 it was decided to analyze the behavior of the coatings to protect TSA AA2024-T3 due to its relevance in aerospace applications. Figure 2.10 and Figure 2.11 show the images of the samples exposed to NSS and the quantification of pits and creepage respectively. The detailed counting of pits on each sample can be found in support information Figure SI 2.3.

When the DE-containing coatings were applied on TSA and exposed to NSS three remarkable differences were observed in general: (i) no creepage during the entire 1000 h test period was observed for any of the TSA samples. This is likely due to the improved coating adhesion resulting from the TSA pretreatment; (ii) white corrosion products were observed already at 168 h exposure for all coatings even if at different degrees. This is likely due to the incapability of the corrosion inhibitors used to stop the strong galvanic couple between the more anodic aluminum oxide layer used for the anodizing and the more cathodic underlying Cu-rich AA2024-T3 substrate. This is supported by, (iii) the pit counts (Figure 2.11) showing a higher number of pits in all samples compared to those observed for the same coatings on the bare AA2024-T3 (Figure 2.9).

When comparing the samples, the DE-HDMTD coating exhibited a high number of pits initially at 168 h, but showed no significant growth from that moment until the end of the test at 1000 h. Conversely, the coating without inhibitor (DE) and the coatings containing KDMTD showed the highest number of pits, suggesting that KDMTD alone is insufficient to prevent pit formation when strong galvanic couples are created despite showing the highest inhibitor release. Consistent with the results for bare AA2024-T3 in NSS, the DE-Ce and DE-Ce/DE-HDMTD coatings on

TSA AA2024-T3 showed the lowest number of pits among all coatings, hence classifying them as the best coatings in NSS.

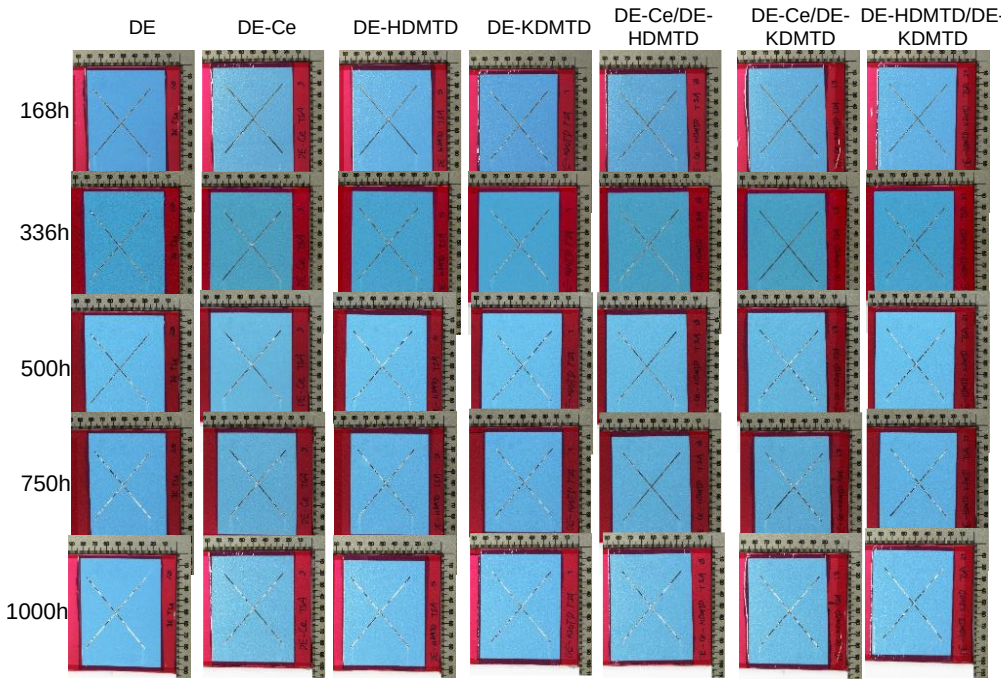


Figure 2.10 Salt fog spray tests results of the 7 coating systems on TSA AA2024-T3.

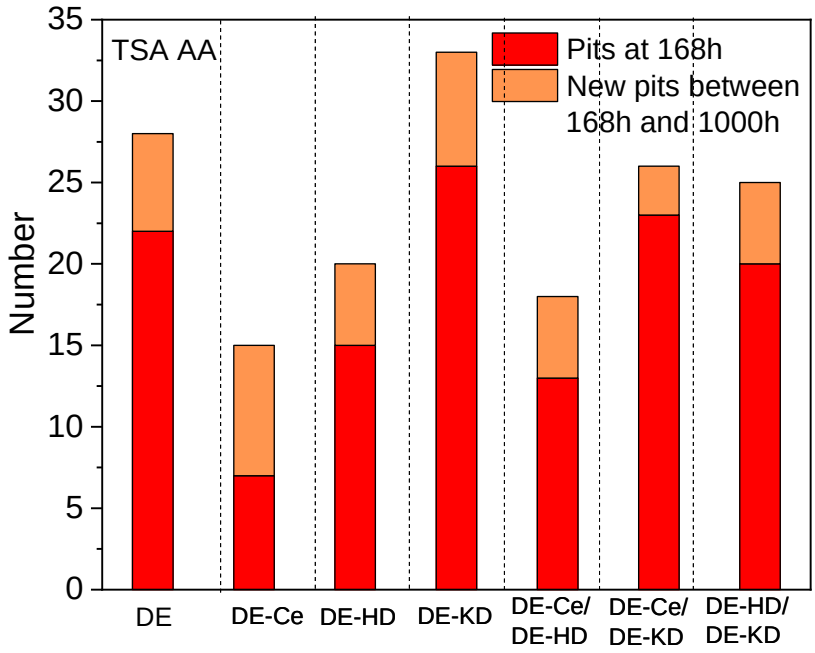


Figure 2.11 Pits count for DE-containing coatings applied on anodized AA2024-T3 during exposure to NSS for 1000h. Note: in these samples no creepage was observed.

## 2.4 Conclusions

Three model organic and inorganic inhibitors ($Ce(NO_3)_3$, HDMTD, and KDMTD) were incorporated into naturally occurring porous silica microparticles (diatomite, DE), loaded into epoxy-amine coatings and applied in different particle combinations onto bare AA2024-T3 and anodized (TSA) AA2024-T3. The coatings anticorrosion performance was evaluated using droplet tests during 7 days and salt fog spray tests for 1000 h.

Although the DE-HDMTD coating initially delayed corrosion in droplet test, it proved ineffective over the long term, possibly due to instability on the metallic surface or insufficient release from the coating. The DE-Ce coating and coatings containing DE-KDMTD (DE-KDMTD, DE-Ce/DE-KDMTD, DE-HDMTD/DE-KDMTD) behaved the best in droplet test. This is attributed to an efficient inhibitor release at damaged locations by these coatings as demonstrated by SEM/EDS analysis confirming the presence of cerium and KDMTD local deposition at the exposed metal. However, the results also demonstrated an over-release of KDMTD, which posed risks of blistering and delamination as well as long term protection. The negative effect of this high release for KDMTD samples was confirmed by a relatively high creepage yet with low pitting for KDMTD containing samples applied on bare AA2024-T3 exposed to NSS tests. This highlights the need for different loading strategies of this KDMTD inhibitor in diatomite for more efficient protection without detriment of other coating properties.

In neutral salt fog spray tests, the coatings applied onto TSA AA2024-T3 showed no creepage due to the improved adhesion provided by the anodized layer. However, white corrosion products appeared earlier together with more pits than for the coated bare AA2024-T3 samples. This is attributed to the difficulty of these inhibitors to fully stop strong galvanic couple-induced corrosion between the cathodic AA2024 substrate and the anodic TSA layer. On both types of substrates (bare/TSA), the DE-Ce and DE-Ce/DE-HDMTD coatings exhibited the lowest number of pits and creepage, indicating superior protection, primarily attributed to the release of cerium and the synergistic effect provided by HDMTD, which is consistent with our earlier work. Notably, unlike the droplet test, NSS tests involve washing processes where the solution with released inhibitors is continuously washed off. This could potentially explain the synergistic effect resulting from the good stability of HDMTD or the formation of Ce-DMTD complex on AA2024-T3.

Overall, the strategy of loading inhibitors into diatomite revealed that inorganic inhibitors such as $Ce(NO_3)_3$ performed better than the organic inhibitors HDMTD and its potassium salt, KDMTD, although for different reasons. While KDMTD effectively inhibits corrosion due to large inhibitor release, its highly hygroscopic nature leads to rapid depletion of the inhibitor and coating failure (blistering, creepage). This points at the need to understand its behavior compared to HDMTD and to find alternative loading strategies that control better its interaction with the surrounding binder as studied in Chapters 3 and 4 using a model epoxy-amine coating system. Concerns about HDMTD include its stability on AA2024 that needs further understanding as will

be discussed in Chapter 5 and its negative interaction with the epoxy-amine binder negatively affecting its ability to release from the coating as will be further explored in Chapter 6.

# 2.5 References

(1) Yasakau, K. A.; Zheludkevich, M. L.; Lamaka, S. V.; Ferreira, M. G. Mechanism of corrosion inhibition of AA2024 by rare-earth compounds. *The Journal of Physical Chemistry B* **2006**, *110* (11), 5515-5528.
(2) Visser, P.; Liu, Y.; Zhou, X.; Hashimoto, T.; Thompson, G. E.; Lyon, S. B.; van der Ven, L. G.; Mol, A. J.; Terryn, H. A. The corrosion protection of AA2024-T3 aluminium alloy by leaching of lithium-containing salts from organic coatings. *Faraday Discussions* **2015**, *180*, 511-526.
(3) Harvey, T.; Hardin, S.; Hughes, A.; Muster, T.; White, P.; Markley, T.; Corrigan, P.; Mardel, J.; Garcia, S.; Mol, J. The effect of inhibitor structure on the corrosion of AA2024 and AA7075. *Corrosion science* **2011**, *53* (6), 2184-2190.
(4) Zadeh, M. A.; Tedim, J.; Zheludkevich, M.; van Der Zwaag, S.; Garcia, S. J. Synergetic active corrosion protection of AA2024-T3 by 2D-anionic and 3D-cationic nanocontainers loaded with Ce and mercaptobenzothiazole. *Corrosion Science* **2018**, *135*, 35-45.
(5) Zheludkevich, M.; Tedim, J.; Ferreira, M. "Smart" coatings for active corrosion protection based on multi-functional micro and nanocontainers. *Electrochimica Acta* **2012**, *82*, 314-323.
(6) Denissen, P. J.; Garcia, S. J. Cerium-loaded algae exoskeletons for active corrosion protection of coated AA2024-T3. *Corrosion Science* **2017**, *128*, 164-175.
(7) Denissen, P. J.; Shkirskiy, V.; Volovitch, P.; Garcia, S. J. Corrosion Inhibition at Scribed Locations in Coated AA2024-T3 by Cerium- and DMTD-Loaded Natural Silica Microparticles under Continuous Immersion and Wet/Dry Cyclic Exposure. *ACS Appl Mater Interfaces* **2020**, *12* (20), 23417-23431. DOI: 10.1021/acsami.0c03368 From NLM PubMed-not-MEDLINE.
(8) Doppke, T. S.; Bryant, A. W. The salt spray test-past, present, and future. *SAE Transactions* **1983**, 1137-1152.
(9) Altmayer, F. Critical aspects of the salt spray test. *Plating Surface Fin.* **1985**, *72* (9), 36-40.
(10) Tsutsumi, Y.; Nishikata, A.; Tsuru, T. Pitting corrosion mechanism of Type 304 stainless steel under a droplet of chloride solutions. *Corrosion science* **2007**, *49* (3), 1394-1407.
(11) Thomson, M.; Frankel, G. Atmospheric pitting corrosion studies of AA7075-T6 under electrolyte droplets: part I. Effects of droplet size, concentration, composition, and sample aging. *Journal of The Electrochemical Society* **2017**, *164* (12), C653.
(12) Williams, G.; Coleman, A. J.; McMurray, H. N. Inhibition of Aluminium Alloy AA2024-T3 pitting corrosion by copper complexing compounds. *Electrochimica Acta* **2010**, *55* (20), 5947-5958.
(13) Tavaststjerna, M. J.; Picken, S. J.; Garcia, S. J. Role of Molecular Water Layer State on Freezing Front Propagation Rate and Mode Studied with Thermal Imaging. *Langmuir* **2024**.
(14) Campestrini, P.; Terryn, H.; Hovestad, A.; De Wit, J. Formation of a cerium-based conversion coating on AA2024: relationship with the microstructure. *Surface and Coatings Technology* **2004**, *176* (3), 365-381.
(15) Qin, T. T.; Li, J.; Luo, H. Q.; Li, M.; Li, N. B. Corrosion inhibition of copper by 2, 5-dimercapto-1, 3, 4-thiadiazole monolayer in acidic solution. *Corrosion Science* **2011**, *53* (3), 1072-1078.
(16) Fateh, A.; Aliofkhazraei, M.; Rezvanian, A. Review of corrosive environments for copper and its corrosion inhibitors. *Arabian journal of Chemistry* **2020**, *13* (1), 481-544.
(17) Zhao, J.; Santoso, A.; Garcia, S. J. Small concentrations of NaCl help building stable inhibiting layers from 2, 5-dimercapto-1, 3, 4-thiadiazole (DMTD) on AA2024-T3. *Corrosion Science* **2023**, *225*, 111562.
(18) Denissen, P. J.; Garcia, S. J. Reducing subjectivity in EIS interpretation of corrosion and corrosion inhibition processes by in-situ optical analysis. *Electrochimica Acta* **2019**, *293*, 514-524.
(19) Maiti, N.; Chadha, R.; Das, A.; Kapoor, S. Surface selective binding of 2, 5-dimercapto-1, 3, 4-thiadiazole (DMTD) on silver and gold nanoparticles: a Raman and DFT study. *RSC advances* **2016**, *6* (67), 62529-62539.

# 2.6 Support information

*SI-2.1 Calibration curves*

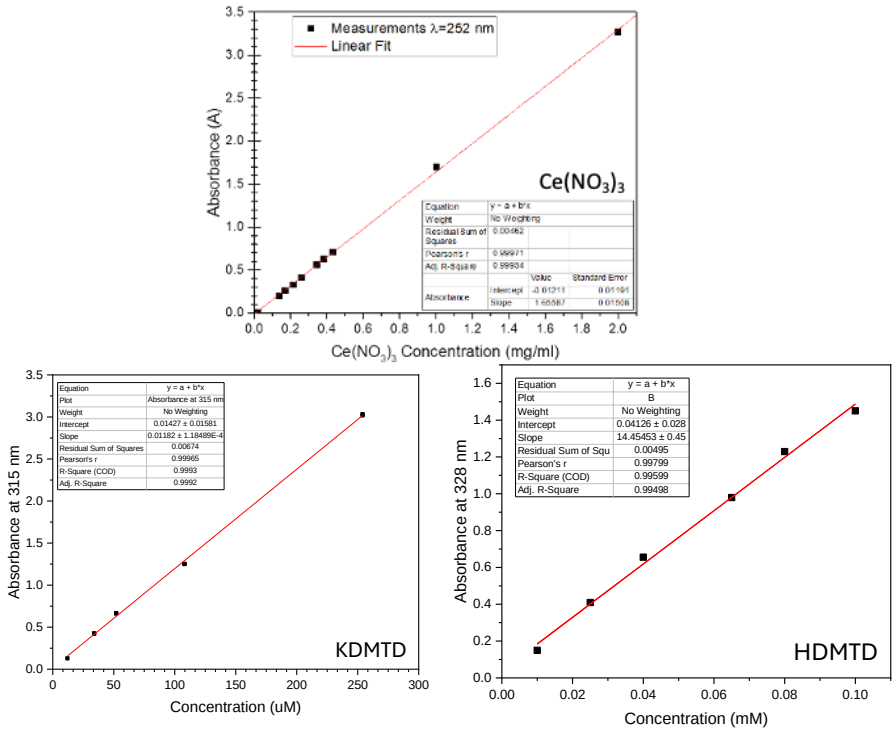


Figure SI 2.1 Calibration curves for UV-Vis spectrophotometric determination of $Ce(NO_3)_3$, HDMTD and KDMTD aqueous solutions.

*SI-2.2 NSS results of coated bare AA2024-T3*

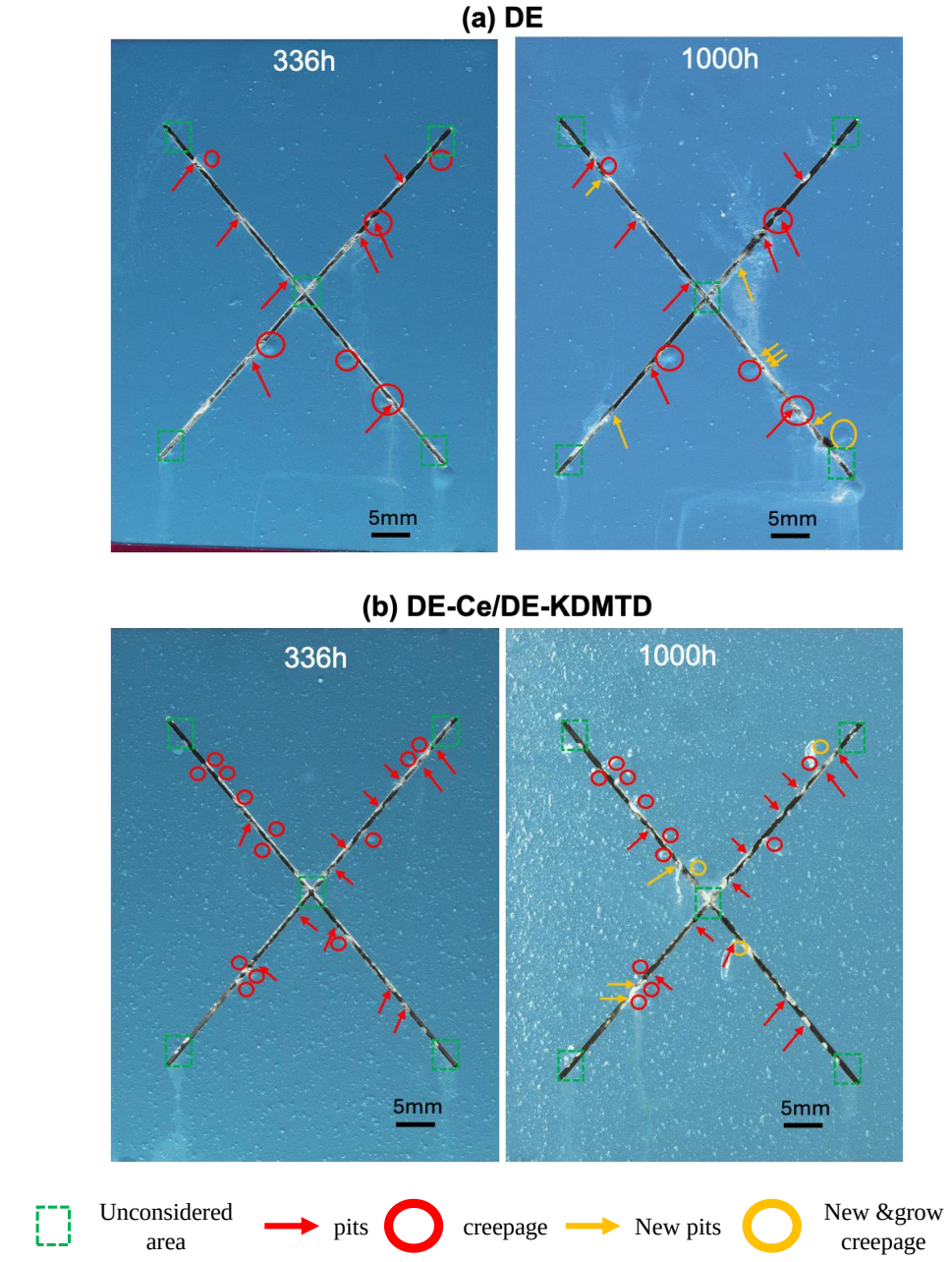


Figure SI 2.2-1 NSS results of (a) DE and (b) DE-Ce/DE-KDMTD coatings.

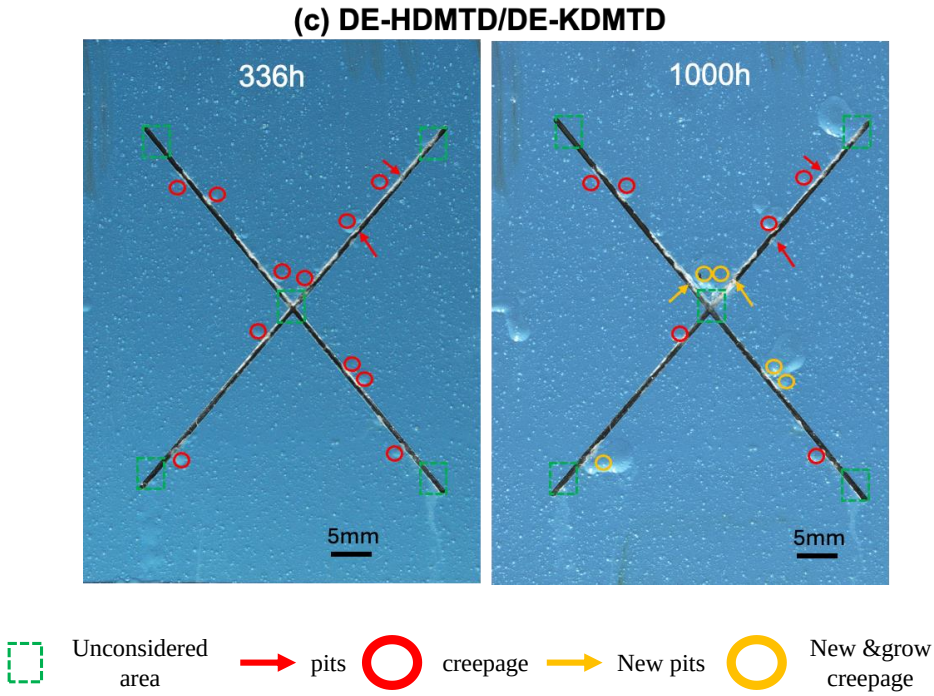


Figure SI 2.2-2 NSS results of (c) DE-HDMTD/DE-KDMTD coatings.

*SI-2.3 NSS results of coated TSA AA2024-T3*

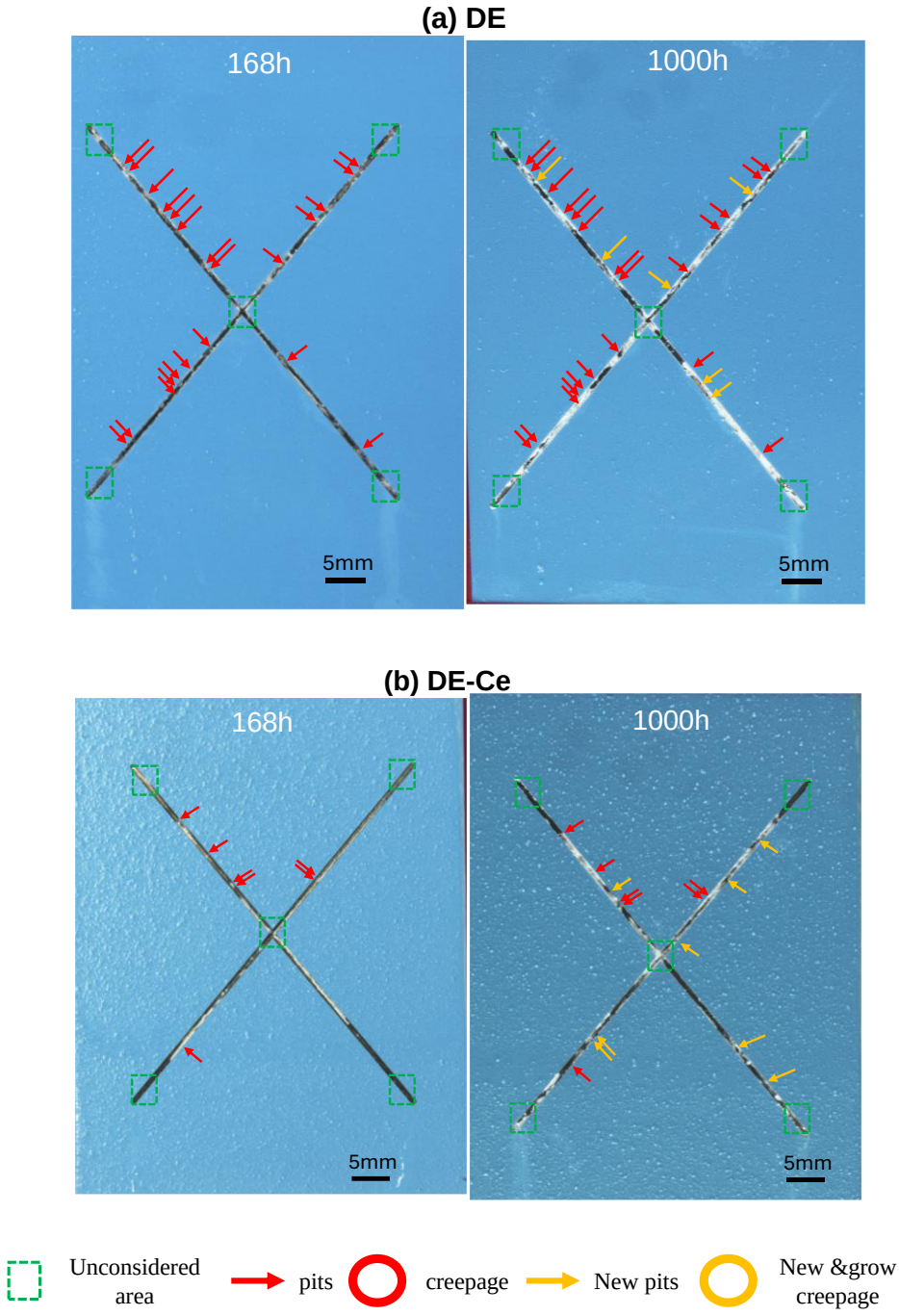


Figure SI 2.3-1 NSS results of (a) DE and (b) DE-Ce coatings.

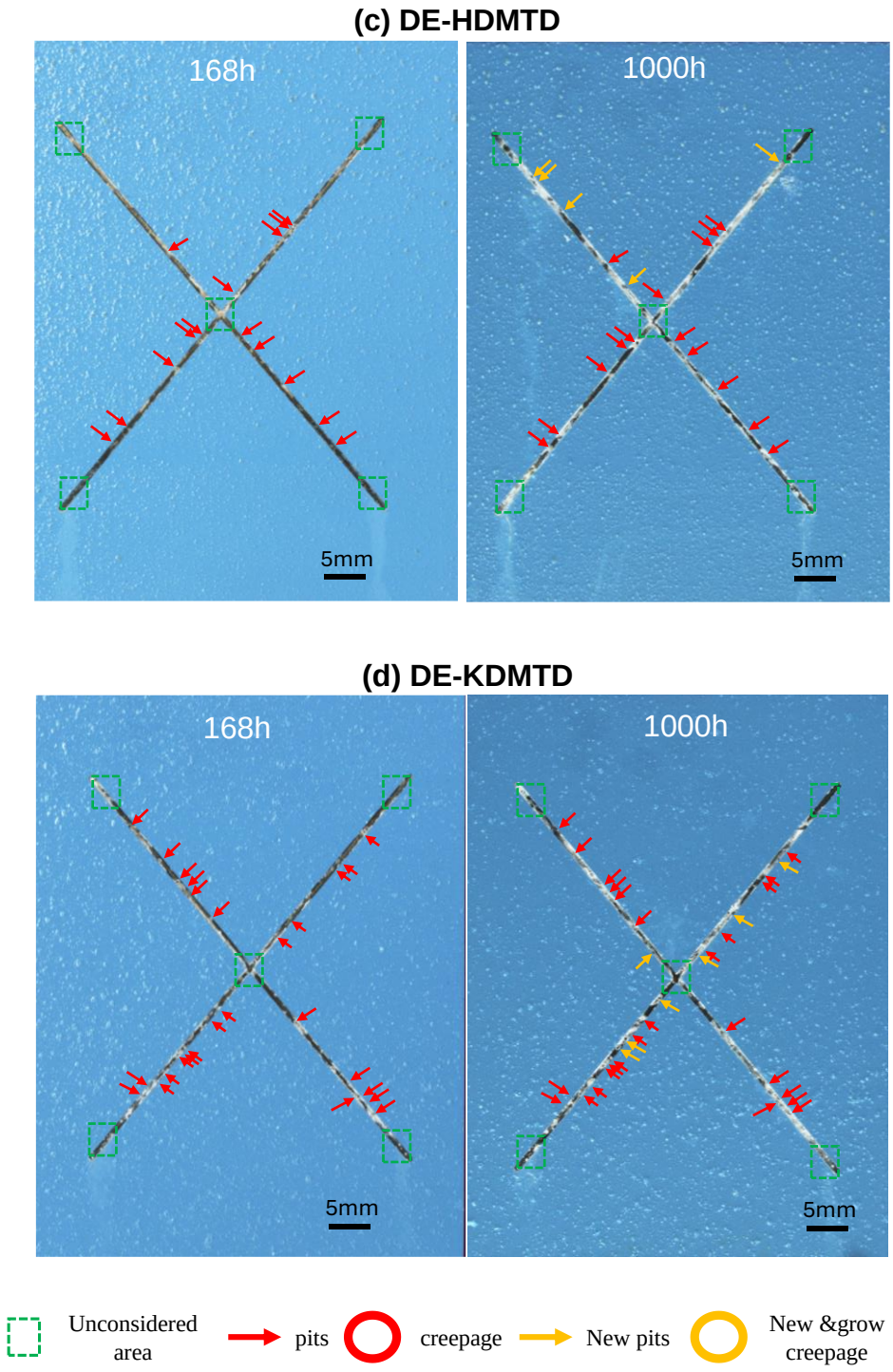


Figure SI 2.3-2 NSS results of (c) DE-HDMTD and (d) DE-KDMTD coatings

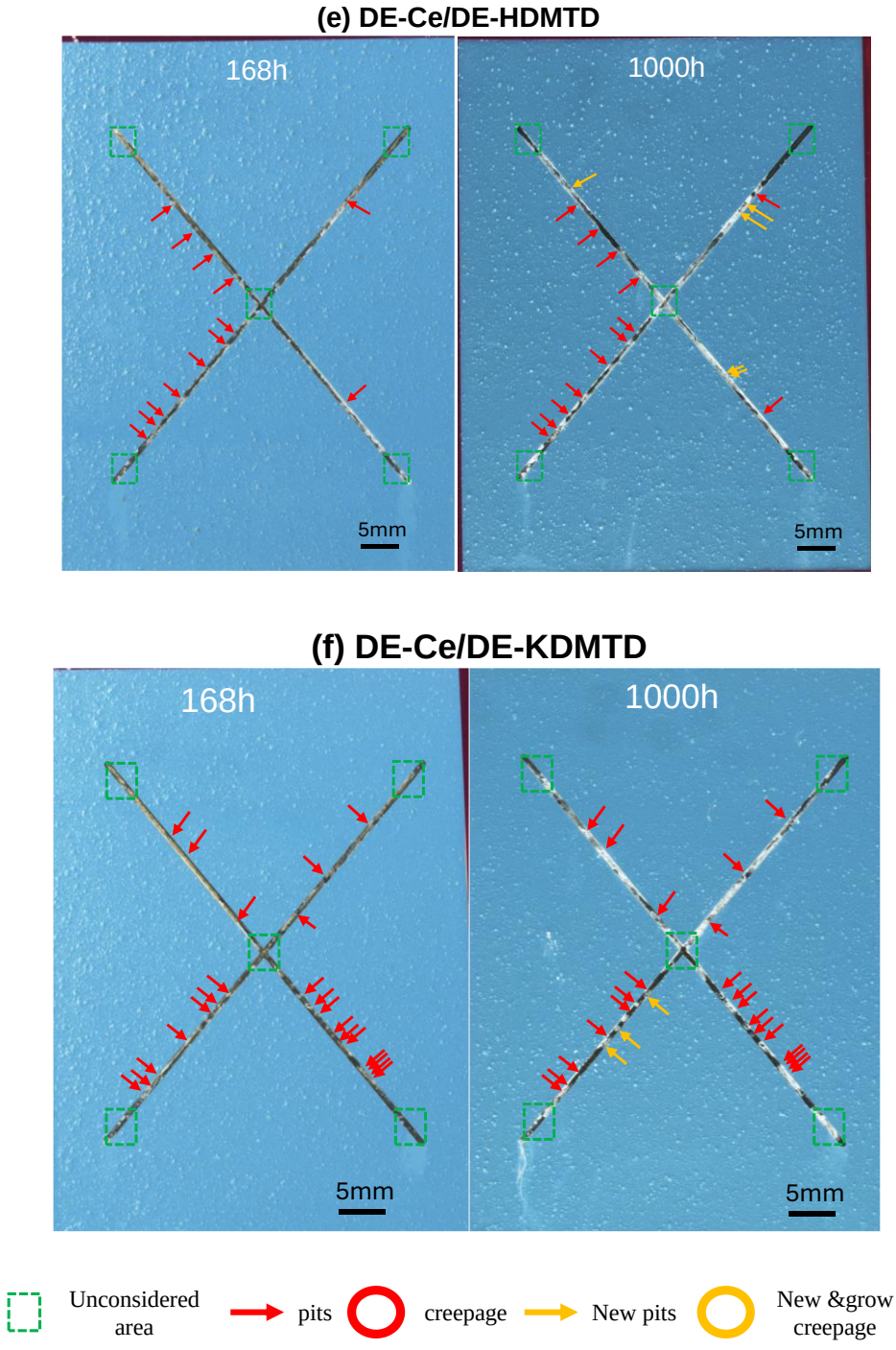


Figure SI 2.3-3 NSS results of (e) DE-Ce/DE-HDMTD and (f) DE-Ce/DE-KDMTD coatings.

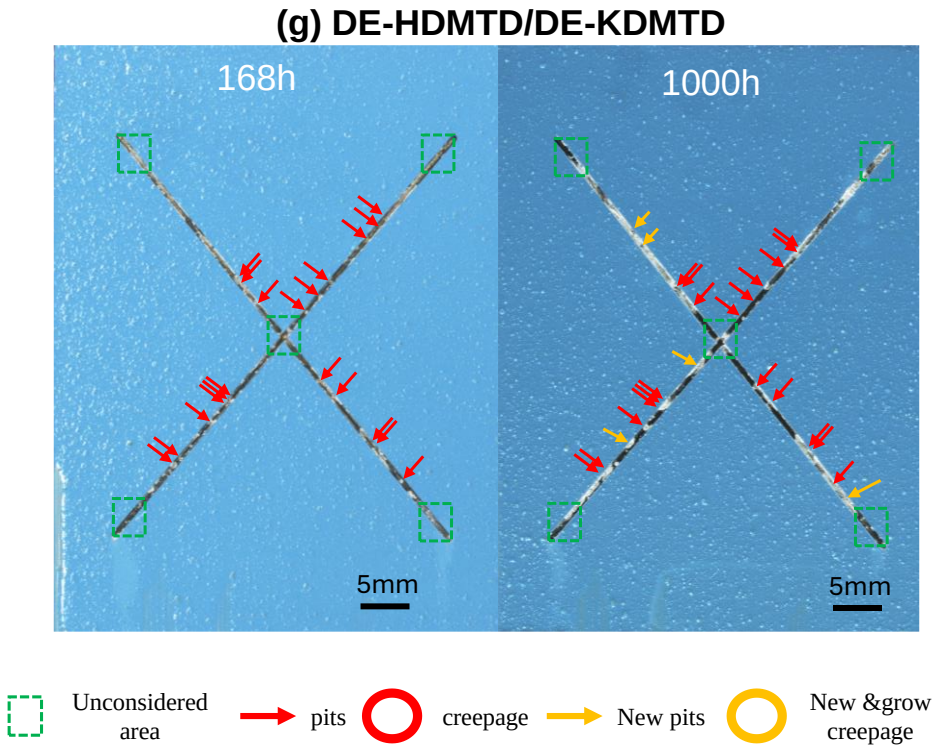


Figure SI 2.3-4 NSS results of (g) DE-HDMTD/DE-KDMTD coating.

# Chapter 3

# When Ionic State is more Important than Inhibitor Concentration: A Comparison of Epoxy-Amine Coatings with 2,5-Dimercapto-1,3,4-thiadiazolate (DMTD) Salts Loaded in Diatom Exoskeletons

*In this work, we investigate the effect of pH on the ionic states and inhibition power in the coatings by using two chemically similar organic corrosion inhibitors. While 2,5-dimercapto-1,3,4-thiadiazole (HDMTD) shows high intrinsic protection in solution, side reactions and limited release hinder its performance in organic epoxy coatings. Herein, we introduce 2,5-dimercapto-1,3,4-thiadiazolate dipotassium salts (KDMTD), which have strong ionic bonds that offer several advantages for use in the organic coating, including high water solubility and reduced reactivity with the polymer matrix. Both inhibitors are integrated into coatings using diatom exoskeletons as microcarriers. Thermo-gravimetric analysis (TGA), Differential Scanning Calorimetry (DSC) and UV-visible spectroscopy confirm that KDMTD interacts less with the coating matrix, allowing for faster and more abundant release than HDMTD. Image reflectometry demonstrates that despite the slower release of HDMTD, there was only minor corrosion (less than 6% surface activity) observed on the damaged coating when exposed to different pH levels (5, 7, 10). This indicates the effective anti-corrosion properties of HDMTD during short-term exposure (2 hours), attributed to its inherent acidic nature. Interestingly, by slight acid exposure (pH=5) of coating damage, KDMTD is protonated and the corrosion inhibition effectiveness of KDMTD is significantly enhanced. This study highlights the importance of the correct inhibitor structure controlled over inhibitor concentration to enhance corrosion protection and provides insights for developing active organic inhibitors in organic coatings.*

# 3.1 Introduction

Organic corrosion inhibitors are notably valuable for their inherent effectiveness, relatively low toxicity, low molecular weight, and versatility of design. [1-3] They are well-suited for protecting steel in pipeline liquids [4] but are less effective for coated structures like aircraft aluminum alloys. This is due to the negative reactions with the organic binders in coating primers (e.g., epoxy-amine). Such matrix-inhibitor interactions can hinder the release of inhibitors from the coating, compromising their capability to protect metal surfaces from corrosion. [5, 6] Encapsulating inhibitors within nano or micro-sized inorganic carriers is a straightforward strategy to isolate the organic inhibitors from the coating matrix. Such carriers allow controlling the release of inhibitors by various methods, such as water dissolution, pH, diffusion, and ion exchange. [7, 8] However, these methods are limited by the small local amount of inhibitors available at a damaged locations, which can lead to insufficient coverage of the metal surface therefore reducing the inhibition efficiency. [9, 10]

The inhibition principle of organic inhibitors involves the adsorption (physisorption and/or chemisorption) of organic molecules or/and ions onto the metal surface to form a protective layer. [11] Physical adsorption occurs due to the electrostatic attraction between charged organic inhibitors and the charged metal surface. This process is significantly affected by the pH of the solution, as protonated organic inhibitors are attracted to the negatively charged metal surface, forming a protective layer. [12-14] Chemisorption involves the interaction of the metal atom vacant orbital with the lone pair electrons of heteroatoms in the organic inhibitor. This interaction forms strong chemical bonds between the nonionic organic corrosion inhibitor molecules and the metal surface. [15, 16] The adsorption process can be influenced by factors such as the chemical structure and concentration of the inhibitors, the surface charge distribution of the metals, and environmental conditions (e.g., ions, pH, temperature, UV, etc.). [17, 18]

Among organic inhibitors, mercapto inhibitors like 2,5-Dimercapto-1,3,4-thiadiazolate salts, e.g., 2,5-Dimercapto-1,3,4-thiadiazole (HDMTD) and its di-potassium salt (KDMTD), have been identified as very effective organic inhibitors for Cu, iron, and Cu-rich Al-alloys, [14, 19-21] thanks to their heteroatoms (S, N) with lone electron pairs, capable of forming strong interactions with metal surfaces, enhancing adsorption and protection against corrosion. KDMTD replaces the hydrogen atoms in the mercapto groups of HDMTD with potassium ions, forming an ionic compound that offers several advantages for use in the organic coating, including high water solubility and reduced reactivity with the polymer matrix. Our previous work [19] reported the encapsulation of HDMTD in natural porous silica microparticles (diatom exoskeletons or diatomaceous earth or diatomite), and found that while protection was initially offered, it was not sustained. It was then hypothesized but not demonstrated that besides low inhibitor loading, inhibitor release was reduced due to the unwanted interaction between thiol groups in the organic HDMTD and amine or/and epoxy in the resin used for the matrix. Despite KDMTD has also been used in the corrosion protection of AA2024, [2, 22] its comparison with HDMTD and optimal loading in coatings remains underexplored.

In this work, we dig into the mechanisms responsible for the inhibition of AA2024 using coatings loaded with two apparently similar organic inhibitors. To this aim, we loaded KDMTD and HDMTD into diatom exoskeletons (DE). The interaction between these inhibitors and the matrix was studied by thermogravimetric analysis (TGA), differential scanning calorimetry (DSC), and ex-situ UV-Vis spectroscopy for release kinetics. The impact of pH on the ionic states of KDMTD and HDMTD is assessed using UV-Vis spectroscopy. The corrosion inhibition and inhibitor layer stability are evaluated by exposing the damaged coatings with HDMTD or KDMTD to electrolytes with varying pH, using *in-situ*, high-resolution image reflectometry. This study highlights the significance of ionic states over inhibitor concentrations, which may explain previously unexplored, unexpected results in corrosion inhibition.

# 3.2 Experimental

*3.2.1 Materials*

2,5-dimercapto-1,3,4-thiadiazole (HDMTD >99%) and its di-potassium salt (KDMTD >99%) powders were purchased from Sigma-Aldrich to be used as corrosion inhibitors. Diatom exoskeletons (DE, natural silica nanoporous hollow microparticles) mainly from the *Aulacoseiraceae* family, was supplied by Profiltra Customized Solutions (NL) and used as the carrier for the inhibitors. The DE was refined following the procedure reported in our previous work. [19] Commercial grade bare 2.5mm thick AA2024-T3 plates were cut into 10cm x 10cm pieces and used as metal substrates. The coating matrix was prepared from a bisphenol-A based epoxy resin (Epikote™ 828) and an amine crosslinker (Ancamine®2500), both sourced by AkzoNobel (NL), and used in their unmodified form with xylene (99%) serving as the solvent. Sodium chloride (NaCl, purity > 98%) was acquired from VWR Chemicals, and Milipore® filtered water was used in all the study. The pH of 0.05 M NaCl solutions was adjusted to 5, 7, or 10 by dropwise addition of a hydrogen chloride solution (HCl, 37%, Sigma-Aldrich) or a 0.1 mM sodium hydroxide solution (NaOH, ≥ 98%, Sigma-Aldrich), monitored with an inoLab® pH Meter.

*3.2.2 Inhibitors loading in DE silica microcarriers*

0.5 g of DE was added to 20 mL 0.5M KDMTD water solution or HDMTD Butanone (MEK) solution (used for HDMTD instead of water due to the relatively low solubility of HDMTD in water). The dispersions were mixed vigorously with a high-speed mixer at 3500 rpm for 5 min. Then, the mixtures were stirred for 24 h at 320 rpm using a shaking table. Next, the loaded particles were separated by centrifugation at 4000 rpm for 10 min followed by the removal of the supernatant. The particles were further dried at 70 °C for 6 h and stored in a desiccator before use. The supernatant was used to quantify the inhibitor loading in the DE particles.

*3.2.3 Release of inhibitors from DE powders*

The release kinetics of inhibitor from DE-HDMTD and DE-KDMTD particles was studied with a PerkinElmer LAMBDA 35 UV/Vis spectrometer. To this aim, 10 mg particles were placed inside a Whatman® 42 paper filter on top of a glass jar filled with 100mL 0.05M NaCl solution. 4 ml aliquots of solution were taken at different immersion times and tested using the UV-Vis spectrometer. After each measurement, the aliquots were returned to the glass jar. Aliquots were taken at 2, 4, 6, 8, 10, 15, 20, 25, 30, 40, 50, 60, 90, 120, 150 and 180 minutes after the initial exposure of the DE powders to the NaCl solution. At each instance, absorbance magnitude was measured at the peak absorbance wavelength (328 nm for HDMTD and 315 nm for KDMTD) and converted to concentration using a calibration curve for each inhibitor. All measurements were repeated three times for each coating.

*3.2.4 Coatings preparation*

Coatings were prepared on AA2024 and Teflon to perform corrosion studies and freestanding film tests, respectively. The AA2024 surface cleaning consists of the following steps: (1) removal of the native oxide layer and surface roughness increase with Scotch Brite 3M in $H_2O$; (2)

degreasing with a paper wet in acetone;(3) pseudo-boehmite treatment to increase the amount of reactive hydroxyl groups on the surface by 10 s immersion in 2 M NaOH followed by a 30 s immersion in distilled water and drying with nitrogen.

The coating compositions were prepared as listed in Table 3.1. The coatings' formulation is given as a function of epoxy resin (phr=parts per hundred epoxy resin in weight). Briefly, Epikote™ 828, Ancamine®2500 and xylene (weight ratio 2.70:1.57:1.06) were mixed for 5 min in a high-speed mixer at 2500 rpm and pre-cured at room temperature for 15 min. Right after precuring, the inhibitor-loaded particles (DE, DE-HDMTD, DE-KDMTD) were added, and the coating formulation was manually stirred for 3 min. After 1 min resting time the coats were applied using a doctor blade with a wet thickness of 100 µm onto Teflon sheets to obtain free-standing films for thermal analysis and on the AA2024 metal coupons to obtain coated panels for release and corrosion tests. After a flash-off period of 30 min at room temperature, the coatings were cured at 60ºC for 24h in a dosed oven. After cooling down, the samples were stored in a desiccator until testing.

Table 3.1 Coating formulations as function of Epikote™ 828 (phr=parts per hundred epoxy resin in weight). The calculated inhibiting active component in wt% of the total coating dry weight. The pigment volume concentration (PVC%) was set at 30%.

| **Sample Name** | **DE pigment type** | **DE particles (phr)** | **Inhibiting active component (phr)** | **Inhibiting active component (wt.%)** | **Dry thickness (µm)** |
|---|---|---|---|---|---|
| Epoxy | - | 0 | 0 | 0 | 65±3 |
| Epoxy/DE | DE | 33.7 | 0 | 0 | 68 ±3 |
| Epoxy/DE-HDMTD | DE-HDMTD | 25.3 | 8.4 | 4.4 | 70±3 |
| Epoxy/DE-KDMTD | DE-KDMTD | 25.3 | 8.4 | 4.4 | 70±3 |

*3.2.5 Thermal analysis of free-standing films*

The coatings applied on Teflon sheets were separated with the help of a spatula and used for thermal analysis. The thermal stability of the coatings was analyzed by Thermogravimetric analysis (TGA). The TGA tests were conducted from 30 ºC to 600 ºC at a rate of 10 ºC/min under nitrogen gas with a flow rate of 20 mL/min. Differential scanning calorimetry (DSC) analyses were performed to investigate the inhibitor influence on the glass transition temperature ($T_g$) of the epoxy/amine coating systems. To this aim, a Modulated DSC TA Instruments was operated in nitrogen flow. Each sample was heated at a temperature range from -10 ºC to 80 ºC at a heating rate of 10ºC/min.

*3.2.6 Release of inhibitors from coatings on AA2024-T3*

The coatings with DE-HDMTD and DE-KDMTD applied into AA2024-T3 were surface ground by 1000-grit paper for 15s to remove top epoxy layer and expose inhibiting particles, prior to exposure to 20mL 0.05M NaCl solution using a container of 1 cm diameter. The concentration of the released HDMTD and KDMTD in NaCl solution was measured by UV-Vis spectrometer. To this aim, aliquots of 3 mL were collected at different times (1, 5, 15, 30, 60, 120, 240, 360, 1440 and 2880 min), tested with UV-Vis and put back to the main solution to maintain a constant volume of release medium. A plastic film was used to prevent evaporation. All release experiments were repeated three times for each coating.

*3.2.7 Corrosion inhibition test at damages*

A Roland EGX-350 engraver equipped with an end mill carbide tip of 1mm in diameter was used to create circular damages on the coated panels prior to exposure to the 0.05M NaCl water electrolyte. Drills of 1mm diameter and 0.25mm deep (i.e. around 0.15 mm into the metallic substrate) with respect to the coating surface were created without delamination. The resulting chips from the engraved zone were removed by vacuum cleaner and air blowing.

The corrosion inhibition at damage sites was evaluated with an operando optical electrochemical set-up as described in previous works. [5, 10, 19] To this aim, the scribed coating sample was mounted in a magnetic Raman electrochemical flow cell from Redox.me. This cell allows a total electrolyte volume of 4.5 ml and the use of a small Ag/AgCl (3 M KCl) reference electrode. The electrochemical cell was placed vertically in a Faraday cage on an optical table from ThorLabs to avoid any electromagnetic and vibrational disturbances. A 150x Dino-Lite digital microscope was placed at the window side of the electrochemical cell. This allows for obtaining 330 nm/pixed images every minute during exposure. The electrolyte (pH 5, 7, or 10 0.05M NaCl solution) was injected through side openings allowing to obtain optical information of the metal surface right after exposure to the electrolyte. The optical analysis based on image correlation at the pixel level was conducted in ImageJ software as described in earlier works. [5, 10, 19] The technique is based on a pixel-by-pixel analysis to monitor the progression of surface activity at the region of interest (ROI) over time. Images were converted to greyscale at an 8-bit resolution allowing the definition of 256 different levels of intensity between black and white, able to identify small surface changes leading to local ROI variations (i.e. activity). For the exposed metal surface, a static thresholding bin limit of 10 was used due to the small intensity changes and reduced optical noise.

After exposure, the solutions were collected and measured by UV-Vis spectroscopy to determine the concentration and structure of inhibitors in solution released from the damaged coatings.

# 3.3 Results and discussion

*3.3.1 Inhibitor interaction with coating matrix and effect on release*

Figure 3.1 shows the (a) weight loss with temperature, and the (b) glass transition temperature ($T_g$) of the epoxy coating without pigments and coatings loaded at 30% PVC with DE, DE-HDMTD and DE-KDMTD.

The epoxy coating without inhibitors shows three stages in agreement with the literature [20]: (i) Weight loss starts at 100°C, followed by a near-stable plateau up to 325°C with a related 25% mass loss attributed to low Mw chemicals; (ii) From 325°C to 450°C, rapid mass loss to reach approximate 50% mass loss, corresponding to the degradation of the epoxy-amine crosslinking networks; and (iii) From 450°C, carbonization of residual materials.

In the first degradation stage (i), coatings containing DE and DE-KDMTD particles exhibit a higher thermal stability than epoxy coating, with only a 15% mass loss. This improvement is attributed to the DE particles, in good agreement with previous work on diatomite polymer composites. [21] Conversely, when load with DE-HDMTD, no clear plateau in stage (i) and weight loss (25%) comparable to unloaded epoxy-amine are observed. As observed in our previous work,[19] when HDMTD was loaded into DE particles, it was distributed both inside and outside the DE particles. Additionally, the epoxy-amine matrix can penetrate the DE particles, allowing full contact with HDMTD. Thus, the lower thermal stability here is attributed to the interaction between the epoxy matrix and HDMTD, [23] leading to weaker C-S bonds in the crosslinking network and/or a decrease in crosslinking density. In the second degradation stage (ii), between 325°C and 450°C, coatings with DE and DE-KDMTD reach roughly 40% mass loss, while coatings with DE-HDMTD experience a 30% weight loss, all due to the breakdown of the epoxy-amine crosslinks. Notably, by the end of this stage (ii), all three coatings demonstrated an identical mass loss of 55%, which is 20% higher than that of the epoxy coating, attributed to the inclusion of DE particles. In the final stage (iii), all three coatings show a small mass loss (<5%), like the epoxy-amine coating.

Figure 3.1b shows the heat flow curves with the marks of mid-points standing for the glass transition temperature ($T_g$) of the four coatings. No effect of DE and KDMTD on $T_g$ are observed, suggesting no interaction between DE and KDMTD particles. In contrast, when DE-HDMTD particles are used, the $T_g$ decreases from 45±0.5°C to 38±0.5°C, indicating that HDMTD reacts with epoxy-amine matrix.

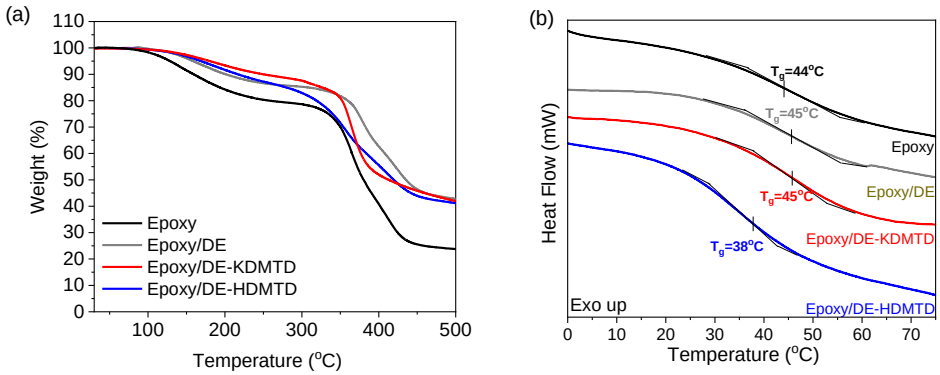


Figure 3.1 (a) Weight loss profile with temperature and (b) DSC plot of Epoxy, Epoxy/DE, Epoxy/DE-KDMTD, and Epoxy/DE-HDMTD coatings.

Both TGA and DSC unveil a potential difference in chemical reactivity between HDMTD and KDMTD with the epoxy-amine matrix even when loaded into DE carriers. As shown in Scheme 3.1a, the thiol groups (-SH) in HDMTD are deprotonated by the base amino groups from the organic matrix. These highly nucleophilic thiolate groups ($-S^-$) can effectively open the oxirane rings. As a result, they interfere with the crosslinking process by incorporating linear bonds and reducing crosslinking density, hence decreasing thermal stability and $T_g$ as shown here, as well as Young's Modulus, stress at break, and adhesion. [24-26] As for KDMTD, we used a non-polar solvent (i.e., xylene) which limited the dissociation of KDMTD into reactive thiolate anion.[27] Consequently, its reactivity with the epoxy-amine matrix is highly reduced (scheme 3.1b). This reduction in reactivity inhibits its interaction with oxirane groups in a water-free epoxy-amine-xylene environment, resulting in minimal effects on $T_g$ and thermal stability.

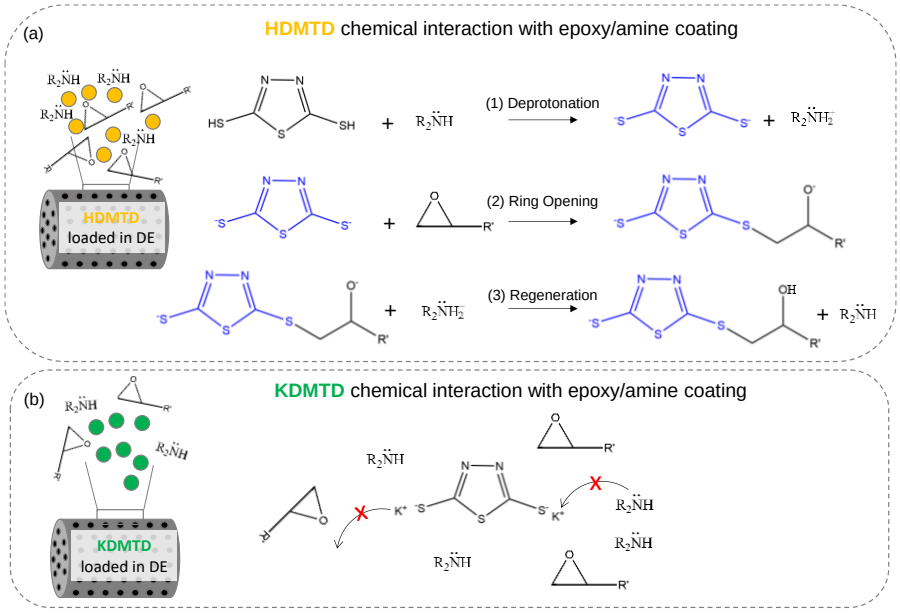


Scheme 3.1 Chemical interaction of (a) HDMTD and (b) KDMTD loaded in DE with the surrounding epoxy/amine polymer. Scheme shows lack of negative reactivity with KDMTD.

Figure 3.2a shows the release profiles of the ground Epoxy/DE-HDMTD and Epoxy/DE-KDMTD coatings. Notably, the Epoxy/DE-KDMTD releases higher inhibitor amounts and at higher release rate than the Epoxy/DE-HDMTD coating, well in line with the weaker interaction between KDMTD and the epoxy matrix. In anticorrosion coatings, a rapid initial and a higher inhibitor release are considered essential for achieving a minimum local protective concentration able to stop the rapid dealloying of AA2024 intermetallic particles (IMs) which occurs within the first 5 minutes of immersion. [28] Moreover, optimal inhibition coatings is theoretically obtained by an initial quick release followed by a prolonged, steady release. [29] The Epoxy/DE-KDMTD coating releases 38% of the total available KDMTD at the exposed location in the first 2 hours and then slows down, reaching a 40% release plateau at 6 hours. This can be attributed to the water diffusion-controlled accessibility of KDMTD in thicker polymer films (approximately 70 ±3 µm). In contrast, the Epoxy/DE-HDMTD coating shows only a 10% release of available HDMTD in the first 2 hours, followed by a slowing down of the release to reach 25% after 1 day and 34% after 2 days. To verify the effect of the inhibitor-coating interaction on release, a release study of the inhibitor-loaded DE particles was preformed (Figure 3.2b, c). Unlike the release from coatings, the release profiles of inhibitors from DE-HDMTD and DE-KDMTD particles into NaCl solutions (Figure 3.2b) are very comparable despite more HDMTD was loaded (Figure 3.2c). Both types of particles show a comparable rapid release within the initial 30 minutes of exposure, reaching 70% (out of a loading capacity of around 270mg/g of DE as seen in Figure 3.2c) of the available inhibitors loaded in the DE particles. This is followed by slower release rate until approximately 80% is released after 3 hours. This further confirmed that the differences in release from the coatings are not due to the interaction between the DE particles and the inhibitors, but the result of more pronounced unwanted inhibitor-coating side reactions with the use of

HDMTD. Based on the inhibition theory from coatings, these results suggest a potentially higher corrosion inhibition efficiency of the KDMTD coating compared to the HDMTD coating.

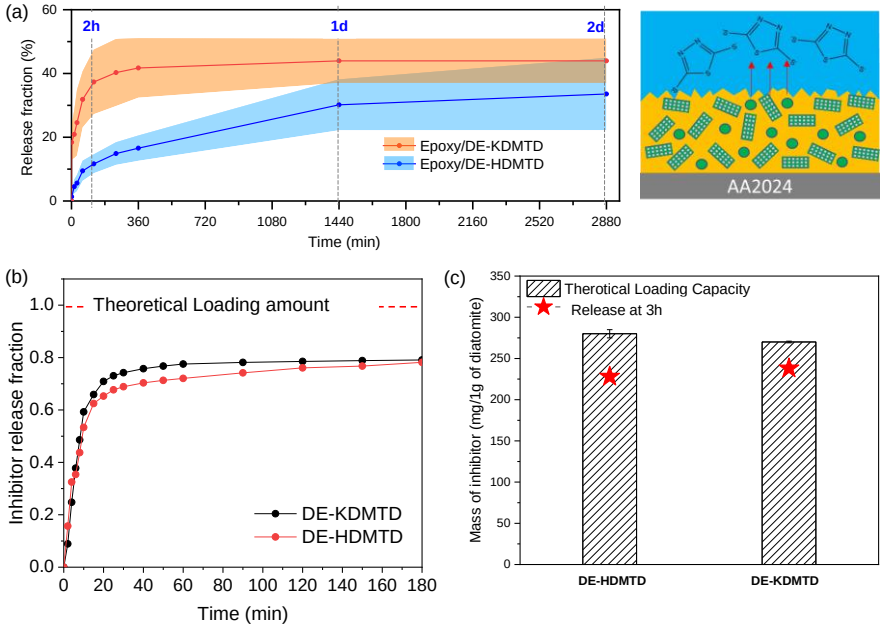


Figure 3.2 (a) Release profile of HDMTD and KDMTD from ground coatings exposed to 0.05M NaCl solution over 2 days. The release profile shows the average of several measurements (line) and the standard deviation (color band). The scheme on the right shows the release of DMTD ions from the ground coating. (b) Release profile of DE-HDMTD and DE-KDMTD particles for 3h. (c) Mass of HDMTD and KDMTD loaded in 1g diatomite and their maximum release at 3h (stars).

### *3.3.2 Active corrosion protection at damaged coatings: effect of pH*

The above results demonstrate that loading KDMTD in DE exhibits lower negative interaction with the surrounding epoxy/amine polymer matrix, and significantly higher inhibitor release than HDMTD loaded in silica exoskeletons. To study the relation between inhibitor release and inhibition at damaged sites, the coatings were damaged as explained in the experimental section and exposed to NaCl solutions at different pHs (5, 7, 10). During the exposure, the damaged site was monitored with an operando optical imaging (image reflectometry) setup as described in the experimental section. The total exposure time to 0.05M NaCl solution was picked at 2h based on the release kinetics study shown in Figure 3.2a, to capture the near plateau release of KDMTD (38%) and a low HDMTD inhibitor release (10%). The surface activity at the damage metal surface was extracted from the optical images by a pixel-by-pixel image correlation analysis protocol as described in our previous works. [28] The results of the reference epoxy coating without DE microcarriers or inhibitors, epoxy coating with DE-HDMTD, and DE-KDMTD exposed to pH 10, 7, and 5 0.05 M NaCl aqueous solutions are shown in Figure 3.3. Overall, the surface

activity at the damage site decreased in all three coatings as the pH level drops, but clear difference can be seen between samples.

At pH 10 (Figure 3.3a), epoxy coatings without inhibitors (black curve) shows rapid local activity growth, leading to around 70% surface area coverage within a half hour, and stabilize at around 1 hour. This reflects the rapid generation of corrosion products at pH 10 in good agreement with the Pourbaix diagram of Al. [30] The relation between optical activity and degradation was confirmed with the local post-mortem image (right column) revealing a widespread global corrosion shown as trenching around intermetallic particle sites, colorings (Cu re-deposition), and white corrosion product deposition over the metal surface. The DE-KDMTD coating (blue curve) displays a two-stage increase in surface coverage: (i) a relatively slow surface change during the first hour reaching a surface activity area coverage of 25%; and (ii) a quick increase in surface activity reached 70% after 2 hours of exposure. The local post-mortem image shows less white product compared to the coating without inhibitors with minimum trenching or dealloying but some surface colouring. These results indicate that KDMTD delays local corrosion attack at an early immersion stage, even though protection diminishes over time, opposite to the coating containing HDMTD (red curve) exposed to pH 10 shows very low-level of surface activity (9%) localized at the intermetallic sites as confirmed by the post-mortem photograph (i.e., absence of corrosion signs).

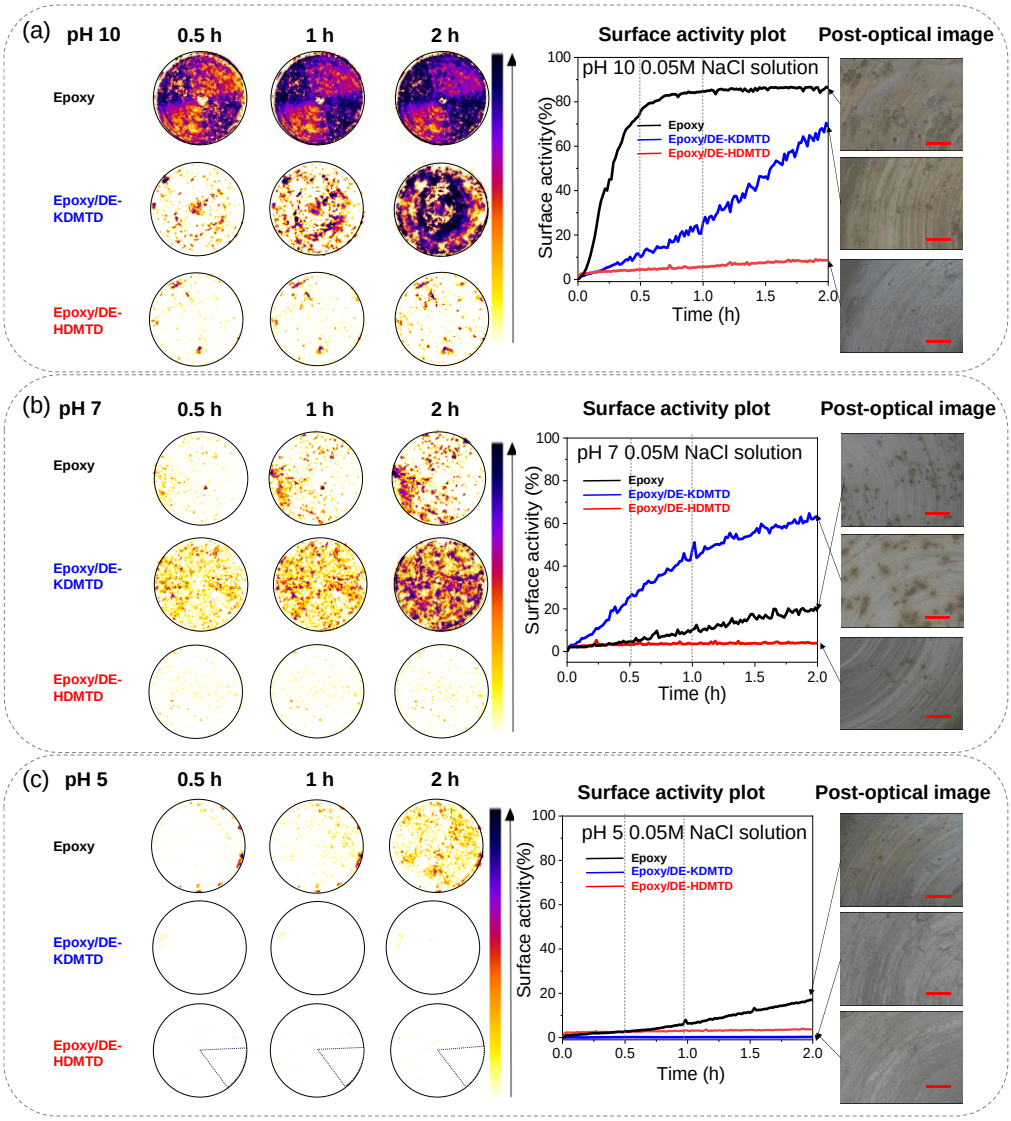


Figure 3.3 The global activity maps, quantified surface activity curves, and local post-mortem images (left to right) at the damage location at the end of the 2h exposure in (a) pH 10; (b) pH 7; and (c) pH 5 0.05M NaCl solution for Epoxy (black), Epoxy/DE-KDMTD (blue) and Epoxy/DE-HDMTD (red) coatings. The diameter of the damage hole is 1mm. Red scale bar in post-optical images: 50 µm. The sector with a dashed outline on the activity map of the Epoxy/DE-HDMTD (in c) represents a non-quantifiable location due to the presence of an air bubble and has therefore been omitted from the analysis.

When exposed to pH 7 NaCl solution (Figure 3.3b), the epoxy coating without inhibitors (black curve) shows a significantly lower surface activity (20% after 2 hours of exposure) than at pH 10. In good agreement with our previous research, [5, 28, 31] activity is very localized and related to dealloying at intermetallic particle sites, followed by trenching and pitting corrosion confirmed in the post-mortem image analysis (right column). Surprisingly, the DE-KDMTD coating (blue

curve) shows rapid localized attack short after exposure, increasing to 23% surface activity after half an hour and reaching 53% in two hours. Post-mortem imaging reveals trenching and pitting at the intermetallic sites. Although the results are reproducible, the reason for the higher surface activity at the damaged area of the DE-KDMTD coating compared to the epoxy coating remains unclear. This discrepancy may be attributed to micro-scale variations on metallic surfaces, such as the size and distribution of intermetallic particles. This aspect will be explored in future research. Conversely, the DE-HDMTD coating (red curve) exhibits rapid surface activity within the first 2 minutes, however plateauing immediately at a maximum of 2.3% surface coverage, with minor dealloying at intermetallic sites confirmed by post-mortem image analysis.

At pH 5 (Figure 3.3c), the epoxy coating (black curve) shows similar results as exposed to pH 7 NaCl solution (15% after 2 hours of exposure) yet with lower pixel intensity change. Remarkably, epoxy coatings with either DE-KDMTD (blue curve) or DE-HDMTD (red curve) exhibit near zero local activity over 2 hours of exposure. This observation aligns well with the local post-mortem images, which show no evidence of any corrosion signs. For the Epoxy/DE-KDMTD coating, this represents a notable improvement compared to the significant surface activity (> 50%) observed on the damaged Epoxy/DE-KDMTD when exposed to basic (Figure 3.3a) and neutral pH, (Figure 3.3b) as previously discussed. Regarding the damaged Epoxy/DE-HDMTD coating, it shows a similar behavior as the exposure in neutral pH (Figure 3.3b), i.e., minor surface activity (<2%).

Figure 3.4 shows the UV-Vis spectrum of the KDMTD and HDMTD released from the damaged coatings after 2h exposure. In agreement with the release kinetics study (Figure 3.2a) under neutral pH, the amount of inhibitors released from the Epoxy/DE-KDMTD coating is significantly higher (>100 times) than from the Epoxy/DE-HDMTD coating at all pH levels. The amount of inhibitor release is also increase with the pH for two coatings (i.e., maximum release at pH 10).

Besides peak intensity, the wavenumber location varies from sample to sample. For the Epoxy/DE-KDMTD coating (Figure 3.4a), the peak shifts to a higher wavelength as the pH decreases. Although the concentrations remain at a similar level ($10^{-4}$ M) and even increase with pH, which is theoretically within the protection range [31, 32], this coating provides good corrosion protection only at pH 5 (Figure 3.3). We attribute the effective protection to different chemical structures, as indicated by the varying peak locations at different pH levels. This aspect will be further investigated in next section 3.3.3.

The UV-Vis spectrum of HDMTD released from the damaged coating (Figure 3.4b) shows absorption peaks at 326 nm at pH 5 and pH 7, and 313 nm at pH 10, although the concentrations are at extremely low levels (<$10^{-6}$ M). This indicates HDMTD is in the same chemical state (thiol-thiolate and thione-thiolate) at pH 5 and pH 7 as shown in our previous work[5], contributing to effective corrosion inhibition, as demonstrated in Figure 3.3. These findings highlight the importance of the chemical structure of the corrosion inhibitors upon release, to protect the metal substrate.

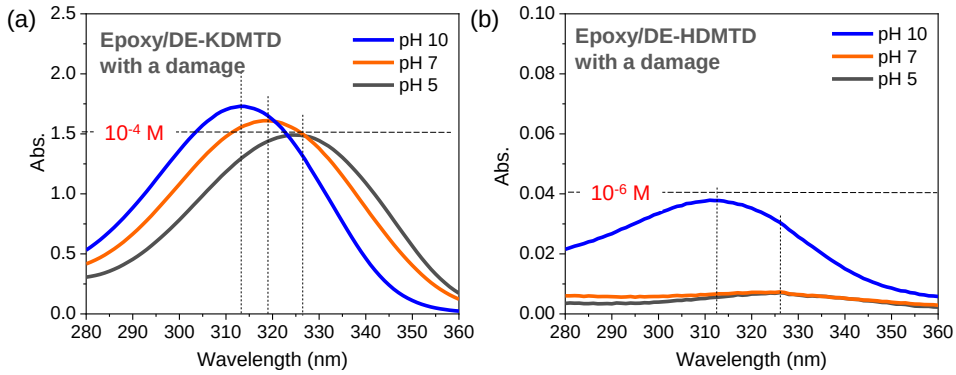


Figure 3.4 UV-Vis spectrums of (a) KDMTD and (b) HDMTD released from coatings with damage after 2h exposure to NaCl solutions with varying pH.

### *3.3.3 Effect of pH on the ionic state of DMTD salts*

To gain insights into the structural features of HDMTD and KDMTD, UV-Vis spectra of HDMTD and KDMTD in NaCl solution at the same concentration but different pH levels (5, 7, and 10) were compared. The UV-Vis absorption spectrums of HDMTD and KDMTD solutions are shown in Figure 3.5a and Figure 3.5b. The strong peaks ranging from $\lambda_{min}$=313 nm to $\lambda_{max}$=328 nm represent π–π* transition in both HDMTD and KDMTD. [33, 34] HDMTD exhibits absorption peak centered at 328 nm at pH 5 and pH 7, and 313 nm at pH 10 (Figure 3.5a). The proton dissociation constants of DMTD ions are known as: pKa1=1.4 and pKa2=7.5 [33, 34] and contribute to six tautomers depending on pH as described in literature [34-36] and illustrated in Figure 3.5c. Based on this, at pH 5 and 7, HDMTD exists mostly in the thione-thiolate and thiol-thiolate forms, resulting in overlapping UV-Vis adsorption spectrums as seen in Figure 3.5a. In the alkaline pH 10, the absorption peak shifted to a lower wavelength, which can be attributed to the HDMTD deprotonation and mostly exists in dithiolate forms.

For the KDMTD, the peak exhibits a shift to a higher wavelength as the pH decreases as observed in Figure 3.5b. At pH 5 and pH 10, the peaks are centered at 328 nm and 313 nm respectively, well aligned with the peak locations of HDMTD at acid and alkaline pH, this indicates the same predominant structure at these two pH values (i.e., thione-thiolate and thiol-thiolate at pH 5 and dithiolate at pH 10). In neutral pH, the absorption peak is centered at $\lambda_{mid.}$=320 nm. The factor that might influence the UV-Vis spectra of KDMTD differently under neutral conditions is the dissociation equilibrium of $DMTD^{2-}$ $2K^{+}$. This assumption can be supported by the UV-Vis study of another inhibitor: 2-mercaptobenzothiazole (MBT), which forms an ion-pair between $MBT^{-}$ and cation under near neutral and basic pH. [37]

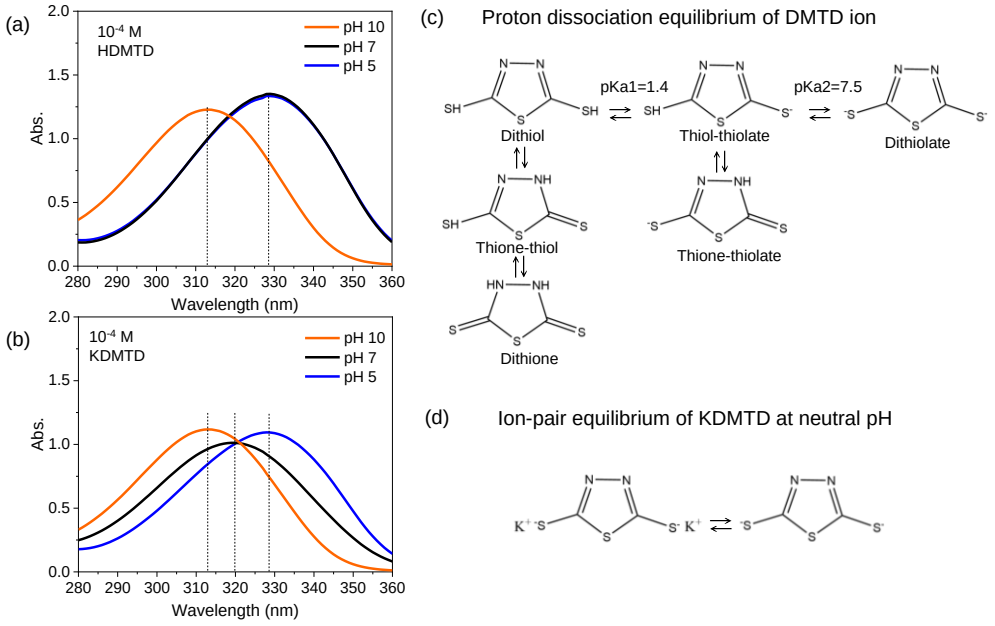


Figure 3.5 UV-Vis spectra of $10^{-4}$ M HDMTD (a) and KDMTD (b) in pH 5, pH 7, and pH 10 0.05M NaCl solutions. Schemes showing the (c) proton dissociation equilibrium of HDMTD and KDMTD and (d) ion-pair equilibrium of KDMTD.

### *3.3.4 Stability of the organic inhibitor layer formed at slight acidic pH*

In an anticorrosion coating system, it is widely recognized that the protection offered by corrosion inhibitors will eventually diminish. This reduction in effectiveness is attributed to the discontinuous release of inhibitors from the coating and/or the instability of the inhibitory layer. The latter factor largely depends on the structure of the inhibitors and their interaction with the metallic substrate. In our earlier research, we reported that inhibitor layers formed from 1mM HDMTD in 0.05M NaCl solutions on AA2024-T3 show high levels of stability when re-exposed to 0.05M NaCl neutral solutions. [5] We also found that $10^{-4}$ M HDMTD, released from a coating with HDMTD particles coated with nanolayers [31] can form stable protective layers at damage of the same size (1mm diameter, 250µm deep) used in this study. To investigate the stability aspects, the best-preforming coatings in terms of inhibition at damages (i.e., Epoxy/DE-KDMTD and Epoxy/DE-HDMTD exposed to pH 5 NaCl solution) were selected and re-exposed to neutral pH 0.05M NaCl solutions.

During re-exposure, the DE-HDMTD coating displays rapid surface reactivation, reaching 5% in about 5 min and increasing to 6.5% surface activity within 2 hours (Figure 3.6a). This is in good agreement with activity localized at the intermetallic particle sites as seen in post-mortem image analysis (Figure 3.6b). We relate this activity to film breakdown and slight dealloying likely due to an insufficient release of HDMTD ($<10^{-6}$ M) during both the acid-exposure process (Figure 3.3b) and subsequent re-exposure (Figure 3.6c) leading to an initial protective layer being formed. While a small amount of HDMTD can inhibit metal corrosion during a short exposure time (2

hours), its inhibitory effectiveness tends to diminish over time, particularly once the initially released inhibitor is depleted from the system. Nevertheless, it should be noted the partial loss of protection does not grow after 1h immersion unveiling a very effective protection. The re-exposed Epoxy/DE-KDMTD coating shows lower surface activity at the metal surface, with surface activities stabilizing at about 2% surface coverage already at 2 minutes. This is consistent with the local post-mortem image (Figure 3.6b), which displays minor dealloying at the intermetallic particle sites. The low release of KDMTD from the Epoxy/DE-KDMTD coating during re-exposure (Figure 3.6c, $7x10^{-6}$ M), indicates that even though the inhibitor release during re-exposure is below typical protective levels, the surface remains inhibited due to the high stability of the inhibiting layer formed during first immersion with 0.1mM KDMTD released in acid solution (Figure 3.4a). These results support the idea that the acid exposure process can help creating more stable inhibitor layers from KDMTD capable of protecting the metal surface, even with a reduced supply of inhibitors from the coating.

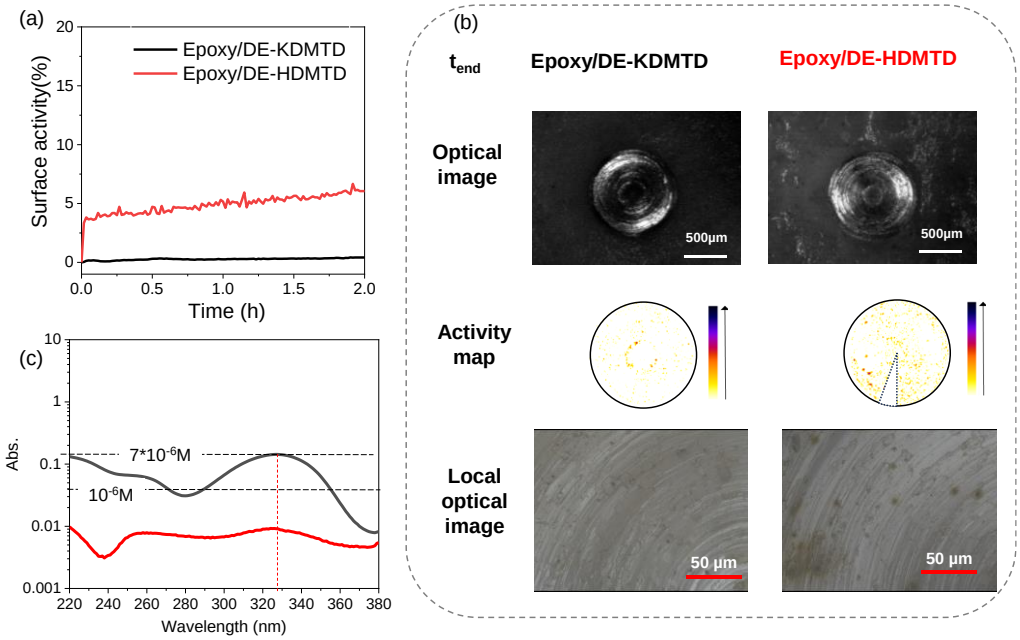


Figure 3.6 Stability of the inhibitor layer formed at pH 5 and re-exposed to pH 7 0.05M NaCl solution. Figure shows (a) the quantified surface activity curves, (b) optical images, global activity maps, and local post-mortem images at the damage location at the end of the 2h re-exposure in neutral 0.05M NaCl solution for Epoxy/DE-KDMTD and Epoxy/DE-HDMTD coatings. The diameter of the damage hole is 1mm. The sector with a dashed outline on the activity map of the Epoxy/DE-HDMTD (in b) represents a non-quantifiable location due to the presence of an air bubble and has therefore been omitted from the analysis. (c) shows UV-Vis spectrums of the NaCl solutions containing KDMTD or HDMTD released from the damaged coatings.

*3.3.5 Relation between ionic state, concentration and protection*

The above discussion highlights how pH affects the ionic states of KDMTD and HDMTD in NaCl solution, which in turn impacts their corrosion inhibition effectiveness. Figure 3.7 depicts the relationship between the predominant ionic state, the concentration of inhibitors released into the solution, and the surface activity at damage (SA%) at various pH conditions, and upon re-exposure to pH 7 NaCl solutions for Epoxy/DE-KDMTD and Epoxy/DE-HDMTD coatings.

For Epoxy/DE-HDMTD (Figure 3.7a), low surface activity (less than 9%) was shown at all tested pH levels, exposure and re-exposure. SA% decreased as the pH decreased, nevertheless higher inhibitor concentration was released at pH 10 ($10^{-3}$ mM at pH 10 compared to $10^{-4}$ mM at pH 5 and 7). We attribute the effective inhibition of HDMTD at all pH levels to the intrinsic acidity of HDMTD, which can remove the instinct thin Al oxide layer as shown in previous work. [5] As shown in Figure 3.5c, under pH 5 and 7, HDMTD exists in thiol-thiolate and thione-thiolate forms where the heteroatoms (N and S) can strongly adsorb to the metallic surface through electrochemical interactions facilitated by dissociated protons. At pH 10, despite there were initial corrosion activities and dealloying (Figure 3.3a), the dissociated protons from HDMTD can interact with the $OH^-$ ions on the metal surface, allowing DMTD in the dithiolate state (Figure 3.5c) to adsorb on metal effectively. This suggests that higher concentrations of HDMTD rule out the effect of pH.

For the Epoxy/DE-KDMTD coatings (Figure 3.7b), effective inhibition was only observed at pH 5, showing nearly zero SA%, although the concentration of inhibitors released is much higher than DE-HDMTD coating across all pH levels, exceeding 0.1 mM (at least 100 times that of DE-HDMTD coatings at all pHs). At pH 7 and 10, the predominant dithiolate forms (both dissociated and non-dissociated, Figure 3.5c, d) of KDMTD lead to the repulsion of DMTD ions from the metal surface, resulting in corrosion. However, in the presence of protons, KDMTD transforms to thiol-thiolate and thione-thiolate states, showing effective inhibition. Furthermore, when the inhibitor layer formed under acidic conditions is re-exposed, KDMTD exhibits superior stability (SA=2%) compared to HDMTD (SA=6.5% in Figure 3.7a), attributed to the 100 times release of KDMTD than HDMTD during pH 5 exposure and the small initial extra release (0.1 mM for KDMTD vs. $10^{-4}$ mM for HDMTD). This suggests that more stable layers can be formed at higher concentrations and acidic pHs for both HDMTD and KDMTD and that high levels of protection can be obtained with HDMTD at all pHs even at very low inhibitor concentration released.

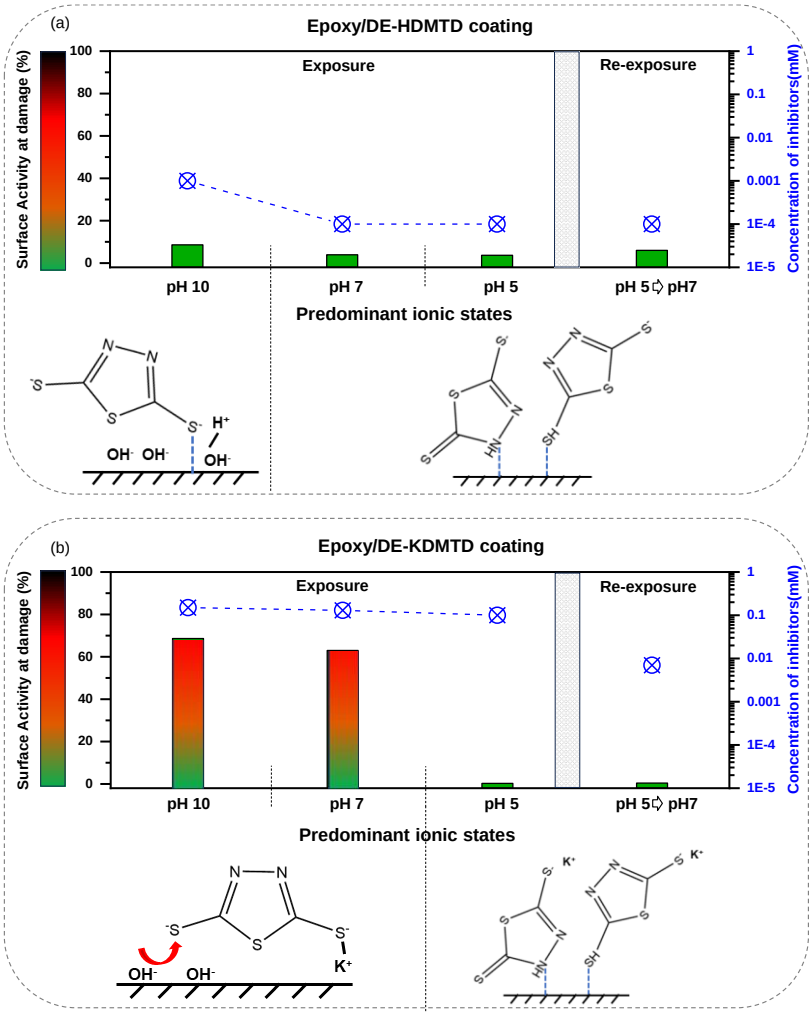


Figure 3.7 Overview of the surface activity percentage (SA%) at damage (obtained from Figure 3.3 and Figure 3.6), the concentration of inhibitors being released (obtained from Figure 3.4 and Figure 3.6), and the predomination ionic states after each exposure, and re-exposure for (a) Epoxy/DE-KDMTD and (b) Epoxy/DE-HDMTD coatings.

# 3.4 Conclusions

In this study, two organic inhibitors, KDMTD and HDMTD, with highly similar chemical structures, are loaded in natural microcarriers and integrated with epoxy-amine coatings applied onto AA2024-T3 to assess their anti-corrosion performance. KDMTD exhibits a lower level of interaction with the epoxy matrix, resulting in higher release rates and amounts than HDMTD, as evidenced by Thermal Gravimetric Analysis (TGA), Differential Scanning Calorimetry (DSC), and UV-visible spectroscopy. The critical role of pH in determining the ionic states and inhibition efficiency of KDMTD and HDMTD as corrosion inhibitors. KDMTD exhibits effective and

stable corrosion protection under pH 5 acidic conditions, due to its protonation capability, and rapid and large release from exoskeletons due to low reactivity with coatings. Conversely, HDMTD demonstrates remarkable corrosion inhibition capability during short exposures at all pH levels. Nevertheless, its interaction with the epoxy matrix limits its early-stage release, leading to protective inhibitor layer slight less protective upon subsequent exposures. This study highlights the importance of understanding inhibitor-coating interactions and pH effects on inhibitor chemistry for designing more effective anti-corrosion coatings.

# 3.5 References

(1) Yasakau, K. A.; Zheludkevich, M. L.; Lamaka, S. V.; Ferreira, M. G. Mechanism of corrosion inhibition of AA2024 by rare-earth compounds. *The Journal of Physical Chemistry B* **2006**, *110* (11), 5515-5528.
(2) Williams, G.; Coleman, A. J.; McMurray, H. N. Inhibition of Aluminium Alloy AA2024-T3 pitting corrosion by copper complexing compounds. *Electrochimica Acta* **2010**, *55* (20), 5947-5958.
(3) Costa, M.; Klein, C. B. Toxicity and carcinogenicity of chromium compounds in humans. *Critical reviews in toxicology* **2006**, *36* (2), 155-163.
(4) Olajire, A. A. Corrosion inhibition of offshore oil and gas production facilities using organic compound inhibitors-A review. *Journal of Molecular Liquids* **2017**, *248*, 775-808.
(5) Zhao, J.; Santoso, A.; Garcia, S. J. Small concentrations of NaCl help building stable inhibiting layers from 2, 5-dimercapto-1, 3, 4-thiadiazole (DMTD) on AA2024-T3. *Corrosion Science* **2023**, *225*, 111562.
(6) Harvey, T.; Hardin, S.; Hughes, A.; Muster, T.; White, P.; Markley, T.; Corrigan, P.; Mardel, J.; Garcia, S.; Mol, J. The effect of inhibitor structure on the corrosion of AA2024 and AA7075. *Corrosion science* **2011**, *53* (6), 2184-2190.
(7) Soleymanibrojeni, M.; Shi, H.; Udoh, I. I.; Liu, F.; Han, E.-H. Microcontainers with 3-amino-1, 2, 4-triazole-5-thiol for enhancing anticorrosion waterborne coatings for AA2024-T3. *Progress in Organic Coatings* **2019**, *137*, 105336.
(8) Fix, D.; Andreeva, D. V.; Lvov, Y. M.; Shchukin, D. G.; Möhwald, H. Application of inhibitor‐loaded halloysite nanotubes in active anti‐corrosive coatings. *Advanced Functional Materials* **2009**, *19* (11), 1720-1727.
(9) Raj, R.; Morozov, Y.; Calado, L.; Taryba, M.; Kahraman, R.; Shakoor, R.; Montemor, M. Calcium carbonate particles loaded with triethanolamine and polyethylenimine for enhanced corrosion protection of epoxy coated steel. *Corrosion Science* **2020**, *167*, 108548.
(10) Denissen, P. J.; Homborg, A. M.; Garcia, S. J. Requirements for corrosion inhibitor release from damaged primers for stable protection: a simulation and experimental approach using cerium loaded carriers. *Surface and Coatings Technology* **2022**, *430*, 127966.
(11) Ech-chihbi, E.; Salim, R.; Ouakki, M.; Koudad, M.; Guo, L.; Azam, M.; Benchat, N.; Rais, Z.; Taleb, M. Corrosion resistance assessment of copper, mild steel, and aluminum alloy 2024-T3 in acidic solution by a novel imidazothiazole derivative. *Materials Today Sustainability* **2023**, *24*, 100524.
(12) Guo, L.; Dong, W.; Zhang, S. Theoretical challenges in understanding the inhibition mechanism of copper corrosion in acid media in the presence of three triazole derivatives. *RSC advances* **2014**, *4* (79), 41956-41967.
(13) Malik, M. A.; Hashim, M. A.; Nabi, F.; Al-Thabaiti, S. A.; Khan, Z. Anti-corrosion ability of surfactants: a review. *International journal of electrochemical science* **2011**, *6* (6), 1927-1948.
(14) Qin, T. T.; Li, J.; Luo, H. Q.; Li, M.; Li, N. B. Corrosion inhibition of copper by 2, 5-dimercapto-1, 3, 4-thiadiazole monolayer in acidic solution. *Corrosion Science* **2011**, *53* (3), 1072-1078.
(15) Verma, D. K.; Dewangan, Y.; Dewangan, A. K.; Asatkar, A. Heteroatom-based compounds as sustainable corrosion inhibitors: an overview. *Journal of Bio-and Tribo-Corrosion* **2021**, *7* (1), 15.
(16) Verma, C.; Verma, D. K.; Ebenso, E. E.; Quraishi, M. A. Sulfur and phosphorus heteroatom‐containing compounds as corrosion inhibitors: An overview. *Heteroatom Chemistry* **2018**, *29* (4), e21437.

(17) Guo, L.; Qi, C.; Zheng, X.; Zhang, R.; Shen, X.; Kaya, S. Toward understanding the adsorption mechanism of large size organic corrosion inhibitors on an Fe (110) surface using the DFTB method. *RSC advances* **2017**, *7* (46), 29042-29050.
(18) Hackerman, N.; Makrides, A. Action of polar organic inhibitors in acid dissolution of metals. *Industrial & Engineering Chemistry* **1954**, *46* (3), 523-527.
(19) Denissen, P. J.; Shkirskiy, V.; Volovitch, P.; Garcia, S. J. Corrosion inhibition at scribed locations in coated AA2024-T3 by cerium-and DMTD-loaded natural silica microparticles under continuous immersion and wet/dry cyclic exposure. *ACS applied materials & interfaces* **2020**, *12* (20), 23417-23431.
(20) Levchik, S. V.; Weil, E. D. Thermal decomposition, combustion and flame‐retardancy of epoxy resins—a review of the recent literature. *Polymer International* **2004**, *53* (12), 1901-1929.
(21) Kucuk, F.; Sismanoglu, S.; Kanbur, Y.; Tayfun, U. Effect of silane-modification of diatomite on its composites with thermoplastic polyurethane. *Materials Chemistry and Physics* **2020**, *256*, 123683.
(22) Snihirova, D.; Lamaka, S.; Taheri, P.; Mol, J.; Montemor, M. Comparison of the synergistic effects of inhibitor mixtures tailored for enhanced corrosion protection of bare and coated AA2024-T3. *Surface and Coatings Technology* **2016**, *303*, 342-351.
(23) Zhao, J.; van Ommen, J. R.; Garcia, S. J. Gas-phase deposited nanolayers guard organic microparticles in polymer matrices for active corrosion protection at damages. *Progress in Organic Coatings* **2024**, *192*, 108522.
(24) Carioscia, J. A.; Stansbury, J. W.; Bowman, C. N. Evaluation and control of thiol–ene/thiol–epoxy hybrid networks. *Polymer* **2007**, *48* (6), 1526-1532.
(25) Chan, J. W.; Hoyle, C. E.; Lowe, A. B.; Bowman, M. Nucleophile-initiated thiol-Michael reactions: effect of organocatalyst, thiol, and ene. *Macromolecules* **2010**, *43* (15), 6381-6388.
(26) Konuray, A. O.; Fernández-Francos, X.; Ramis, X. Analysis of the reaction mechanism of the thiol–epoxy addition initiated by nucleophilic tertiary amines. *Polymer chemistry* **2017**, *8* (38), 5934-5947.
(27) Patrick, S. C.; Beer, P. D.; Davis, J. J. Solvent effects in anion recognition. *Nature Reviews Chemistry* **2024**, *8* (4), 256-276.
(28) Olgiati, M.; Denissen, P. J.; Garcia, S. J. When all intermetallics dealloy in AA2024-T3: Quantifying early stage intermetallic corrosion kinetics under immersion. *Corrosion Science* **2021**, *192*, 109836.
(29) Hughes, A. E.; Cole, I. S.; Muster, T. H.; Varley, R. J. Designing green, self-healing coatings for metal protection. *NPG Asia Materials* **2010**, *2* (4), 143-151.
(30) Pourbaix, M. Atlas of electrochemical equilibria in aqueous solutions. *NACE* **1966**.
(31) Zhao, J.; van Ommen, J. R.; Garcia, S. J. Gas-phase deposited nanolayers guard organic microparticles in polymer matrices for active corrosion protection at damages. *Progress in Organic Coatings* **2024**, *192*. DOI: 10.1016/j.porgcoat.2024.108522.
(32) Denissen, P. J.; Garcia, S. J. Reducing subjectivity in EIS interpretation of corrosion and corrosion inhibition processes by in-situ optical analysis. *Electrochimica Acta* **2019**, *293*, 514-524. DOI: 10.1016/j.electacta.2018.10.018.
(33) Stanovnik, B.; Tišler, M. Contribution to the Structm· e of 2, 5-Dimercapto-1, 3, 4-thiadiazole and Related Compounds. *Croatica Chemica Acta* **1965**, *37* (1), 17-23.
(34) Maiti, N.; Chadha, R.; Das, A.; Kapoor, S. Surface selective binding of 2, 5-dimercapto-1, 3, 4-thiadiazole (DMTD) on silver and gold nanoparticles: a Raman and DFT study. *RSC advances* **2016**, *6* (67), 62529-62539.
(35) Picart, S.; Geniès, E. Electrochemical study of 2, 5-dimercapto-1, 3, 4-thiadiazole in acetonitrile. *Journal of Electroanalytical Chemistry* **1996**, *408* (1-2), 53-60.
(36) Esmaiel, M. H.; Basuony, H. A.; Al-Nawasany, M. K.; Shulkamy, M. M.; Shaaban, I. A.; Abuelela, A. M.; Zoghaib, W. M.; Mohamed, T. A. Thiadiazole-2-thiol-5-thione and 2, 5-dimercapto-1, 3, 4-thiadiazol tautomerism, conformational stability, vibrational assignments, inhibitor efficiency and quantum chemical calculations. *Zeitschrift für Physikalische Chemie* **2020**, *234* (3), 415-440.
(37) Galvão, T. L.; Kuznetsova, A.; Gomes, J. R.; Zheludkevich, M. L.; Tedim, J.; Ferreira, M. G. A computational UV–Vis spectroscopic study of the chemical speciation of 2-mercaptobenzothiazole corrosion inhibitor in aqueous solution. *Theoretical Chemistry Accounts* **2016**, *135*, 1-11.

# Chapter 4

# Surface Modification of Natural Porous Silica Microparticles to Control the Loading and Release of Organic Corrosion Inhibitors

*In this work we study the impact of particle surface modification on the loading and release of organic corrosion inhibitors from diatomaceous earth particles in solution and coatings. To this aim, we selected three types of trichlorosilanes with varying alkyl chain lengths (C4, C8 and C18) to modify the surface of sp. Aulacoseira type diatomite (Diatomaceous Earth particles, DE). 2,5-Dimercapto-1,3,4-thiadiazolate di-potassium salts (KDMTD) were used as model corrosion inhibitors due to their high solubility and efficiency to protect Cu-rich aerospace alloys such as AA2024-T3. Successful grafting of these functional silane chains was confirmed using FTIR spectroscopy. The loading and release capacity from the particles as a function of the silane hydrophobic chain length was studied by in-electrolyte ultraviolet-visible spectroscopy (UV-Vis). A relation between chain length and loading capacity and release was found, with mid-length silane (C8, octyl trichlorosilane, OTS) leading to the best results (approximately 3.5 times more adsorbed inhibitor). When embedded in an epoxy-amine organic coating, the C8 surface modification led to a significant improvement of DE particle dispersion and improved isolation of the inhibitor in the DE particles from the surrounding polymer matrix. This prevented unwanted side chemical reactions between the inhibitor and matrix and allowed to increase the readily available active organic corrosion inhibitor for protection at damage. Operando microscopy during immersion and postmortem analysis of damaged coatings demonstrated high corrosion protection levels and the formation of stable protective layers at damaged sites.*

This Chapter has been submitted to NPG Asia Materials, under review.

# 4.1 Introduction

While organic corrosion inhibitors offer a less toxic alternative to inorganic ones for protecting metallic surfaces, [1-8] integrating them into coatings in high amounts without triggering unwanted reactions remains a significant challenge. [9-11] Inhibitor encapsulation in nano or micro-sized inorganic particles has been largely explored to prevent negative interactions and provide triggered inhibitor release. [12-14] Amongst the different carriers presented in the literature, diatomaceous earth microparticles or diatomite (DE) offer very attractive opportunities as they are readily available as mining products and are currently used as fillers in coatings due to their innocuous amorphous silica composition and price amongst other properties. In our previous works, we demonstrated the potential of these DE particles as carriers of inorganic salts (Ce-salts) leading to very efficient corrosion inhibition levels at large damaged locations [15, 16] and explored their potential as carriers of 2,5-Dimercapto-1,3,4-thiadiazole (HDMTD), a highly effective corrosion inhibitor. [17] Nevertheless, when loaded in DE particles embedded in an epoxy coating, HDMTD showed limited protection at damage locations. This was related to (i) a very low loading below 2% of the available internal volume of DE particles, and (ii) side reactions with the organic matrix or the coating leading to reduced release. [16]

Surface modification of silica particles, such as nanoparticles and diatomaceous earth (DE) microparticles, has been investigated for various applications. These include their use as fillers to improve the mechanical properties of polymeric matrices and carriers for drugs to improve loading and release efficiency. [18, 19] Among the different approaches, DE surface modification with opposite water affinities (i.e., hydrophobicity) to DE particles and/or different charges to those in drugs led to increased loading capacities attributed to enhanced chemisorption and environment triggered release attributed to pH sensitivity of the surface functional groups. [20, 21] Despite significant differences in molecular structure and size, organic inhibitors and drugs are somewhat similar in terms of water solubility and the presence of certain reactive functional groups (e.g. amines, thiols). However, unlike drugs, corrosion inhibitors must be evenly distributed in organic matrices while isolated to avoid unwanted side chemical reactions. They must also retain their activity for long periods of time (years), dissolve quickly but not too quickly to prevent blistering and fast depletion amongst others and be transported from the coating to a damage location to react with the exposed metal surface in adequate quantities. These requirements pose an extra challenge when dealing with loading with organic inhibitors in DE microparticles beyond loading and release in aqueous solutions.

In this work, we studied to what extent the hydrophobic nature of surface modifications can affect the loading and release of an organic inhibitor from DE microparticles in solution and in a coating. To this aim, we chose 2,5-Dimercapto-1,3,4-thiadiazolate di-potassium salts (KDMTD), a hygroscopic organic inhibitor of relevance for Cu-rich aluminum structures yet difficult to load in DE particles and resins without side reactions. To control the surface hydrophobicity, and the surface wettability difference with the hydrophilic organic inhibitor, three hydrophobic silanes with varying chain lengths (C4, C8, and C18) were selected. The modified DE particles exhibiting the most optimal combination of high loading capacity and release kinetics and efficiency were further embedded into a prototype epoxy-amine coating and applied onto aerospace-grade AA2024-T3. The coating properties, including aspects like pigment distribution, resin penetration

into pigments, and release kinetics, were evaluated using confocal microscopy, scanning electron microscopy (SEM), energy-dispersive X-ray spectroscopy (EDS), and UV/Vis spectroscopy. Additionally, the corrosion inhibition efficiency and inhibitor layer stability at damaged locations were investigated by exposing the damaged coating to NaCl electrolytes and monitored and quantified using an in-situ, high-resolution image reflectometry set-up and image treatment protocols.

# 4.2 Experimental

*4.2.1 Materials*

Diatomaceous earth (DE) DiaFil525 particles were supplied by Profiltra Customized Solutions. A cleaning protocol using the principle of water separation was used to maximize the content of intact DE particles as reported earlier. [15, 16] Commercial grade bare AA2024-T3 (2.5 mm thick rolled sheets) were cut into 3 × 3 cm pieces and used as the substrate for the coated panels. 2,5-dimercapto-1,3,4-thiadiazolate di-potassium salts (KDMTD >99%), Butyl trichlorosilane (BTS), Octyl trichlorosilane (OTS) and Octadecyl trichlorosilane (ODTS) (>97%), and hydrogen peroxide (30%) were purchased from Sigma-Aldrich and used without further purification. Sodium chloride (NaCl, >98%), ethanol (>99.9%), anhydrous toluene (99.85>%), and toluene (98>%) were purchased from VWR Chemicals and used as received.

*4.2.2 Surface modification of DE particles*

Firstly, the cleaned DE particles were hydrolyzed to increase the content of active hydroxyl sites for silanization as reported elsewhere. [22] Specifically, 10 g of cleaned DE particles were dissolved in 30 ml of 30 wt% hydrogen peroxide and sonicated for 10 min. The sonicated solution was refluxed at 90 ºC for 3 h. DE particles were filtered using Whatman® filter paper with grade 595 with vacuum suction. Filtered DE particles were dried at 80 ºC for 6 h.

After hydroxylation, the DE particles were modified using three different hydrophobic silanes using the following silanization protocol based on a previously reported protocol: [20] (i) DE particles were dried in nitrogen at 150 ºC for 15 h; (ii) 0.5 g of DE particles were submerged in 20 ml of anhydrous toluene and stirred using magnetic stirring for 30 min; (iii) A solution composed of 16 ml of toluene and 4 ml of silane was added dropwise to a solution prepared in the previous step. The solution was refluxed at 150 ºC for 24 h in a nitrogen atmosphere. After 24 h, the solution was cooled for 2 h; (iv) DE particles were filtered using Whatman® filter paper with grade 595 with vacuum suction; (v) Filtered DE particles were sonicated in 30 ml of ethanol for 5 min; (vi) DE particles were filtered using Whatman R filter paper with grade 595 with vacuum suction; (vii) Repeated the last two steps twice and dried the filtered DE particles in vacuum condition at 80 ºC for 4 h.

At the end of the surface modification procedures four type of DE particles were obtained: cleaned, silanized with BTS, silanized with OTS, and silanized with ODTS.

*4.2.3 Loading of organic corrosion inhibitors*

Figure 4.1 shows the loading protocol of KDMTD organic corrosion inhibitor inside the DE particles.

The inhibitor loading process consisted of the following sequential steps:

-Step 1: KDMTD was dissolved in demineralized water under magnetic stirring to create a 0.5M KDMTD aqueous solution.

-Step 2: 0.5 g DE particles (with/without surface modification) were mixed vigorously with the 20 mL 0.5 M KDMTD aqueous solution in a glass jar by a high-frequency mixer for 5

min. After this, the mixtures were transferred to a stirring table and kept stirring for 24 h at 300 rpm.

-Step 3: The mixture was centrifuged at 4000 rpm for 10 min.

-Step 4: The excess solution on top of the densely packed DE particles at the bottom of the glass jar was removed and collected using a glass pipette. After removing the excess solution, the mass of the leftover solution and DE particles was measured in a balance.

-Step 5: The glass jar with the DE cake was moved to a vacuum oven at 70 $^{o}$C for 6 h to evaporate the remaining water. The inhibitor-loaded DE particles were then collected with a spatula. After drying, the particles were loose and did not require grinding, making them ready for use.

The protocol presented in Figure 4.1 allowed quantifying the amount of loaded inhibitor adsorbed, and the amount of inhibitor absorbed in the DE carrier as illustrated in Figure 4.2.

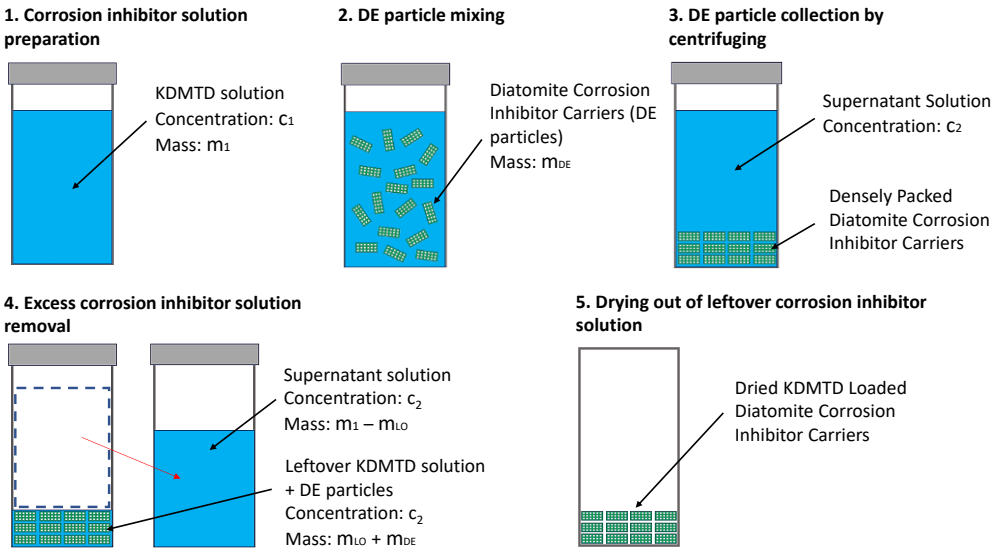


Figure 4.1 Step protocol to load KDMTD in DE particles. This method allows approximating in a quantified manner the inhibitor loading in the carriers as adsorbed and absorbed inhibitor loading.

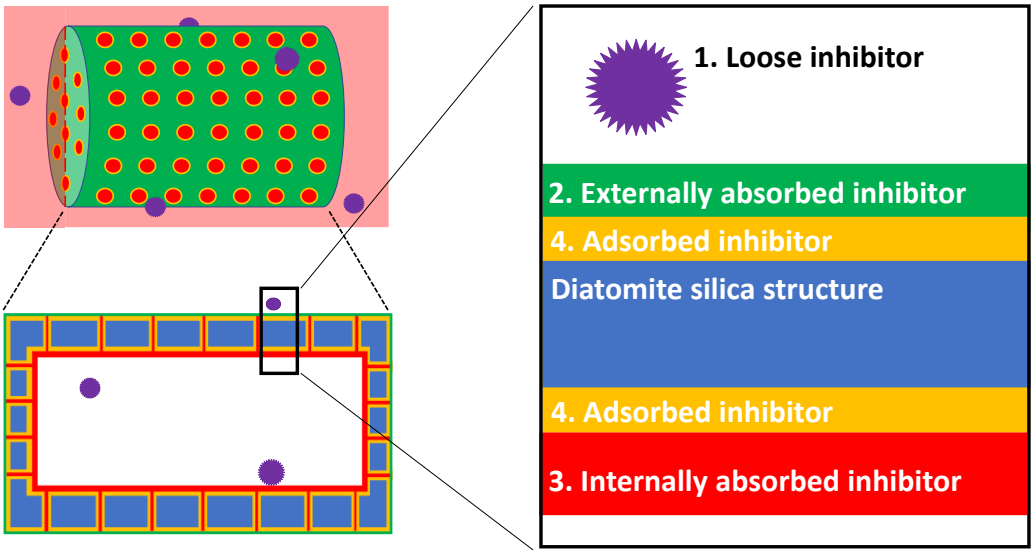


Figure 4.2 Schematic showing the different state options for a corrosion inhibitor present at the loaded DE particles: adsorbed onto the silica frustule walls (surface loading), absorbed (bulky loading) around the carrier and non-bound (loose) inhibitor salts mixed with the DE particles.

Adsorbed KDMTD inhibitor loaded onto the DE particles as depicted by the yellow region of Figure 4.2 occurred due to the attraction forces between DMTD ions and the DE silica (-modified) surface and ion exchange happening during the 24h dispersion. Inhibitor absorption, which happened during the final drying step, can be at the same time subdivided into three different categories depending on the loading process used, namely: (i) externally absorbed, (ii) internally absorbed, and (iii) non-bound (loose) inhibitor salts. During the centrifugation step, DE particles were densely packed. This minimized the KDMTD solution presence between the external surfaces of the DE particles. However, a small portion remained trapped between the particles, leading to inhibitor salt precipitation absorbed on the outer surfaces of the DE particles. As the DE particles are hollow, KDMTD solution gets also trapped during centrifugation inside the DE particles, this leading to inhibitor being absorbed on the internal surface of the DE particles during the drying process. Besides this, some KDMTD-rich pockets remain trapped between the DE particle dry cake leading to non-bound (loose) KDMTD agglomerate salts.

The loading protocol used, allowed quantifying to some extent the ratio between inhibitor absorbed (of more easy release) and adsorbed (slower release). To calculate the adsorbed inhibitor occurring during the stirring process the concentration of inhibitor in the stirring solution was measured at 24h after centrifuge. The difference between the initial concentration and the concentration at 24h lead to the mass of inhibitor adsorbed onto the DE particles ($m_{AD}$ in mg) as shown in (Eq1).

$$m_{AD} = 1000 * (c_1 - c_2) * m_1 * M_{KDMTD} / \rho_1 \quad - \qquad \text{(Eq1)}$$

where, $c_1$ (mol/L) and $m_1$(g) represent the concentration and mass of the KDMTD solution prepared for the loading process. $c_2$ (mol/L) is the concentration of KDMTD solution after the

centrifugation. $M_{KDMTD}$ (g/mol) is the molar mass of KDMTD. $\rho_1$(g/L) is the density of the solution.

Absorption loading capacity ($m_{AB}$ in mg) was determined by the remaining solution during the final drying step as shown in (Eq2).

$$m_{AB} = 1000 * c_2 * m_{LO} * M_{KDMTD} / \rho_2 \quad - \quad \text{(Eq2)}$$

where, $c_2$ (mol/L) is the concentration of KDMTD solution after the centrifugation. $m_{LO}$ is the mass of the leftover KDMTD solution filling the inter and intra volume of the densely packed DE particles. Ideally, when the diatomite particles are stacked very densely, $m_{LO}$ should be 1.6 times heavier than $m_{DE}$. This is based on the 160 wt% water absorption capacity mentioned in the datasheet of diatomite particles provided by Profiltra. $M_{KDMTD}$ (g/mol) is the molar mass of KDMTD. $\rho_1$(g/L) is the density of the solution.

*4.2.4 Particles characterization*

The structural integrity of DE before and after surface modification was analyzed by SEM-EDS in a JEOL JSM-7500F field emission scanning electron microscope equipped with energy dispersive X-ray spectroscopy. Note: surface modification did not have impact on particle size distribution (i.e., all in the range of 5 to 15 μm). For SEM image generation, both secondary electron mode (SEM) and backscattered electron mode (BSE) were used with magnification ranging between ×250 up to ×3000 and voltage of 5.0 kV and 15.0 kV. To reduce the impact of static electricity, DE particles were first sputtered with a 15 nm thick gold layer. To verify the result of the hydrophobic surface modification with BTS, OTS and ODTS hydrophobic silanes, FTIR spectroscopy was used with a wavenumber ranging from 700 up to 4000 $cm^{-1}$ and a wavenumber resolution of 0.5 ($cm^{-1}$). To construct the final spectrum for each sample, 40 scans were averaged.

The loading and release capacity of the corrosion inhibitor in and out of the DE particles was quantified by UV-Vis spectrum accompanied by a calibration curve of KDMTD in NaCl aqueous solution and KDMTD in distilled water. All the tests were repeated three times. Since the corrosion inhibitor solution shows the highest absorbance at 315 nm, this wavelength was used for the calibration and as identifier of KDMTD in solution. For the release capacity calculations, corrosion inhibitor-loaded DE particles were inserted in a Whatman® filter paper with grade 595 which was placed on top of a quartz cuvette for the UV-vis spectrometer. A magnet rotating at 1800 rpm was used to homogenize inhibitor diffusion in water. By monitoring the increase of absorbance measured over time, both release capacity and release kinetic could be determined.

*4.2.5 Preparation of coatings and coated panels*

2.5 mm thick bare aerospace-grade aluminum alloys AA2024-T3 metal plates were surface cleaned as follows: (1) grinding with Scotch Brite 3M in water to remove the native oxide layer; (2) wiping with a paper tissue wet in acetone; (3) immersing in 2 M NaOH for 10 s followed by 30 s rinsing in distilled water and drying with $N_2$ gas. The coating compositions were prepared as shown in Table 4.1. Briefly, Epikote™ 828, Ancamine® 2500, and xylene (weight ratio of 2.70:1.57:1.06) were mixed in a high-speed mixer at 2500 rpm for 5 minutes. This mixture was then pre-cured at ambient temperature for 15 minutes. DE particles loaded with inhibitors (DE-KDMTD, C8@DE-KDMTD) were introduced by stirring the coating formulation manually for 3 minutes. This mixture was then applied onto AA2024 metal coupons with a spiral bar of 100 μm

wet film. Following a 30-minute flash-off period at room temperature, the coatings were cured at 60°C for 24 hours leading to a coating dry thickness of 73±5 μm. Before release and corrosion testing, the coated panels were preserved in a desiccator.

Table 4.1 Coating formulations as a function of Epikote™ 828 (phr=parts per hundred epoxy resin in weight), and the calculated inhibiting active component in wt% of the total coating dry weight. The DE pigment volume concentration (PVC%) was set at 30%.

| **Sample Name** | **Pigment** | **DE particles (phr)** | **Inhibiting active component (phr)** | **Inhibiting active component (wt.%)** | **Dry thickness (μm)** |
|---|---|---|---|---|---|
| Epoxy/DE-KDMTD | DE-KDMTD | 26.5 | 7.2 | 3.8% | 73± 5 |
| Epoxy/C8@DE-KDMTD | C8@DE-KDMTD | 25.9 | 7.8 | 4.1% | 73± 5 |

*4.2.6 Coatings characterization*

The distribution of particles in the as-prepared coatings was evaluated by a Keyence VK-X1000 confocal scanning microscope. The coatings were analyzed for a second time after manually wet-grinding up to 4000 grit sanding paper under SEM-EDS.

The release capacity of the coatings containing DE-KDMTD and C8@DE-KDMTD was quantified by exposing a ground coating surface to 20 mL 0.05M NaCl solution in a 1 cm diameter container. Electrolyte aliquots were measured with a UV-Vis spectrometer as shown above to quantify inhibitor release. Surface grinding before exposure to solution was performed with 1000-grit paper for 15 seconds. This process allowed directly exposing the loaded particles to the solution by removing the top thin polymer barrier layer formed during the coating deposition. Aliquots of 3 mL were taken at 1, 5, 15, 30, 60, 120, 240, 360, 1440, and 2880 minutes and returned to the solution to keep the exposure volume constant. A parafilm cover prevented evaporation during the release test. The coating release tests for each sample were repeated three times.

*4.2.7 Wet/dry cyclic corrosion inhibition tests*

Damages of 1mm diameter and 0.25mm deep from the coating surface were performed on the coated panels with the help of a Roland EGX-350 engraver equipped with an end mill carbide tip (1mm in diameter). The resulting chips were removed by a vacuum cleaner.

The damaged samples were placed in a Raman electrochemical flow cell with 4.5 ml electrolyte and a Ag/AgCl (3 M KCl) reference electrode. This setup was placed vertically on an optical table inside a Faraday cage to avoid electromagnetic and vibrational disturbances. Visualization

was achieved through a 150x magnification Dino-Lite digital microscope, positioned adjacent to the viewing window of the cell, thereby enabling the acquisition of high-resolution imagery at one-minute intervals throughout the electrolyte exposure period.

Image analysis was performed using ImageJ software, applying a pixel-level correlation method described in our earlier studies. [15, 16] To do so, images were processed into 8-bit greyscale, offering 256 levels of intensity from black to white. This approach allows detecting slight surface variations in refractive index affecting the histogram at pixel level (330 nm) produced by corrosion and inhibition processes over time within a specified region of interest (ROI). A static thresholding limit of 10 was used to analyze the metallic surface, to address low-intensity changes, and to optimize signal-to-optical noise ratio without losing relevant information.

After the immersion, the electrolyte solutions were analyzed with UV-Vis spectroscopy to quantify the corrosion inhibitor released from the damaged coatings. The damaged-coated panels were finally analyzed with a Keyence VK-X1000 confocal scanning microscope at 50x magnification.

# 4.3 Results and discussion

*4.3.1 Surface modification of DE using hydrophobic silanes*

Figure 4.3a illustrates the chemical structures of the three hydrophobic silanes, BTS, OTS and ODTS used to modify the surface of the DE particles. DE particles modified with BTS, OTS and ODTS are referred to as C4@DE, C8@DE and C18@DE. The cleaned DE particle without surface modification is used as reference. Figure 4.3b shows the SEM images of the DE particles with and without surface modification with hydrophobic silanes. SEM images show that the silanization process does not damage the intact DE particles.

To verify the success of silane modification, FTIR spectroscopy was used. As shown in Figure 4.3c for all 4 DE particle samples, the following five main characteristic peaks were visible: (i) a peak at 800 $cm^{-1}$ attributed to the stretching vibration of Al-O-Si; [23, 24] (ii) a peak at 1060 $cm^{-1}$ attributed to the asymmetric stretching mode of Si-O-Si bonds; (iii) a peak at 1635 $cm^{-1}$ due to absorbed water; [25] (iv) a shoulder peak at 3619 $cm^{-1}$ due to the surface hydroxyl moieties; and (v) a broadening OH peak in the wavenumber range between 3100 $cm^{-1}$ and 3700 $cm^{-1}$. [19] These features were present in all the samples, regardless of whether they underwent silane surface modification, and indicate that the surface modifications did not change the basic particle chemistry.

Besides the above peaks, the silane-modified DE particles show the presence of IR peaks at 2929 $cm^{-1}$ attributed to -$CH_2$- asymmetric stretching and 2869 $cm^{-1}$ attributed to -CH symmetric stretching, [19] in good agreement with the presence of the carbon alkyl chains corresponding to the hydrophobic silanes. The relatively higher amplitudes of the -$CH_2$- and -CH peaks in the order of C18, C8, and C4 is in good agreement with the increasing length, and hence carbon content, of the alkyl chains used for surface modification. As expected, DE sample did not show the IR peaks related to the alkyl chain.

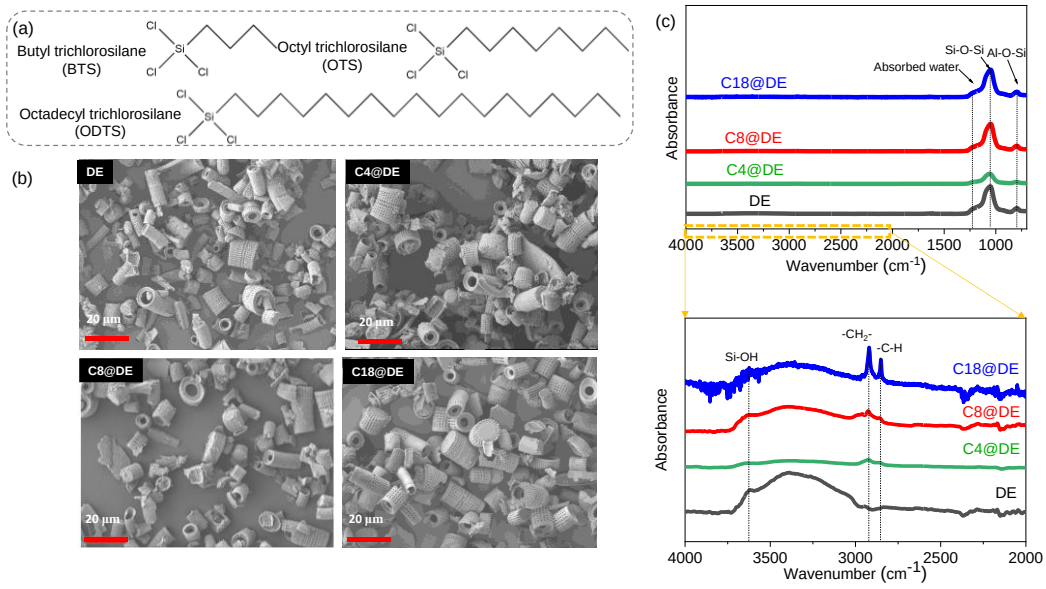


Figure 4.3 (a) Chemical structures of the 3 hydrophobic trichlorosilanes used for hydrophobic surface modification of the DE particles; (b) SEM micrographs of DE particles with and without hydrophobic surface modification; (c) FTIR absorbance spectra (4000-700 $cm^{-1}$) with enlarged region (4000-2000 $cm^{-1}$) of DE particles with and without hydrophobic surface modification.

### *4.3.2 Effect of surface modification on loading and release of organic inhibitors in DE microparticles*

Figure 4.4 a-c show loading and release quantification as a function of the surface modification. The overall loading capacity of KDMTD corrosion inhibitor, as shown in Figure 4.4a, increased for DE samples modified with longer alkyl chains (C8 and C18) compared to unmodified DE, while the C4-modified sample showed a decrease in overall loading capacity. This overall trend can be explained by the differences in absorbed and adsorbed loading states.

The absorbed loading (blue column related to absorbed inhibitor in Figure 4.4a) decreased across all silanized DE samples, indicating that surface modification generally reduced the capacity for absorption. The differences in absorption loading capacity may be due to the limitations of the loading method, where the hydrophobic nature of silanized DE particles made it challenging to completely remove the solution during the process.

On the other hand, the adsorbed loading increased significantly in the C8@DE-KDMTD and C18@DE-KDMTD samples, particularly in comparison to unmodified DE-KDMTD (orange column related to adsorbed inhibitor in Figure 4.4a). The adsorbed loading occurred due to the attractive force between the DE particles and the DMTD ions in the corrosion inhibitor solution used during the loading process. DE particles intrinsically had abundant hydroxyl moieties on their surface. DMTD ions were adsorbed onto the DE particles through the formation of hydrogen bonds with these hydroxyl moieties, as illustrated in Figure 4.4d. For the C8 and C18 modified samples, although the surface density of hydroxyl moieties was reduced due to silanization (as

silanization replaced hydroxyl groups at a 3:1 ratio, Figure 4.4d), the creation of hydrophobic zones, which favored the presence of less polar DMTD (ionic state) over polar water molecules, promoted adsorption of DMTD ions near the DE surface. This effect was not observed in the C4@DE-KDMTD sample, where the hydrophobic zone was either absent or insufficiently large, leading to lower adsorption loading. When comparing C8@DE-KDMTD to C18@DE-KDMTD, the adsorption loading capacities were similar despite C18@DE-KDMTD having a higher hydrophobic nature. This similarity was likely due to the coiling effect of the longer C18 silane chains, which slightly limited the expansion of the hydrophobic zone compared to C8.

Figures 4.4b and 4.4c show the release kinetics of the corrosion inhibitor as function of the DE surface treatment during 3 h of immersion in water and in 0.05M NaCl solution, respectively. As shown in Figure 4.4a (blue and red dots within the columns), the presence of NaCl ions did not significantly increase the total inhibitor release after 3h immersion for any sample. Similarly, NaCl in solution did not have a major effect on the release kinetics profile as seen when comparing Figures 4.4b and 4.4c. This suggests release is dominated by rapid water dissolution and internal diffusion in the particles while ion charge balance does not play a measurable role as observed in other loaded systems. [26]

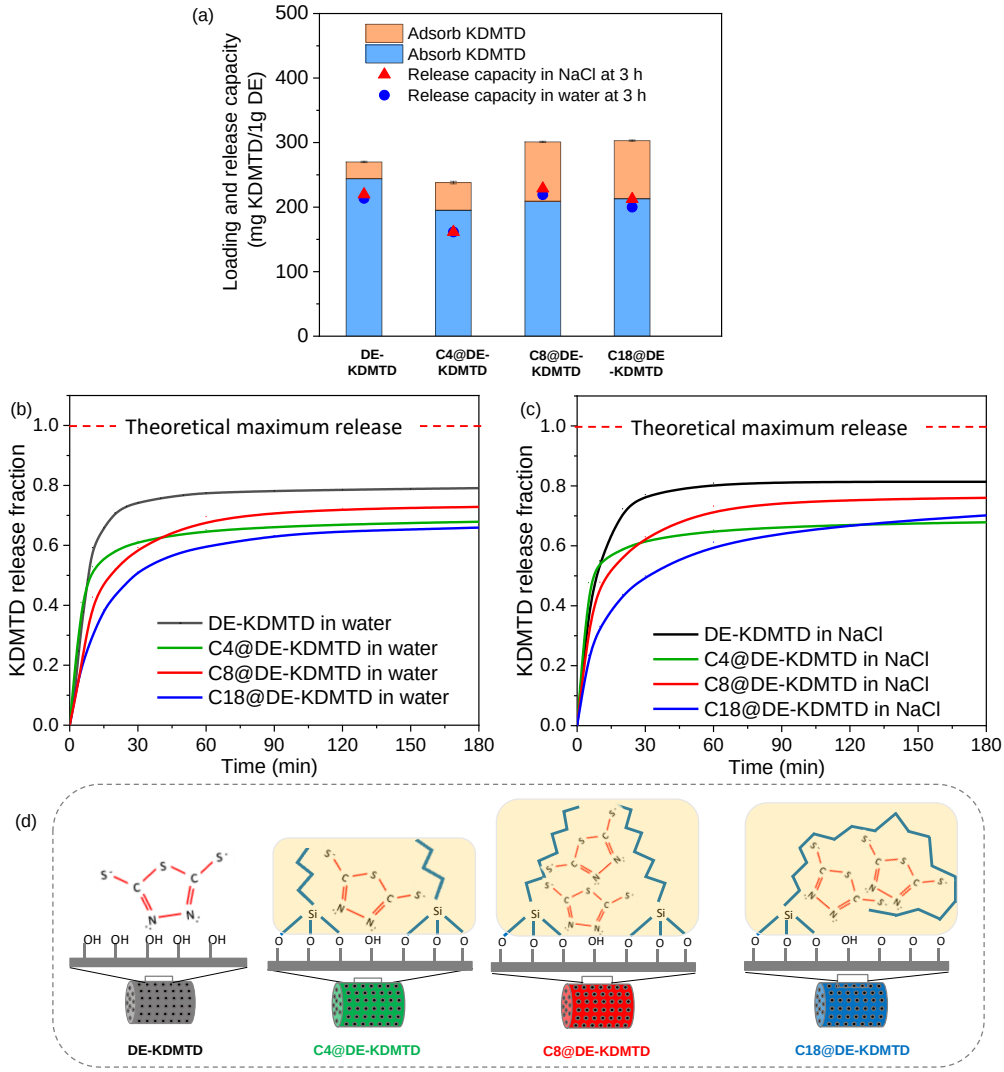


Figure 4.4 (a) Loading and release capacity of KDMTD corrosion inhibitor in the DE particles as function of the surface modification; (b and c) Fractional release kinetics of KDMTD corrosion inhibitor as function of the surface modification in distilled water (b) and in 0.05 M NaCl aq. solution (c). Theoretical maximum release is given by the total loading shown in Figure 4a.; (d) Schematic describing the loading principle of KDMTD corrosion inhibitor as function of the DE surface modification. The yellow blocks indicate the hydrophobic zones governed by the alkyl chains.

A clearer effect of the surface modification on the release kinetics and overall release with respect to loading was observed (Figures 4.4a-4.4c). The release profile of the DE-KDMTD particles without surface modification plateaued at around 45 minutes at a 80% release of the maximum theoretical release capacity calculated based on the loading capacity. The surface modified DE-KDMTD particles with hydrophobic silanes showed a slower release profile and lower relative release capacity at the end of the experiment (3h) than the DE particles. In spite of this lower

release, the total inhibitor released for the same particle amount was comparably high for DE-KDMTD, C8@DE-KDMTD and C18@DE-KDMTD and lower for the C4@DE-KDMTD samples (blue and red dots in Figure 4.4a). The samples modified with C4 silane showed a comparable release profile (kinetics and plateau at 60 min immersion) to the DE-KDMTD sample yet plateauing at 65% release. The samples modified with the C8 and C18 silanes showed slower release kinetics profiles plateauing at around 90 min for the C8@DE-KDMTD and with no clear plateau for the C18@DE-KDMTD sample even at the end of the immersion time (3h). This slower release rate can be explained by the hydrophobic character of the surface modification. While C4@DE-KDMTD did not seem to have a big impact on the release rate, the interactions between inhibitor and surface modification may have affected the total inhibitor released in a comparable manner to the surface modification with C8 and C18. Nevertheless, more inhibitors can be stored when the more hydrophobic silanes were used, as shown in Figure 4.4d and discussed above, which in turn affects the diffusion kinetics of the adsorbed inhibitors. As expected, long carbon chains (C18) may collapse in water media and decrease release kinetics of release when compared to C8@DE-KDMTD. This may also affect the total amount of inhibitor released in the studied time of 3h (C8@DE-KDMTD 75% and C18@DE-KDMTD 70% at 3h, yet with C18@DE-KDMTD still increasing). Considering the requirements for corrosion inhibitor loading (as high as possible) and release (sufficient amount quickly released to rapidly protect the metal and then sustained release in time for maintenance of the protective layer), the C8 surface modified particles perform the best as they combine high loading (almost 3 folds the DE-KDMTD sample), faster release behaviour (faster than C18@DE-KDMTD) and higher maximum inhibitor percentage released (75%). For this reason, in the remaining part of the work, it was decided to compare the behaviour between coatings loaded with DE-KDMTD and C8@DE-KDMTD particles.

*4.3.3 Effect of surface modification on particle dispersion in the coating*

Figure 4.5a shows representative confocal microscope images of the coatings prepared with 30% PVC DE and C8@DE microparticles loaded with KDMTD. In both coatings, the particles appeared to be well dispersed in the absence of large (>100 μm) agglomerates. Nevertheless, the particles modified with C8 silane showed a clear improvement in particle dispersion with individual DE particles clearly identifiable (Figure 4.5a-right).

Figure 4.5b shows SEM/EDS micrographs of the epoxy coatings containing KDMTD loaded in DE and C8@DE after wet-grinding. In agreement with the confocal images, both coatings showed homogeneous particle distributions without agglomerates over the entire coating surface, eventhough the particles modified with C8(OTS) were more clearly identifiable and presented an even more homogeneous dispersion. When looking at the particles a bit closer (Figure 4.5b), it became clear that the inner volume of the DE particles without silane modification was completely filled by organic matter (elemental C map) attributed to the epoxy-amine matrix, in good agreement with our previous reports with such DE-loaded coatings.[27] Quite opposite to this, the C8@DE-KDMTD particles appeared empty after polishing. This is attributed to a barrier effect induced by the silane surface modification that ensured epoxy-amine polymerization at the surface and prevented it from getting into the DE inner volume as also shown in the EDX mapping.

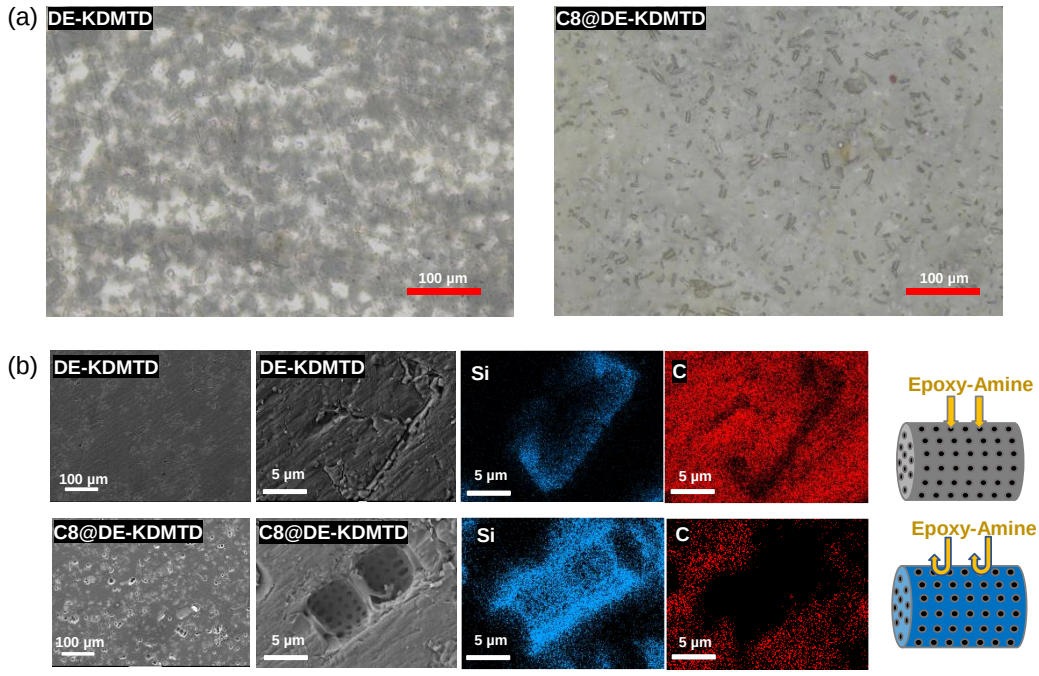


Figure 4.5 (a) Confocal microscope images of as-prepared coatings with DE-KDMTD and C8@DE-KDMTD particles; (b) SEM-EDX analysis of wet-ground coatings containing DE-KDMTD and C8@DE-KDMTD particles. EDX is unable to detect the presence of KDMTD because it was removed during the grinding process. The images show how the C8 treatment help decreasing the penetration of the epoxy-amine resin into the DE particles as opposed to the DE-KDMTD particles as shown in the right scheme.

### *4.3.4 Effect of surface modification on inhibitor release from coatings*

The effect of surface modification on KDMTD release from the coatings was investigated by immersing surface ground (Figure 4.6a) and as-produced (Figure 4.6b) coatings in 0.05M NaCl solutions and monitoring DMTD concentration with UV-Vis spectroscopy.

As shown in Figure 4.6a, when the surface was ground, there was an immediate burst release of KDMTD for both coatings. Such an effect was also observed in the as produced (i.e., intact) coatings (Figure 4.6b), although due to different reasons. For the ground samples, C8@DE-KDMTD showed 2 times more initial release than DE-KDMTD. Since the inhibitor content in the particles was not two times higher in the case of C8 modified DE (Figure 4.4), and the dispersion degree was comparably good (Figure 4.5), this effect can be better attributed to a larger proportion of chemically available KDMTD (i.e. non-reacted with the epoxy-amine polymer) probably due to the lower resin penetration in the DE particles (Figure 4.5 and Figure 4.6c). For the intact coatings, a similar amount (20%) of KDMTD was released from both coatings. It is worth mentioning that droplets came out from the intact coating surfaces (both on DE-KDMTD and C8@DE-KDMTD coatings) as seen in the zoomed optical images on the coatings (left column in Figure 4.7) and illustrated in Figure 4.6d. These droplets may result from the hygroscopicity of KDMTD, indicating that KDMTD came out of the coating surfaces by water diffusion. This phenomenon was also observed in the coatings containing KDMTD in Chapter 2,

where we demonstrated that these droplets were composed of KDMTD and amine. Furthermore, the droplets on the C8@DE-KDMTD coating were smaller than those on DE-KDMTD coating owing to its hydrophobic nature. Additionally, this phenomenon was observed only during the first 2 h of exposure to the NaCl solution. As shown in the right column of Figure 4.7, no additional droplets emerged from the coating after 2 h of exposure to the NaCl solution, followed by drying and subsequent exposure to the ambient environment for 1 day.

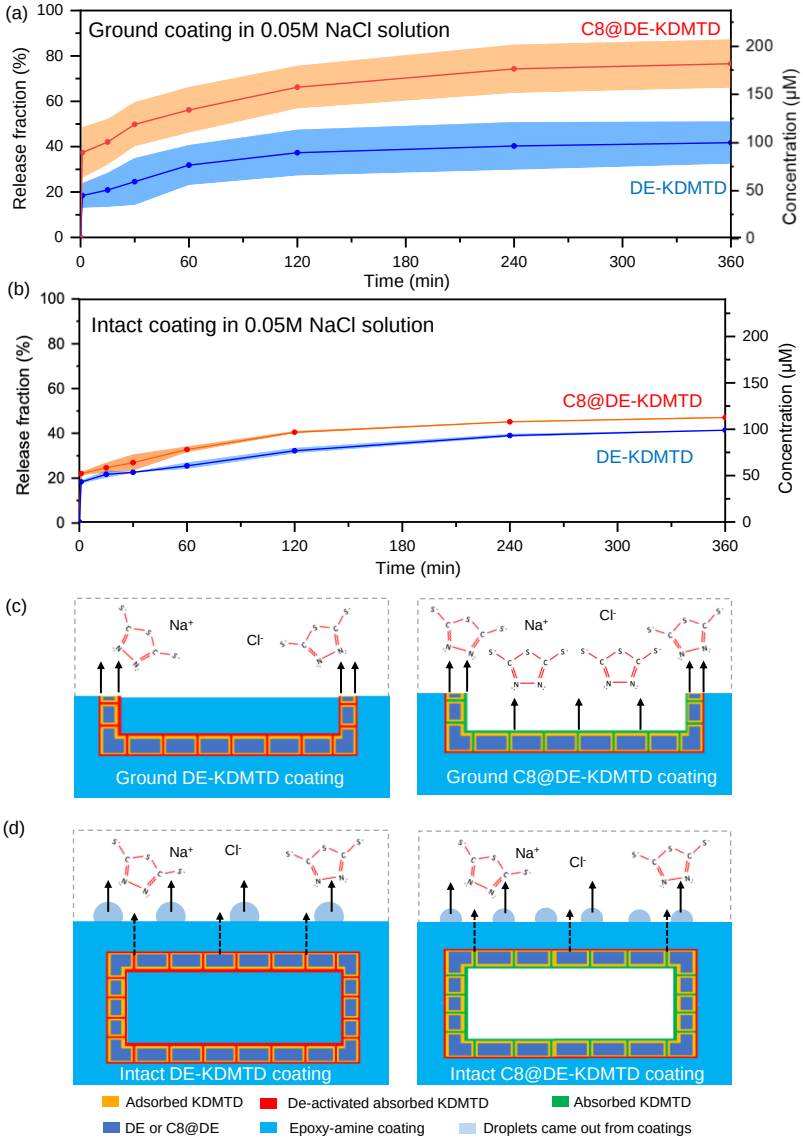


Figure 4.6 (a) The release profile of (a) dry-ground coatings and (b) as-produced intact coatings containing DE-KDMTD and C8@DE-KDMTD particles in 0.05M NaCl solution over 6 h; And schematic diagram of KDMTD inhibitor released from the (c) ground and (d) intact DE-KDMTD and C8@DE-KDMTD coatings showing the resin getting into the DE-KDMTD particles and not in the C8@DE-KDMTD particles. This leads to more inhibitor availability.

Following the initial release, the release of the two intact coatings (Figure 4.6b) gradually increased and reached a plateau at 2 h, with release amounts of up to 48% for C8@DE-KDMTD and 40% for DE-KDMTD. This similar release amount suggests that the majority of the available KDMTD originated from the droplets on the coating surfaces. Only a limited amount of inhibitors were able to across the polymer matrix during the exposure period (Figure 4.6d). On the other hand, the release rate of the two ground samples was quite comparable during the first 60 minutes immersion, likely due to a predominant release of absorbed KDMTD in the coating regions closer to the surface. While DE-KDMTD samples reached a release pseudo plateau at 120 min immersion, the C8@DE-KDMTD coating showed a consistently higher release rate without a clear plateau during the 6 h immersion and reached about 80% inhibitor content released (calculated as the inhibitor available at the coating volume beneath the extraction cell). This corresponds to around 35% more KDMTD released than that release from the DE-KDMTD coating for the same immersion time. This difference significantly exceeds the 10% additional inhibitor initially loaded into the C8-modified DE particles (Figure 4.4a). As illustrated in Figure 4.7c, we attribute this to the difference in reaction degree between the KDMTD and the surrounding coating resin. The surface modification in the C8@DE particles acts as a loading layer (Figure 4.4d) but also as a barrier layer that prevents the epoxy matrix from penetrating into the DE particles. As a consequence, lower amounts of KDMTD are deactivated due to unwanted chemical reactions with the epoxy-amine resin and hence more KDMTD is available to be released when the surface modified particles are used. Overall, these results suggest a higher corrosion inhibition efficiency would be expected for the coatings containing C8 surface-modified DE particles with KDMTD.

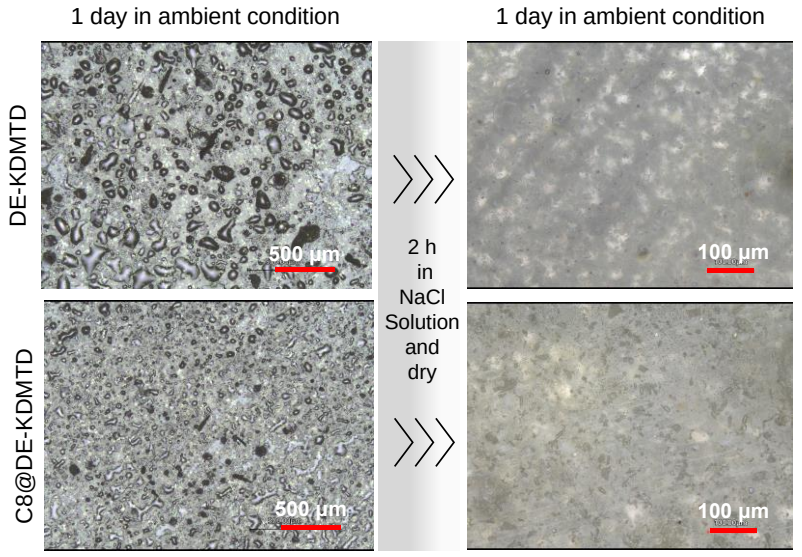


Figure 4.7 Confocal microscopic images of the intact coatings containing DE-KDMTD and C8@DE-KDMTD particles were captured after 1 day of exposure to ambient conditions (left column). The coatings were then exposed to a NaCl solution for 2 hours, followed by drying and an additional 1 day of exposure to the ambient environment (right column).

*4.3.5 Effect of surface modification on active corrosion protection at damaged coatings*

Figure 4.8 shows optical images, surface activity maps, global surface activity time evolution, and the post-mortem confocal microscopic images of the damages for the coatings containing DE-KDMTD and C8@DE-KDMTD particles exposed to pH 7 0.05M NaCl solution for 2 h. Results at 2h are shown as, at this immersion time, most of the releasable KDMTD (from the damaged wall and intact coating areas) should be released as shown in Figure 4.6. As shown in Figure 4.8a, the local activity at damage location for the coating with DE-KDMTD started short after immersion (black curve in 4.8a starting to rise at around 5min), increasing to 45% surface coverage within 1 h and 64% surface coverage at 2 h, when started plateauing. This activity was identified as corrosion-related activity as confirmed with post-mortem imaging revealing dealloying and trenching (Figure 4.8b). The coating with KDMTD loaded in C8@DE showed significantly lower surface activity coverage, kinetics and intensity of activity (seen by the histogram colors at the metal surface being mostly yellow-red rather than purple as in the case of DE-KDMTD). The imaged dynamic process stabilizes (surface activity plateaus) at 1.5 h and reaches 25% surface coverage at significantly lower intensity levels. Post-mortem images confirmed the extent of localized corrosion was significantly lower than for the DE-KDMTD samples (Figure 4.8c). Moreover, a UV-Vis analysis of the aliquots at 2h (Figure 4.8d) showed there was 21% more KDMTD released from the damaged C8@DE-KDMTD coating than from the DE-KDMTD coating ($1.6 \cdot 10^{-4}$ vs $1.3 \cdot 10^{-4}$ M). Despite the clear improvement in KDMTD release when using C8@DE particles, in both cases, the levels of inhibitor released are lower, especially during the first 60 min immersion, than the inhibitor concentration threshold necessary to fully stop the initial dealloying of intermetallic particles occurring within the first 5-10 min immersion. [17, 28] Nevertheless, the continuous inhibitor release during immersion allowed stopping the dealloying and trenching process after 1.5 h immersion in the case of the C8@DE particles as seen by the plateau in surface activity and intensity colour map.

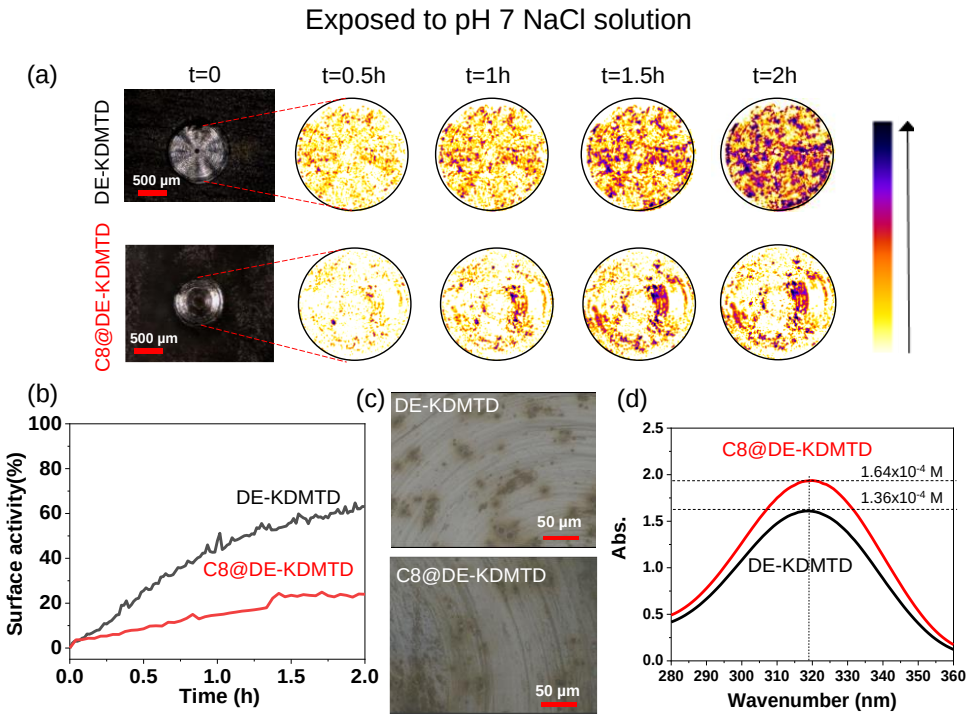


Figure 4.8 (a) Optical images at t=0, global activity maps at selected immersion times, (b) time evolution of surface activity and related intensity histogram, (c) local post-mortem confocal microscopic images of the damage, and (d) UV-Vis spectra of the electrolyte at the end of the 2h exposure in pH 7 NaCl solutions of damaged coatings containing DE-KDMTD (black lines) and C8@DE-KDMTD (red lines). The diameter of the damage hole is 1mm.

Previous studies demonstrated that HDMTD provides superior active protection compared to KDMTD in a neutral pH environment (Chapter 3). This was attributed to the protonation state of HDMTD and its acidity. [11, 17] To evaluate the effect of acid pH on protection, the corrosion study was repeated at pH 5. As shown in Figure 4.9, when the damaged coatings were exposed to pH 5, no relevant signs of surface activity during the whole immersion time were measured. This indicates a full degree of protection in both cases, as confirmed by the post-mortem analysis illustrated by the two confocal images in Figure 4.9c. Notably, the post-mortem solutions at pH 5 exhibited a higher absorbance wavelength (326 nm) than those exposed at neutral pH (320 nm) even though at one order of magnitude lower concentration. (Figure 4.9d) This shift in wavenumber indicates a higher protonation state of the inhibitor when exposed to more acidic pH [29, 30] and hints at higher levels of local protection at acidic pHs when KDMTD inhibitors are used, independently of the surface modification of the DE carrier. This increase in inhibition efficiency is not attributed to a higher release as confirmed by UV-Vis, but to a double effect of removal of the natural oxide layer on the aluminum surface[17] and to the protonation state of the inhibitor, both enhancing surface adsorption.

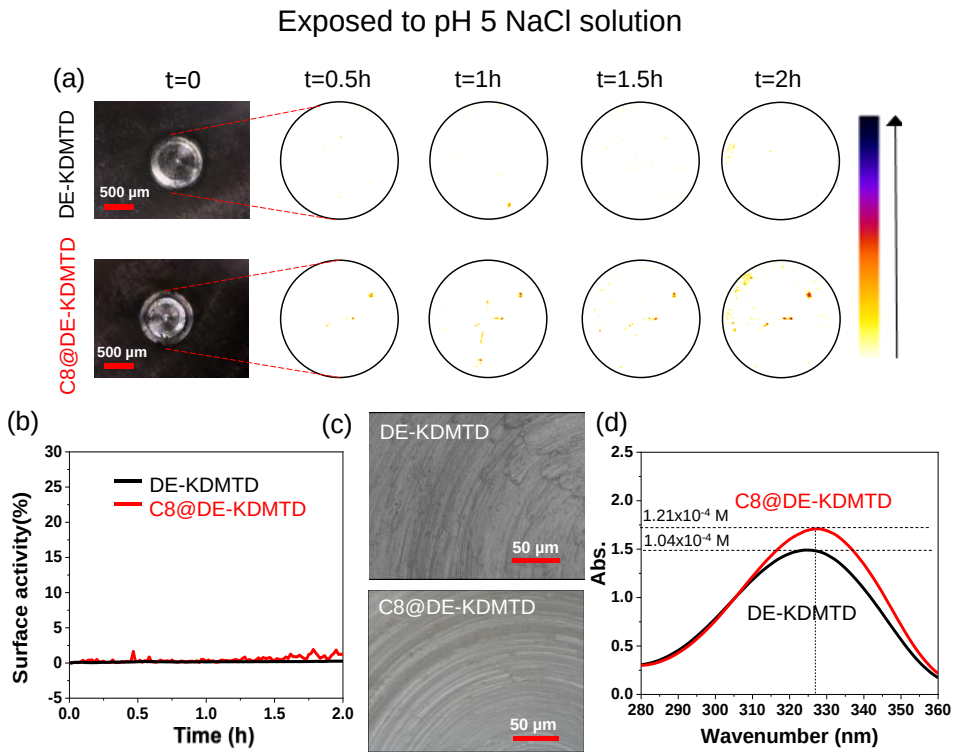


Figure 4.9 (a) Optical images at t=0, global activity maps at selected immersion times, (b) time evolution of surface activity and related intensity histogram, (c) local post-mortem confocal microscopic images of the damage, and (d) UV-Vis spectra of the electrolyte at the end of the 2h exposure in pH 5 NaCl solutions of damaged coatings containing DE-KDMTD (black lines) and C8@DE-KDMTD (red lines). The diameter of the damage hole is 1mm.

### *4.3.6 Effect of surface modification on inhibiting layer stability: wet-dry cyclic tests*

As highlighted in our previous works, [11, 17] inhibitor layer stability during re-exposure appears as a major, yet largely unattended, factor to consider when developing anticorrosive coatings. Figure 4.10 shows the effect of sequentially re-exposing to neutral NaCl solution the damaged coatings exposed to pH 5 in a first exposure event shown in Figure 4.9; i.e. exposure to pH 5 + drying + 1st re-exposure to pH 7 + drying + 2nd re-exposure to pH 7.

Upon first re-exposure to pH 7 NaCl solution (as shown in Figure 4.10a-d), the C8@DE-KDMTD coating continued to exhibit negligible surface activity at the damaged site, whereas the DE-KDMTD coating showed initial local activity that stabilized at around 2.5% surface coverage within 5 minutes of exposure. This aligns with the post-mortem imaging suggesting slight dealloying at local intermetallic particles (Figure 4.10c). Nevertheless, the activity phenomena occurring at the intermetallic particles stopped after the initial 5 min of immersion. It is suggested that the further inhibitor release measured by UV-Vis (Figure 4.10d) contributed to the stabilization of the inhibiting layer after some initial destabilization induced by the neutral pH. In contrast with this initial activity, the sample with C8@DE-KDMTD particles showed no local

activity, in good agreement with the 2.7 times more inhibitor release during this re-immersion (Figure 4.10d) and the post-mortem image (Figure 4.10c) showing no local corrosion signs. In any case, both systems showed significant robustness of the protective system in the event of a wet-dry-wet cycle.

A more noticeable difference between the two coatings emerged during the second re-exposure event (Figure 4.10e-h). During this second re-immersion, the coating with non-modified particles (DE-KDMTD coating) exhibited immediate surface activity propagating at a surface coverage propagation rate of 17% $h^{-1}$ and stabilizing at 25 % surface activity after 1.5 h exposure. Interestingly, the surface analysis showed large optical fluctuations, which, considering the relatively reduced local corrosion extension observed by the confocal microscope (Figure 4.10g), may be related to the continuous adsorption-desorption of inhibitors. This suggests that the inhibiting layer formed during immersion was too unstable and/or that the inhibitor release at similar amounts as in the first re-immersion (Figure 4.10a) was insufficient to fully counterbalance the instability of the inhibiting layer at pH 7.

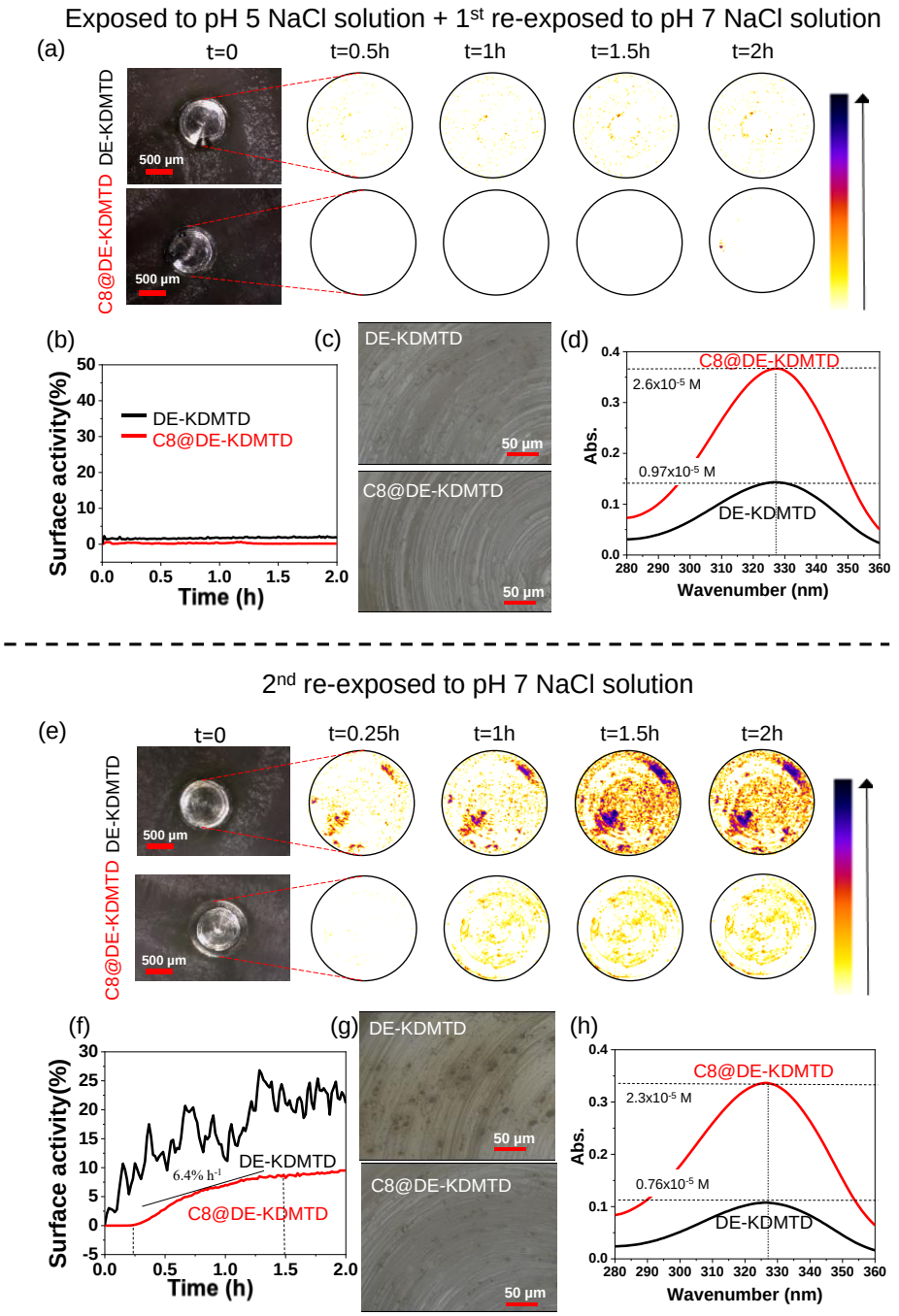


Figure 4.10 Optical images at t=0, global activity maps at selected immersion times, time evolution of surface activity and related intensity histogram, local post-mortem confocal microscopic images of the damage, and UV-Vis spectra of the electrolyte at the end of the 2 h exposure in pH 5 NaCl solutions of damaged coatings containing DE-KDMTD (black lines) and C8@DE-KDMTD (red lines) exposed to pH 5 NaCl solution, following by (a-d) 1st re-exposed to pH 7 NaCl solution and (e-h) 2nd re-exposed to pH 7 NaCl solution. The diameter of the damage hole is 1mm.

In contrast, the coating loaded with C8@DE-KDMTD particles showed: (i) a delayed onset of surface activity (onset after 15 min immersion); (ii) a surface activity propagation rate significantly lower (6.4% $h^{-1}$) and at significantly lower intensity (yellow color activity instead of the purple); (iii) a rapid end of the surface activity progression after 1.5h immersion at a low surface coverage of 8.9% ; and (iv) absence of noise in the activity progression. The postmortem analysis confirmed the surface activity was related to very reduced localized activity at intermetallic particles (Figure 4.10g). Interestingly, also in this case, the amount of inhibitor released was similar to the amounts measured during the first re-exposure test ($2.5\times10^{-5}$ M, being 3 times higher than for the DE-KDMTD sample, Figure 4.10h) and points at a threshold concentration of inhibitor needed to maintain the stability of the inhibiting layers formed at first instance at pH 5; intrinsically more stable when more inhibitor was released in the first instance (i.e. first immersion step). The release level during re-exposure for the C8@DE-KDMTD coating is also comparable to our previous work using nanolayer gas-phase deposited HDMTD particles ($2.5\times10^{-5}$ M during re-exposure). [11] This threshold of inhibitor being released during re-immersions ($1\times10^{-5}$ M<[inhibitors] <$2.3\times10^{-5}$ M) can better be supported by DE particles with a C8 silane surface treatment that ensures particle isolation from the coating and a higher adsorbed inhibitor.

The results and hypothesis discussed are summarized in Figure 4.11, for the coatings with DE-KDMTD and C8@DE-KDMTD particles when exposed to a (a) pH 7 0.05M NaCl solution and (b) pH 5 0.05M NaCl solution, followed by two subsequent exposures to pH 7 0.05M NaCl solution. DE-KDMTD and C8@DE-KDMTD particles show different degrees of dispersion (better dispersion for C8-modifed particles). More relevantly, while non surface modified particles are filled with polymer, the C8(OTS) surface modification prevents resin infiltration resulting in the presence of empty particles well dispersed in the coating (as shown in Figure 4.5). Consequently, more inhibitors remain protected from the surrounding matrix and therefore active to be ready to be quickly released at damaged locations.

When exposed to a pH 7, 0.05M NaCl solution (Figure 4.11a), a significant improvement in KDMTD release and corrosion inhibition was observed with the use of C8@DE particles. This improvement is attributed to better particle dispersion and the prevention of resin penetration. However, the initial dealloying and trenching corrosion could not be completely avoided in both coatings due to the complex ionic state of KDMTD and its limited release.

In contrast, despite the particle dispersion and resin infiltration differences, both coatings show high levels of protection at damage sites when exposed to pH 5 0.05M NaCl solution (Figure 4.11b), with a more stable protective layer formed by the higher release of inhibitors (Figure 4.9d) from the C8@DE-KDMTD coating. Upon re-exposure to the pH 7 NaCl solution, both damaged areas remain well-protected, likely related to the robust stability of the inhibiting layer on the metal and a sufficient resupply of inhibitor (Figure 4.10d). During the second re-exposure to the pH 7 NaCl solution, the samples loaded with C8@DE-KDMTD particles supply a comparable amount of inhibitor allowing the damage to be well protected. Nevertheless, the amount of inhibitor from the DE-KDMTD is estimated to be below a critical level. This does not allow maintaining the stability of the protective layer leading to the observation of surface activity related to local degradation. The release of 3 times (Figure 4.10h) more inhibitors from the

C8@DE-KDMTD coating compared to the DE-KDMTD coating during re-immersion, presumably combined with a concentration above a certain critical inhibitor supply level, indicates that continuous inhibitor release in the correct inhibitor chemical state is crucial for maintaining the stability of the inhibiting layer and hence long term protection as observed for the C8@DE particles loaded with KDMTD.

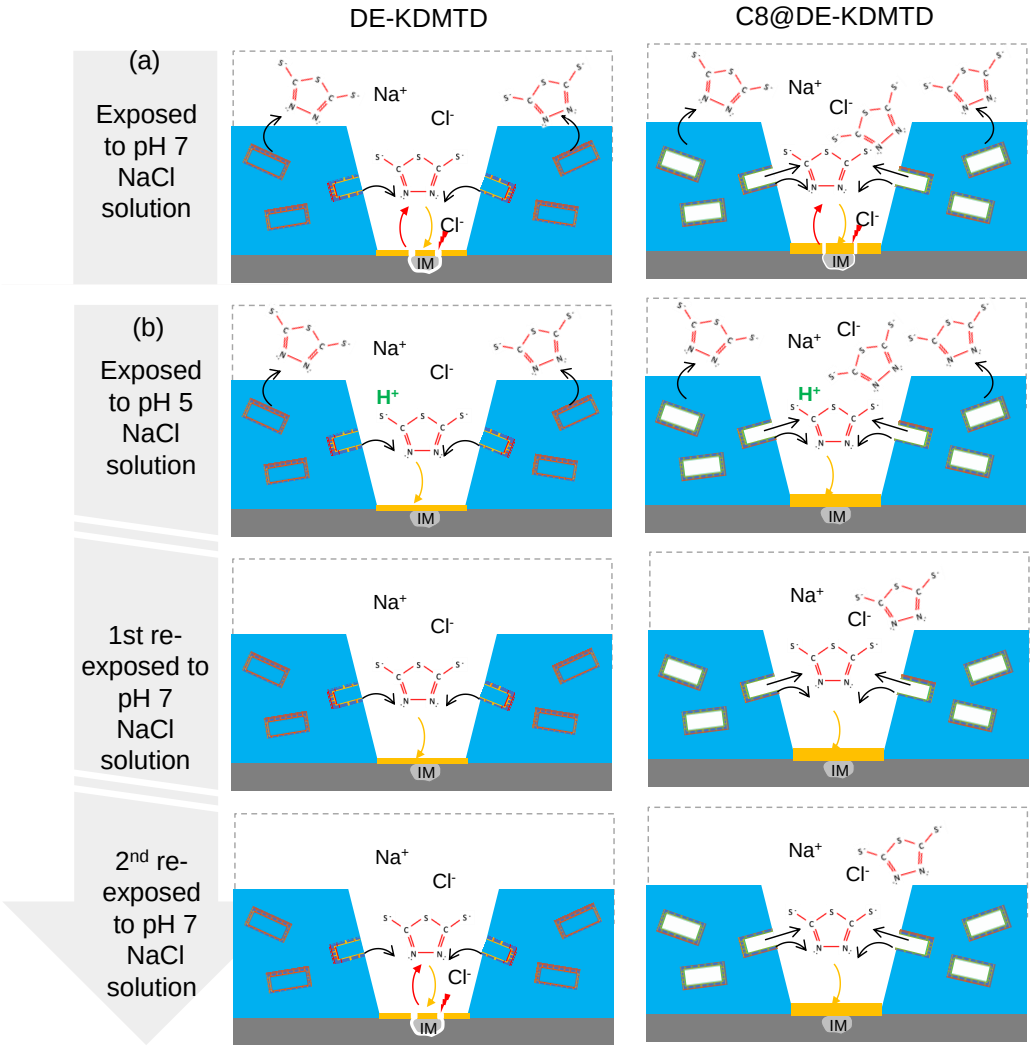


Figure 4.11 Scheme of the damaged coatings containing DE-KDMTD and C8@DE-KDMTD particles exposed to (a) pH 7 0.05M NaCl solution, and (b) pH 5 0.05M NaCl solution followed by two subsequent exposures to a pH 7 0.05M NaCl solution. The continuous supply of inhibitor beyond a critical level as achieved by C8(OTS) surface modification allows sustaining the inhibiting layer efficiently protecting the exposed metal surface.

## 4.4 Conclusions

This study demonstrated that the loading and release of organic inhibitors from diatomite particles can be tuned using hydrophobic silanes. Of the three alkyl silanes used (BTS (C4), OTS (C8), and ODTS (C18)) the mid-length silane (OTS, C8) led to the best combination of higher inhibitor loading, higher inhibitor adsorption ratio of about 3.5 times higher than the reference non-modified diatomite, sustained time release, and high percentage of inhibitor released with respect to loading (70-75%).

When added to organic coatings, the C8-modified DE particles displayed superior particle dispersion within epoxy-amine matrices with minimal resin infusion into the hollow core of the diatomite particles. As a consequence, about 35% more inhibitor was available to protect damage locations. Operando microscopy showed slightly better protection at damaged sites (1 mm diameter) of the coatings using C8-modified particles when exposed to pH 7, even though the local corrosion attack was not completely stopped in neither of the two coatings. At pH 5 both coatings showed excellent protection of the damage site with no apparent corrosion. Re-immersion of samples pre-exposed to pH 5 in pH 7 0.05M NaCl demonstrated very high stability of the inhibiting layers during the first re-immersion cycle of 2 h. In a second re-immersion in neutral pH 0.05M NaCl, the coatings loaded with unmodified diatomite slightly lost their highly protective efficiency while the coatings loaded with C8 modified particles maintained it due to higher inhibiting layer stability and inhibitor supply due to lower inhibitor reactivity with the surrounding matrix. This study demonstrates organic corrosion inhibitors can be efficiently loaded into diatomite particles through surface modification to allow reduced negative interactions with the surrounding coating matrix and therefore enhanced and sustained protection at damaged locations

# 4.5 References

(1) Sørensen, P. A.; Kiil, S.; Dam-Johansen, K.; Weinell, C. E. Anticorrosive coatings: a review. *Journal of coatings technology and research* **2009**, *6*, 135-176.
(2) Lyon, S. B.; Bingham, R.; Mills, D. J. Advances in corrosion protection by organic coatings: What we know and what we would like to know. *Progress in Organic Coatings* **2017**, *102*, 2-7.
(3) Cui, G.; Bi, Z.; Wang, S.; Liu, J.; Xing, X.; Li, Z.; Wang, B. A comprehensive review on smart anti-corrosive coatings. *Progress in organic coatings* **2020**, *148*, 105821.
(4) Sinko, J. Challenges of chromate inhibitor pigments replacement in organic coatings. *Progress in organic coatings* **2001**, *42* (3-4), 267-282.
(5) Visser, P.; Liu, Y.; Terryn, H.; Mol, J. Lithium salts as leachable corrosion inhibitors and potential replacement for hexavalent chromium in organic coatings for the protection of aluminum alloys. *Journal of Coatings Technology and Research* **2016**, *13*, 557-566.
(6) Rodič, P.; Milošev, I. Corrosion inhibition of pure aluminium and alloys AA2024-T3 and AA7075-T6 by cerium (III) and cerium (IV) salts. *Journal of The Electrochemical Society* **2015**, *163* (3), C85.
(7) Lamaka, S. V.; Zheludkevich, M. L.; Yasakau, K.; Montemor, M.; Ferreira, M. G. High effective organic corrosion inhibitors for 2024 aluminium alloy. *Electrochimica Acta* **2007**, *52* (25), 7231-7247.
(8) Obot, I.; Macdonald, D.; Gasem, Z. Density functional theory (DFT) as a powerful tool for designing new organic corrosion inhibitors. Part 1: an overview. *Corrosion Science* **2015**, *99*, 1-30.
(9) Zheludkevich, M.; Tedim, J.; Ferreira, M. "Smart" coatings for active corrosion protection based on multi-functional micro and nanocontainers. *Electrochimica Acta* **2012**, *82*, 314-323.
(10) Denissen, P. J.; Homborg, A. M.; Garcia, S. J. Requirements for corrosion inhibitor release from damaged primers for stable protection: a simulation and experimental approach using cerium loaded carriers. *Surface and Coatings Technology* **2022**, *430*, 127966.
(11) Zhao, J.; van Ommen, J. R.; Garcia, S. J. Gas-phase deposited nanolayers guard organic microparticles in polymer matrices for active corrosion protection at damages. *Progress in Organic Coatings* **2024**, *192*, 108522.
(12) Grigoriev, D.; Akcakayiran, D.; Schenderlein, M.; Shchukin, D. Protective organic coatings with anticorrosive and other feedback-active features: micro-and nanocontainers-based approach. *Corrosion* **2014**, *70* (5), 446-463.
(13) Altin, A.; Rohwerder, M.; Erbe, A. Cyclodextrins as carriers for organic corrosion inhibitors in organic coatings. *Journal of The Electrochemical Society* **2017**, *164* (4), C128.
(14) Kim, C.; Karayan, A. I.; Milla, J.; Hassan, M.; Castaneda, H. Smart coating embedded with pH-responsive nanocapsules containing a corrosion inhibiting agent. *ACS applied materials & interfaces* **2020**, *12* (5), 6451-6459.
(15) Denissen, P. J.; Garcia, S. J. Cerium-loaded algae exoskeletons for active corrosion protection of coated AA2024-T3. *Corrosion Science* **2017**, *128*, 164-175.
(16) Denissen, P. J.; Shkirskiy, V.; Volovitch, P.; Garcia, S. J. Corrosion inhibition at scribed locations in coated AA2024-T3 by cerium-and DMTD-loaded natural silica microparticles under continuous immersion and wet/dry cyclic exposure. *ACS applied materials & interfaces* **2020**, *12* (20), 23417-23431.
(17) Zhao, J.; Santoso, A.; Garcia, S. J. Small concentrations of NaCl help building stable inhibiting layers from 2, 5-dimercapto-1, 3, 4-thiadiazole (DMTD) on AA2024-T3. *Corrosion Science* **2023**, *225*, 111562.
(18) Mahtabani, A.; La Zara, D.; Anyszka, R.; He, X.; Paajanen, M.; Van Ommen, J. R.; Dierkes, W.; Blume, A. Gas phase modification of silica nanoparticles in a fluidized bed: Tailored deposition of aminopropylsiloxane. *Langmuir* **2021**, *37* (15), 4481-4492.
(19) Bariana, M.; Aw, M. S.; Kurkuri, M.; Losic, D. Tuning drug loading and release properties of diatom silica microparticles by surface modifications. *International journal of pharmaceutics* **2013**, *443* (1-2), 230-241.
(20) Aw, M. S.; Bariana, M.; Yu, Y.; Addai-Mensah, J.; Losic, D. Surface-functionalized diatom microcapsules for drug delivery of water-insoluble drugs. *Journal of biomaterials applications* **2013**, *28* (2), 163-174.
(21) Bariana, M.; Aw, M. S.; Losic, D. Tailoring morphological and interfacial properties of diatom silica microparticles for drug delivery applications. *Advanced Powder Technology* **2013**, *24* (4), 757-763.

(22) Kumeria, T.; Bariana, M.; Altalhi, T.; Kurkuri, M.; Gibson, C. T.; Yang, W.; Losic, D. Graphene oxide decorated diatom silica particles as new nano-hybrids: towards smart natural drug microcarriers. *Journal of Materials Chemistry B* **2013**, *1* (45), 6302-6311.
(23) Yu, Y.; Addai-Mensah, J.; Losic, D. Functionalized diatom silica microparticles for removal of mercury ions. *Science and technology of advanced materials* **2012**, *13* (1), 015008.
(24) Sheng, G.; Wang, S.; Hu, J.; Lu, Y.; Li, J.; Dong, Y.; Wang, X. Adsorption of Pb (II) on diatomite as affected via aqueous solution chemistry and temperature. *Colloids and Surfaces A: Physicochemical and Engineering Aspects* **2009**, *339* (1-3), 159-166.
(25) Sheng, G.; Hu, J.; Wang, X. Sorption properties of Th (IV) on the raw diatomite—effects of contact time, pH, ionic strength and temperature. *Applied Radiation and Isotopes* **2008**, *66* (10), 1313-1320.
(26) Peng, Y.; Hughes, A. E.; Mardel, J. I.; Deacon, G. B.; Junk, P. C.; Forsyth, M.; Hinton, B. R.; Somers, A. E. Leaching behavior and corrosion inhibition of a rare earth carboxylate incorporated epoxy coating system. *ACS applied materials & interfaces* **2019**, *11* (39), 36154-36168.
(27) Denissen, P. J.; Shkirskiy, V.; Volovitch, P.; Garcia, S. J. Corrosion Inhibition at Scribed Locations in Coated AA2024-T3 by Cerium- and DMTD-Loaded Natural Silica Microparticles under Continuous Immersion and Wet/Dry Cyclic Exposure. *ACS Appl Mater Interfaces* **2020**, *12* (20), 23417-23431. DOI: 10.1021/acsami.0c03368 From NLM PubMed-not-MEDLINE.
(28) Mopon Jr, M.; Mol, A.; Garcia, S. J. Effect of delayed inhibitor supply on AA2024-T3 intermetallic activity: A local in situ analysis with reflected microscopy. *Corrosion Science* **2024**, *230*, 111910.
(29) Stanovnik, B.; Tišler, M. Contribution to the Structm· e of 2, 5-Dimercapto-1, 3, 4-thiadiazole and Related Compounds. *Croatica Chemica Acta* **1965**, *37* (1), 17-23.
(30) Galvão, T. L.; Kuznetsova, A.; Gomes, J. R.; Zheludkevich, M. L.; Tedim, J.; Ferreira, M. G. A computational UV–Vis spectroscopic study of the chemical speciation of 2-mercaptobenzothiazole corrosion inhibitor in aqueous solution. *Theoretical Chemistry Accounts* **2016**, *135*, 1-11.

# Chapter 5

# Small concentrations of NaCl help building stable inhibiting layers from 2,5-dimercapto-1,3,4-thiadiazole (DMTD) on AA2024-T3

*The interaction of 2,5-dimercapto-1,3,4-thiadiazole (DMTD) with the AA2024-T3 local microstructure (S-phase, secondary phases and matrix) as function of the NaCl concentration is studied. The inhibiting power and the local interaction of DMTD with the metal were studied by in–situ opto-electrochemistry, XPS and Raman spectroscopy. The stability of the inhibiting layers was evaluated by re-exposing the samples to NaCl solutions without inhibitor. The amount of DMTD and its interaction state (chemisorption/physisorption) vary with the local microstructural composition and NaCl concentration. Higher stability of the inhibiting layers is obtained when these are formed in presence of small amounts of NaCl (0.025M-0.25M).*

This Chapter has been published as:

*Zhao, J.; Santoso, A.; Garcia, S. J.Small concentrations of NaCl help building stable inhibiting layers from 2, 5-dimercapto-1, 3, 4-thiadiazole (DMTD) on AA2024-T3. Corrosion Science 2023, 225, 111562.*

# 5.1 Introduction

Corrosion protection through coatings loaded with corrosion inhibitors is a widespread strategy to control corrosion. In these systems, protection is both passive (barrier) and active (corrosion inhibitor interaction with the metallic surface). In presence of a macroscopic damage (e.g. scratch), the inhibitors dissolve and diffuse to the damaged location using water paths in the coatings to ultimately react with the metallic surface to create a new protective layer (namely corrosion protective layer, passive layer or inhibiting layer). [1-3] Despite this is the most common strategy, and often the only viable one, it is generally accepted that the protection at damaged and corrosion-inhibited locations will be ultimately lost after cyclic or long-term exposure to the aggressive electrolyte. This is typically attributed to a drop in inhibitor supply from the coating and implicitly suggests that the formed inhibiting layers are non-stable, reversible or imperfect to ensure long-term protection of the metal in the absence of continuous inhibitor supply. To overcome this problem, most of the ongoing research focuses on controlling the inhibitor release through nano or microcarriers amongst others. [4-6] However, little research has been dedicated to the study of the factors affecting the formation of a more or less stable or homogeneous protective layer. Arguably, a better understanding on how inhibiting layers can be made more stable can contribute to the development of more efficient anticorrosion systems, even when the inhibitor supply from the coating is reduced. In this work, we make a first step into this direction by studying if and how the NaCl concentration present in the inhibiting solution used to form the protective layers affects the stability of such layers during a subsequent re-exposure step.

Amongst the many alternative corrosion inhibitors called to replace Cr(VI)-based salts to protect Cu-rich aluminum alloys such as AA2024-T3, rare earth salts (e.g., Ce(III) nitrate, Ce(III) dibutyl-phosphate, Ce(III) cinnamate, Ce(III) tartarate) [4-9] have called significant attention and are broadly being studied. The most accepted mechanism of protection using these salts is the deposition of Ce(III)/Ce(IV) oxide/hydroxide layers at active cathodic sites due to local environmental changes (e.g., changes in pH) [7, 8, 10] followed by the deposition of the organic counterion on the whole surface when organic rare earth salts are used. [11] Despite the high levels of protection and relatively good collective understanding on how these layers are formed, recent reports suggest that cerium-based layers do not continuously protect under specific re-exposure conditions. For instance, cerium–rich inhibiting layers on AA2024-T3 formed from 0.05 M NaCl with 1 mM $Ce(NO_3)_3$ become reversible, or inefficient, in a relatively short re-immersion time ranging from 0.5 to 5 hours when the samples are re-immersed from the inhibiting solution directly into a non-inhibited 0.05 M NaCl solution. [12]

Besides cerium salts, organic inhibitors such as DMTD (2,5-dimercapto-1,3,4-thiadiazole), 2-MBT (mercaptobenzothiazole), and DEDTC (diethyldithiocarbamate) have shown remarkable corrosion inhibition efficiency in solution [13, 14] generally attributed to their complexation with the metal surface. [13] Generally, heteroatoms such as nitrogen and sulfur along with π-electrons of multiple bonds act as adsorption centers during metal-inhibitor interactions[15] and are therefore generally related to highly efficient corrosion inhibitors. [16-18] To form the inhibiting layer, it has been suggested that physisorption may be followed by the more stable chemisorption state of the

inhibitor. [19, 20] Due to the wide structural possibilities of organic inhibitors and the potential weight gain in coating systems, it is relevant to understand the actual protective mechanisms and the mechanisms behind the resistance or loss of their protective behavior.

Amongst the reported organic inhibitors, DMTD is a very effective corrosion inhibitor with inhibiting mechanisms not yet fully understood. DMTD, is a thiadiazole derivative consisting of a conjugated heterocyclic ring with S and N atoms with two likely to happen tautomers and several speciation possibilities as function of pH. Its corrosion inhibition power for AA2024-T3 has been attributed to the formation of Cu–DMTD complexes, which have limited aqueous solubility and are able to reduce the oxygen reduction reactions on Cu-rich intermetallics (IMs). [5, 13, 21] This hypothesis is supported by recent works on Cu alloys showing that DMTD forms strong chemical interactions instead of just physical adsorption. [22] On the other hand, reports showing that DMTD's functional groups of pyrrolic N from the azole ring and thiol S from the mercapto anchoring group are responsible for the chemisorption on Ag, Au and Cu[23] suggest that, also in the case of aluminum alloys, the interactions may go beyond the suggested Cu-DMTD complexation at some IMs.

In this work, we use DMTD as a model organic corrosion inhibitor for AA2024-T3 to learn more about the effect of NaCl concentration on the inhibiting mechanisms, (local) inhibitor layer formation, and the stability of such layers. To this aim, we exposed AA2024-T3, in presence or absence of 1mM DMTD, to a range of NaCl concentrations (0 M to 0.5 M NaCl) and studied how the inhibiting layers form and vary as function of the local metal composition. The stability of the inhibiting layers was evaluated by exposing the protected alloys to fresh NaCl solutions with no inhibitor. During exposure and re-exposure, the samples were monitored using a hyphenated optical and electrochemical set-up. [12, 24, 25] Ex-situ surface analysis techniques including SEM/EDS, local and global Raman spectroscopy and XPS, complemented the study. The results show a strong relation between inhibiting layer stability and the NaCl concentration present during the inhibiting layer formation. The findings of this work highlight the relevance of dedicated studies dealing with the stability of inhibiting layers formed on the metal surface and its relation to long-term corrosion protection at damage locations using anticorrosive coatings. A better understanding on how to make inhibiting layers more stable will contribute to the development of new or/and more efficient strategies to protect metals using active anticorrosive coatings.

# 5.2 Experimental

*5.2.1 Materials*

Commercial grade bare AA2024-T3 (3mm rolled sheets) were cut into 3 x 3cm pieces and used as substrate in all the tests. 2,5-dimercapto-1,3,4-thiadiazole (DMTD >99%) was purchased from Sigma-Aldrich. Sodium chloride (NaCl, >98%) was purchased from VWR Chemicals. All chemicals were used as received. Aqueous solutions at 0, 0.025, 0.05, 0.25, 0.4, and 0.5 M NaCl were prepared using Milipore® Elix 3 UV filtered water.

*5.2.2 Experimental protocol*

The experimental protocol followed in this research is schematically shown in the Supporting Information Figure S5.1 and detailed in this section. All the tests were repeated two or three times for reproducibility check.

*5.2.2.1 Surface preparation of AA2024-T3 prior to exposure to inhibited NaCl solutions*

AA2024-T3 was cut into 3 cm x 3 cm x 3 mm small sheets and sequentially ground with 1000, 2400, and 4000 SiC paper and polished with 3 µm and 1 µm diamond pastes during approximately 1 min for each grit size (Supporting Information Figure S5.1a).

*5.2.2.2 Exposure: in-situ monitoring of inhibitor-metal interaction in DMTD-inhibited NaCl solutions*

The inhibitor-metal interaction during exposure to different NaCl and DMTD containing electrolyte solutions was monitored using a home-built set-up hyphenating optics and electrochemistry as described in earlier works (Supporting Information Figure S5.1b). [24] Herein, the AA2024-T3 sheets (working electrode) were mounted in a magnetic Raman electrochemical flow cell from Redox.me. This cell allowed a total electrolyte volume of 4.5 ml and the use of a small Ag/AgCl (3 M KCl) reference electrode and a platinum wire (0.6/150 mm) counter electrode. The electrochemical cell was placed vertically in a Faraday cage on an optical table from ThorLabs to avoid any electromagnetic and vibrational disturbances. A digital microscope was placed at the window side of the electrochemical cell. This allows obtaining high-resolution images during exposure to electrolyte simultaneously to the electrochemical potential noise (EPN) measurements as function of the exposure time. The electrolyte was injected through side openings allowing capturing optical and electrochemical information right after metal exposure to the electrolyte. A range of NaCl aqueous solutions containing 0, 0.025, 0.05, 0.25, 0.4, 0.5 M NaCl and 1mM DMTD were used as electrolyte. 1 mM inhibitor concentration was selected based on the necessary inhibitor concentration to provide efficient protection within the solubility range of DMTD. [14] Exposure to electrolytes was carried for 6 hours. The exposure time was determined based on a preliminary lab study, wherein both the EPN signal and optical surface activity consistently reached stabilization before the 6-hour exposure, thereby indicating a surface equilibrium state.

The EPN measurements were conducted simultaneously to the optical measurements in a 2-electrode configuration: the working electrode was connected to the reference electrode through

a Compactstat from Ivium Technologies, working as a potentiometer. The potentiometer was connected to a Windows-based PC running dedicated software. The maximum range of the potentiometer was set at ±1 V vs Ag/AgCl. The interval time between data points was set to 0.05 s (sampling frequency of 20 Hz) combined with a low-pass filter of 10 Hz.

The optical analysis was conducted in ImageJ software in a similar fashion as described in earlier works. [24] The technique is based on a pixel-by-pixel analysis of the progression of surface changes over time at a global and local (i.e., intermetallics) scale. For the analysis, images were converted to grey scale at an 8-bit resolution allowing the definition of 256 different levels of intensity between black and white. Image correlation was then applied and high-intensity pixels were then isolated from low-intensity pixels to discriminate between active Affected Area and potential background noise using an appropriate threshold (30 to 255). This threshold is used to ensure surface changes are not affected by optical noise. This allows to relate optical changes between images to dealloying, corrosion or deposition (e.g., inhibition) phenomena. [25] Out of the optical global analysis, information as the global Affected Area in % as a function of time and characteristic parameters of the kinetics of degradation can be obtained. In this work, the Affected Area corresponds to the area of the metal surface exposed to the electrolyte that showed cumulative optical variations with respect to the starting surface and is a measure of the degradation degree with time.

*5.2.2.3 Surface analysis: Interaction of DMTD with AA2024-T3 at the global and local level*

To deepen into the reactivity mechanisms of DMTD with AA2024-T3 surfaces, a separate set of tests was prepared to perform Raman and XPS analysis (Supporting Information Figure S5.1c and S5.1d). Metal surfaces were prepared as indicated in 5.2.2.1. After exposure to the same saline solutions as used in 5.2.2.2, the metal plates were rinsed with distilled water and let dry in air for 10 minutes. Subsequently, the samples were analyzed using a Renishaw inVia Confocal Raman spectrometer equipped with a 32 mW laser source at 532 nm and a Leica objective of 5× magnification. The Raman analysis was performed at an effective laser power of 5% at 60 s exposure time over 2 accumulations per point. The samples were also analyzed using a ThermoFisher K-alpha XPS system equipped with a monochromatic Al anode X-ray source with a spot size of 400 µm. The photo-electrons are detected by a 128-channel detector, with a 0.1 eV resolution. For survey spectra, the pass energy and step size were set to 140 eV and 0.40 eV respectively. For high-resolution, spectra were obtained with 50 eV pass energy and 0.1 eV resolution. All spectra were calibrated by assigning the true energy value (284.8 eV) corresponding to the position of a C 1s peak. The deconvolution of XPS peaks was conducted with using a mixed Gaussian-Lorentzian fit after subtracting the background using the standard Shirley method. All spectra were curve fitted to the minimum number of peaks required for an optimum fit and to the most probable species needed for the corresponding chemical assignment, with the envelopes smoothed using an SG Quadratic algorithm. The quantitative analysis of the species at the surface was derived from the peak area intensities.

To identify the DMTD interaction at the local IM level a new set of samples was prepared. In this case, prior to exposure to the inhibited NaCl solutions, 4 indents were performed around a selected area of 200 µm x 140µm to be able to always identify the area of interest. This area of interest was analyzed by SEM-EDS (point analysis with 15 kV of accelerating voltage and 10 µA of emission current) to obtain individual IM compositions. To remove possible traces of organic

contamination coming from the SEM-EDS, the electrodes were quickly re-polished (≈ 20 s) with 1µm diamond paste before exposure to electrolyte. After this, the samples were immersed in 1 mM DMTD+0.05 M NaCl solution as the model solution to study the local interaction of DMTD with the IMs. After exposure, the samples were rinsed in demineralized water and dried in air before local Raman analysis. The studied IMs were found within the area of interest limited by the indents. The Raman mappings were obtained through point-by-point measurement with the 532 nm laser source and a Leica objective of 50× magnification and numerical aperture of 0.55 (spot size about 1µm) on the IMs identified during the SEM-EDS.

*5.2.2.4 Re-exposure: study of the stability of the previously formed inhibiting layers*

The samples exposed to the inhibited solutions as indicated in 5.2.2.2, were rinsed with distilled water, let dry for 10 min and re-exposed to a fresh electrolyte solution containing 0.05M NaCl and no inhibitor while being monitored in real time with the same opto-electrochemical set-up as in 5.2.2.2. To ensure the same area exposed to the first solution was re-exposed to the new electrolyte some marks were placed on the metal substrate. The re-exposure to a corrosive solution allowed studying the stability of the DMTD inhibiting layers on AA2024-T3. Same data analysis as in 5.2.2.2 was performed. 15h re-exposure period was selected to allow for a complete stabilization of the surface in all cases as determined by a plateau in both the EPN signal and the Affected Area (AA%) measurements. After 15h re-exposure, the samples were rinsed, dried in air and analyzed with SEM-EDS (JEOL JSM-7500F field emission scanning electron microscope equipped with energy dispersive X-ray spectroscopy and operated in back-scattered electrons (BSE) mode) and Raman spectroscopy (Supporting Information Figure S5.1f).

# 5.3 Results and discussion

*5.5.1 Exposure to solutions with DMTD and different NaCl concentrations*

Table 5.1 shows an overview of the EPN and visually detectable Affected Area variation with the exposure time and the pH values before and after the exposure. Duplicates can be found in Supporting Information Table S5.1. As can be seen in Table 5.1, the Affected Area (%AA) in 0.05M NaCl without DMTD reached 3.3% at 1h exposure. Within 20 min of exposure, a surface attack equivalent to the IM surface area coverage, which was calculated as 1.6% (Supporting Information Figure S5.2), was achieved. In contrast, the total %AA after 6h exposure to all NaCl solutions with DMTD is almost negligible (<0.05%) for all NaCl concentrations with the exception of solutions containing 0.5 M NaCl which showed 0.5% Affected Area at 6h exposure. The EPN of the sample exposed to 0.05 M NaCl stabilized at -437mV vs Ag/AgCl, well in line with the corrosion potential of AA2024 at thermodynamic equilibrium after IM dealloying and pitting initiation. [7] The EPN of samples exposed to solutions containing DMTD are all very smooth after the first 2500-5000 s of exposure, when rapid EPN increase and decrease events are observed. Exposure to high NaCl concentrations with same DMTD concentration lead to a more negative EPN plateau (between -537 and -627 mV). Even though SEM analysis only showed an increase of 0.1% IM surface area coverage after exposure (Supporting Information Figure S5.2), the results are compatible with an overall decrease in total anodic area due to Al matrix dissolution or/and increase in cathodic area due to increase of IM sites with absence of local attack as seen in the Affected Area (%AA) results. In line with this, at the end of the 6h exposure, all solutions (with starting pH between 3.1 and 3.4) are less acidic, with a relatively higher pH variation in samples with higher NaCl content. The pH values and the EPN measurements are compatible with a NaCl and acid-induced partial dissolution of the aluminum matrix and the native oxide/hydroxide layer (for Al, at pH 3, $Al(OH)^{2+}$, $AlO^{+}$ and $Al(OH)_3(aq)$ coexist [26]) followed by a passivation of the surface due to the presence of DMTD anions ($DMTD^{-}$).

Table 5.1 Evolution of EPN and optically detectable Affected Area (%AA) during 6 h exposure to solutions containing DMTD and NaCl at different concentrations. Extracted characteristic parameters (i.e., AA (%) final, EPN final, and pH (initial and final)) are shown for clarity. Note: the final exposure time for all solutions with DMTD was 6h but 1h when no DMTD was used.

| Salt concentrations (M) | | OCP and total Affected Area (AA in %) by optics | %AA | OCP(mV) | pH | |
|---|---|---|---|---|---|---|
| NaCl | DMTD | | | | initial | final |
| 0.05 | 0 | 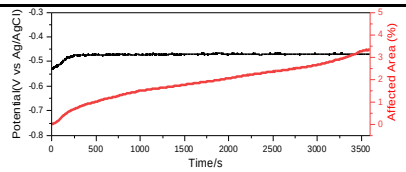 | 3.30 | -437 | 6.9 | 7.2 |
| 0 | 0.001 | 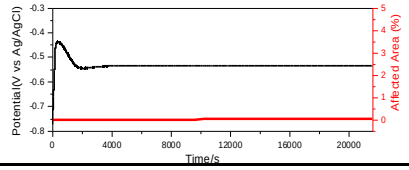 | 0.02 | -537 | 3.4 | 4.4 |
| 0.025 | 0.001 | 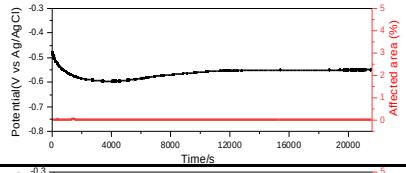 | 0.00 | -551 | 3.2 | 4.6 |
| 0.05 | 0.001 | 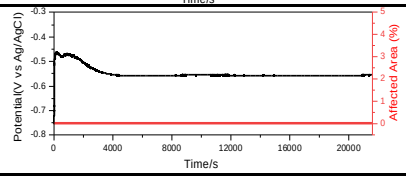 | 0.00 | -557 | 3.2 | 5.1 |
| 0.25 | 0.001 | 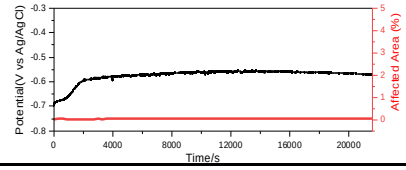 | 0.04 | -572 | 3.1 | 4.9 |
| 0.4 | 0.001 | 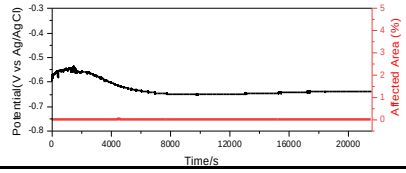 | 0.01 | -639 | 3.1 | 5.0 |
| 0.5 | 0.001 | 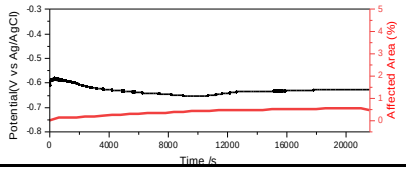 | 0.46 | -627 | 3.1 | 5.2 |

Based on surface activity (%AA), EPN and pH behavior, the samples can be clustered in three groups depending on NaCl concentration in spite of the differences between samples in each group: (a) NaCl solution with no DMTD, showing high surface activity (high %AA), noisy EPN plateauing around -440mV, and neutral pH; (b) DMTD solutions with low NaCl concentrations

(0-0.25 M), showing (almost) no optically-detectable degradation (%AA≈0%), smooth EPN around -550 ±20mV, and acid pH; and (c) DMTD solutions with high NaCl concentrations (0.4-0.5 M), showing some surface activity, smooth EPN around -630 ±10mV and acid pH.

Figure 5.1 shows a close-up comparison of EPN and surface activity (Affected Area, %) as function of exposure time to 0.05 M NaCl (Figure 5.1a), DMTD with 0.05 M NaCl (Figure 5.1b) and DMTD with 0.5 M NaCl (Figure 5.1c), as representative of the three main behavior groups mentioned above. Micrographs obtained during exposure (Figure 5.1) and the obtained global and local activity maps (Figure 5.2) at characteristic times are included for a better observation of the surface phenomena responsible for the measured EPN and surface activity (%AA).

For solutions without DMTD (Figure 5.1a), generalized local attack at IM level occurs within the first 5 min of exposure. This first kinetic degradation stage ($k_1$ = 2.4E-3% $s^{-1}$) coincides in time with the sample EPN increase until plateau and with our previous reports on local IM dealloying. [24] However, an Affected Area change and dealloying kinetics slightly lower than in previous works under comparable conditions was observed (2.4E-3 vs. 6E-3 % $s^{-1}$). [24, 25] We attribute the difference to the use of different working electrode surface (3.5$cm^2$ vs 500$\mu m^2$) for same counter electrode and threshold value used for the calculations as well as to differences in IM surface area distribution. Similar to previous reports, the second kinetic stage ($k_2$=8E-4% $s^{-1}$), related to dealloying beyond the IM surface area, is slower than the first stage. [24] In this second stage, the Affected Area increases at a near-to-constant EPN with some low amplitude fluctuations indicating the growth of trenching, pitting penetration, and the further deposition of corrosion products. After 1h exposure, 3.3% of the surface area is affected by the corrosion process.

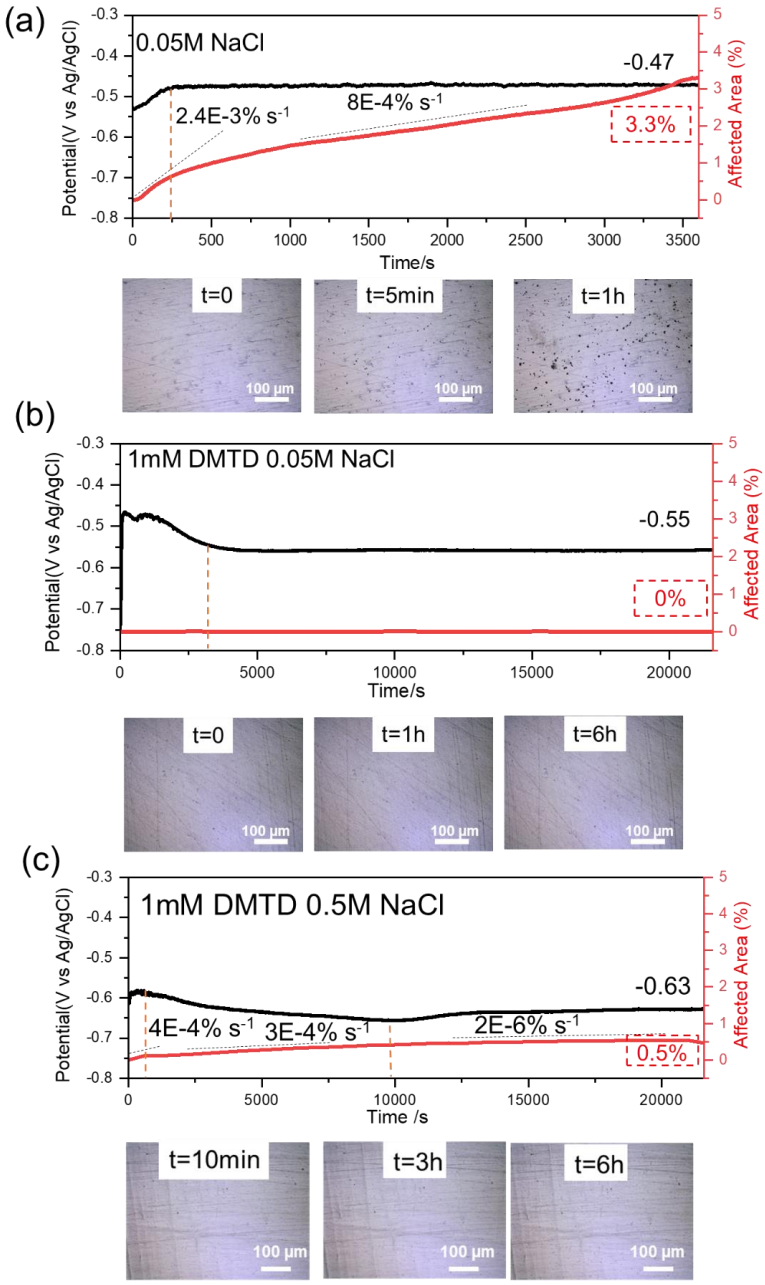


Figure 5.1 Plots showing EPN and Affected Area (%AA), and underwater micrographs at three characteristic times: (a) 1 h exposure in 0.05 M NaCl solution; (b) 6h exposure in 1 mM DMTD 0.05 M NaCl solution; and (c) 6 h exposure in 1 mM DMTD 0.5 M NaCl solution.

Samples exposed during 6h to low NaCl concentrations in the presence of 1 mM DMTD show trends as reported in Figure 5.1b. After an initial fast increase of the potential, the EPN starts to decrease to more negative values and, within 1h, flattens into a very stable plateau at an almost

constant value of -550mV. This trend of potential is accompanied by no detectable surface activity (0% AA) in the 6h of exposure using the optical threshold of 30 (Figure 5.2b). It should be noted that the lack of surface activity at the selected threshold does not exclude optically detectable surface activity at different threshold levels, an aspect that will be addressed in future works, but limits optical noise influence. In any case, these results confirm the excellent inhibition properties of DMTD under these exposure conditions. The initial fast EPN increase (within 2 min) is here attributed to (i) a fast physical adsorption to form a mono-/muti-layer across the exposed surface; and/or (ii) removal of the native oxide/hydroxide layer due to NaCl and acidic conditions in agreement with the pH results shown in Table 5.1. Although the initial pH (3.1 to 3.4) is marginally below the stability threshold for AA2024, variations in the oxide thickness, integrity, or local distribution at this pH are likely to occur, leading to discernible changes in the EPN readings. The subsequent decrease of the potential to a very stable value can be attributed to the DMTD inhibitor deposition and layer build up leading to an overall more anodic surface.

At high NaCl concentrations in 1 mM DMTD solution, samples behave as shown in Figure 5.1c. Most of the surface activity (up to 0.5%AA) takes place within the first 3h of immersion, as can be seen with the Affected Area kinetics changing from 3E-4 % $s^{-1}$ to 2E-6 % $s^{-1}$ at 3h. As in Figure 5.1b, the EPN shows a fast initial increase with small transients followed by a smoother decrease until plateau even if at a more negative potential (-630 mV vs. -550 mV). The surface activity (Figure 5.2c) accompanied by low amplitude fluctuations during the first 3h is attributed to the local corrosion process and/or the dynamic adsorption of inhibitors. Compared to low NaCl concentrations, the longer time till plateau (Figure 5.1b) suggests a slower DMTD film growth till absorption equilibrium or/and different DMTD-surface interactions. The presence of some level of local activity can be better seen in the magnified local activity maps shown in Figure 5.2d. Here, low intensity activity is seen to be restricted to some IM locations.

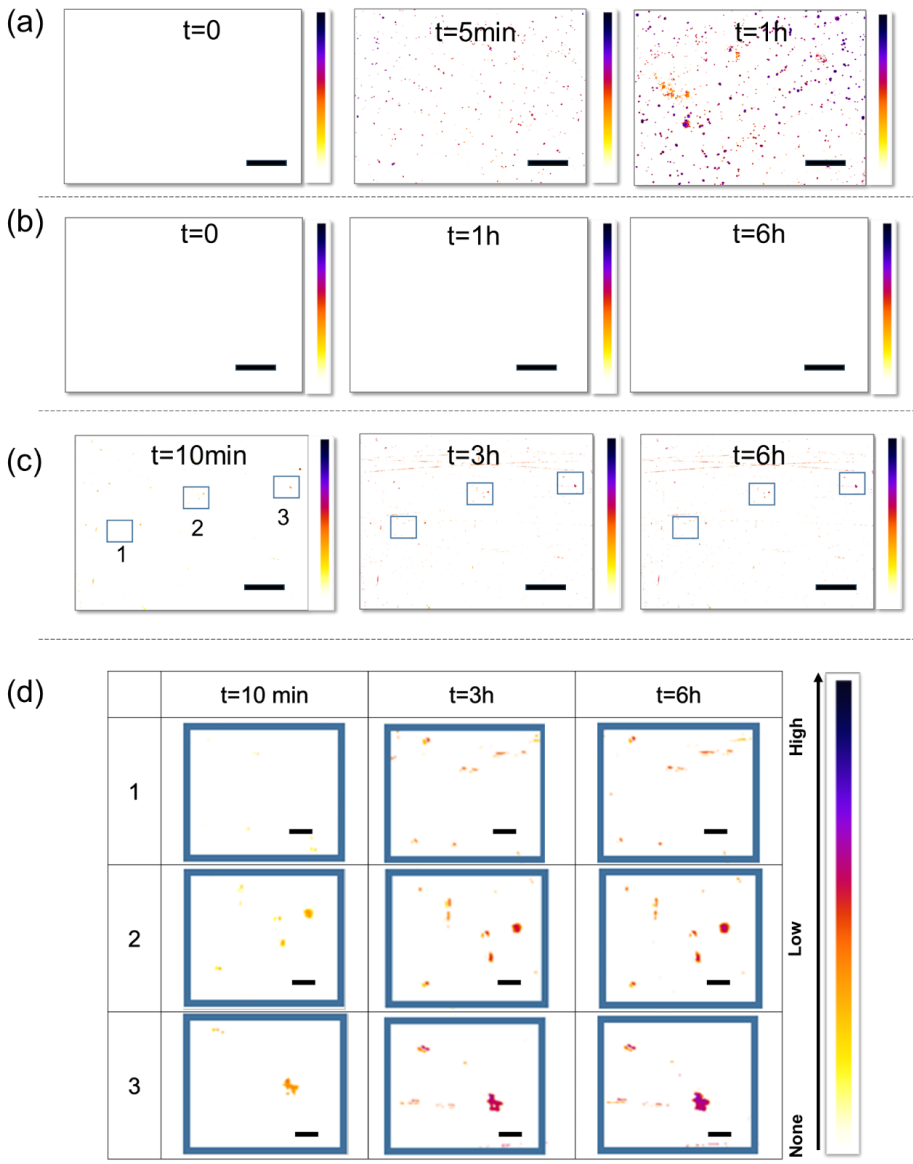


Figure 5.2 The activity maps at three characteristic times: (a) 1 h exposure in 0.05 M NaCl solution; (b) 6h exposure in 1 mM DMTD 0.05 M NaCl solution; and (c) 6 h exposure in 1 mM DMTD 0.5 M NaCl solution. No local activity is visible in Figure 5.2b, hence the absence of color in the white background. Scale bar on global activity maps: 100 µm. Sub-Figure (d) shows local activity maps of the three selected regions marked in Figure 5.2c for samples exposed for 6 h in 1 mM DMTD 0.5 M NaCl solution. Scale bars on local activity maps: 10 µm.

In order to elucidate if the low activity found at high NaCl concentrations is related to local corrosion (trenching or pitting) or other surface phenomena such as inhibitor deposition, an ex-situ SEM-EDS surface analysis was performed at the end of the exposure. As can be seen in Figure 5.3, no visible signs of corrosion attack are detected. This, together with the presence of

N and S at some S-phase and Al-Cu-Fe-Mn-Mg-Si IMs and the pH and EPN results suggest that the optically detected surface activity at high NaCl concentrations is most likely related to local matrix dissolution around IMs followed by deposition of DMTD at IM level. In order to better monitor and understand the level of interaction between DMTD and the Al matrix and IMs a detailed global XPS and Raman surface analysis of all samples was performed.

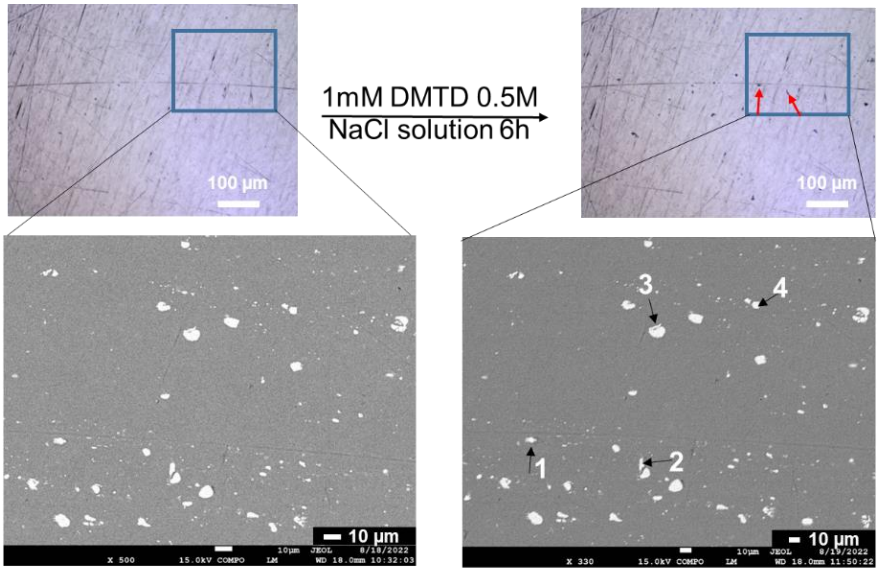


| Loc. | Al | Cu | Mg | Fe | Mn | O | S | N | Total | Possible IM type |
|---|---|---|---|---|---|---|---|---|---|---|
| 1 | 44.7 | 21.9 | 1.5 | 0 | 0 | 21.5 | 5.2 | 5.2 | 100 | S-phase |
| 2 | 50.8 | 20.6 | 4.8 | 1.4 | 0 | 15.0 | 3.4 | 3.5 | 100 | Al-Cu-Fe-Mn-Mg-Si |
| 3 | 52.2 | 25.0 | 22.4 | 0 | 0 | 0 | 0.4 | 0 | 100 | S-phase |
| 4 | 70.4 | 20.6 | 0 | 5.8 | 3.2 | 0 | 0 | 0 | 100 | Al-Cu-Fe-Mn-Mg-Si |

Figure 5.3 Ex-situ analysis of AA2024-T3 before and after exposure to 1 mM DMTD 0.5 M NaCl solution for 6 h.

In order to establish a relation between DMTD deposition and the presence of native oxide/hydroxide layer as function of NaCl concentration, an XPS study with a spot size of 400 µm was performed to the surfaces exposed to 1 mM DMTD solutions with 0 to 0.5 M NaCl. A polished AA2024 sample exposed to water was used as reference. Figure 5.4 shows the S2p and Al2p XPS spectra at different NaCl concentrations as well as relative composition ratios as function of NaCl concentration. The resolved spectra of Al2p, and the data reproducibility tests can be found in Supporting Information Figure S5.3. Figure 5.4a shows two peaks at binding energies (BEs) of 169.0 eV and 162.6 eV corresponding to sulfate and sulfide, respectively. [27-29] The presence of sulfide is in good agreement with the sulfur atoms originating from thiol/thiolate

groups in DMTD, likely in coordination with metal elements. We attribute the presence of sulfate on the surface to the local oxidation of thiol/thiolate groups into organic sulfur acids (sulfenic/sulfinic/sulfonic acids) during exposure to the corrosive solution, with the potential involvement of copper as a catalyst, as reported elsewhere for thiol-rich proteins. [30-33] This hypothesis requires more in-depth future analysis due to its potential effect in the overall corrosion inhibiting efficiency of organic corrosion inhibitors. All in all, XPS analysis confirms the presence of DMTD and oxidized DMTD on all the surfaces after exposure to electrolyte, rinsing and drying. Figure 5.4b shows the atomic ratio between 'DMTD' and 'Surface elements' (i.e. DMTD/Surface) as a way to quantify the relative DMTD presence on the surface as function of the NaCl concentration. As can be seen, higher relative DMTD is measured for the samples exposed to solutions with low concentrations of NaCl. Accordingly, the absence of NaCl or high concentrations of NaCl led to comparably lower amounts of DMTD at the surface. The Al2p spectrum shown in Figure 5.4c consisted of two components at binding energies around 75.0 and 73.0 eV, corresponding to Al (hydro)oxide and Al metal, respectively. [34, 35] The resolved Al2p peaks of all surfaces can be found in Supporting Information Figure S5.3. The shoulder at low binding energy (Al metal) of the spectrum shifts to the right with the increase of NaCl concentration, indicating less Al (hydro)oxide presence with higher NaCl concentration. As reference, the Al2p of the sample exposed to water without DMTD or NaCl does not show the Al2p shoulder corresponding to 'Al metal' and indicates there is a thicker (hydro)oxide in this sample. Figure 5.4d (and Supporting Information Figure S5.3-2) shows the atomic ratio of Al (hydro)oxide/Al metal and highlights a decreasing trend of (hydro)oxide with the NaCl concentration. The XPS results hence reveal the capability of DMTD (due to acidity increase) and NaCl to remove the native (hydro)oxide layer followed by DMTD deposition with or without oxidation. The observed trend is in good agreement with the EPN and pH evolution shown in Table 5.1 suggesting the dissolution of the native Al (hydro)oxide and its effect on an increased deposition of DMTD at the surface as previously suggested for other alloys[36-38] and other inhibitors e.g. MBT. [16, 17]

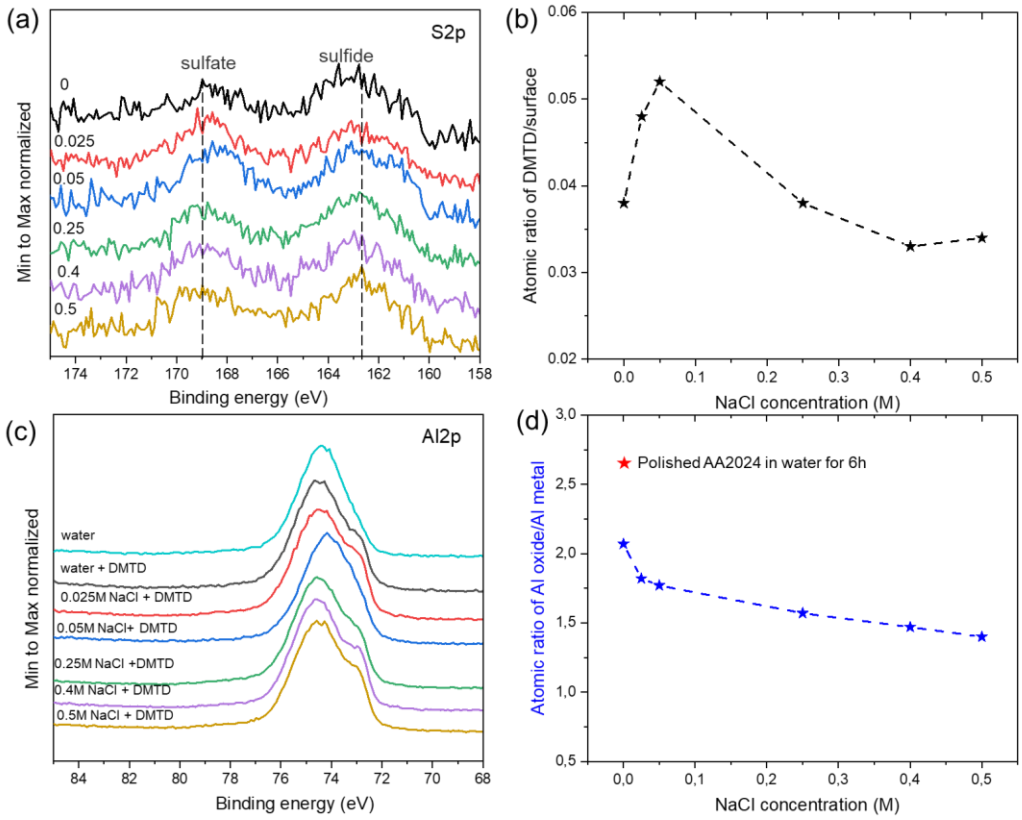


Figure 5.4 XPS spectra obtained from AA2024 surfaces exposed to water and 0 to 0.5 M NaCl in 1 mM DMTD solutions: (a) S2p; (b) DMTD/'surface elements' atomic molar ratio as function of NaCl; (c) Al2p; and (d) Al oxide/Al metal atomic ratio as function of NaCl. Note: in (d), the red star corresponds to the Al oxide/Al metal atomic ratio of a polished AA2024 surface exposed to water. Note: the atomic percentage of DMTD is determined by summing up the signals of N1s and S2p. The atomic percentage of the surface is calculated by summing up the signals of all metal elements and O1s.

In order to obtain more information about the DMTD-AA2024 interactions, Raman analysis was performed. Figure 5.5 shows the Raman spectra of all samples with a laser spot diameter of 50 µm. The three main characteristic vibration peaks related to DMTD[39] can be observed when analyzing DMTD powder and used to identify DMTD chemical state (Supporting Information Figure S5.4) on the AA2024 surface: (i) stretching vibration of S-H at 2485 $cm^{-1}$; (ii) C=N vibration at 1450 $cm^{-1}$ related to dithiol (in acidic pH), thiol-thiolate and thione-thiolate (in neutral pH) or dithiolate (in alkaline pH) states, and; (iii) C-NH vibration at 1510 $cm^{-1}$ related to thione-thiol and dithione (acidic pH) or thione-thiolate (in neutral pH) states. The presence of S-H broad peak and dominance of C=N over C-NH suggest a predominance in the powder DMTD of the dithiol with dithione presence. Although shifted to higher wavenumbers (peaks at ~1450 $cm^{-1}$ shift to ~1460 $cm^{-1}$, and ~1510 $cm^{-1}$ shift to ~1524 $cm^{-1}$) or lower ones (peak at ~2485 $cm^{-1}$ shift to ~2437 $cm^{-1}$) the three characteristic DMTD peaks are observed in all AA2024-T3 samples exposed to solutions containing DMTD. Similar to the XPS results, Raman analysis confirms the

presence of the inhibitor at the AA2024-T3 surface after exposure, rinsing and drying. The upward peak shifts of C=N (1450 to 1460 $cm^{-1}$) and C-NH (1510 to 1524 $cm^{-1}$) when DMTD is at the surface reveal a transfer of negative charge of the bonds to the surface and points at the presence of a molecule-surface electronic interaction stabilizing the bonds. The S-H bond, on the other hand, shifted to a lower wavenumber compared to the S-H bond in the powder DMTD (2485 to 2437 $cm^{-1}$). This suggests a weakening of the S-H bond (decrease in the stretching vibration frequency) here attributed to the formation of a strong hydrogen bonding between S-H from DMTD and O atoms from the oxides on the surface. The state of the DMTD at the surface can be inferred from a more detailed analysis. Unlike for the powder DMTD, the peak intensities of C=N and C-N is very comparable in all metal samples. This suggests DMTD is adsorbed on the metallic surface either in an equal ratio of dithiol and dithione or as thione-thiolate or/and, thione-thiol, as previously reported for the DMTD interaction with Au and Ag. [40] Moreover, a new peak at ~480 $cm^{-1}$ corresponding to Cu-S stretching vibration (Cu-sulfide and/or Cu-sulfate [41-43]) appears for the samples containing NaCl concentrations between 0.025 and 0.4 M. This peak is absent when samples were exposed to DMTD solutions containing no NaCl or very high NaCl concentration (0.5 M) and suggests absence of thiolate and its oxidation product chelation with Cu in these cases. Figure 5. 5b shows a quantification of the ratio between chemical and physical DMTD-surface interactions obtained from the Raman analysis. Herein, Raman intensity of Cu-S peak at ~480 $cm^{-1}$ was used to represent chemisorption. Physisorption on the other hand, is represented by the Raman intensity of C-NH (thione) + S-H (thiol) signals since, according to DMTD chemical states (Supporting Information Figure S5.4), C-NH bonds in DMTD appear only in presence of thione (NH-C=S) while C=N can be present with both thiolate ($N=C-S^-$) and thiol (N=S-H). The ratio of chemisorption to physisorption (i.e., the peak intensity of Cu-S divided by the sum of C-N and S-H) is then plotted as function of NaCl concentration (Figure 5.4b). As this Figure shows, the chemisorption of DMTD on the surface predominates in the NaCl concentration range of 0.025 M to 0.4 M, while lower chemisorption is measured when no NaCl or high NaCl amounts (0.5 M) were present in the DMTD solution. In summary, the global Raman analysis indicates that the DMTD equally physisorbs as dithione, dithiol and thione-thiol at the surface oxides of AA2024-T3 at all NaCl concentrations but reaches a more stable chemisorbed state through Cu-S chelation of thione-thiolate/thiol-thiolate/dithiolate and oxidized thiol/thiolate at low and mid NaCl concentrations.

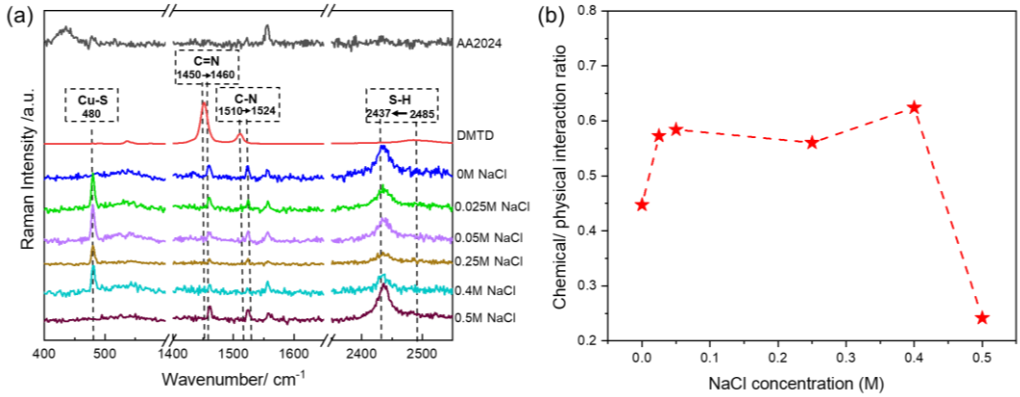


Figure 5.5 Global Raman analysis (a) showing from top to bottom: polished AA2024-T3, DMTD powder, and AA2024-T3 exposed to 1mM DMTD solutions containing 0, 0.025, 0.05, 0.25, 0.4 and 0.5 M NaCl; and (b) quantified chemical/physical interaction ratio from Raman peak intensity ratio of Cu-S/C-N+S-H.

In order to obtain specific local information about the interactions between DMTD and the AA2024-T3 local composition variations (i.e. IM composition) as function of NaCl concentrations, local Raman analysis was performed on a new set of samples. To this aim, a region with known local composition at IM level was defined with the help of SEM-EDS prior to exposure to 1 mM DMTD solution with 0.05 M NaCl. The IMs are grouped in two main IM types based on composition (Supporting Information Figure S5.5): (i) S-phase ($Al_2CuMg$), and; (ii) Al-Cu-Fe-Mn-Mg-Si. After SEM-EDS, the sample was slightly re-polished, exposed to the solution for 6h, rinsed with demineralized water, dried with pressurized air and finally analyzed with Raman. This allowed locating the IMs identified in SEM during the Raman study in order to correlate IM composition to DMTD local presence. Figure 5.6 shows the local Raman spectra and mappings of DMTD powder, polished AA2024-T3, and five locations of the AA2024 surface pre-exposed to the NaCl/DMTD solutions (named as: “on” and “around” S-phase, “on” and “around” Al-Cu-Fe-Mn-Mg-Si, and bulk Al matrix).

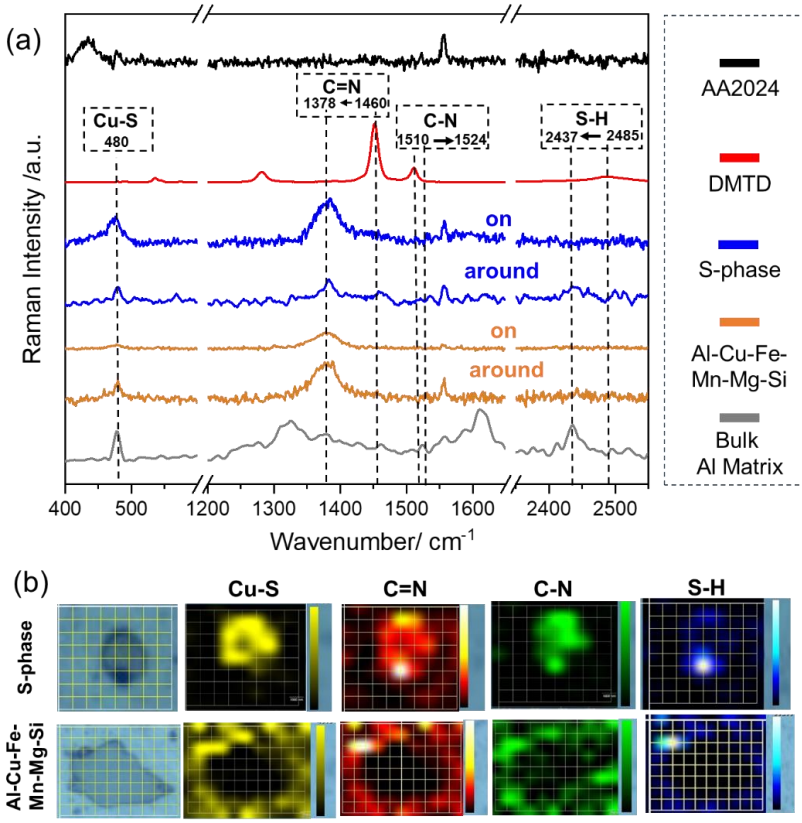


Figure 5.6 Raman local analysis of AA2024 pre-exposed to 1mM DMTD 0.05M NaCl solution: (a) point measurements on S-phase, around S-phase, on Al-Cu-Fe-Mn-Mg-Si, around Al-Cu-Fe-Mn-Mg-Si and at bulk Al matrix; (b) Raman mapping of S-phase and Al-Cu-Fe-Mn-Mg-Si. Mappings were obtained through point-by-point measurement, distance of each point is 1µm. After exposure, and for all samples, C=N bond at ~1460 $cm^{-1}$ shifted to ~1378 $cm^{-1}$, the C-N bond at ~1510 $cm^{-1}$ shifted to ~1524 $cm^{-1}$ and S-H bond at ~2485 $cm^{-1}$ shifted to ~2437 $cm^{-1}$ and a Cu-S bond appeared at 480 $cm^{-1}$.

In agreement with the global Raman analysis (Figure 5.5a), characteristic peaks for DMTD were found at all locations (Figure 5.6). Nevertheless, the state in which the DMTD interacts with the Al matrix and IMs is local-composition dependent. Similar to the DMTD powder, on and around both IM types there is a higher peak ratio of C=N than C-N, yet the C=N bond shifted to ~1378 $cm^{-1}$ and the C-N (mostly visible for the matrix locations) bond shifted to ~1524 $cm^{-1}$. This suggests electronic interaction of DMTD mostly as thiol-thiolate. A strong SH signal (~2485 $cm^{-1}$) is mostly detected at the matrix and around the IMs. This, together with the C=N signal, suggests DMTD mainly exists in the dithiol/thiol-thiolate forms on and around the S-phase and Al-Cu-Fe-Mn-Mg-Si intermetallic, with also dithiol, dithione and thiol-thione on the matrix. Besides this, a strong Cu-S vibration is detected at all locations but mostly at S-phase, around Al-Cu-Fe-Mn-Mg-Si and at the matrix (i.e., lower presence around S-phase or at the Al-Cu-Fe-Mn-Mg-Si). At S-phases, DMTD seems to preferentially chemisorb through Cu-S chelation with less chemisorption in the area surrounding the S-phase. Contrary to this, DMTD seems to preferentially chelate (Cu-S) around the Al-Cu-Fe-Mn-Mg-Si rather than on the Al-Cu-Fe-Mn-Mg-Si IM itself. The results confirm DMTD is not just interacting at S-phases, as previously

suggested, but all over the surface as a universal inhibitor even if with different interaction states. Preferred interaction is through Cu-S chelation at matrix and S-phases. Physisorption is present and dominant at Al-Cu-Fe-Mn-Mg-Si intermetallics.

*5.3.2 Re-exposure to non-inhibited NaCl solutions: stability of DMTD inhibiting layers*

The AA2024-T3 samples exposed to DMTD solutions at different NaCl concentrations were exposed, after rinsing and drying, to a non-inhibited 0.05 M NaCl solution (i.e., without DMTD) for 15h and monitored by the same optical-electrochemical setup as in section 5.3.1. Relevant results are shown in Table 5.2 with reproducibility tests in Supporting Information Table S5.2.

As seen in Table 5.2, at the end of the 15h re-exposure, all samples show EPN values comparable to that of the AA2024-T3 directly exposed to a non-inhibited solution of 0.05 M NaCl after 1h exposure (Table 5.1) even in the absence of signs of significant corrosion attack (max 5 %AA). The surface activity (%AA) of the samples that were pre-exposed to DMTD solutions containing 0.025 M to 0.25 M NaCl reached a surface activity below 0.5%AA within the first 1-2h of re-exposure that remained constant until the end of the re-exposure test (15h). This surface activity percentage is well below the IM surface area coverage of 1.6% reported earlier. The results suggest a high level of stability of the DMTD inhibiting layers and therefore high level of protection against corrosion under these conditions. On the other hand, samples pre-exposed to high NaCl concentrations (0.4-0.5 M) reached a surface activity of 4-5%AA at 15h re-exposure, even though the 0.4 M NaCl sample reached the maximum surface activity at 4h immersion as opposite to 0.5 M NaCl that kept increasing until ~10h exposure. Figure 5.5, shows that under the studied conditions using 0.4M NaCl solutions, DMTD chemisorption is the dominant surface interaction process. Nevertheless, the layers formed at such NaCl concentration are less stable than the ones formed at lower concentrations; hence the instability during reimmersion seen in optics and the lower DMTD concentration measured with XPS and comparable to samples pre-exposed to 0.5M NaCl. The exact NaCl concentration at which the formed inhibiting layer undergoes instability remains undetermined but expected to be somewhere above 0.25 and below 0.4M. Interestingly, samples exposed to DMTD solutions without NaCl apparently behave in a similar fashion (comparable %AA and EPN) to those pre-exposed to high NaCl concentrations (0.4 and 0.5M). This final area activity coverage is slightly higher than that observed for a sample exposed to 0.05 M NaCl for 1h showing high levels of local corrosion attack (3.3%AA, Table 5.1).

Table 5.2 Evolution of EPN and surface activity (Affected Area, %AA) of AA2024 pre-exposed to 1 mM DMTD solutions at different NaCl concentrations (0 to 0.5 M) and re-exposed to a non-inhibited 0.05 M NaCl solution for 15h. Last columns show extracted characteristic parameters (i.e. AA(%) final, EPN final)

| NaCl conc. (M) | | OCP and total Affected Area (AA in %) by optics | %AA | OCP(mV) |
|---|---|---|---|---|
| expo. | re-expo. | | | |
| 0 | 0.05 | 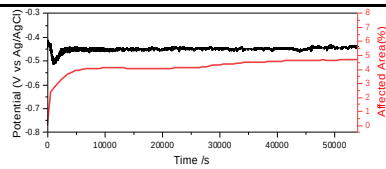 | -456 | 4.68 |
| 0.025 | 0.05 | 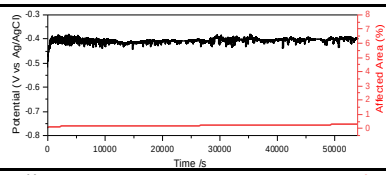 | -401 | 0.25 |
| 0.05 | 0.05 | 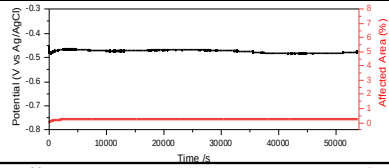 | -479 | 0.23 |
| 0.25 | 0.05 | 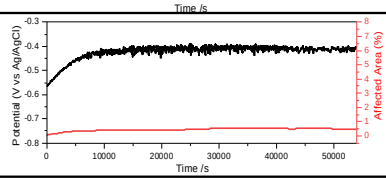 | -412 | 0.45 |
| 0.4 | 0.05 | 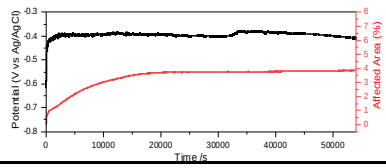 | -410 | 3.83 |
| 0.5 | 0.05 | 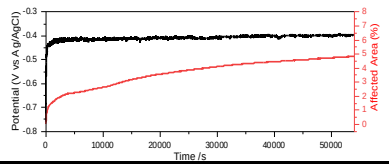 | -396 | 4.80 |

In order to identify the source of the surface activity during re-exposure, a detailed analysis of the activity maps and an ex-situ surface analysis after re-exposure was performed to three representative samples. Figure 5.7 to 9 shows the detailed analysis of the re-exposed samples as function of the NaCl concentration present during the first exposure to the inhibiting solutions: (i) 0.05 M NaCl as representative of limited %AA during re-exposure; and (ii) 0 and 0.5 M NaCl as representative of samples showing clear surface activity during re-exposure. The EPN and surface activity (%AA) plots and characteristic kinetic parameters are included in Figure 5.7. The underwater micrographs and activity maps are shown in Figure 5.8. The post-mortem SEM-EDX

analysis and global Raman analysis are shown in Figure 5.9 and Supporting Information Figure S5.6.

Samples that were exposed to DMTD solution without NaCl and then re-exposed to NaCl solution (Figure 5.7a) show a rapid surface change ($k_{r1}$=4E-3 $\%s^{-1}$) during the first 10 min re-exposure reaching a surface area coverage (2%) similar to that expected for IMs (1.6%). Interestingly, the kinetics of this first stage are similar to those attributed to initial de-alloying stage of AA2024-T3 in 0.05 M NaCl without inhibitors (2.4E-3 $\%s^{-1}$, (Figure 5.1a). This first optical activity is accompanied by an EPN drop, all in all suggesting localized processes at IM level. A second stage (10min to ~1h) shows a one order of magnitude decrease in optically detectable activity ($k_{r2}$=4E-4 $\%s^{-1}$) until a plateau at 3.5%AA. This is accompanied by an EPN increase until plateau at -450mV in a process with a high level of potential fluctuations (noise). According to the local activity maps in Figure 5.8a, the activity remains located at or around the IMs. The last stage observed during immersion (1h until 15h) shows a further slowing down of the optical activity kinetics ($k_{r3}$=2E-5 $\%s^{-1}$) till a plateau at 4.7%AA at ~3h with no further variation in EPN, both being signs of stabilization of the process with no further significant activity within this exposure time. At the end of the re-exposure time (15h) an SEM-EDX and Raman analysis was performed (Figure 5.9a). In spite of the detected optical activity during re-exposure, the post-mortem results (SEM) only revealed limited trenching around some IMs, mostly at S-phase. Raman analysis on the other hand shows the presence of physisorbed DMTD. The results suggest that the detected optical activity in combination with EPN trend and low amplitude potential noise is related to DMTD desorption/resorption and/or $Al(OH)_3$/$Al_2O_3$/Al-matrix dissolution processes in a dynamic process until a steady state is reached. This suggests the inhibiting layers formed in the absence of NaCl during the exposure step are unstable at IMs even though the maintained level of corrosion protection is significantly high (absence of signs of severe corrosion attack after 15h re-exposure).

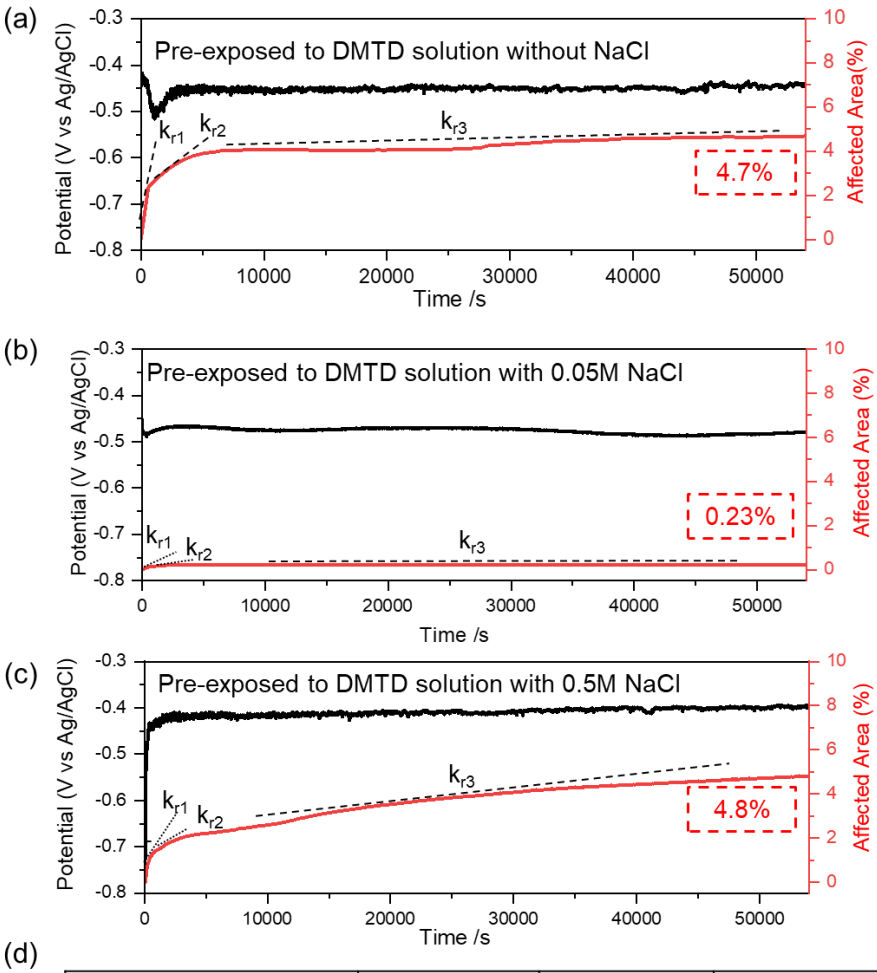


(d)

| Pre-exposed to | $k_{r1}$ (% $s^{-1}$) at 0 to 10 min | $k_{r2}$ (% $s^{-1}$) at 10 min to 1h | $k_{r3}$(% $s^{-1}$) at 1h to 15h |
|---|---|---|---|
| water with DMTD | 4E-3 | 4E-4 | 2E-5 |
| 0.05M NaCl with DMTD | 2E-4 | 3E-5 | 0 |
| 0.5M NaCl with DMTD | 2E-3 | 3E-4 | 5E-5 |

Figure 5.7 EPN and surface activity (%AA) plots, at three characteristic times for samples re-exposed to 0.05 M NaCl solution for 15h: (a) sample pre-exposed to 1mM DMTD solution without NaCl; (b) sample pre-exposed to 1 mM DMTD solution with 0.05 M NaCl; (c) sample pre-exposed to 1 mM DMTD solution with 0.5 M NaCl. And (d) AA% kinetic characteristic parameter of three samples. $k_{r1}$, $k_{r2}$ and $k_{r3}$ represent the %AA kinetics of the 3 time ranges: 0 to 10 min; 10 min to 1 h; and 1h to 15 h, respectively.

As represented in Figure 5.7b, the sample that was pre-exposed to low NaCl concentration shows very limited optical activity (0.23%). The local activity maps in Figure 5.8b reveal that the source of this minimal activity is located at a couple of IMs that activate during the first hour of re-exposure with surface activity kinetics dropping from $k_{r1}$=3E-5% $s^{-1}$ in the first stage to $k_{r2}\approx k_{r3}=0$

after 1h re-exposure. This initial optical activity stage is accompanied by an EPN increase until a maximum at around one hour until a plateau at -473mV. The EPN is relatively smooth accompanied by limited transients till the end of the re-exposure in the absence of optical activity and is here attributed to surface adsorption/desorption of DMTD molecules or/and local redox at the inhibiting layer. [44, 45] As shown in Figure 5.9b, the SEM analysis performed at the end of the re-exposure (15h) confirmed the absence of any corrosion signs. The Raman analysis on the other hand, revealed clear signals corresponding to Cu-S, C=N, C-N, and S-H vibrations. These vibration peaks are more evident than those revealed for the sample that was exposed to no NaCl during the inhibiting layer formation and suggest a stronger binding of the DMTD molecules to the metal surface in the sample exposed to small NaCl concentrations. This is in line with the findings reported in section 5.1 where low NaCl concentrations lead to higher amounts of DMTD at the alloy surface (Figure 5.5) with predominance of chemisorption-related bonds (Figure 5.6).

Samples that were pre-exposed to high NaCl concentrations (Figure 5.7c) show a similar optical activity to those pre-exposed to no NaCl (Figure 5.7a) with activity located at IM level (see local activity maps in Figure 5.8c) and with comparable optical activity kinetics at the different stages of re-exposure ($k_{r1}$=2E-3 $\%s^{-1}$, $k_{r2}$=3E-4 $\%s^{-1}$, $k_{r3}$=5E-5$\%s^{-1}$). In spite of some differences in the optical activity evolution, at the end of the re-exposure time the Affected Area (%) coverage is equally comparable (4.5%AA). The EPN shows an initial rapid increase until plateau with small potential noise transients but reaches steady state within 1h re-exposure. The post-mortem SEM-EDX analysis reveals that the detected surface activity is associated to trenching around some IMs mostly identified as S-phases but also Al-Cu-Fe-Mn-Mg-Si (Figure 5.9c and Supporting Information Figure 5.S6c). Moreover, the Raman analysis (Figure 5.9c) revealed the absence of strong signals related to DMTD adsorption after re-exposure. All in all, the results suggest the DMTD inhibiting layer formed in the presence of high NaCl concentrations are less stable than when the same layers are formed in the presence of small NaCl concentrations even if the level of corrosion protection achieved remains high and stabilizes after some hours of exposure (i.e., no significant activity progress after 10h re-exposure).

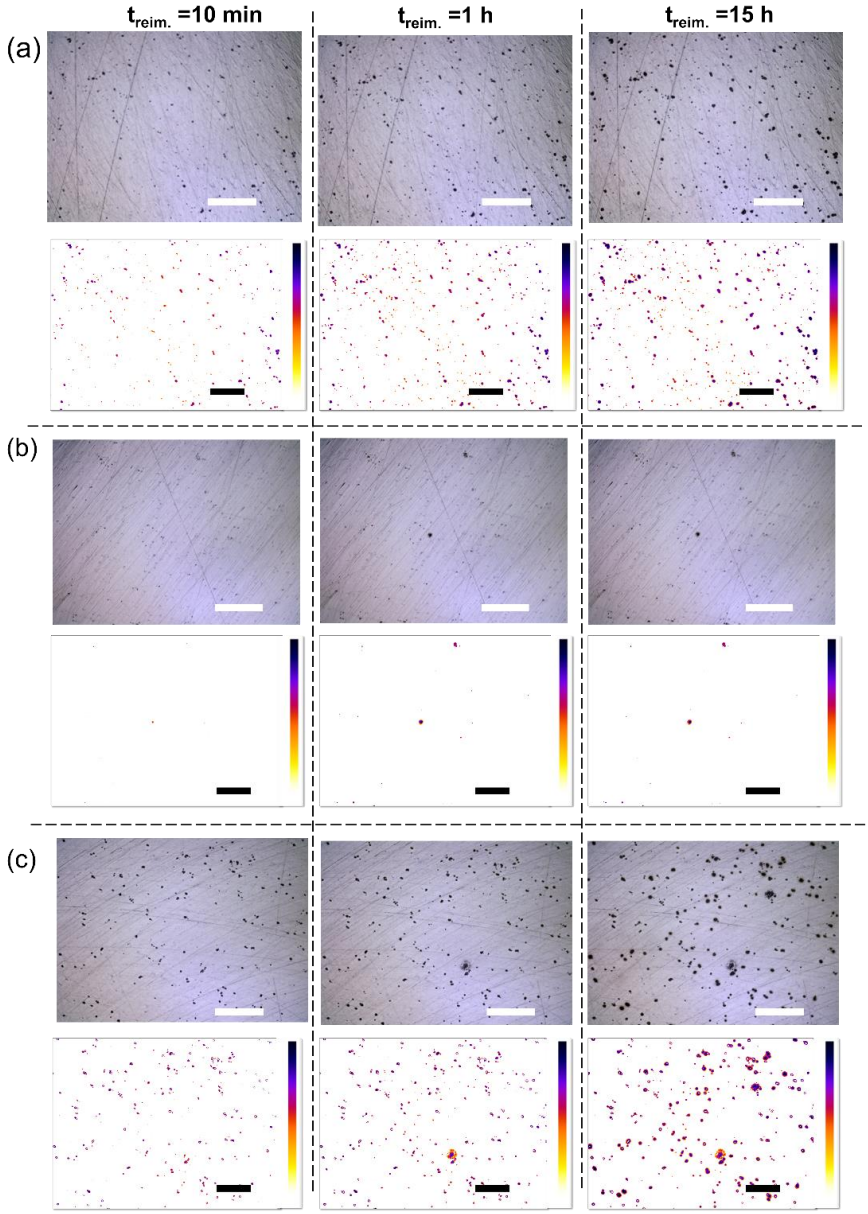


Figure 5.8 Underwater micrographs and Activity maps at three characteristic times for samples re-exposed to 0.05 M NaCl solution for 15h: (a) sample pre-exposed to 1mM DMTD solution without NaCl; (b) sample pre-exposed to 1 mM DMTD solution with 0.05 M NaCl; (c) sample pre-exposed to 1 mM DMTD solution with 0.5 M NaCl. Scale bar: 100µm

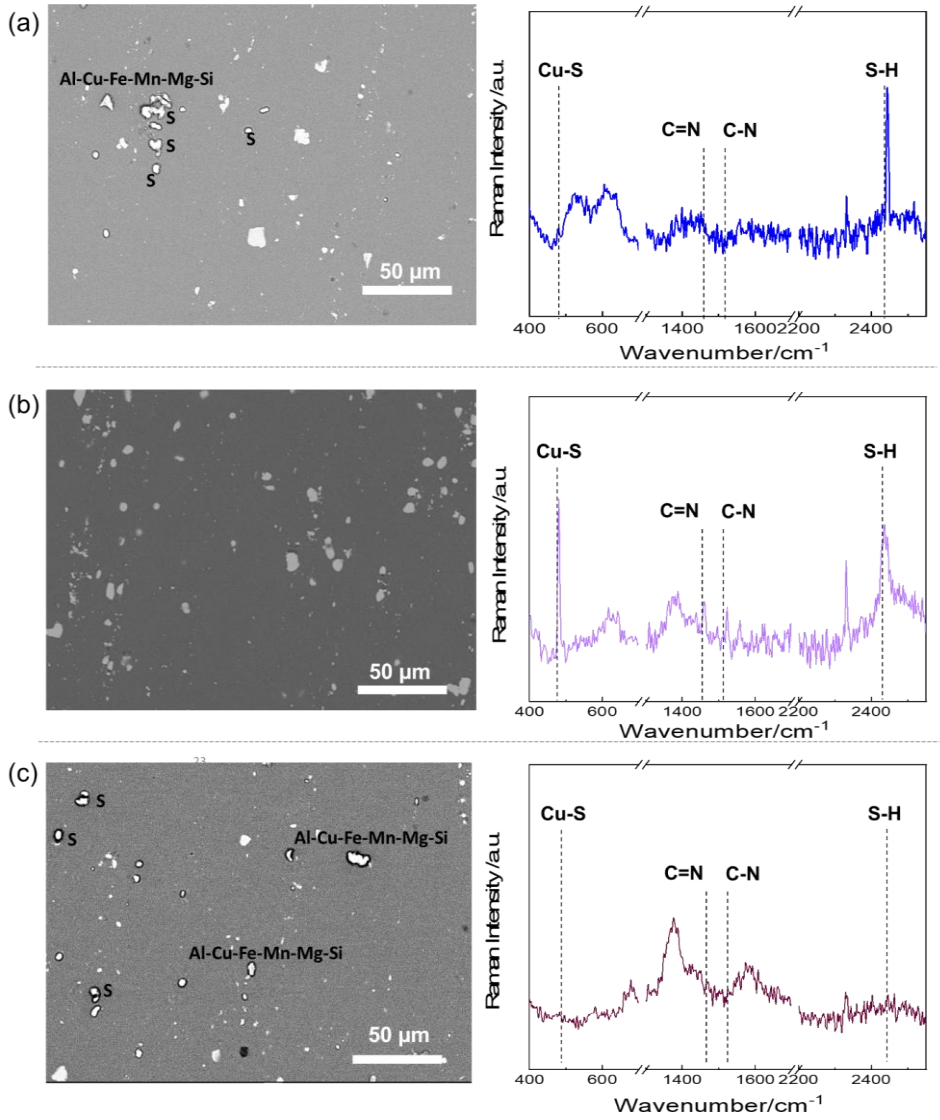


Figure 5.9 Post-mortem SEM micrographs and global Raman analysis of the samples re-exposed to 0.05 M NaCl solution for 15h: (a) sample pre-exposed to 1mM DMTD solution without NaCl; (b) sample pre-exposed to 1 mM DMTD solution with 0.05 M NaCl; (c) sample pre-exposed to 1 mM DMTD solution with 0.5 M NaCl.

### *5.3.3 Effect of NaCl on the formation and stability of inhibiting layers made from DMTD on AA2024-T3*

From sections 5.1 and 5.2 it becomes clear that NaCl concentration influences the formation of DMTD protective layers on AA2024-T3 as well as the stability of these layers in subsequent exposure to non-inhibited solutions. Figure 5.10 summarizes the proposed mechanism for the

formation and stability of DMTD inhibiting layers as function of the NaCl concentration present during exposure to the inhibitor, as discussed here below.

In the absence of NaCl (Figure 5.10a), DMTD is able to partially remove the native Al oxide/hydroxide layer due to its self-deprotonation and local acidity increase. The dissolution of the oxide layer is accompanied by the adsorption of $DMTD^-$ as measured by Raman. However, the presence of high O1s/Al2p ratios obtained from XPS analysis (Figure 5.4b), and the preferential physisorption of DMTD (thiol or thione state DMTD) suggest the negative influence of (hydr-)oxides in an efficient and strong adsorption of DMTD on the AA2024 surface microstructure.

When small concentrations of NaCl are present during exposure to DMTD-rich solutions (Figure 5.10b) the dissolution of $Al(OH)_3/Al_2O_3$ layer and/or the Al matrix is accelerated due to a combination of $Cl^-$ and acidic environment caused by the DMTD deprotonation (during 6h exposure: more negative EPN, negligible surface activity, slight pH increase consistent with a general decrease in total anodic area caused by Al matrix dissolution or/and an increase in IM sites). This process allows a more efficient deposition of stable DMTD on the surface predominantly through chemisorption (Figure 5.5b) combined with significant amounts of DMTD physisorption at some locations (Figure 5.4b). XPS (Figure 5.4) and Raman (Figure 5.5, Figure 5.6) showed that DMTD adsorbed all over the surface, mostly but not only as thiolate and/or organic sulfuric acid, through DMTD-Cu chelation in the preferential deposition S-phase>matrix≥ Al-Cu-Fe-Mn-Mg-Si.

As the NaCl concentration increased further, the amount of DMTD adsorbed at the surface decreased (Figure 5.4b), and physisorption took over chemisorption (Figure 5.5b). As shown in Figure 5.10c, the plummeted DMTD chemisorption in presence of high NaCl concentrations suggests a competition between $DMTD^-$ and $Cl^-$ adsorption and/or a too unstable surface due to adsorption and dissolution competing processes. Under these circumstances, negatively charged $Cl^-$ may accumulate closely to the metal/solution interface and restrain the efficient adsorption of $DMTD^-$, which is in agreement with previous studies on synergistic and competition effect of $Cl^-$ and inhibitor ions [47-49]. [11, 46, 47]

In all cases, and independently of the NaCl concentration, DMTD proves to form inhibiting layers able to stop the (local) corrosion processes during immersion even if the layers show local differences governed by local microstructure and different levels of inhibitor-metal adsorption, as represented in the second column in Figure 5.10.

During a re-exposure step to a 0.05M NaCl solution without DMTD, the formed inhibiting layers behave differently (last two columns in Figure 5.10). In general, the EPN values are within the corrosion potential of the AA2024 after IM dealloying and trenching initiation even though no significant corrosion attack (max 5 %AA) after 15h re-exposure (Table 5.2) is observed. This result confirms the high stability of all inhibiting layers formed in different NaCl concentrations. In spite of the general layer stability, clear differences are observed between them: the inhibiting layers created in presence of no NaCl and high NaCl concentrations are less stable showing some localized attack. This is attributed the predominance of physisorbed DMTD as opposite to chemisorbed related to an insufficient oxide/hydroxide layer dissolution and competition with high $Cl^-$ concentrations during exposure, respectively. During the early re-exposure time (<3h), DMTD desorption/resorption and dissolution of remaining oxide take place (third column, Figure

5.10) and lead to some minor trenching at IM sites (mainly at S-phase as shown in Figure 5.9a). The cessation of activity within 3h suggests the resorption of DMTD at some locations where the corrosion process initiated. Similarly, the samples that were exposed to high NaCl also undergo DMTD desorption/resorption process (Figure 5.10c) leading to some IM attack. This is attributed to the lower amount of DMTD present and the dominance of physical interaction with the surface. In spite of this, the local activity stabilized at ~10h (Figure 5.7c) thereby suggesting again a restoration of the inhibiting/protective layer (self-healing). Finally, the inhibiting layers formed at low NaCl concentrations (Figure 5.10b) exhibit high levels of stability during re-exposure (EPN and surface activity stabilizing within 1h in absence of local attack and with %AA<0.5%). The higher stability of the inhibiting layers formed in presence of small concentrations of NaCl is consistent with the strong and predominant chemisorption of DMTD on Al matrix and IM sites detected for these samples.

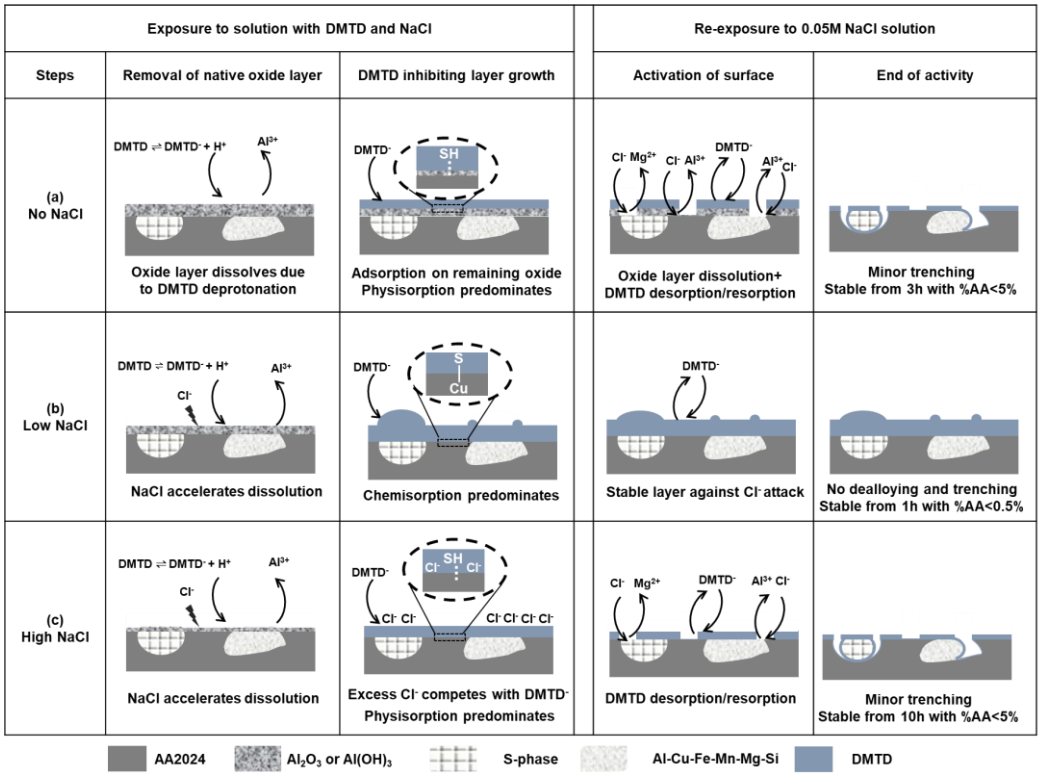


Figure 5.10 Proposed mechanism Proposed mechanism of DMTD inhibiting layer formation and stability during re-exposure when inhibiting layer is formed in presence of (a) no NaCl; (b) low NaCl; and (c) high NaCl.

## 5.4 Conclusions

The effect of NaCl concentration on the corrosion inhibition power of DMTD for AA2024-T3 and the formation of an inhibiting layer and its stability during subsequent exposure in non-inhibited solutions was studied. DMTD in small concentrations (1 mM) was found as an effective corrosion inhibitor during immersion even for high NaCl concentrations (up to 0.5 M) as seen with hyphenated optical-electrochemical test during exposure. XPS, optics and Raman showed that DMTD adsorption increases with the reduction of Al(hydro)oxide (which is more pronounced with higher NaCl concentrations). Dedicated local Raman surface analysis showed DMTD is present on all the metallurgical compositional features although with more DMTD present at S-phase and Al matrix than on secondary phases. Even if DMTD adsorption increases with NaCl the state of interaction varies with the NaCl concentration as revealed with Raman: chemisorption of DMTD through Cu-S chelation (thiolate and/or oxidized thiol/thiolate) was found to be more predominant at low NaCl concentrations than at no NaCl or high NaCl concentrations, for which physisorption through thiol and thione dominates. During re-exposure, all samples showed high levels of corrosion protection and therefore inhibiting layer stability. Nevertheless, higher levels of stability with total absence of local corrosion attack during re-exposure in non-inhibited NaCl solutions was observed for the samples in which the inhibiting layer was created in presence of small amounts of NaCl. This suggests that small amounts of NaCl and acidic pH (given by DMTD at 1mM) help building more stable and corrosion protective inhibiting layers, likely due to the improved equilibrium between dissolution of the oxide/hydroxide layer and the chemisorption of DMTD at available binding sites at the metal surface for thiolate DMTD chemisorption. The results here presented provide new insights in the protection mechanism of DMTD as a corrosion inhibitor for AA2024-T3. The detection of compositional variations of DMTD on the metal surface and the role of NaCl and acidity in the formation of stable inhibiting layers paves the way to investigate how to increase corrosion inhibition efficiency with organic inhibitors through the formation of more stable inhibiting layers and ultimately develop more efficient anticorrosive coatings.

## 5.5 References

(1) Yue, J.; Cao, Y. Corrosion prevention by applied coatings on aluminum alloys in corrosive environments. *International journal of electrochemical science* **2015**, *10* (7), 5222-5237.
(2) Montemor, M. F. Functional and smart coatings for corrosion protection: A review of recent advances. *Surface and Coatings Technology* **2014**, *258*, 17-37.
(3) Ulaeto, S. B.; Rajan, R.; Pancrecious, J. K.; Rajan, T.; Pai, B. Developments in smart anticorrosive coatings with multifunctional characteristics. *Progress in Organic Coatings* **2017**, *111*, 294-314.
(4) Denissen, P. J.; Garcia, S. J. Cerium-loaded algae exoskeletons for active corrosion protection of coated AA2024-T3. *Corrosion Science* **2017**, *128*, 164-175.
(5) Denissen, P. J.; Shkirskiy, V.; Volovitch, P.; Garcia, S. J. Corrosion inhibition at scribed locations in coated AA2024-T3 by cerium-and DMTD-loaded natural silica microparticles under continuous immersion and wet/dry cyclic exposure. *ACS applied materials & interfaces* **2020**, *12* (20), 23417-23431.
(6) Zadeh, M. A.; Tedim, J.; Zheludkevich, M.; van Der Zwaag, S.; Garcia, S. J. Synergetic active corrosion protection of AA2024-T3 by 2D-anionic and 3D-cationic nanocontainers loaded with Ce and mercaptobenzothiazole. *Corrosion Science* **2018**, *135*, 35-45.

(7) Yasakau, K. A.; Zheludkevich, M. L.; Lamaka, S. V.; Ferreira, M. G. Mechanism of corrosion inhibition of AA2024 by rare-earth compounds. *The Journal of Physical Chemistry B* **2006**, *110* (11), 5515-5528.
(8) Rodič, P.; Milošev, I. Corrosion inhibition of pure aluminium and alloys AA2024-T3 and AA7075-T6 by cerium (III) and cerium (IV) salts. *Journal of The Electrochemical Society* **2015**, *163* (3), C85.
(9) Zheludkevich, M.; Serra, R.; Montemor, M.; Yasakau, K.; Salvado, I. M.; Ferreira, M. Nanostructured sol–gel coatings doped with cerium nitrate as pre-treatments for AA2024-T3: corrosion protection performance. *Electrochimica Acta* **2005**, *51* (2), 208-217.
(10) Paussa, L.; Andreatta, F.; De Felicis, D.; Bemporad, E.; Fedrizzi, L. Investigation of AA2024-T3 surfaces modified by cerium compounds: a localized approach. *Corrosion science* **2014**, *78*, 215-222.
(11) Garcia, S.; Markley, T.; Mol, J.; Hughes, A. Unravelling the corrosion inhibition mechanisms of bi-functional inhibitors by EIS and SEM–EDS. *Corrosion Science* **2013**, *69*, 346-358.
(12) Homborg, A.; Olgiati, M.; Denissen, P.; Garcia, S. J. An integral non-intrusive electrochemical and in-situ optical technique for the study of the effectiveness of corrosion inhibition. *Electrochimica Acta* **2022**, *403*, 139619.
(13) Snihirova, D.; Lamaka, S.; Taheri, P.; Mol, J.; Montemor, M. Comparison of the synergistic effects of inhibitor mixtures tailored for enhanced corrosion protection of bare and coated AA2024-T3. *Surface and Coatings Technology* **2016**, *303*, 342-351.
(14) Denissen, P. J.; Garcia, S. J. Reducing subjectivity in EIS interpretation of corrosion and corrosion inhibition processes by in-situ optical analysis. *Electrochimica Acta* **2019**, *293*, 514-524.
(15) Khaled, K. Electrochemical investigation and modeling of corrosion inhibition of aluminum in molar nitric acid using some sulphur-containing amines. *Corrosion Science* **2010**, *52* (9), 2905-2916.
(16) Vernack, E.; Zanna, S.; Seyeux, A.; Costa, D.; Chiter, F.; Tingaut, P.; Marcus, P. ToF-SIMS, XPS and DFT study of the adsorption of 2-mercaptobenzothiazole on copper in neutral aqueous solution and corrosion protection in chloride solution. *Corrosion Science* **2023**, *210*, 110854.
(17) Vernack, E.; Costa, D.; Tingaut, P.; Marcus, P. DFT studies of 2-mercaptobenzothiazole and 2-mercaptobenzimidazole as corrosion inhibitors for copper. *Corrosion Science* **2020**, *174*, 108840.
(18) Goni, L. K.; Jafar Mazumder, M. A.; Quraishi, M.; Mizanur Rahman, M. Bioinspired heterocyclic compounds as corrosion inhibitors: a comprehensive review. *Chemistry–An Asian Journal* **2021**, *16* (11), 1324-1364.
(19) Awad, M.; Metwally, M.; Soliman, S.; El-Zomrawy, A. Experimental and quantum chemical studies of the effect of poly ethylene glycol as corrosion inhibitors of aluminum surface. *Journal of Industrial and Engineering Chemistry* **2014**, *20* (3), 796-808.
(20) Milošev, I.; Kokalj, A.; Poberžnik, M.; Carrière, C.; Zimerl, D.; Iskra, J.; Nemes, A.; Szabó, D.; Zanna, S.; Seyeux, A. The effects of perfluoroalkyl and alkyl backbone chains, spacers, and anchor groups on the performance of organic compounds as corrosion inhibitors for aluminum investigated using an integrative experimental-modeling approach. *Journal of The Electrochemical Society* **2021**, *168* (7), 071506.
(21) Williams, G.; Coleman, A. J.; McMurray, H. N. Inhibition of Aluminium Alloy AA2024-T3 pitting corrosion by copper complexing compounds. *Electrochimica Acta* **2010**, *55* (20), 5947-5958.
(22) Qafsaoui, W.; Et Taouil, A.; Kendig, M.; Heintz, O.; Cachet, H.; Joiret, S.; Takenouti, H. Corrosion protection of bronze using 2, 5-dimercapto-1, 3, 4-thiadiazole as organic inhibitor: spectroscopic and electrochemical investigations. *Journal of Applied Electrochemistry* **2019**, *49*, 823-837.
(23) Rahmani, H.; Meletis, E. I. Corrosion inhibition of brazing Cu-Ag alloy with 1, 2, 3-benzotriazole and 2, 5-dimercapto-1, 3, 4-thiadiazole. *Corrosion* **2021**, *77* (1), 29-39.
(24) Olgiati, M.; Denissen, P. J.; Garcia, S. J. When all intermetallics dealloy in AA2024-T3: Quantifying early stage intermetallic corrosion kinetics under immersion. *Corrosion Science* **2021**, *192*, 109836.
(25) Denissen, P. J.; Homborg, A. M.; Garcia, S. J. Interpreting electrochemical noise and monitoring local corrosion by means of highly resolved spatiotemporal real-time optics. *Journal of The Electrochemical Society* **2019**, *166* (11), C3275.
(26) Zhu, J.; Hihara, L. Corrosion of continuous alumina-fibre reinforced Al–2 wt.% Cu–T6 metal–matrix composite in 3.15 wt.% NaCl solution. *Corrosion Science* **2010**, *52* (2), 406-415.
(27) Castner, D. G.; Hinds, K.; Grainger, D. W. X-ray photoelectron spectroscopy sulfur 2p study of organic thiol and disulfide binding interactions with gold surfaces. *Langmuir* **1996**, *12* (21), 5083-5086.
(28) Wang, Y.-S.; Yau, S.; Chau, L.-K.; Mohamed, A.; Huang, C.-J. Functional biointerfaces based on mixed zwitterionic self-assembled monolayers for biosensing applications. *Langmuir* **2018**, *35* (5), 1652-1661.

(29) Madaan, N.; Romriell, N.; Tuscano, J.; Schlaad, H.; Linford, M. R. Introduction of thiol moieties, including their thiol–ene reactions and air oxidation, onto polyelectrolyte multilayer substrates. *Journal of colloid and interface science* **2015**, *459*, 199-205.
(30) Poole, L. B. The basics of thiols and cysteines in redox biology and chemistry. *Free Radical Biology and Medicine* **2015**, *80*, 148-157.
(31) Schilter, D. Thiol oxidation: A slippery slope. *Nature Reviews Chemistry* **2017**, *1* (2), 0013.
(32) Rigo, A.; Corazza, A.; di Paolo, M. L.; Rossetto, M.; Ugolini, R.; Scarpa, M. Interaction of copper with cysteine: stability of cuprous complexes and catalytic role of cupric ions in anaerobic thiol oxidation. *Journal of inorganic biochemistry* **2004**, *98* (9), 1495-1501.
(33) Falcone, E.; Ritacca, A. G.; Hager, S.; Schueffl, H.; Vileno, B.; El Khoury, Y.; Hellwig, P.; Kowol, C. R.; Heffeter, P.; Sicilia, E. Copper-catalyzed glutathione oxidation is accelerated by the anticancer thiosemicarbazone Dp44mT and further boosted at lower pH. *Journal of the American Chemical Society* **2022**, *144* (32), 14758-14768.
(34) Zhang, B.; Zhou, Q.; Ma, L.; Fan, X.; Xu, D. Advances in Materials Toward Anti-Corrosion and Anti-Biofoulings. Frontiers Media SA: 2022; Vol. 9, p 968100.
(35) Šekularac, G.; Kovač, J.; Milošev, I. Comparison of the Electrochemical Behaviour and Self-sealing of Zirconium Conversion Coatings Applied on Aluminium Alloys of series 1xxx to 7xxx. *Journal of The Electrochemical Society* **2020**, *167* (11), 111506.
(36) Dlouhy, M.; Kokalj, A. How adsorbed H, O, OH, and Cl affect plain adsorption of imidazole on copper. *Corrosion Science* **2022**, *205*, 110443.
(37) Kozlica, D. K.; Kokalj, A.; Milošev, I. Synergistic effect of 2-mercaptobenzimidazole and octylphosphonic acid as corrosion inhibitors for copper and aluminium–An electrochemical, XPS, FTIR and DFT study. *Corrosion Science* **2021**, *182*, 109082.
(38) Kozlica, D. K.; Ekar, J.; Kovač, J.; Milošev, I. Roles of chloride ions in the formation of corrosion protective films on copper. *Journal of The Electrochemical Society* **2021**, *168* (3), 031504.
(39) Huang, L.; Shen, J.; Ren, J.; Meng, Q.; Yu, T. The adsorption of 2, 5-dimer-capto-1, 3, 4-thiadiazole (DMTD) on copper surface and its binding behavior. *Chinese Science Bulletin* **2001**, *46*, 387-389.
(40) Maiti, N.; Chadha, R.; Das, A.; Kapoor, S. Surface selective binding of 2, 5-dimercapto-1, 3, 4-thiadiazole (DMTD) on silver and gold nanoparticles: a Raman and DFT study. *RSC advances* **2016**, *6* (67), 62529-62539.
(41) Cheng, Y.; Deng, S.; Sun, F.; Zhou, Y.-H. Synthesis of luminescent Cu9S5 nanoclusters from copper-2, 5-dimercapto-1, 3, 4-thiadiazole coordination polymer as pH sensor. *Journal of Luminescence* **2019**, *210*, 38-46.
(42) Andrew, C. R.; Yeom, H.; Valentine, J. S.; Karlsson, B. G.; van Pouderoyen, G.; Canters, G. W.; Loehr, T. M.; Sanders-Loehr, J.; Bonander, N. Raman spectroscopy as an indicator of Cu-S bond length in type 1 and type 2 copper cysteinate proteins. *Journal of the American Chemical Society* **1994**, *116* (25), 11489-11498.
(43) Martens, W.; Frost, R. L.; Kloprogge, J. T.; Williams, P. A. Raman spectroscopic study of the basic copper sulphates—implications for copper corrosion and 'bronze disease'. *Journal of Raman Spectroscopy* **2003**, *34* (2), 145-151.
(44) Markhali, B.; Naderi, R.; Mahdavian, M.; Sayebani, M.; Arman, S. Electrochemical impedance spectroscopy and electrochemical noise measurements as tools to evaluate corrosion inhibition of azole compounds on stainless steel in acidic media. *Corrosion Science* **2013**, *75*, 269-279.
(45) Ramezanzadeh, B.; Arman, S.; Mehdipour, M.; Markhali, B. Analysis of electrochemical noise (ECN) data in time and frequency domain for comparison corrosion inhibition of some azole compounds on Cu in 1.0 M H2SO4 solution. *Applied surface science* **2014**, *289*, 129-140.
(46) Li, X.; Deng, S.; Fu, H.; Xie, X. Synergistic inhibition effects of bamboo leaf extract/major components and iodide ion on the corrosion of steel in H3PO4 solution. *Corrosion Science* **2014**, *78*, 29-42.
(47) Fazayel, A.; Khorasani, M.; Sarabi, A. The effect of functionalized polycarboxylate structures as corrosion inhibitors in a simulated concrete pore solution. *Applied Surface Science* **2018**, *441*, 895-913.

# 5.6 Support information

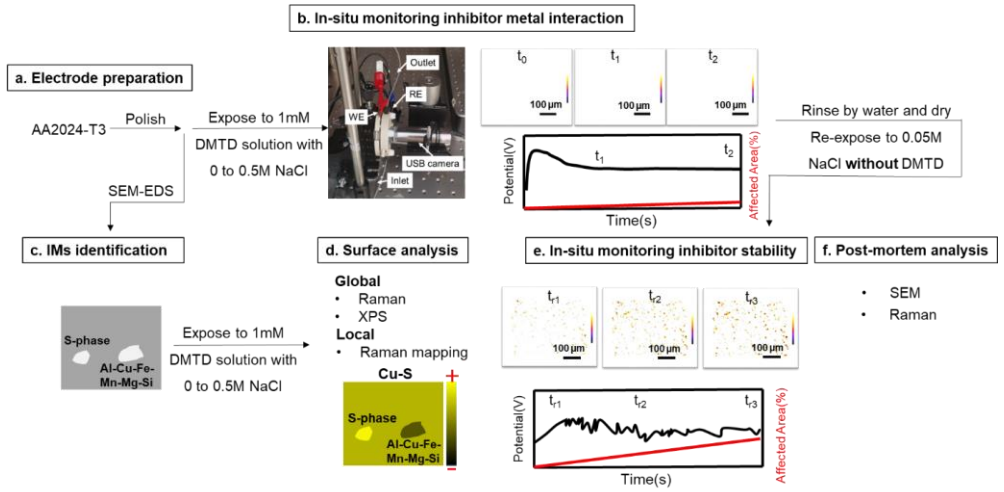


Figure S5.1 Procedure used to study inhibitor-metal interaction and layer stability. (a) Electrode preparation; (b) In situ monitoring of inhibitor-metal interaction and electrochemical and optical data analysis; (c) IMs identification; (d) surface analysis; (e) In situ monitoring inhibitor stability test in hyphenated opto-electrochemistry and electrochemical and optical data analysis; (f) Post-mortem analysis.

Table S5.1 Reproducibility results of exposure tests. OCP and AA% for 6 h exposure of AA2024-T3 in 1mM DMTD 0 to 0.5 M NaCl solution.

| Salt concentrations (M) | | OCP and total affected area (AA in %) by optics | OCP (mV) | %AA |
|---|---|---|---|---|
| NaCl | DMTD | | | |
| 0 | 0.001 | 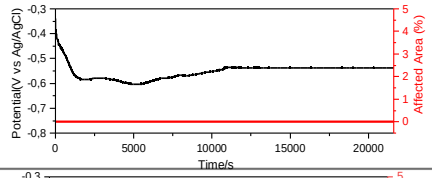 | -537 | 0.02 |
| 0.05 | 0.001 | 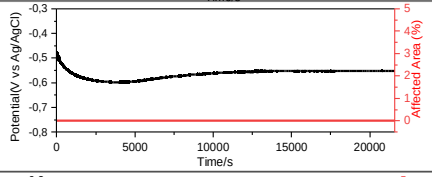 | -551 | 0.00 |
| 0.4 | 0.001 | 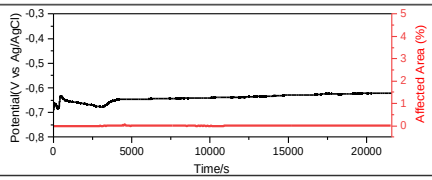 | -623 | 0.01 |
| 0.5 | 0.001 | 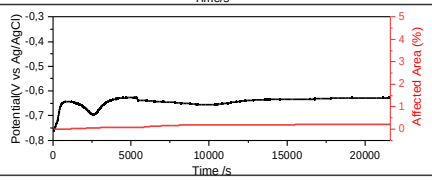 | -627 | 0.21 |



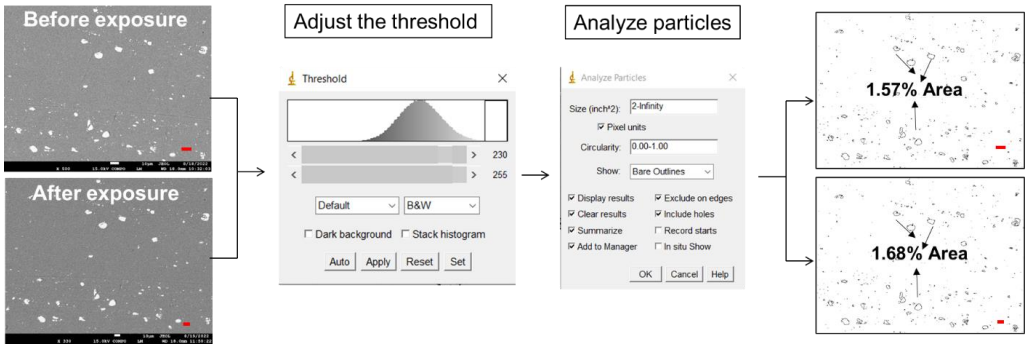


Figure S5.2 Protocol to calculate the area coverage (%) of IM on a AA2024 surface before and after exposure to 1mMDMTD 0.5M NaCl solution for 6h with Image J. Scale bar: 10µm.

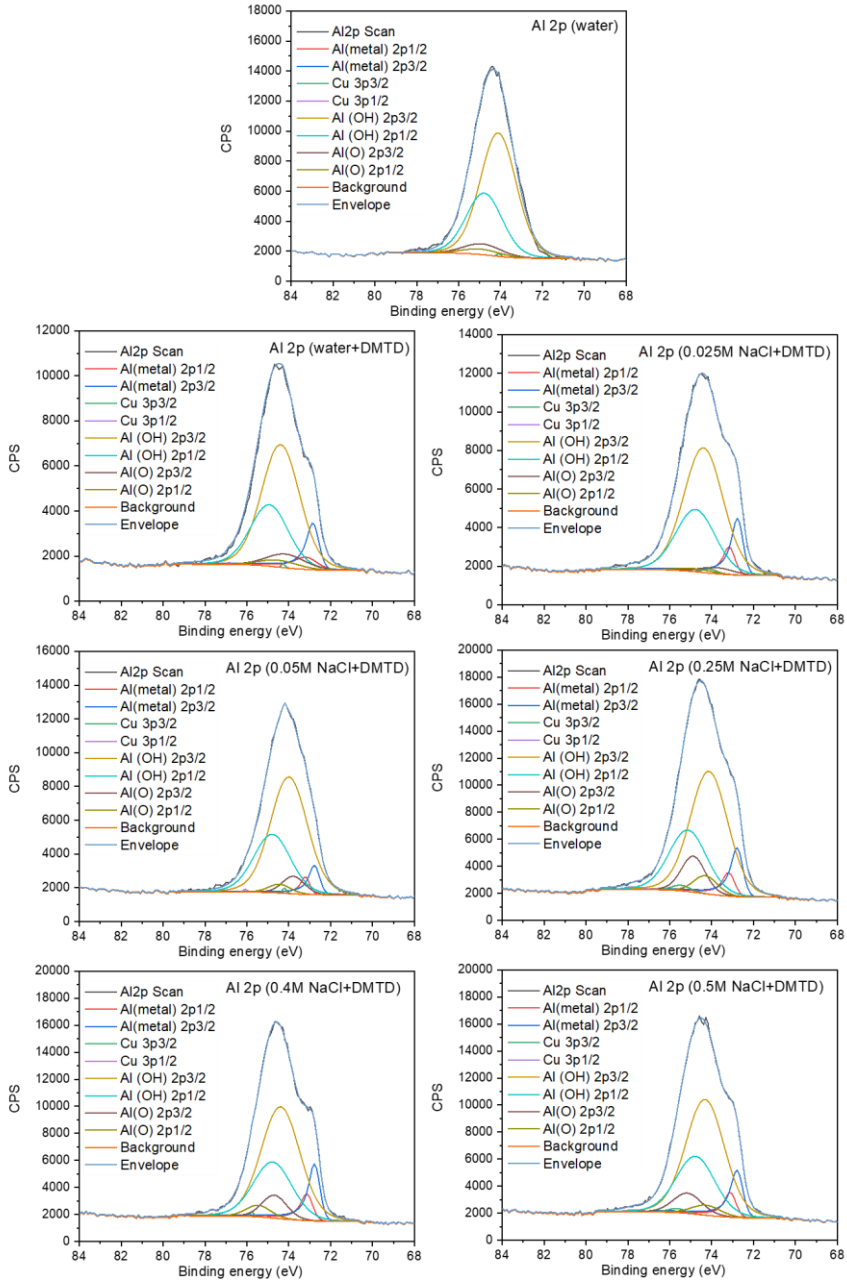


Figure S5.3-1 XPS spectra for resolved Al2p of samples exposed to water and 1mM DMTD solutions with different NaCl concentrations (0 to 0.5 M NaCl)

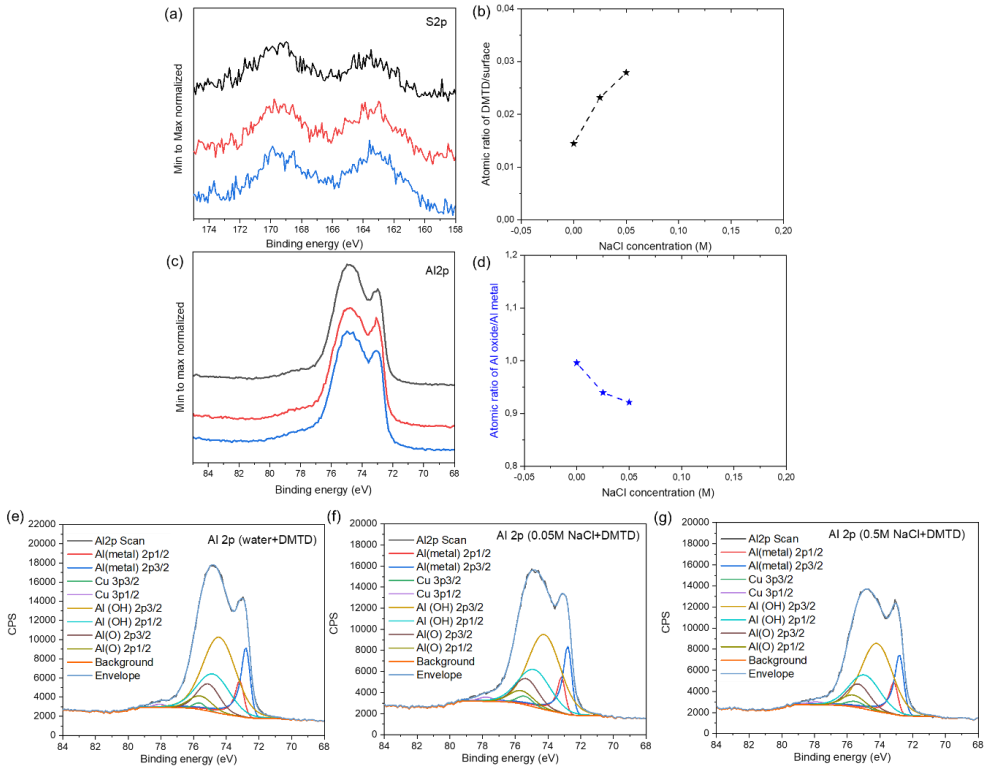


Figure S3-2 XPS spectra for (a) S2p, (b) DMTD/surface, (c) Al2p, (d) Al oxide/Al metal atomic ratio and (e-g) resolved Al2p peaks acquired from three repeating samples.

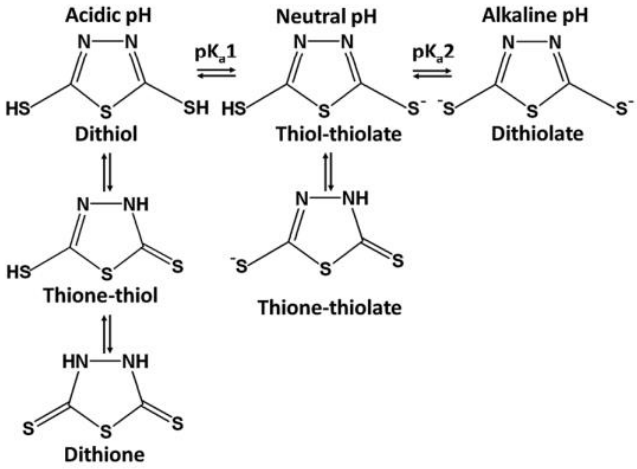


Figure S5.4 The proton dissociation equilibria of DMTD.[1]

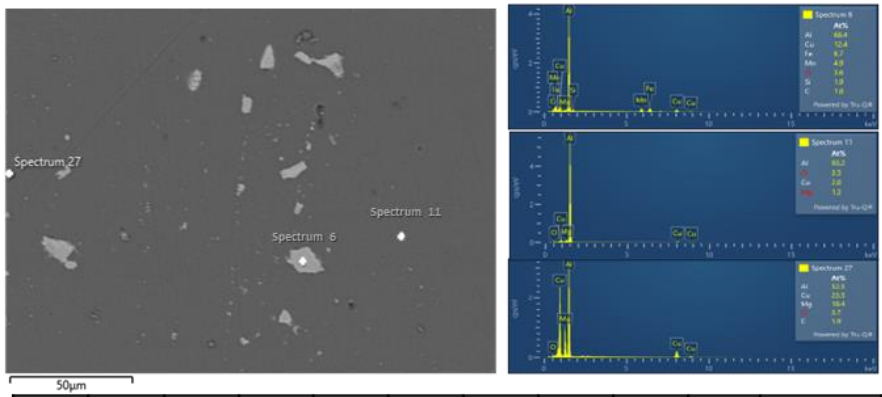


| Loc. | Al | Cu | Mg | Fe | Mn | O | Si | C | Tot al | Most likely IM type |
|---|---|---|---|---|---|---|---|---|---|---|
| 6 | 68.4 | 12.4 | - | 6.7 | 4.9 | 3.6 | 1.9 | 1.8 | 100 | Al-Cu-Fe-Mn-Mg-Si |
| 11 | 93.2 | 2.0 | 1.3 | - | - | 3.5 | - | - | 100 | matrix |
| 27 | 52.5 | 23.5 | 18.4 | - | - | 3.7 | - | 1.9 | 100 | S-phase |

Figure S5.5 SEM-EDS analysis before Raman local analysis

Table S5.2 Reproducibility results of re-exposure tests. OCP and AA% after 15h re-exposure to 0.05 M NaCl solution of AA2024-T3 samples previously exposed to solutions of 1mM DMTD without NaCl and with NaCl at 0.05 and 0.5M.

| NaCl conc. (M) | | OCP and total Affected Area (AA in %) by optics during re-exposure | OCP (mV) | AA (%) |
|---|---|---|---|---|
| expo. | re-expo. | | | |
| 0 | 0.05 | 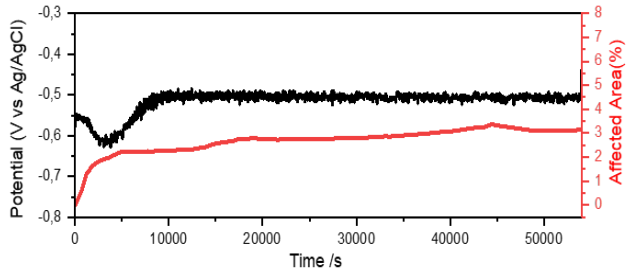 | -456 | 3.15 |
| 0.05 | 0.05 | 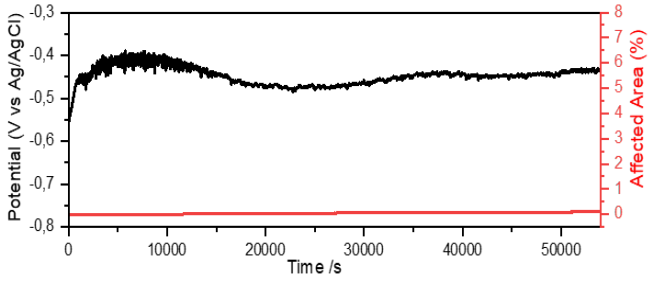 | -473 | 0.12 |
| 0.5 | 0.05 | 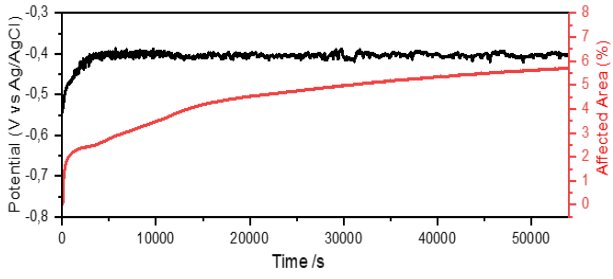 | -403 | 5.70 |

(a)

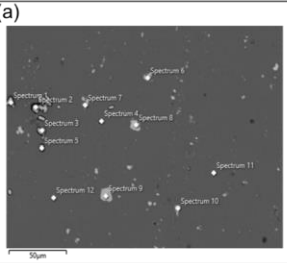

| Spectrum Label | N | O | Mg | Al | Si | S | Mn | Fe | Cu | Total | Possible IM type before exposure |
|---|---|---|---|---|---|---|---|---|---|---|---|
| Spectrum 1 | | 29.44 | | 29.16 | | 4.97 | 1.8 | 13.8 | 20.83 | 100 | |
| Spectrum 2 | 8.59 | 15.22 | | 7.82 | | 12.44 | | | 55.93 | 100 | |
| Spectrum 3 | 9.98 | 14.78 | | 29.64 | | 11.8 | | | 33.8 | 100 | |
| Spectrum 4 | | 15.73 | | 44.67 | | 9.17 | | | 30.42 | 100 | |
| Spectrum 5 | | 17.84 | | 21 | | 12.5 | | | 48.66 | 100 | |
| Spectrum 6 | | | | 64.18 | 1.44 | | 6.44 | 15.87 | 12.06 | 100 | |
| Spectrum 7 | | | | 63.35 | 1.44 | | 6.54 | 16.37 | 12.3 | 100 | |
| Spectrum 8 | | 2.2 | | 62.78 | | | 2.54 | 12.56 | 19.92 | 100 | |
| Spectrum 9 | | | | 65.28 | 1.96 | | 6.41 | 16.35 | 9.99 | 100 | |
| Spectrum 10 | | | | 64.56 | 2.42 | | 6.65 | 15.35 | 11.02 | 100 | |
| Spectrum 11 | | 2.92 | 1.22 | 93.74 | | | | | 2.12 | 100 | |
| Spectrum 12 | | 2.55 | 1.55 | 93.82 | | | | | 2.08 | 100 | |

(b)

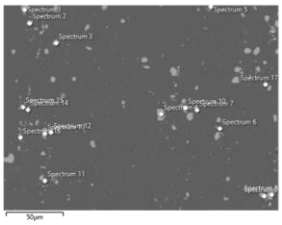

| Spectrum Label | C | O | Mg | Al | Si | Mn | Fe | Cu | Total | Possible IM type before exposure |
|---|---|---|---|---|---|---|---|---|---|---|
| Spectrum 1 | | 1.11 | 15.16 | 33.79 | 0.20 | 0.18 | 0.00 | 49.56 | 100 | |
| Spectrum 2 | | 1.08 | 14.93 | 33.97 | 0.11 | 0.00 | 0.00 | 49.91 | 100 | |
| Spectrum 3 | 10.18 | 0.76 | 12.91 | 29.78 | 0.16 | 0.10 | 0.00 | 46.09 | 100 | |
| Spectrum 4 | 7.75 | 1.08 | 13.30 | 30.57 | 0.13 | 0.00 | 0.07 | 47.10 | 100 | |
| Spectrum 5 | 7.53 | 0.98 | 11.85 | 32.00 | 0.16 | 0.31 | 0.39 | 46.78 | 100 | |
| Spectrum 6 | 12.81 | 2.55 | 1.19 | 75.14 | 0.00 | 0.13 | 0.64 | 7.53 | 100 | |
| Spectrum 7 | | 1.73 | 11.38 | 45.48 | 0.11 | 0.22 | 0.47 | 40.61 | 100 | |
| Spectrum 8 | 7.11 | 0.82 | 13.89 | 30.57 | 0.13 | 0.00 | 0.25 | 47.22 | 100 | |
| Spectrum 9 | 8.16 | 1.20 | 13.30 | 32.34 | 0.05 | 0.10 | 0.00 | 44.85 | 100 | |
| Spectrum 10 | | 0.73 | 12.39 | 43.42 | 0.24 | 0.00 | 0.48 | 42.74 | 100 | |
| Spectrum 11 | 9.63 | 1.45 | 8.40 | 37.81 | 0.13 | 0.50 | 1.93 | 40.15 | 100 | |
| Spectrum 12 | | 1.88 | 0.30 | 53.76 | 0.22 | 3.68 | 6.54 | 33.61 | 100 | |
| Spectrum 13 | | 2.39 | 14.94 | 33.75 | 0.09 | 0.00 | 0.52 | 48.31 | 100 | |
| Spectrum 14 | | 1.67 | 0.93 | 79.11 | 0.42 | 2.99 | 1.79 | 13.09 | 100 | |
| Spectrum 15 | | 1.83 | 0.54 | 58.16 | 0.15 | 3.61 | 5.00 | 27.18 | 100 | |
| Spectrum 16 | | 1.95 | 0.77 | 66.02 | 0.17 | 2.37 | 5.04 | 23.68 | 100 | |
| Spectrum 17 | | 1.87 | 0.73 | 72.36 | 0.10 | 1.74 | 3.28 | 19.92 | 100 | |

(c)

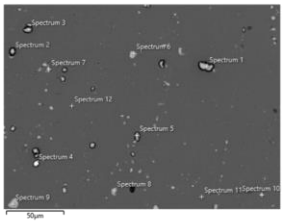

| Spectrum Label | N | O | Mg | Al | Si | S | Cl | Mn | Fe | Cu | Total | Possible IM type before exposure |
|---|---|---|---|---|---|---|---|---|---|---|---|---|
| Spectrum 1 | 8.75 | 28.21 | | 8.97 | 1.02 | 11.82 | 1.06 | 0.84 | 1.16 | 38.18 | 100 | |
| Spectrum 2 | | 26.4 | | 16.89 | | 9.63 | | | | 47.07 | 100 | |
| Spectrum 3 | 8.24 | 23.63 | | 11.64 | | 10.7 | | | | 45.8 | 100 | |
| Spectrum 4 | | 29.37 | | 23.48 | | 3.47 | 0.5 | | | 43.17 | 100 | |
| Spectrum 5 | | 35.15 | | 28.45 | 1.08 | 4.72 | | 1.75 | 12.29 | 16.55 | 100 | |
| Spectrum 6 | | 2.31 | | 63.97 | 1.94 | | | 6.23 | 14.77 | 10.78 | 100 | |
| Spectrum 7 | | 5.44 | | 64.99 | | | | | | 29.58 | 100 | |
| Spectrum 8 | | 2.65 | | 76.87 | 1.45 | | | 4.33 | 8.31 | 6.39 | 100 | |
| Spectrum 9 | | 2.9 | | 64.67 | 1.99 | | | 6.6 | 13.96 | 9.88 | 100 | |
| Spectrum 10 | | 3.32 | | 66.95 | | | | | | 29.74 | 100 | |
| Spectrum 11 | | 3.53 | 1.31 | 93.18 | | | | | | 1.98 | 100 | |
| Spectrum 12 | | 2.98 | 1.8 | 92.82 | | | | 0.53 | | 1.87 | 100 | |

matrix S-phase Al-Cu-Fe-Mn-Mg-Si

Figure S5.6 Post-mortem SEM-EDS analysis after 15h re-exposure to 0.05 M NaCl solution of AA2024-T3 samples previously exposed to solutions of 1mM DMTD without NaCl (a) and with NaCl at 0.05 (b) and 0.5M (c).

## References

(1) Maiti, N.; Chadha, R.; Das, A.; Kapoor, S. Surface selective binding of 2, 5-dimercapto-1, 3, 4-thiadiazole (DMTD) on silver and gold nanoparticles: a Raman and DFT study. *RSC advances* **2016**, *6* (67), 62529-62539.

# Chapter 6

# Gas-Phase Deposited Nanolayers Guard Organic Microparticles in Polymer Matrices for Active Corrosion Protection at Damages

*The most common way to protect metallic structures from corrosion is through the use of passive and active corrosion protection with coatings containing dispersed corrosion inhibitor particles. Current approaches use inorganic microparticles containing mostly toxic and/or critical elements (e.g. CrVI, Li-salts). Organic inhibitors have been identified as a potential replacement technology due to their high inhibiting efficiency in solution, high versatility and lower toxicity. Nevertheless, when brought into organic coatings these inhibitors lose their efficiency due to unwanted side reactions with the surrounding organic matrix (coating). In this work we propose a novel strategy to isolate the organic corrosion inhibitor microparticles from the surrounding matrix. The new approach is based on the gas-deposition of an oxide nanolayer on the microparticles using gas deposition in a fluidized bed reactor. As a result, the organic particles are better dispersed in the coating and do not react with the surrounding matrix. Upon coating damage the particles are exposed to water and release sufficiently high amounts of the organic corrosion inhibitor at the damaged location. The work introduces a technique that can be used in other applications with similar challenges and a new technology that enables for the first time to store large amounts of active organic corrosion inhibitors in reactive organic coatings for efficient protection of metallic infrastructure. This opens the path to the practical use of highly efficient organic inhibitors in coatings for corrosion protection.*

This Chapter has been published as:

*Zhao, J.; van Ommen, J. R.; Garcia, S. J. Gas-phase deposited nanolayers guard organic microparticles in polymer matrices for active corrosion protection at damages. Progress in Organic Coatings 2024, 192, 108522.*

# 6.1 Introduction

The need to replace highly toxic corrosion inhibitors in coatings has become widely acknowledged, representing a complex and multi-dimensional challenge. Organic corrosion inhibitor complexes and salts such as 2,5-Dimercapto-1,3,4-thiadiazole (DMTD) are considered promising alternatives to toxic Cr(VI)-based inhibitor salts and Lithium and Rare Earth salt alternatives because of their comparable intrinsic corrosion inhibition efficiency in solution, surface stability, reduced environmental impact, low molecular weight and design versatility. [1, 2] Unfortunately, the efficient incorporation of organic inhibitors in organic coatings in sufficiently large amounts and without unwanted inhibitor-polymer matrix reactions has been so far largely elusive. As a result of matrix-inhibitor reactions, the coating properties are negatively affected and/or the inhibitors cannot be released from the coating to protect the underlying metal from corrosion, hence resulting in underperformance. [3, 4] The hygroscopic, powder state and highly reactive nature of most good performing organic inhibitors limit the use of emulsion encapsulation techniques used in liquid encapsulation for self-healing coatings. [5] Alternative encapsulation strategies using nano[6-8] or micro[9-11] inorganic particles as carriers have been proposed and shown to be successful up to a certain point. These approaches allow the introduction of relatively low amounts of organic inhibitors in coatings and control their release by different mechanisms such as water dissolution and diffusion, pH or ion exchange but offer limited amounts of inhibitor locally. [10] In this work, we introduce the use of gas-phase deposition in a fluidized bed as a new strategy to embed large amounts of unreacted corrosion inhibitor microparticles in organic coatings through the use of a protective thin metal oxide nano-layer.

Gas-phase deposition methods such as (pulsed) chemical vapor deposition (CVD) and atomic layer deposition (ALD) are used to create non-selective homogeneous nanometer-thick (oxide) layers on flat, porous and regular substrates used mostly in electronic devices. [12-14] The introduction of gas-phase deposition in fluidized beds has recently allowed extrapolating the concept of thin layer deposition to microparticles relevant for the pharmaceutical sector. In particular, layers of $Al_2O_3$, $TiO_2$ and $SiO_2$ have been applied as nanoscale thin films on organic drug particles via atomic layer deposition in fluidized bed reactors in order to control the particle dissolution rate in solution. [15-19] Besides controlling the drug release kinetics, such nanolayers on drug microparticles have been used to tune the surface chemistry to improve their dispersibility, flowability, and stability. [18-21] Organic corrosion inhibitors, share some properties with drug microparticles regarding moisture sensitivity (hygroscopic, solubility), and adhesive and cohesive character, but also tend to have more irregular shapes and broad particle size distributions affecting the local surface energy levels relevant to initiate gas-phase deposition. These factors leading to reduced flowing, increased agglomeration and formation of irregular layers increase the challenge in gas-phase fluidized bed deposition on reactive particles such as corrosion inhibitors and make developments non-obvious. Moreover, corrosion inhibitors are to be dispersed in organic matrices in an isolated form to prevent minimal negative side reactions but at the same time remain accessible to water ingress so that the inhibitors can be dissolved, transported and released rapidly at sufficiently large quantities from the coating (within 30 seconds for the case of aerospace alloys as AA2024-T3) [22] and sustained in time in order to protect the underlying metallic structure from corrosion and ultimate mechanical failure. This work

explores for the first time these aspects using gas-phase deposition in the context of anticorrosive coatings.

To proof the concept, we use pulsed gas-phase deposition in a fluidized bed to deposit a $TiO_x$ nanoscale layer on a selected model organic inhibitor (2,5-dimercapto-1,3,4-thiadiazole, DMTD) at 40°C and atmospheric pressure (1 bar). The modified organic inhibitor particles are then incorporated in a solvent borne epoxy-amine coating and applied on an aerospace-grade aluminum alloy AA2024-T3 to test corrosion performance. The fluidized bed reactor provides good mixing between gas and solid phases, which benefits depositing a conformal titanium oxide layer. The deposition layer was studied by transmission electron microscopy (TEM), X-ray photoelectron spectroscopy (XPS) and in-situ ultraviolet-visible spectroscopy (UV-vis). The effect of the titanium oxide layer on the interaction between DMTD and epoxy-amine matrix was studied by thermogravimetric analysis (TGA), differential scanning calorimetry (DSC) and release kinetics using ex-situ UV-Vis. The impact of the nanolayer formed around DMTD microparticles on the active corrosion protection at damaged coatings (1mm diameter damages) was evaluated under wet/dry cyclic exposure using in-situ highly resolved image reflectometry with image correlation and electrochemical potential noise measurements. The results allow presenting gas-phase deposition in a fluidized bed as a promising strategy to efficiently introduce large amounts of very reactive organic corrosion inhibitors in coatings and opens the path to the use of so far elusive functional chemicals in coatings and other polymeric matrices.

# 6.2 Experimental

*6.2.1 Materials*

2,5-dimercapto-1,3,4-thiadiazole (DMTD >99%) particles were purchased from Sigma-Aldrich and used as substrates for the deposition. The precursor, titanium tetrachloride ($TiCl_4$) was purchased from Strem Chemicals and used as received. The demineralized water was used as a co-reactant with $TiCl_4$. Commercial grade bare 2.5mm thick AA2024-T3 were cut into 10cm x 10cm pieces and used as metal substrates for coatings. Commercially available bisphenol-A based epoxy resin (Epikote™ 828) and amine crosslinker (Ancamine®2500) were supplied by AkzoNobel (NL) and used as-received to form the coating binder using xylene (99 %) as solvent. Sodium chloride (NaCl, >98%) was purchased from VWR Chemicals. Milipore® filtered water was employed in all steps requiring water.

*6.2.2 Gas-phase deposition experiments*

The gas-phase deposition experiments were carried out in a vibrated fluidized-bed reactor operating at atmospheric pressure, as has been described in previous works. [16, 17, 19] DMTD powders were prepared by hand-milling and sieving under 120 µm. Before deposition, a fluidization test on DMTD particles was applied. $N_2$ (99.999 v/v%) was used as the carrier and purging gas. As a result, it was found that a maximum of 10 g DMTD (around 1/10 bed height) could be well-fluidized under 5 L/min nitrogen flow on a vibration table. Based on the fluidization test and the experience of earlier works [16, 17], it was decided to use 0.5 L/min of precursor and co-reactant vapor with 4.5 L/min of nitrogen to keep the constant gas velocity in the whole reactor. Prior to the injection and fluidization of the DMTD, the reactor was heated up to 40 °C and kept at constant with the help of a heating jacket wrapped around the glass column. The precursor, $TiCl_4$, and the co-reactant, $H_2O$, stored in bubblers were fed to the reactor through separate inlet tubing. The stainless-steel tubing that connects the bubblers to the reactor was maintained at 30°C above the bubblers at room temperature to prevent the precursor from condensing. The deposition process consisted of sequential exposures of the DMTD to $TiCl_4$ for 45s, 5 min purging with only nitrogen gas, and $H_2O$ for 60s (one cycle) followed by another 5 min nitrogen gas purging step prior to the next cycle of exposure to precursor and co-reactant. The exposure time to $TiCl_4$ and $H_2O$ were chosen based on the experience of earlier works using also cohesive but nano-sized particles, allowing sufficient exposure time. [16, 17] The purge time of 5 min allows for any excess reactants or by-products to be cleared from the system before a subsequent cycle begins. The reaction: $TiCl_4 + H_2O \rightarrow TiO_x + HCl$ allowed for the deposition of a Ti oxide layer on the DMTD microparticles. The by-product, HCl, was neutralized by 1% NaOH solution in the wash bottle connected to the outlet of the reactor. The gas-phase depositions of $TiO_x$ were run for 20, 30, 40, 50, and 60 cycles. To get an impression of the effect of the fluidization on the particle size distribution, a test was performed doing 20 cycles without precursor and co-reactant.

*6.2.3 Particles characterization*

The images of the gas-phase deposited DMTD particles were taken by Keyence Laser Scanning Confocal Microscope and used to evaluate the particle size distribution with the ImageJ software, according to the following protocol: (1) Calibrating the image scales (pixels->microns) in Image J by the function of "setting scale"; (2) The threshold of each image is adjusted (150 to 255); (3) The particles are analyzed by the function of "Analyze particles", to give the area of each particle; (4) All the particles are assumed as circles to get the diameters; (5) Finally, we plot the histogram of all the diameters to get the particle size distribution. The presence of the deposition layer on DMTD was assessed by transmission electron microscopy (TEM) and X-ray photoelectron

spectroscopy (XPS). In TEM, the samples were dispersed in Hexane and drop cast into a C foil supported with a Cu grid. The particles were very beam sensitive so only low magnification (~100kx) could be used. The XPS was equipped with a monochromatic Al anode X-ray source with a spot size of 400 µm. The photo-electrons are detected by a 128-channel detector, with a 0.1 eV resolution. For survey spectra, the pass energy and step size were set to 140 eV and 0.40 eV respectively. High-resolution spectra were obtained with 50 eV pass energy and 0.1 eV resolution. All spectra were calibrated by assigning the true energy value (284.8 eV) corresponding to the position of a C 1s peak. The dissolution kinetics of DMTD/$TiO_x$ particles in real time was studied with a PerkinElmer LAMBDA 35 UV/VIS spectrometer operated at a constant wavelength representative of the DMTD inhibitor presence in NaCl solution (i.e., 328nm). This allowed a scan rate of one measurement per second during the 2 h duration of the release tests. A calibration curve made with DMTD solutions (see supporting information Figure S6.1) was used to convert absorption intensity of the representative wavelength to inhibitor concentration in solution. To this aim the powders (inhibitors) were placed inside a Whatman® grade 1 paper filter on top of a UV cuvette filled with 0.05M NaCl solution. As seen in Fig S1.b, release of the inhibitor was captured short after immersion as a result of inhibitor dissolution. In order to ensure an even DMTD dispersion in the cuvette and to avoid false measurements the solution was constantly magnetically stirred at 1600 rpm.

*6.2.4 Coatings preparation*

The 2.5 mm thick AA2024-T3 metal sheets were cut into pieces of 100x100 mm prior to surface cleaning and coating application. The surface cleaning consists of the following steps: (1) removal of the native oxide layer and surface roughness formation by Scotch Brite 3M; (2) degreasing with acetone;(3) pseudo-boehmite treatment on the coupons to increase the amount of reactive hydroxyl groups on the surface by 10 s immersion in 2 M NaOH followed by a 30 s immersion in distilled water and drying with nitrogen.

Three different coating compositions are prepared as listed in Table 6.1. Different inhibitor pigments are added to the identical coating binder formulation. The coatings formulation is given as a function of epoxy resin (phr=parts per hundred epoxy resin in weight). Briefly, Epikote™ 828, Ancamine®2500 and xylene (weight ratio 2.70:1.57:1.06) were mixed for 5 min in a high-speed mixer at 2500 rpm and pre-cure at room temperature for 15 min. After adding the inhibitor pigments, the coating formulation was manually stirred and applied onto the Teflon sheets for thermal analysis and metal coupons for release and corrosion tests using a doctor blade with a wet thickness of 100 µm. After a flash-off period of 30 min the coatings were cured at 60°C for 24h. The samples were stored in a desiccator before the following tests.

Table 6.1 Coatings formulations as a function of Epikote™ 828 (phr=parts per hundred epoxy resin in weight), and the calculated inhibiting active component in wt% of the total coating dry weight and pigment volume concentration (PVC%) of inhibitor pigment. The weight of $TiO_x$ was ignored.

| Sample Name | Inhibitor pigment | Inhibitor (phr) | Inhibiting active component (wt.%) | PVC (%) | Dry coating thickness (µm) |
|---|---|---|---|---|---|
| Epoxy | - | 0 | 0 | 0 | 68±3 |
| Epoxy-DMTD | DMTD | 25 | 13.7 | 10 | 70±3 |
| Epoxy-DMTD/$TiO_x$ | DMTD/$TiO_x$ 20 cycles | 25 | 13.7 | 10 | 70±3 |

*6.2.5 Thermal analysis*

The coatings applied on Teflon sheets were separated by a spatula and used for thermal analysis. The thermal degradation of the coatings as a function of adding different inhibitor pigments was analyzed by Thermogravimetric analysis (TGA). The TGA tests were conducted from 30 ºC to 600 ºC at a rate of 10 ºC/min under nitrogen gas with a flow rate of 20 mL/min. Differential scanning calorimetry (DSC) analyses were performed to investigate the $TiO_x$ layer influence on the cross-linking density of the epoxy/amine coating systems. DSC tests were carried out via a TA Instr. Modulated DSC under nitrogen flow. Each sample was heated at a temperature range from -10 ºC to 80 ºC at a heating rate of 10ºC/min. The DSC provides information on the glass transition temperature ($T_g$) of the coatings.

*6.2.6 Inhibitor release tests from coatings*

The coating systems with DMTD and DMTD/$TiO_x$ applied on AA2024-T3 in Table 6.1 were surface ground by 1000-grit paper during 15s, followed by exposure to 40mL 0.05M NaCl solution. This allowed direct exposure of the particles to the electrolyte by removing the top polymeric thin layer on the coating. The diameter of the circular exposed ground area is 1cm. Samples of 3 mL were collected at different time points (1, 5, 15, 30, 60, 120, 240, 360, 1440, 2880, and 4320 min) and put back after each measurement to maintain a constant volume of release medium. The aliquots were tested in a UV-Vis spectrometer using a wavelength range from 700 nm to 200 nm. The absorbance at characteristic peak location of 328nm was used to obtain the inhibitor concentration using the calibration curve in Supporting information Figure S6.1.

*6.2.7 Wet/dry cyclic exposure tests*

A Roland EGX-350 engraver equipped with an end mill carbide tip of 1mm in diameter was used to create circular damage on the coated panel surface prior to immersion in electrolyte for the corrosion studies. Drills of 1mm wide and 0.25mm deep (i.e. well into the metallic substrate) with respect to the coated surface were created without delamination. The resulting chips from the engraved zone were removed by air blowing. The corrosion was evaluated with an in-situ optical electrochemical set-up as we described in previous works. [10, 22] The scribed coating sample was mounted in a magnetic Raman electrochemical flow cell from Redox.me. This cell allows a

total electrolyte volume of 4.5 ml and the use of a small Ag/AgCl (3 M KCl) reference electrode. The electrochemical cell was placed vertically in a Faraday cage on an optical table from ThorLabs to avoid any electromagnetic and vibrational disturbances. The EPN signals are recorded with an Ivium Compactstat controlled by IviumSoft V2.86. The maximum range of the potentiometer was set at ±1 V vs Ag/AgCl. The interval time between data points was set to 0.05 s (sampling frequency of 20 Hz) combined with a low-pass filter of 10 Hz. A Dino-Lite digital microscope was placed at the window side of the electrochemical cell. This allows obtaining high-resolution images every minute during exposure simultaneously to the Electrochemical potential noise (EPN) measurements as a function of the exposure time. Due to the 8-led ring light type of the microscope and the high roughness of the damage left by the engraver, the lightness of the images is not even on the damage (shadow can be seen). To eliminate the shadow, a coaxial light cap was equipped. The shadow was still not completely removed but mostly avoided. This will be further improved in future works. The electrolyte (0.05M NaCl solution) was injected through side openings allowing the capturing of optical and electrochemical information right after exposure to the electrolyte. The optical analysis was conducted in ImageJ software as described in earlier works. [10, 22] The technique is based on a pixel-by-pixel analysis of the progression of surface activity on the region of interest (ROI) over time. Images were converted to grey scale at an 8-bit resolution allowing the definition of 256 different levels of intensity between black and white. For both the exposed metal surface, i.e., damage and the surrounding coating, a static thresholding bin limit of 10 was used due to the small intensity changes.

The wet/dry cyclic exposure tests were performed to study the active corrosion protection by inhibitors released from the coating to the scribed site under discontinuous immersion conditions. The tests consist of a process of 2h exposure of damaged coating in 0.05M NaCl solution and monitored by the above optical-electrochemical set-up. And then, the coating was taken out followed by gentle flashing in demineralized water, dry in $N_2$, and placed in an ambient environment for 1h. The coating was put back into the same set-up and started over the new cycles. In total, we performed 1 cycle on Epoxy coating without inhibitors, 3 cycles on Epoxy-DMTD coating and 3 cycles on Epoxy-DMTD/$TiO_x$ coating. After each cycle, the solutions were collected and used to obtain the inhibitor concentration in the same manner as explained in 2.6. The concentrations of DMTD released from a coating without damage were also measured under the same conditions of exposure. To calculate the amount of DMTD released specifically due to the damage, the amount released from the damaged coating was subtracted from the amount that could have been released from the same area of the intact coating.

# 6.3 Results and discussion

*6.3.1 Gas-phase deposition of protective nanolayer on organic inhibitor microparticles*

Figure 6.1a shows the negative effect of organic corrosion inhibitor microparticles (2,5-dimercapto-1,3,4-thiadiazole, DMTD) directly added into a chemically reactive epoxy-amine polymer network. In such polymers, the crosslinking process proceeds through nucleophilic attack of the amine on the oxirane groups leading to ring opening and a reticulated (crosslinked) polymer network. [23, 24] In this environment, the thiol groups (-SH) in the DMTD organic molecule are deprotonated by the base amino groups to create highly nucleophilic thiolates (-S-) able to ring open the oxirane groups and disturb the crosslinking process through the formation of linear chains. [25] Such side chemical reactions ultimately affect the polymer properties (e.g. glass-transition temperature, Young's Modulus, Stress at break, adhesion) but also the release potential of the corrosion inhibitors at damaged locations upon exposure to a corrosive electrolyte (e.g. NaCl solution). To prevent this negative reaction a $TiO_x$ (titanium oxide) nanolayer was deposited on the microparticles using a pulsed-chemical vapor deposition (CVD) process in a sequential approach as done in atomic layer deposition (ALD) processes. Figure 6.1b shows a schematic of the CVD process in a fluidized bed reactor used in this work as explained in the Experimental section and Supporting Information in detail. In this process, the particles are fluidized ("floating") in $N_2$ and the chemical reactants are sequentially added to the fluidized particles with the $N_2$ flow. For the proof of concept shown in this work, $TiCl_4$ was used as the precursor to create the nanolayer. The precursor was chosen in order to obtain a nanolayer (i.e. $TiO_x$) able to first impede the reaction with the surrounding polymer matrix but then allow for inhibitor release through solubility in water. As the TEM-EDX images in Figure 6.1b show, when 20 cycles were used, a $TiO_x$ nanolayer of 20 to 30 nm was deposited on the surface of the organic microparticle. The immediate positive effect of the protective nanolayer (20 cycles) on the DMTD microparticles compatibility with the epoxy-amine polymer matrix can be seen in Figure 6.1c, where the nanolayer led to an improved degree of particle dispersion as seen by the absence of the agglomerates visible in Figure 6.1a, and the uniform orange-like coloration associated with DMTD microparticles.

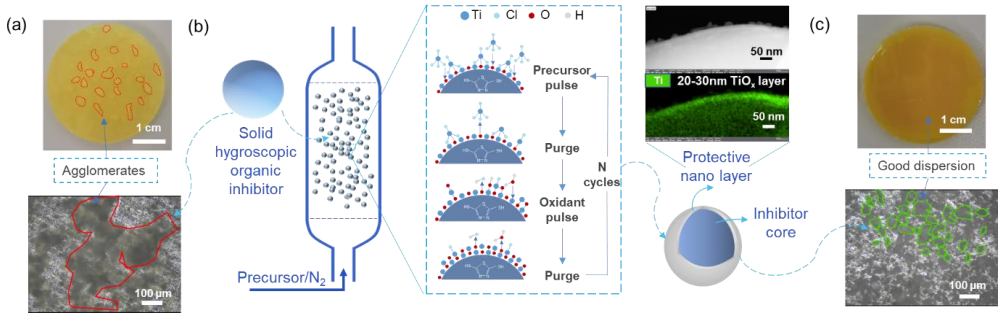


Figure 6.1. (a) Micrographs show the poor dispersion of the organic (DMTD) microparticles in an organic (epoxy-amine) polymer network. The red lines in the micrographs indicate locations of inhibitor agglomerates resulting from the reaction between the organic particle and the surrounding matrix; (b) Schematic illustration of the gas-phase deposition process of a protective nanolayer on organic corrosion inhibitor microparticles in a fluidized bed reactor. Image inserts show TEM-EDX images of a 20-30nm $TiO_x$ nanolayer deposited on an organic corrosion inhibitor particle after 20 cycles; (c) Micrographs show how a deposited nanolayer around the organic particles improves the dispersion quality of the particles in an organic polymer network. The green lines in the bottom micrograph indicate the locations of some inhibitor particles.

Figure 6.2 shows TEM-EDX mappings of DMTD/$TiO_x$ particles, the presence of $TiO_x$ layers on DMTD surface and Ti atomic percentage increasing with deposition cycles. The TEM-EDX images show the efficient deposition of a 20-30 nm $TiO_x$ layer on the inhibitor microparticle (identified with the S marker) after 20 cycles. This suggests the nanolayers were formed through a chemical vapor deposition (CVD) process rather than atomic layer deposition (ALD) despite an alternating supply of the gas phase reactants with $N_2$ purging in between was used instead of continuous reactant supply without purge. As a result of a non-optimized process, the fluidized bed reactor was operated at low temperature, which allows excess amounts of reactants ($TiCl_4$ and $H_2O$) to adsorb onto hygroscopic DMTD surfaces and react during the subsequent reaction.

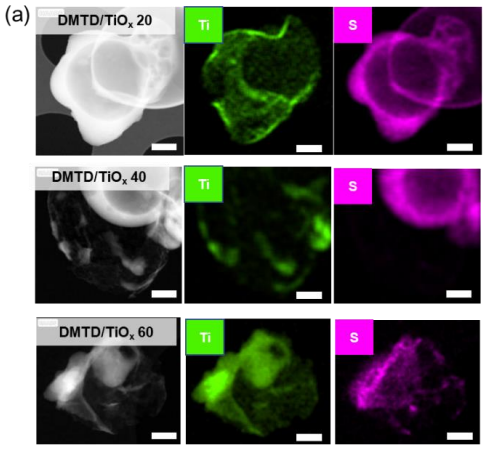


(b)

| Element AF% | C | O | S | N | Cl | Ti |
|---|---|---|---|---|---|---|
| DMTD/ TiO$_x$ 20 | 8.92 | 4.18 | 72.29 | 9.62 | 0.87 | 4.11 |
| DMTD/ TiO$_x$ 40 | 24.06 | 12.06 | 49.76 | 7.51 | 0.12 | 6.47 |
| DMTD/ TiO$_x$ 60 | 18.03 | 47.17 | 5.77 | 6.22 | 0.72 | 22.10 |

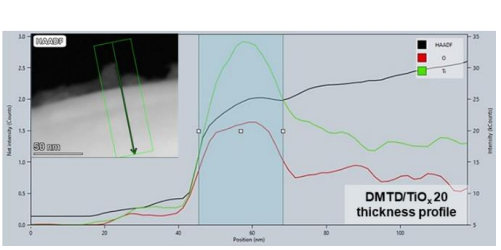


Figure 6.2 (a) TEM-EDX mappings, (b) atomic elements compositions of DMTD/TiO$_x$ particles at 20, 40 and 60 deposition cycles, and (c) thickness profile which is 20 to 30 nm of TiO$_x$ 20 cycles layer on DMTD. Notes: DMTD particles are easily damaged under the electron beam of TEM which shows as "hollow" particles in EDX mappings. The scale bars in EDX are 500 nm. Mappings of S show the presence of DMTD particles. Mappings of Ti represent the success of TiO$_x$ deposition.

Figure 6.3a shows the particle size distribution of the organic microparticles which did not change after 20 cycles gas phase deposition process. When more deposition cycles were employed (30 or 40 cycles), no significant differences in the nanolayer (Figure 6.2a) and particle size distribution (2-8 µm) were found. Nevertheless, at 60 cycles, particle agglomeration resulted in an increased particle size and particle distribution (2-12 µm). This is attributed to the hygroscopic nature and low temperature used during the gas phase deposition process. The chemical compositions of DMTD/TiO$_x$ particles were characterized by XPS. Supporting Information Figure S6.2 shows the two peaks at around 458.5 eV and 464.5 eV reflect the doublet state of Ti2P (i.e., Ti 2p3/2 and Ti2p1/2) [26] although the oxidation states vary with cycle numbers, suggests the uneven growth of TiO$_x$ especially at high cycle numbers, which is corresponding with the bigger particle size obtained at high cycle numbers from PSD analysis as shown in Figure 6.3a. As seen in Figure 6.3b, the normalized intensities of S2p and C1s peaks of the bound thiol (BE=161.9 eV) increase while that of N=C-S bound (BE=286.6 eV) decrease after deposition. [27] This suggests the formation of Ti-O(-Ti)-S at the interface between TiO$_x$ and DMTD. Considering the limited detectable depth of XPS (5 nm), the thickness of the TiO$_x$ layer might not be uniform across the DMTD particles. This possibility of the island growth is evidenced by our TEM-EDX results as shown in Figure 6.1b in which islands are visible on the DMTD/TiO$_x$ particles. Future research focuses on shell optimization should lead to strategies to avoid this phenomenon. Lower cycles (<10) were not investigated in this proof-of-concept work due to the observed limited effect of the number of cycles on the particle size distribution, nanolayer thickness, chemical composition, and dissolution kinetics of the microparticles (Supporting Information Figure S6.1b) but will be objective of study in future works.

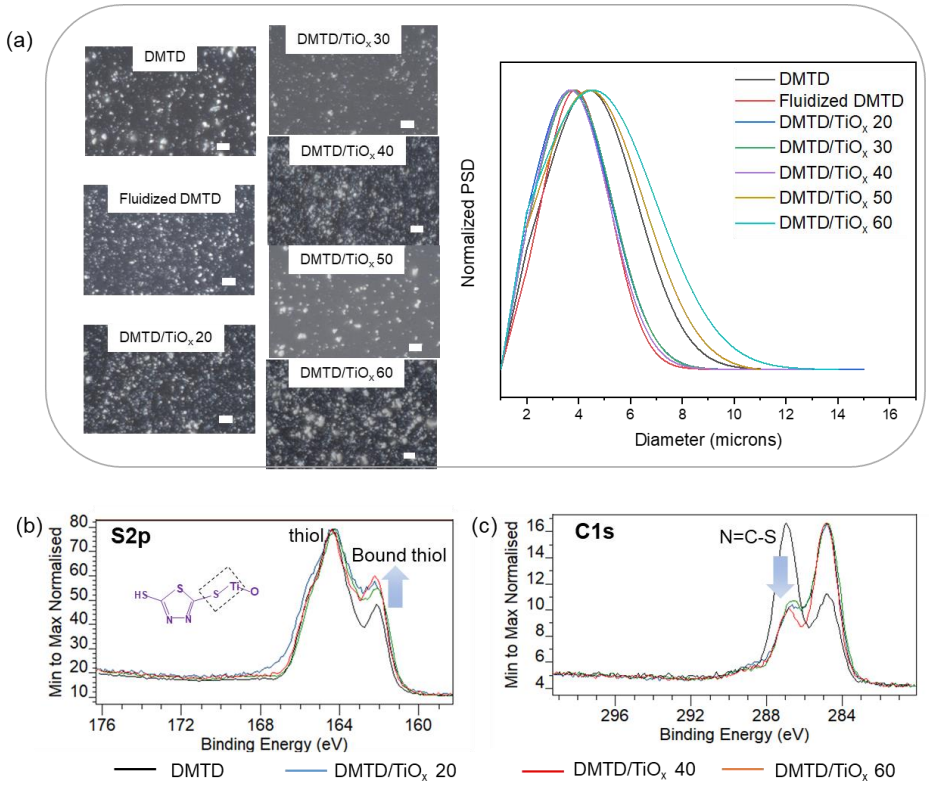


Figure 6.3 (a) Confocal microscope images and particle size distributions of DMTD, fluidized DMTD, and gas-phase deposited DMTD particles at 20 to 60 cycles. Scale bar: 20 µm. And S2p (b) and C1s (c) XPS spectra of DMTD/$TiO_x$ 20, DMTD/$TiO_x$ 40, and DMTD/$TiO_x$ 60 show the interaction of $TiO_x$ depositions with S in the substrate.

### *6.3.2 Effect of protective nanolayer on inhibitor-organic coating interaction*

To further prove the benefit of the nanolayer around the organic inhibitor in reducing its interaction with the organic coating, thermal gravimetry analysis (TGA), differential scanning calorimetry (DSC), and Ultraviolet–visible spectroscopy (UV-Vis) analysis were performed in order to ascertain the effect on polymer film degradation (TGA), glass transition temperature ($T_g$) and inhibitor release kinetics.

As can be seen in Figure 6.4a, the thermal degradation profile of the pristine epoxy coating can be differentiated into three stages: first stage (showing a drop followed by a pseudo-plateau up to 300°C) with 20% mass loss attributed to the loss of low molecular weight components; second stage (300-450°C) with around 55% mass loss attributed to the degradation of epoxy-amine crosslinking networks; and a third stage (above 450°C) due to the carbonization of residuals. [28] When introducing unmodified DMTD into the epoxy coating, the onset degradation temperature of the Epoxy-DMTD coating was increased from 100 to 150°C, suggesting that the excessive epoxy or/and amine monomers are stabilized by the reaction with DMTD in a thiolate-oxirane ring opening reaction process. However, the reaction between DMTD and the epoxy matrix also results in massive weight loss during first and second-stage degradations likely due to the

expected weaker bond formation (S-C vs C-C) and lower crosslinking density. DSC analysis further supports this idea as the mid-point glass transition temperature ($T_g$) of the epoxy matrix decreased from 44ºC to 19ºC when the untreated DMTD particles were added to the epoxy-amine coating (Figure 6.4b). A different effect is observed when the coated DMTD particles (DMTD/$TiO_x$ particles) are used. In this case the coatings exhibit similar thermal stability as the pristine epoxy coating matrix. The only difference is the disappearance of the flat stability stage at 350ºC, which is attributed to the lower thermal stability of side DMTD-Epoxy groups compared to a full epoxy-amine network. In addition, compared to the pristine epoxy matrix, the glass transition temperature dropped from 44±0.5 ºC to 32±0.5 ºC. This shows still some reactivity probably due to non-perfect particle coverage, but 13ºC lower $T_g$ drop than without the protective nanolayer, as seen in Figure 6.4b. The results, even for these non-optimized systems, confirm the protective effect of the $TiO_x$ nanolayer on DMTD leading to a reduced reactivity with the surrounding epoxy matrix and having a lower negative effect on the overall coating performance.

In order to study the effect of the $TiO_x$ nanolayer on the availability of DMTD in the presence of water (release of DMTD from the polymer in an aqueous corrosive media), the surface of Epoxy-DMTD and Epoxy-DMTD/$TiO_x$ coatings were ground with 1000 grid sanding paper, and exposed to 0.05M NaCl solution for 3 days. This allowed direct exposure of the particles to the electrolyte by removing the top polymeric thin layer on the coating. UV-vis measurements of aliquots taken in time and the use of a calibration curve allowed quantifying the DMTD release in time. Figure 6.4c illustrates the release profile and provides a schematic representation of water ingress and inhibitor release of these coatings. The Epoxy-DMTD/$TiO_x$ coating shows higher inhibitor release over time compared to the Epoxy-DMTD coating, which is in agreement with the lower negative interaction between the DMTD and the coating matrix. It should be noted that, in anticorrosive coatings, an initial fast inhibitor release leading to a minimum local concentration able to protect the metal is needed since the initial dealloying of AA2024 happens within 5 min. [22] The desirable coatings therefore rely on a release profile that commences with an initial rapid release followed by a continuous long-term release. [10, 29] For the Epoxy-DMTD/$TiO_x$ coating, 50% of the present DMTD can be released within the initial 2h and is followed by a sustained (slower) release until plateau at 3 days exposure having reached 65% release of the available DMTD. This can be attributed to the unavailability of the DMTD particles to water in relatively thick polymer films used in this test (70±3µm) but also to the partial reactivity between DMTD and the epoxy matrix indicated in Section 3.1. In contrast, the release of DMTD from the Epoxy-DMTD coating reaches a plateau at 40% already within 2h exposure to electrolyte. This lower release from the Epoxy-DMTD coating is attributed to the strong interaction between DMTD and the epoxy-amine matrix resulting from side reactions in absence of a protective nanolayer.

This effect becomes evident when analysing the polymers after exposure. In Figure 6.5 it can be seen how the use of $TiO_x$ nanolayers led to higher particle dispersion and a higher amount of smaller black dots related to holes created upon inhibitor dissolution, in good agreement with higher release fractions in Epoxy-DMTD/$TiO_x$ coatings due to the $TiO_x$ layer protection. While the Epoxy-DMTD/$TiO_x$ coating does not reach the theoretical maximum release (98% considering the $TiO_x$ layer), it is still significantly higher than for Epoxy-DMTD coatings (65% vs 40%). In addition, the total releasing period increased from 2 hours to 3 days when replacing pristine DMTD with DMTD/$TiO_x$, which is beneficial for protecting newly exposed areas and prolonging corrosion protection.

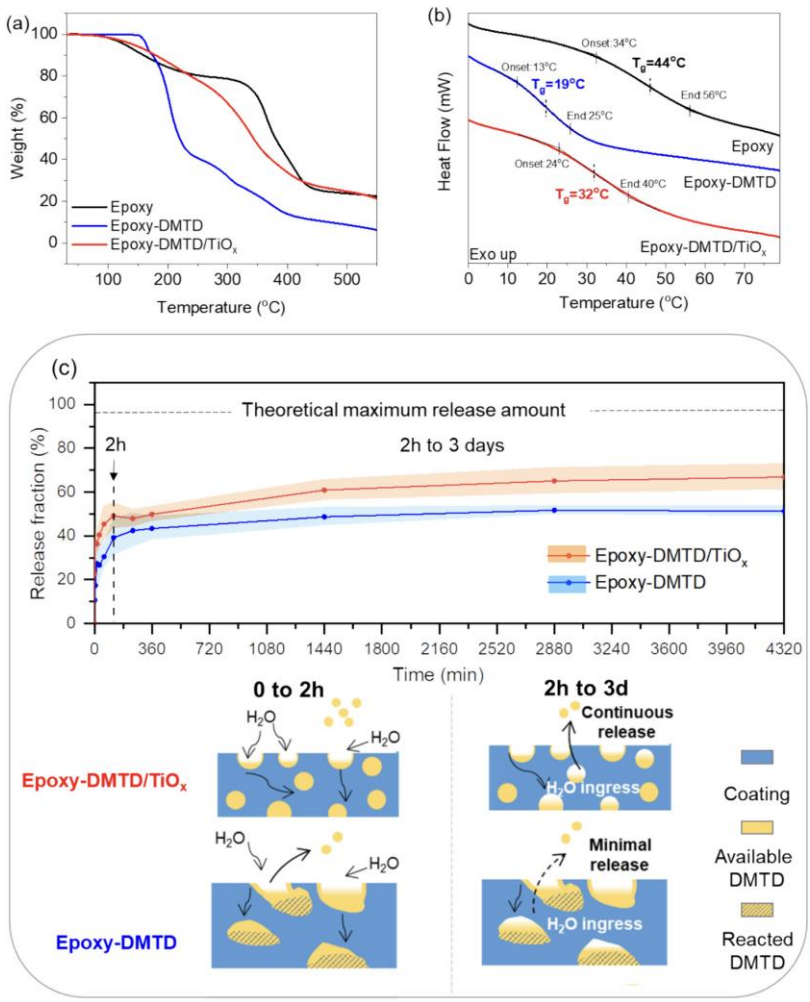


Figure 6.4. (a) TGA and (b) DSC analysis of Epoxy, Epoxy-DMTD, Epoxy-DMTD/$TiO_x$ coatings; (c) Release profile and schematic diagram of DMTD release from coatings exposed to 0.05M NaCl solution over 3 days from Epoxy-DMTD and Epoxy-DMTD/$TiO_x$ coatings. The release profile shows the average of several measurements (line) and the standard deviation (color band). The schematic diagram shows the cross-section of the coatings in two stages: the first stage from 0 to 2h, representing a rapid initial release of the DMTD inhibitor, and the second stage from 2h to 3 days, indicating a prolonged, long-term release in the case of Epoxy-DMTD/$TiO_x$ samples.

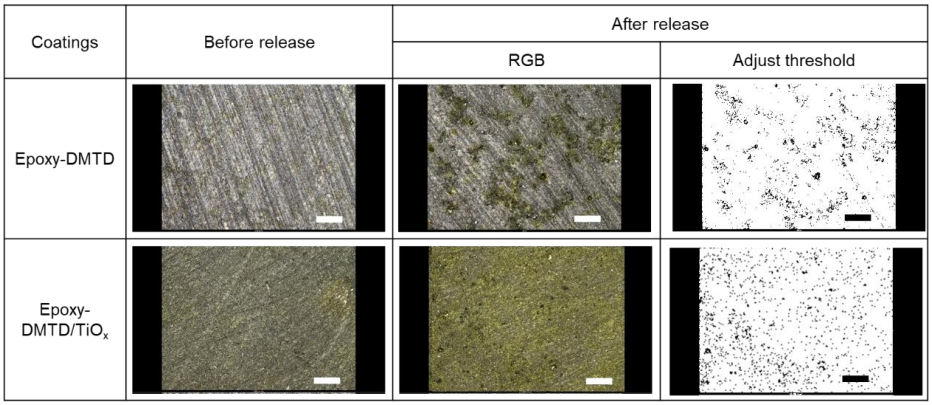


Figure 6.5 The images of Epoxy-DMTD and Epoxy-DMTD/$TiO_x$ coatings before and after the release tests made by confocal microscope. The black points in the third column represent the locations left by the release of DMTD which indicates a larger and homogeneous release from Epoxy-DMTD/$TiO_x$ coatings. Scale bar: 100 µm.

*6.3.3 Effect of protective nanolayer on active corrosion protection at damaged coatings under wet-dry cyclic exposure.*

In an active anticorrosion coating system, it is generally accepted that the protection at corrosion-inhibited locations will be ultimately lost under more aggressive exposure conditions, such as wet-dry cyclic exposure. This decline in corrosion inhibiting power is generally related to a reduction in the inhibitor supply from the coating and indirectly implies that the created inhibiting layers may not be sufficiently stable or robust, thereby failing to guarantee prolonged protection of the metal without a constant supply of inhibitor. Even if the stability of inhibiting layers is a largely unexplored concept, it is now known that inhibitor layers created from 1mM DMTD/0.05M NaCl solutions on AA2024-T3 show high levels of stability during cyclic wet/dry re-exposure to 0.05M NaCl solutions. [30]

In order to study the impact of the $TiO_x$ nanolayer (20 cycles) on the active corrosion inhibition at damaged locations (circular damage with Ø=1mm, 200 um penetration into the metal) given by DMTD-loaded coatings, a detailed study under wet/dry cyclic exposure conditions was performed. Herein, a single wet-dry cycle exposure represents a 2h exposure to 0.05M NaCl solution followed by a 1h drying process. The exposure time to electrolyte was determined based on the release kinetics study shown in Figure 6.4c wherein most of the inhibitor has been released from the grind coating in the first 2 hours of exposure. During a maximum of 3 cycles of exposure, the coating damages were monitored with an in-situ hyphenated electrochemical (electrochemical potential noise) and optical (image reflectometry) home-built setup as described in the experimental section. The electrochemical potential noise (EPN) signals and original optical images at the start and the end of exposure during each cycle are shown in the supporting information Figure S6.3. Without post-treatment, the optical images obtained during immersion do not allow differentiation during exposure thereby requiring image processing to extract quantitative information. Hence, the surface activity at the exposed metal and at the surrounding coating matrix are extracted from the optical images by a pixel-by-pixel changes analysis implemented in ImageJ software as described in our previous works. [10, 22, 30] Figure 6.6 and Figure

6.7 illustrates the resultant surface global activity maps (GAM) and quantified activity plots for the metal damage site, and local post-mortem images of the damage captured by a confocal microscope for the reference Epoxy coating and DMTD-loaded coatings.

As seen in Figure 6.6, an epoxy coating without DMTD rapidly shows the appearance of local activity (within the first minute of exposure) which progresses to a surface area coverage of the damaged location of around 20% after 2h exposure. The progression of the local activity is relatively fast and goes from 2.0E-03 % $s^{-1}$ during the first hour to a slightly faster process 3.1E-03 % $s^{-1}$ after 1.5h exposure (Figure 6.8) in good agreement with dealloying at intermetallic particles followed by trenching. [22] The corresponding EPN signal (Figure S6.3) can be regarded as typical for the corrosion of AA2024-T3, which shows lots of short transients and ends at -431mV vs Ag/AgCl, well in line with the corrosion potential of AA2024 at thermodynamic equilibrium after intermetallic particles (IM) dealloying and trenching. [31] These results are in good agreement with the local post-mortem image (Figure 6.6b) which shows a large extent of corrosion within 2h of exposure (1 cycle).

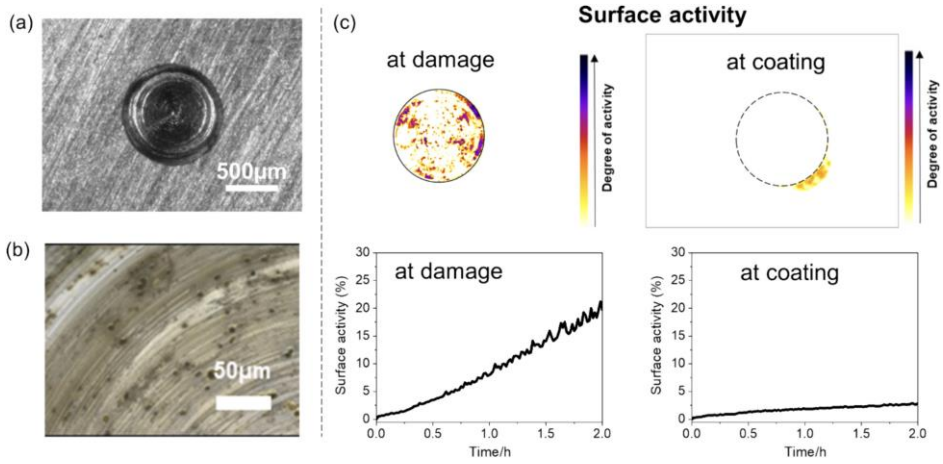


Figure 6.6 (a) Optical image, (b) local post-mortem image, and (c) Surface activity plots, activity map at the damage and coating area for damaged Epoxy coating during 2h exposure in 0.05M NaCl solution. The diameter of the circle in the activity map is 1mm. The minimum activity on the coating area indicates there was only coating delamination on this coating.

A different behavior is observed for coatings containing DMTD in the first cycle of exposure. Figure 6.7a shows that both Epoxy-DMTD and Epoxy-DMTD/$TiO_x$ coatings exhibit low-level surface activities at the metallic surface (low-intensity corrosion activities at less than 2% surface coverage). Additionally, the progression of the surface activity is significantly slower than for the uninhibited system, with Epoxy-DMTD <5.0E-04% $s^{-1}$ and Epoxy-DMTD/$TiO_x$ one extra order of magnitude slower <7.0E-05% $s^{-1}$, as shown in Figure 6.8, in good agreement with the local post-mortem images of the damage (Figure 6.7a) showing no signs of corrosion (no local dark spots). The EPN of Epoxy-DMTD and Epoxy-DMTD/$TiO_x$ coatings in Figure S6.3 are both smooth (no transients) with increase and decrease events and ended with a more negative EPN

value (-556mV and -778mV respectively) compared with the coating without DMTD. The decrease of the potential and absence of potential transients is a clear indication of the interaction of DMTD at the metallic surface preventing local dealloying. These results indicate DMTD is able to come out from both Epoxy-DMTD and Epoxy-DMTD/$TiO_x$ coatings and protect the exposed metal area at the first cycle even if in a more efficient manner in the case of the coating containing DMTD coated with a $TiO_x$ nanolayer (Epoxy-DMTD/$TiO_x$).

Differences between the two inhibited coatings become more obvious during the second cycle (Figure 6.7b). The surface activity of Epoxy-DMTD coating at damage shows surface activity propagation kinetics comparable to the uninhibited system (Figure 6.7b and Figure 6.8): 2.0E-03% $s^{-1}$ in the first half an hour indicating activation of local degradation, followed by a slowing down of the process to 5.0E-04% $s^{-1}$ during the subsequent hour likely due to the effect of inhibitor release or inhibiting layer healing, [28] and finally increasing again to 1.5E-03% $s^{-1}$ as an indication of reactivation of the corrosion process leading to a surface coverage around 9.5% at the end of the second cycle (Figure 6.7b). In very good agreement with this, the EPN signal shows potential noise transients in the initial 1800s (30 min) and turns to smooth signal reaching a potential value of -600mV (Figure S6.3). These findings, together with the post-mortem image showing the presence of some pits and oxides (Figure 6.7b), validate the loss of full protection provided by the Epoxy-DMTD coating during the second cycle.

The Epoxy-DMTD/$TiO_x$ coating on the other hand, initially shows a similar surface activity kinetics (Figure 6.8, k=1.0E-03 % $s^{-1}$ during first 30 min) yet rapidly followed by an activity plateau reaching a maximum of 1.7% surface coverage, still within the boundaries of intermetallic particle surface coverage. [22] The EPN again shows some noise transients in the first 1800s attributed to local dealloying or/and local breakdown of the inhibiting layer followed by a slow smooth decrease indicative of inhibitor repassivation as shown in Figure S6.3. The post-mortem image (Figure 7b) after the second cycle confirms these measurements with minor dealloying at some intermetallic particle sites.

During the third wet-dry cycle, the inhibited Epoxy-DMTD and Epoxy-DMTD/$TiO_x$ coatings show analogous behavior to that shown in cycle 2 in terms of surface activity (Figure 7c) and EPN signal (Figure S6.3). An increasing surface activity with the immersion time observed in the Epoxy-DMTD sample indicates a progression of the local corrosion attack even if still at a slower pace than in the uninhibited coatings. The Epoxy-DMTD/$TiO_x$ coating on the other hand shows again a fast activity during the first half hour of immersion followed by a very slow progression of surface activity and EPN stabilization (Figure S6.3, Figure 6.8) to reach a remarkably low surface activity coverage below 2% (Figure 6.7c). These results demonstrate the advantageous use of a protective thin nanolayer around the organic corrosion inhibitor to induce sustained and efficient corrosion protection at damaged sites.

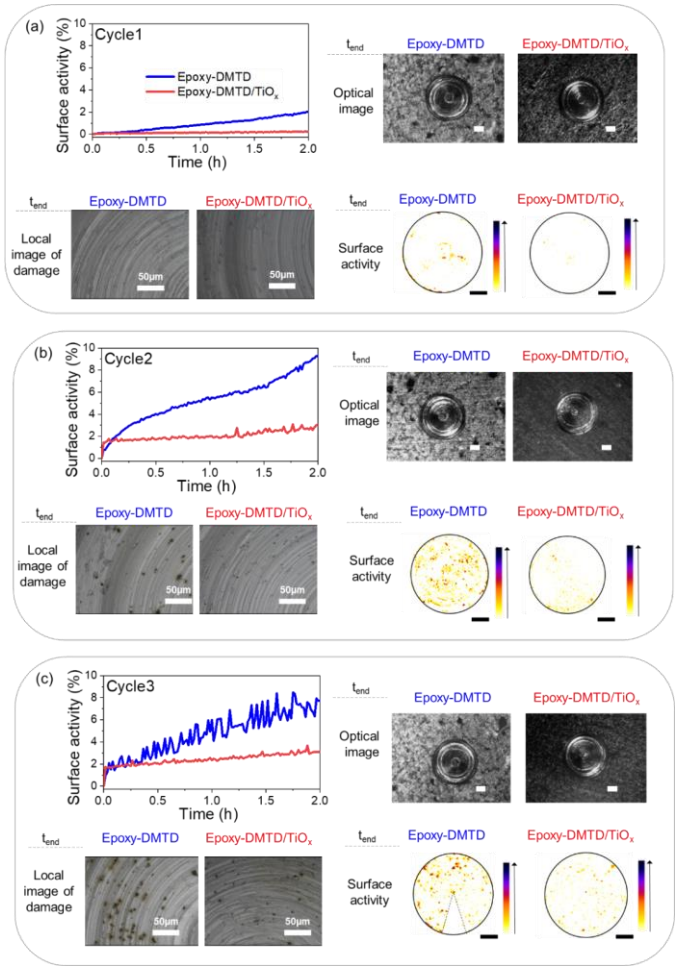


Figure 6.7. Figure shows the quantified surface activity plots (left-top), optical images (right-top), local post-mortem images (left-bottom) and global activity maps (GAM; right-bottom) at the exposed metal surface at the damage location at the end of wet-dry cycle 1 (a), cycle 2 (b) and cycle 3 (c) for Epoxy-DMTD (blue) and Epoxy-DMTD/$TiO_x$ (red) coatings. The diameter of the damage hole in the GAMs is 1mm. The sector with a dashed outline on the activity map of the third cycle (in c) of the Epoxy-DMTD represents a non-quantifiable location due to the presence of an air bubble and has therefore been omitted from the analysis. Scale bars in optical images and activity maps are 200µm. The color bars in the GAMs show the activity intensity increase where yellow is low intensity and red is high activity. The Epoxy reference showing massive activity is shown in the Figure 6.6. The activity maps and plots show the reduction of the local activity (corrosion) when using the organic inhibitors coated with a $TiO_x$ nanolayer.

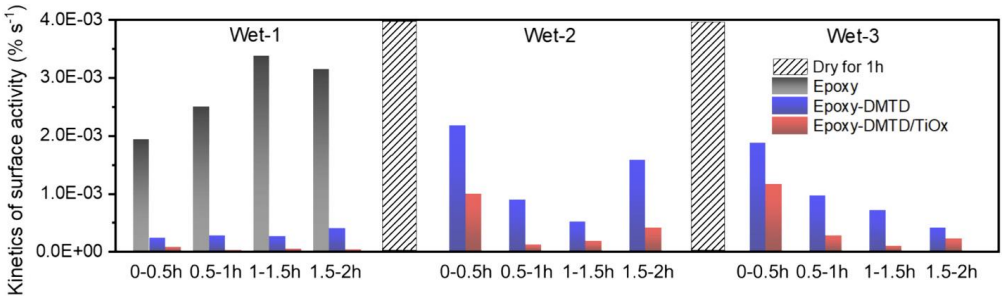


Figure 6.8 Surface activity kinetics at the damage every half hour for 1 cycle Epoxy, 3 cycles Epoxy-DMTD and 3 cycles Epoxy-DMTD/$TiO_x$ coatings exposure.

*6.3.4 Effect of protective nanolayer on the release mechanism responsible for sustained protection.*

The above results clearly demonstrate that gas-deposited protective nanolayers on DMTD reduce the negative interaction with the surrounding polymer matrix, improve inhibitor release and enable better corrosion inhibition. To unveil the mechanism that allowed comparable initial corrosion protection behavior in the two inhibited coating systems and clear differences after the first wet-dry cycle a dedicated release-to-protection analysis was made.

In the studied coatings, the corrosion inhibitors have two paths to release and protect the damage: (i) through the path created during water ingress on the coating surface, and (ii) from the sidewalls at the damage location. The contribution of the former is clearly detectable during the wet exposure monitoring and global activity maps of the coating.

Figure 6.9a shows the related activity (maps and plots) localized and quantified at the surrounding coating matrix around a damage location at the end of each cycle for Epoxy-DMTD and Epoxy-DMTD/$TiO_x$ coatings. Local activity appears homogeneously distributed on the two coatings surfaces, even though this is more evident, intense and growing in time in the case of the Epoxy-DMTD coating. The low local activity observed for the Epoxy-DMTD/$TiO_x$ coating suggests a low contribution of the exposed top surface to the inhibitor release. This coating activity appears different from the activity reported in our previous work with high pigment volume concentration loading (30%) where water ingress from the damage walls and subsequent inhibitor dissolution and transport to the damage location appears as local activity rings progressing outwards from the damage location. [10] The absence of such activity rings in this work suggests that in the studied coatings, no clear interparticle connection paths governing lateral release at the damage location are present, as expected for the relatively low pigment volume concentration used (10%).

To quantify the DMTD release from the damage wall and from the top surface, UV-Vis release studies with an intact coating and a damaged coating were performed in steps of 2h as in the wet-dry cyclic testing. Figure 6.9b shows an overview of the DMTD release amounts for the Epoxy-DMTD and Epoxy-DMTD/$TiO_x$ from coating and from damage for each cycle. In agreement with the global activity maps (Figure 6.9a), for the Epoxy-DMTD coating the majority of the DMTD is released from the coating surface through water diffusion, not from the damaged polymer walls. This is maintained during the three cycles, yet with decreasing DMTD release.

During the first cycle, the Epoxy-DMTD/$TiO_x$ coating released twice the amount of DMTD compared to Epoxy-DMTD, with half of the release coming from the damage coating walls. The same release contribution was observed in the subsequent 2nd and 3rd cycle, yet with lower inhibitor release due to depletion and/or diffusion restrictions.

Figure 6.9b shows that in the first cycle, approximately 0.05mM and 0.1mM DMTD were released from the Epoxy-DMTD and Epoxy-DMTD/$TiO_x$ coatings, respectively. Inhibitor release in these cases comes from the intact top surface of the coating and the walls of the induced hole. The amount of inhibitor released directly from the intact top surface (around 0.05mM in both cases) is significantly lower than that for coatings that have been surface damaged by sandpaper grinding as shown in Figure 6.4c (with 1.7 mM for Epoxy/DMTD and 2.2 mM for Epoxy-DMTD/$TiO_x$ for a comparable exposure area of 2.5 cm in diameter). Such a release difference confirms the reduced reaction in the case of a protected DMTD with a gas-deposited nanolayer and the higher release for such samples in the presence of damage (i.e. hole in this work). As observed in Figure 6.7a, the exposed metal surface at the hole remains protected in both cases in this first exposure cycle. This indicates the inhibitor amounts released are sufficient for corrosion protection. This is confirmed by the results shown in Figure S6.4 demonstrating that the minimum required concentration of DMTD in the electrolyte to protect a Ø=1mm damage on an Epoxy coating is 0.05 mM.

In the second and third cycle, the Epoxy-DMTD coating exhibited some dealloying and trenching on the intermetallic particles as shown in Figure 6.7b, whereas Epoxy-DMTD/$TiO_x$ coating did not display any significant signs of corrosion. During the second cycle, roughly 0.02mM of DMTD was released from Epoxy-DMTD, and 0.03mM was released from Epoxy-DMTD/$TiO_x$ coating. Even a bit less during cycle 3. As shown in Figure S6.4, the damage on an Epoxy coating can be protected with at least 0.05mM in 0.05M NaCl solution. However, once the samples were re-exposed to a fresh 0.05M NaCl solution without DMTD, only the sample pre-exposed to 0.1mM DMTD solution did not show any sign of corrosion (Figure S6.4, second column), indicating a higher inhibiting layer stability. This supports the idea that despite the inhibitor release for the Epoxy-DMTD/$TiO_x$ coating in the second and third cycles being below protection levels, the surface is still protected due to a higher stability of the inhibiting layer created at a 0.1mM concentration during the first cycle and the extra inhibitor released from the coating. These results support the idea demonstrated in our previous work[30] that finding methods to make the inhibiting layer more stable can contribute to the development of more efficient anti-corrosion systems, even when the inhibitor supply from the coating is reduced in time. Moreover, the continuous release at the second and third cycles is also beneficial for keeping the stability of the DMTD layer.

Figure 6.9c schematizes the release and protection at damaged sites in the absence of a protective nanolayer (Epoxy-DMTD) and in the presence of a gas-phase deposited nanolayer around the DMTD (Epoxy-DMTD/$TiO_x$). Supporting Information Figure S6.5 presents the cross-sectional micrographs of both coatings. The cross-section images reveal an enhanced dispersion of inhibitor particles due to the protective nanolayer, consistent with what is observed in the top view of the coatings shown in Figure 6.1. Figure 6.9c illustrates how the nanolayer allows a better homogeneous particle dispersion, with a higher content of available DMTD inhibitor due to reduced reaction with the surrounding matrix that in turn allows for fast formation of stable

inhibiting layers and sustained release of corrosion inhibitors to allow for sustained local corrosion protection.

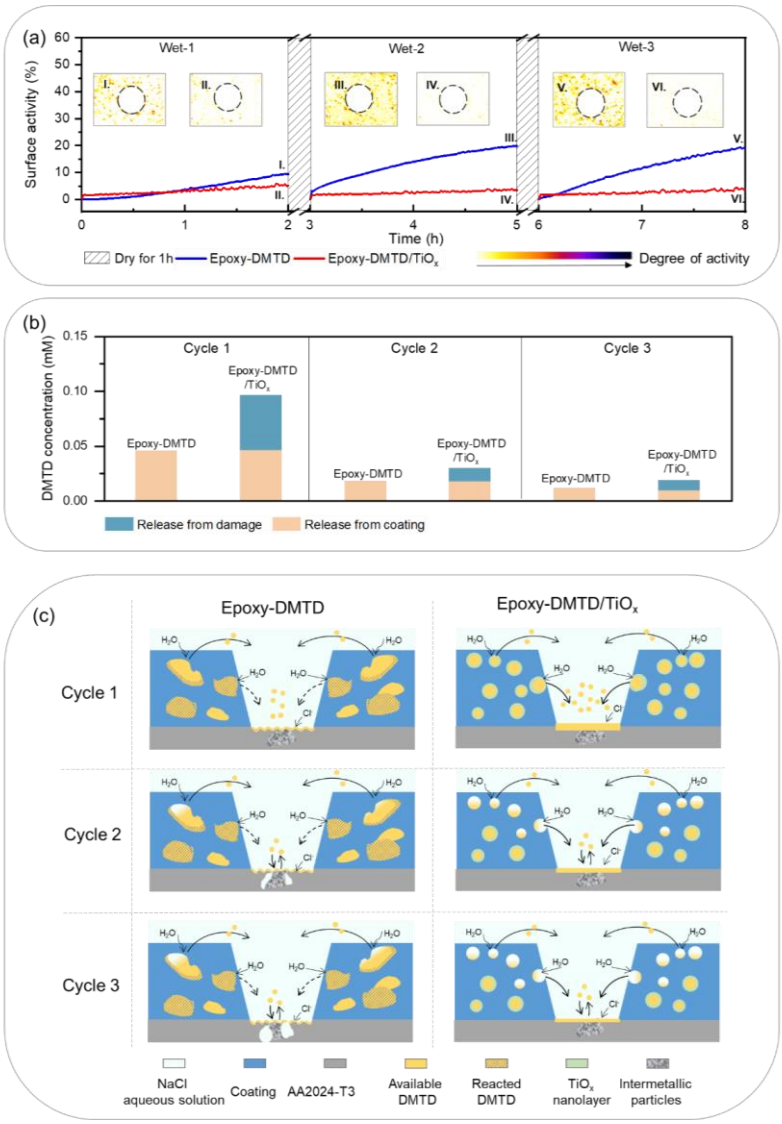


Figure 6.9 (a) Surface activity plots and global activity maps at coating areas around a damage location at the end of each cycle for Epoxy-DMTD and Epoxy-DMTD/$TiO_x$ coatings. For each exposure period, fresh 4.5mL 0.05M NaCl solution was used. The diameter of circles in activity maps is 1mm. Figure shows the higher level of homogeneous activity due to water ingress and inhibitor dissolution in the Epoxy-DMTD coating. Despite the lower activity the Epoxy-DMTD/$TiO_x$ coatings showed higher inhibitory effect. (b) Concentrations of DMTD released into 4.5mL 0.05M NaCl solution from an intact coating and from a coating with a damage for Epoxy-DMTD and Epoxy-DMTD/$TiO_x$ coatings during 3 cycles; (c) Proposed mechanism for the release of DMTD from Epoxy-DMTD and Epoxy-DMTD/$TiO_x$ coatings, and the stability of corrosion inhibition throughout 3 exposure cycles.

# 6.4 Conclusions

In this work, gas-phase deposition in a fluidized bed reactor is presented as a method to modify the surface of organic corrosion inhibitor particles to prevent their interaction with the epoxy-amine coating matrix. TEM of surface-modified inhibitor particles confirms the deposition of a nano-thin $TiO_x$ layer on the surface of DMTD particles. The modified particles were incorporated in highly reactive epoxy-amine coatings. Optical images, thermal analysis and release tests show that a 20 nm nanolayer can effectively improve the particle dispersion and reduce the reaction between DMTD and epoxy-amine matrix. Furthermore, the effect of the nanolayer on the corrosion protection of damaged coating locations exposed to wet/dry cycles was evaluated by in-situ optical-electrochemical tests. The local image reflectometry coupled with electrochemical potential noise and release tests demonstrated that using a gas phase deposited nanolayer around the organic microparticles, not only improves dispersion but improves inhibitor release and efficient long-term protection at damaged locations exposed to wet-wash-dry cycles. The results highlight the importance of sufficient release from the damage sites at the first cycle to (i) offer direct protection but also (ii) stable inhibiting layers during reimmersion, a new paradigm in corrosion protection with inhibitors.

Overall, this work specifically tackles the enduring challenge of incorporating effective organic corrosion inhibitors into organic coatings without triggering unwanted reactions and paves the way for utilizing highly reactive yet functional organic particles with functions such as corrosion inhibition, painkilling, sensing, antifouling, antibacterial, or luminescence in polymers across a wide array of applications. Although these initial results are promising, there is a wealth of potential for further improvements in organic particle selection, nanolayer composition, cycle optimization, and specific process parameters. Furthermore, while gas-phase deposition demonstrates potential in controlling inhibitor release and enhancing coating properties and effectiveness through precise deposition layer growth, it requires further refinement compared to traditional wet chemistry methods, particularly in terms of reducing process complexity, enhancing cost-efficiency, and scaling up.

# 6.5 References

(1) Williams, G.; Coleman, A. J.; McMurray, H. N. Inhibition of Aluminium Alloy AA2024-T3 pitting corrosion by copper complexing compounds. *Electrochimica Acta* **2010**, *55* (20), 5947-5958.
(2) Yasakau, K. A.; Zheludkevich, M. L.; Lamaka, S. V.; Ferreira, M. G. Mechanism of corrosion inhibition of AA2024 by rare-earth compounds. *The Journal of Physical Chemistry B* **2006**, *110* (11), 5515-5528.
(3) Harvey, T.; Hardin, S.; Hughes, A.; Muster, T.; White, P.; Markley, T.; Corrigan, P.; Mardel, J.; Garcia, S.; Mol, J. The effect of inhibitor structure on the corrosion of AA2024 and AA7075. *Corrosion science* **2011**, *53* (6), 2184-2190.
(4) Soleymanibrojeni, M.; Shi, H.; Udoh, I. I.; Liu, F.; Han, E.-H. Microcontainers with 3-amino-1, 2, 4-triazole-5-thiol for enhancing anticorrosion waterborne coatings for AA2024-T3. *Progress in Organic Coatings* **2019**, *137*, 105336.
(5) White, S. R.; Sottos, N. R.; Geubelle, P. H.; Moore, J. S.; Kessler, M. R.; Sriram, S.; Brown, E. N.; Viswanathan, S. Autonomic healing of polymer composites. *Nature* **2001**, *409* (6822), 794-797.
(6) Yabuki, A.; Shiraiwa, T.; Fathona, I. W. pH-controlled self-healing polymer coatings with cellulose nanofibers providing an effective release of corrosion inhibitor. *Corrosion Science* **2016**, *103*, 117-123.
(7) Ferrer, E. L.; Rollon, A. P.; Mendoza, H. D.; Lafont, U.; Garcia, S. J. Double-doped zeolites for corrosion protection of aluminium alloys. *Microporous and mesoporous materials* **2014**, *188*, 8-15.
(8) Fix, D.; Andreeva, D. V.; Lvov, Y. M.; Shchukin, D. G.; Möhwald, H. Application of inhibitor-loaded halloysite nanotubes in active anti-corrosive coatings. *Advanced Functional Materials* **2009**, *19* (11), 1720-1727.
(9) Li, C.; Guo, X.; Frankel, G. S. Corrosion inhibition of AA2024-T3 by a coating containing dual-pH sensitive, corrosion inhibitor loaded microspheres. *Corrosion Science* **2021**, *192*, 109835.
(10) Denissen, P. J.; Homborg, A. M.; Garcia, S. J. Requirements for corrosion inhibitor release from damaged primers for stable protection: a simulation and experimental approach using cerium loaded carriers. *Surface and Coatings Technology* **2022**, *430*, 127966.
(11) Raj, R.; Morozov, Y.; Calado, L.; Taryba, M.; Kahraman, R.; Shakoor, R.; Montemor, M. Calcium carbonate particles loaded with triethanolamine and polyethylenimine for enhanced corrosion protection of epoxy coated steel. *Corrosion Science* **2020**, *167*, 108548.
(12) Knez, M.; Nielsch, K.; Niinistö, L. Synthesis and surface engineering of complex nanostructures by atomic layer deposition. *Advanced materials* **2007**, *19* (21), 3425-3438.
(13) Vervuurt, R. H.; Kessels, W. M.; Bol, A. A. Atomic layer deposition for graphene device integration. *Advanced Materials Interfaces* **2017**, *4* (18), 1700232.
(14) Zhang, S. T.; Maltseva, A.; Herting, G.; Guillemoles, J. f.; Schneider, N.; Odnevall, I.; Volovitch, P. Importance of atmospheric aerosol pollutants on the degradation of Al2O3 encapsulated Al-doped zinc oxide window layers in solar cells. *Progress in Photovoltaics: Research and Applications* **2022**, *30* (5), 552-566.
(15) Kääriäinen, T. O.; Kemell, M.; Vehkamäki, M.; Kääriäinen, M.-L.; Correia, A.; Santos, H. A.; Bimbo, L. M.; Hirvonen, J.; Hoppu, P.; George, S. M. Surface modification of acetaminophen particles by atomic layer deposition. *International Journal of Pharmaceutics* **2017**, *525* (1), 160-174.
(16) La Zara, D.; Zhang, F.; Sun, F.; Bailey, M. R.; Quayle, M. J.; Petersson, G.; Folestad, S.; van Ommen, J. R. Drug powders with tunable wettability by atomic and molecular layer deposition: From highly hydrophilic to superhydrophobic. *Applied Materials Today* **2021**, *22*, 100945.
(17) La Zara, D.; Sun, F.; Zhang, F.; Franek, F.; Balogh Sivars, K.; Horndahl, J.; Bates, S.; Brannstrom, M.; Ewing, P.; Quayle, M. J. Controlled pulmonary delivery of carrier-free budesonide dry powder by atomic layer deposition. *ACS nano* **2021**, *15* (4), 6684-6698.
(18) Gupta, S.; Mittal, M.; Rathore, A. S. Atomic layer deposition coating on the surface of active pharmaceutical ingredients to reduce surface charge build-up. *ACS Applied Materials & Interfaces* **2022**, *14* (23), 27195-27202.
(19) Zhang, F.; Wu, K.; La Zara, D.; Sun, F.; Quayle, M. J.; Petersson, G.; Folestad, S.; Chew, J. W.; van Ommen, J. R. Tailoring the flow properties of inhaled micronized drug powders by atomic and molecular layer deposition. *Chemical Engineering Journal* **2023**, *462*, 142131.

(20) Zhang, D.; Flory, J.; Panmai, S.; Batra, U.; Kaufman, M. Wettability of pharmaceutical solids: its measurement and influence on wet granulation. *Colloids and Surfaces A: Physicochemical and Engineering Aspects* **2002**, *206* (1-3), 547-554.
(21) Vo, C. L.-N.; Park, C.; Lee, B.-J. Current trends and future perspectives of solid dispersions containing poorly water-soluble drugs. *European journal of pharmaceutics and biopharmaceutics* **2013**, *85* (3), 799-813.
(22) Olgiati, M.; Denissen, P. J.; Garcia, S. J. When all intermetallics dealloy in AA2024-T3: Quantifying early stage intermetallic corrosion kinetics under immersion. *Corrosion Science* **2021**, *192*, 109836.
(23) Carioscia, J. A.; Stansbury, J. W.; Bowman, C. N. Evaluation and control of thiol–ene/thiol–epoxy hybrid networks. *Polymer* **2007**, *48* (6), 1526-1532.
(24) Chan, J. W.; Hoyle, C. E.; Lowe, A. B.; Bowman, M. Nucleophile-initiated thiol-Michael reactions: effect of organocatalyst, thiol, and ene. *Macromolecules* **2010**, *43* (15), 6381-6388.
(25) Konuray, A. O.; Fernandez-Francos, X.; Ramis, X. Latent curing of epoxy-thiol thermosets. *Polymer* **2017**, *116*, 191-203.
(26) Biesinger, M. C.; Payne, B. P.; Grosvenor, A. P.; Lau, L. W.; Gerson, A. R.; Smart, R. S. C. Resolving surface chemical states in XPS analysis of first row transition metals, oxides and hydroxides: Cr, Mn, Fe, Co and Ni. *Applied Surface Science* **2011**, *257* (7), 2717-2730.
(27) Castner, D. G.; Hinds, K.; Grainger, D. W. X-ray photoelectron spectroscopy sulfur 2p study of organic thiol and disulfide binding interactions with gold surfaces. *Langmuir* **1996**, *12* (21), 5083-5086.
(28) Levchik, S. V.; Weil, E. D. Thermal decomposition, combustion and flame-retardancy of epoxy resins—a review of the recent literature. *Polymer International* **2004**, *53* (12), 1901-1929.
(29) Hughes, A. E.; Cole, I. S.; Muster, T. H.; Varley, R. J. Designing green, self-healing coatings for metal protection. *NPG Asia Materials* **2010**, *2* (4), 143-151.
(30) Zhao, J.; Santoso, A.; Garcia, S. J. Small concentrations of NaCl help building stable inhibiting layers from 2, 5-dimercapto-1, 3, 4-thiadiazole (DMTD) on AA2024-T3. *Corrosion Science* **2023**, *225*, 111562.
(31) Tita, A. T.; Hauth, J. C.; Grimes, A.; Owen, J.; Stamm, A. M.; Andrews, W. W. Decreasing incidence of postcesarean endometritis with extended-spectrum antibiotic prophylaxis. *Obstetrics & Gynecology* **2008**, *111* (1), 51-56.

# 6.6 Support information

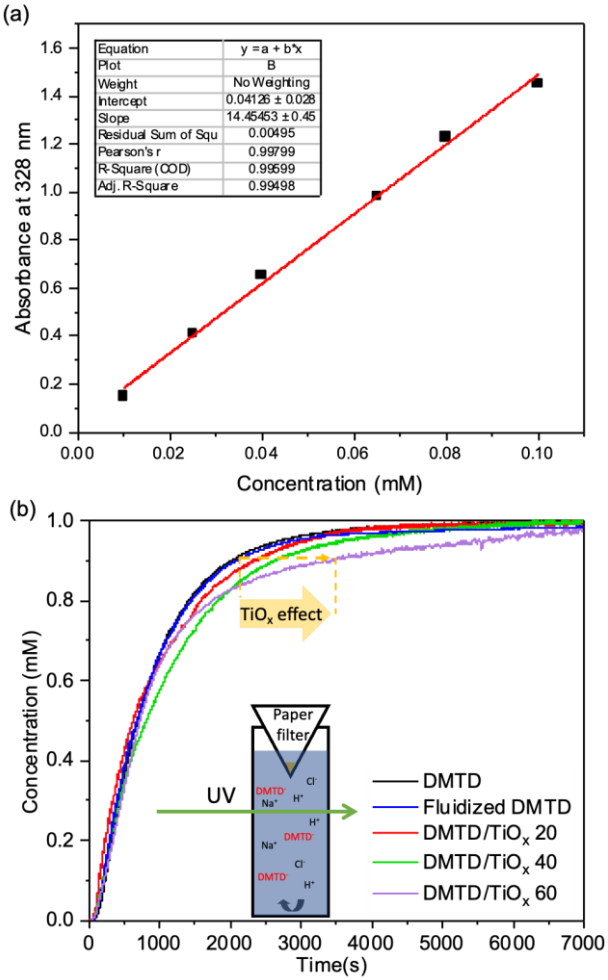


Figure S6.1 (a) Calibration curve of DMTD 0.05M NaCl solution. (b) Dissolution kinetics of DMTD or DMTD/$TiO_x$ particles in 0.05M NaCl solution for 2h. The dissolution of DMTD to the solution was delayed and slowed down due to the $TiO_x$ deposition. DMTD is still totally released independent of the number of cycles, suggesting no significant influence on inhibitor release potential.

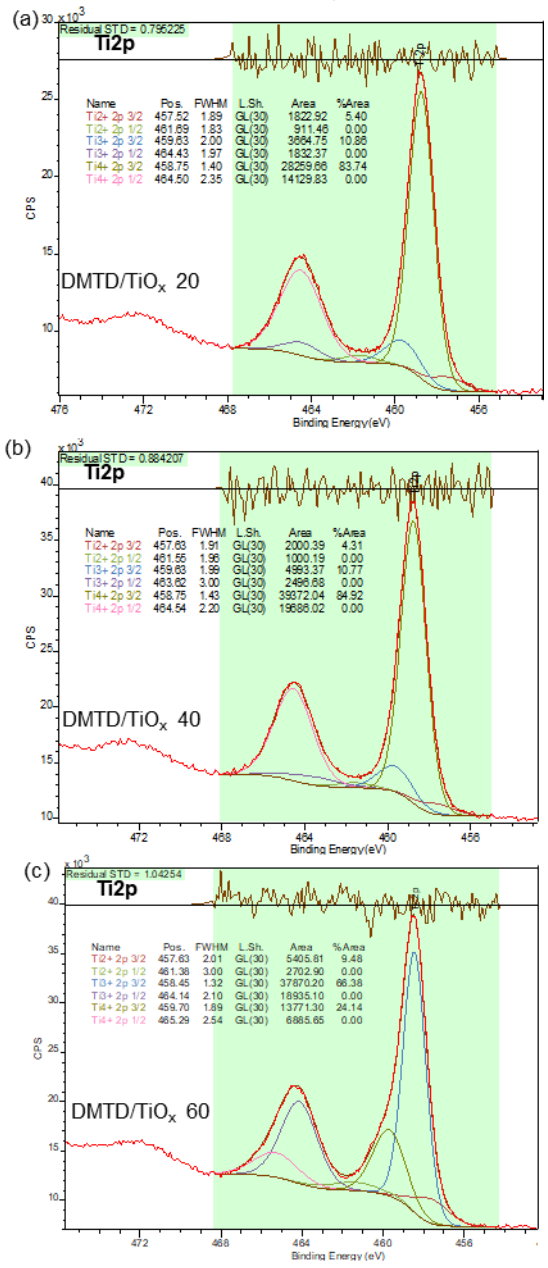


Figure S6.2 Ti2p XPS spectra of (a) DMTD/$TiO_x$ 20, (b) DMTD/$TiO_x$ 40, and (c) DMTD/$TiO_x$ 60 show the presence of $TiO_x$ depositions. The peaks at binding energy (BE) of 458.7 eV (Ti 2p3/2) and 464.5 eV (Ti2p1/2) reflect the doublet state of Ti(IV) 2p, which arise from the orbit coupling. These two peaks predominate in DMTD/$TiO_x$ with 20 and 40 cycles. While further increasing the cycle to 60, these two peaks shift to 458.4 eV(Ti 2p3/2) and 464.1 eV(Ti2p1/2), representing the Ti(III) compounds.

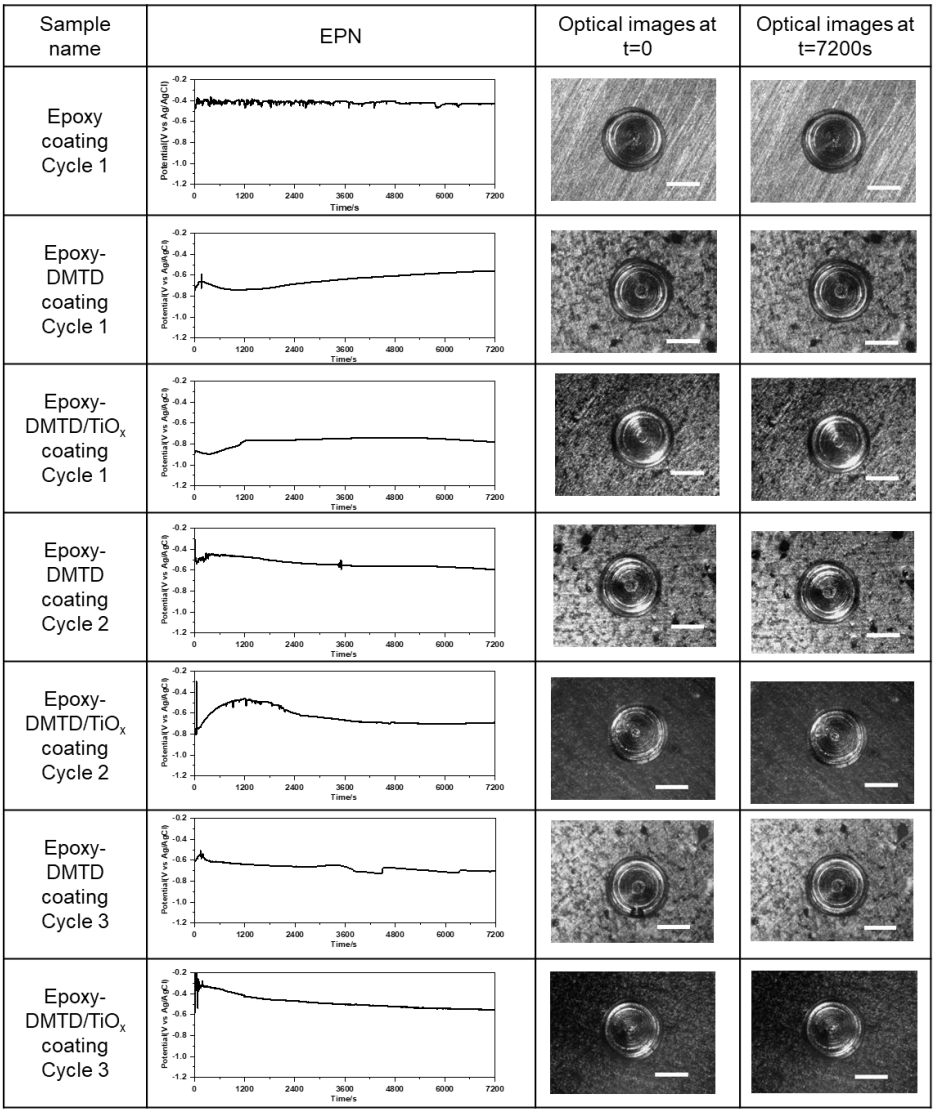


Figure S6.3 Electrochemical potential noise (EPN) signals and Optical images at the start and the end of each exposure for 1 cycle Epoxy, 3 cycles Epoxy-DMTD and 3 cycles Epoxy-DMTD/$TiO_x$ coatings exposure. Scale bars: 0.5mm. Optical images under immersion do not allow differentiation. Image correlation is needed as shown in the manuscript.

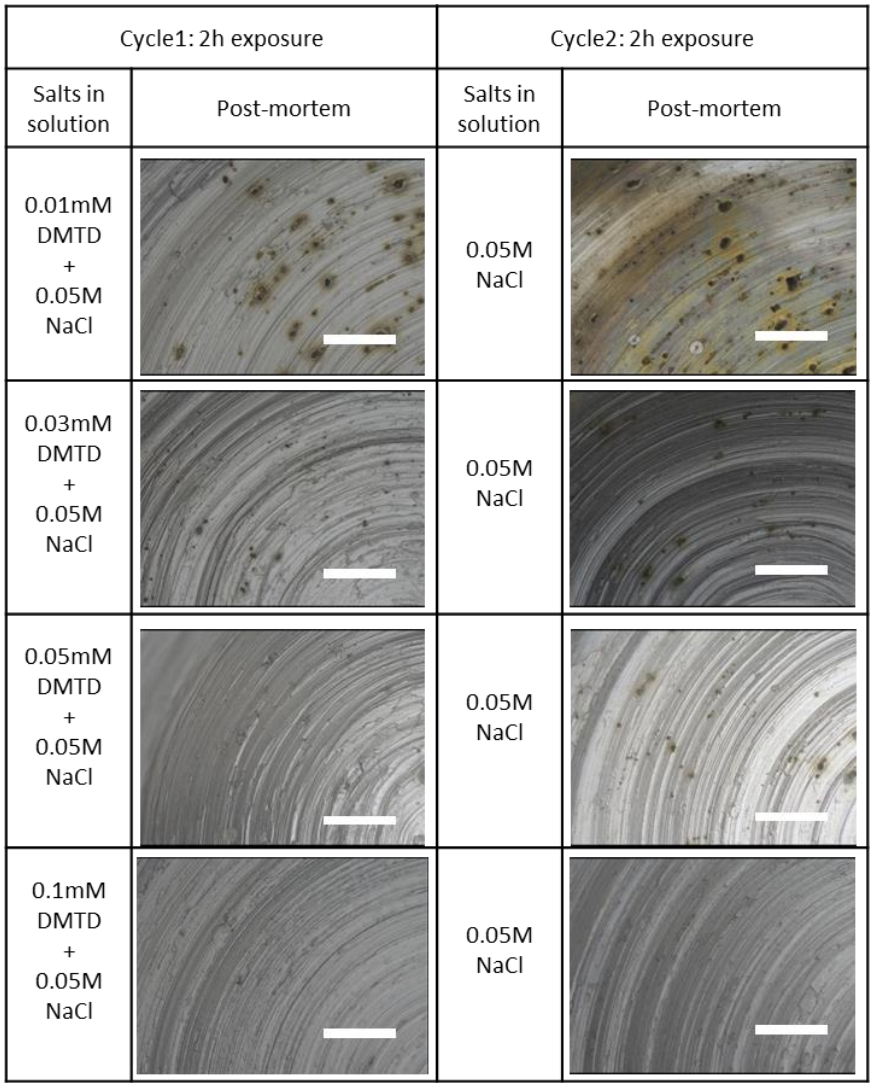


Figure S6.4 Confocal microscope images of epoxy-amine coating with a damage Ø=1mm exposed to 0.05M NaCl solutions with 0.01, 0.03, 0.05, 0.1 mM DMTD and re-exposed in 0.05M NaCl solution without DMTD. Scale bar: 50 µm. Results show 0.05mM DMTD during cycle 1 leads to minimum acceptable protection, and 0.1mM DMTD leads to stable protection. Test shows that inhibition can be obtained at 0.05 mM DMTD concentration but this inhibition is instable during re-immersion in non-inhibited solutions. To obtain fast corrosion inhibition and more stable inhibiting layers ensuring sustained protection, a concentration between 0.05 and 0.1mM DMTD is needed.

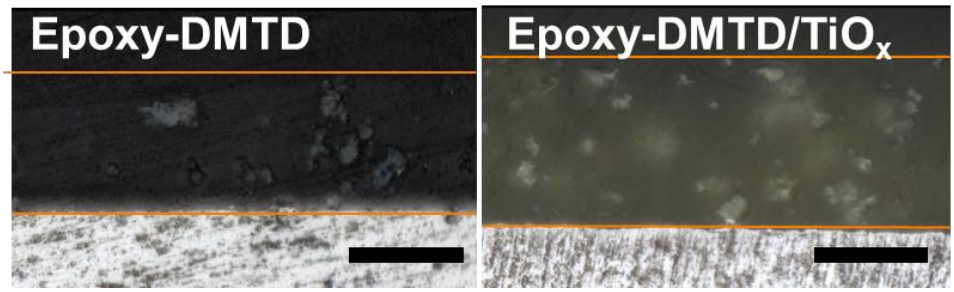


Figure S6.5 Cross-section of Epoxy-DMTD and Epoxy-DMTD/$TiO_x$ coatings. The cross-sections were prepared by embedding them in an epoxy-amine resin, followed by grinding with sanding paper down to a 7µm grit. Scale bar: 100µm.

# Chapter 7

# Corrosion Inhibition Power of Novel Gas-Phase Deposited Organic Inhibitors in Lab-Scale Model Aircraft Primers

*In the previous chapter, we introduced a novel strategy to protect organic corrosion inhibitors from the surrounding polymer coating binder using gas-phase deposited oxide nanolayers in a fluidized bed. Previous study incorporated such particles into a two-component epoxy-amine coating, demonstrating protection of large damages during 2 h of immersion and cyclic testing. In this work, we take this concept one step further by studying the behavior of such protected particles in multicomponent coatings with a formulation closer to industrial coatings, with a strong focus on the effect of the content of inhibiting particles in the coating. To this aim, model aircraft primers containing 3%, 6%, and 10% pigment volume concentration (PVC) of $TiO_x$-coated HDMTD microparticles (HDMTD/$TiO_x$) in 25 % PVC coatings were prepared and applied on bare AA2024-T3 substrates. Corrosion protection at damages was assessed using an in-situ operando reflected microscopy method during 24 h immersion in 0.5M NaCl solution, a 7-days droplet test and a 1000 h neutral salt fog spray (NSS) test. The results show high levels of protection at damage sites in all three tests for all coatings. However, the nanolayer-protected inhibitor pigments induced some blistering during NSS. Among all coatings tested, the 6% HDMTD/$TiO_x$ coating (4.3 wt% inhibitors, same to the coatings in Chapter 2) showed the best compromise between excellent protection at damaged sites in all three tests and reduced blistering. These results highlight the high potential of this new approach to protect aircraft structures as well as the need for further research to improve the concept.*

# 7.1 Introduction

Organic corrosion inhibitors have received significant attention as a strategy to protect steel structures due to their potential direct use in liquids flowing in pipelines. [1, 2] Nevertheless, their use to protect coated structures such as aircraft aluminum alloys, has remained elusive, largely due to the negative reactions between these corrosion inhibitors and the organic binders used in coating primers (e.g., epoxy-amine). [3, 4] Over the past half decade, attempts to overcome this reactivity challenge using nano and micro carriers without compromising their inhibition effectiveness or reducing adhesion and coating barrier properties have proven challenging due to low loading and insufficient isolation from the matrix. [4-7] Previous research (Chapter 5) justified the research focus on 2,5-dimercapto-1,3,4-thiadiazole (HDMTD) as provides high levels of corrosion protection and inhibiting layer stability when used to protect bare AA2024-T3 exposed to NaCl solutions. [8] However, when this highly effective inhibitor was loaded into porous silica microcarriers (diatomite, DE), [7] the amount of inhibitor released at damaged sites was limited, hence leading to a significant reduction in its inhibition power. (Chapter 2&3) This limitation is attributed to: (i) the corrosion-inhibiting chemical moieties in HDMTD (thiol/thiolate groups) which easily react with the epoxy/amine matrix, [9] hence interfering with the cross-linking process, affecting the coating properties and decreasing its release potential from the coating; (Chapter 3) (ii) the highly porous nature of DE particles used for inhibitor loading also allowing the epoxy-amine to enter [10] and react with HDMTD stored in the DE carrier; and (iii) the difficulty to load large amounts of inhibitors only inside DE particles, even with hydrophobic surface modification of DE particles to ensure the isolation of the DE interior from the epoxy-amine matrix. [11] (Chapter 4)

To solve these challenges, in our previous work (Chapter 6), we demonstrated that gas-phase deposition in a fluidized bed can be used to coat and protect the HDMTD organic corrosion inhibitors. [4] The 20 nm thick $TiO_x$ nanolayers improved the compatibility between HDMTD and epoxy-amine coatings by reducing HDMTD agglomeration and reducing unwanted interactions between HDMTD and the epoxy-amine matrix. This approach allowed sufficient quantities of DMTD ions to be released from the scribe walls to the exposed metal at scribe locations leading to high protection levels when exposed to 0.05M NaCl water electrolyte. However, this proof-of-concept work was limited to damaged two-component epoxy-amine coatings without further charges exposed to electrolyte with low NaCl concentrations for three short (2 h) wet-dry cycles (6 h immersion in total).

The present work aims to build upon this initial study by evaluating the corrosion protection performance of a model primer with composition closer to higher TRLs, as that one used in Chapter 2, loaded with nanolayer-treated organic inhibitor particles (HDMTD/$TiO_x$). To this aim, we prepared 3 formulations of aircraft primers with 3%, 6% and 10% PVC of HDMTD/$TiO_x$ pigments in a total of 25% PVC. The decision to use relatively low corrosion inhibitor PVC levels (note CrVI primers use between 20 and 30% PVC to be efficient while Li-salts primers use 30% PVC) was prompted by our previous research [4] indicating that a 10% PVC of HDMTD coating can release sufficient HDMTD to protect large damages for long immersion times. Additionally, the 6% PVC HDMTD/$TiO_x$ coating contains the same weight percent of HDMTD as the DE-

HDMTD system used in Chapter 2, providing insights into the advantages of the new loading strategy. The damaged coatings were immersed in 0.5M NaCl electrolyte for one day while being monitored using microscopy and electrochemical potential noise in a hyphenated opto-electrochemical setup, as previously reported. [4, 10, 12-15] The coatings were further evaluated using droplet tests for 7 days exposure and 1000 h neutral salt-fog spray tests, as described in Chapter 2. SEM/EDX was used to analyze the samples after exposure.

# 7.2 Experimental

### *7.2.1 Materials*

The surface modified 2,5-dimercapto-1,3,4-thiadiazole (HDMTD/$TiO_x$) microparticles with $TiO_x$ nanolayer were produced in a gas-phase deposition fluidized bed reactor, following the same procedure as described previously. [4] (Chapter 6) Briefly, 10 g HDMTD particles were used as deposition substrates. The deposition process consisted of sequential exposures of the HDMTD to $TiCl_4$ for 45s, 5 min purging with only nitrogen gas, and $H_2O$ for 60s (one cycle) followed by another 5 min nitrogen gas purging step prior to the next cycle of exposure to precursor and co-reactant. The deposition was run for 20 cycles and the HDMTD/$TiO_x$ particles were stored in a desiccator before use. No particle agglomeration was observed during storage. A 3 mm thick bare aluminum alloy 2024-T3 (AA2024-T3) panel was used as the substrate. The aircraft primer formulation included same components as Chapter 2, Epoxy resin Beckopox 1 and 2, Amine hardener Ancamine, Ethylmethyl ketone (MEK), Methylisobutyl ketone (MIBK), dispersion and wetting agents supplied by BYK, $TiO_2$, blue pigment, and $BaSO_4$ pigments. Sodium chloride (NaCl, purity > 98%) was obtained from VWR Chemicals, and all aqueous solutions were prepared using Millipore® filtered water.

### *7.2.2 Model aircraft primers preparation*

The bare AA2024-T3 metal sheets were cut into 100 mm x100 mm pieces, hand ground with Scotch Brite 3M to remove the native oxide layer and achieve a surface roughness of approximately 5 µm, degreased with acetone, rinsed with distilled water, air-dried, and stored in a clean environment before coating.

Three different coating compositions were prepared, each with varying amounts of inhibitor pigments added to the standard resin binder as listed in Table 7.1. Two epoxy resins, Beckopox 1 and Beckopox 2 (4.7:1 mass ratio), were mixed at 700 rpm for 2 min. MEK, MIBK, and BYK agents were added and stirred at 700 rpm for 2 min. $TiO_2$, $BaSO_4$, and blue pigment were sequentially added and mixed at 2000 rpm for 2 min each. The mixture was milled with 0.6 mm Zr beads at 3500 rpm for 1 h, filtered, and mixed with Ancamine at 1000 rpm for 1 min, then pre-cured for 15 min. HDMTD/$TiO_x$ particles were added and mixed at 2000 rpm for 1 min. The coating was applied on bare AA2024-T3 at a 150 µm wet thickness, cured at 80°C for 3 h, and stored in a desiccator. Total PVCs of the coatings were all 25%, including 3%, 6% and 10% inhibitor particles, as listed in Table 7.2.

Table 7.1 Composition of the 25% PVC coatings

| Composition | Density (g/cm$^3$) | Weight fraction (phr) |
|---|---|---|
| Beckopox resin 1 | 1.07 | 83 |
| Beckopox resin 2 | 1.12 | 17 |
| Ethylmethyl ketone (MEK) | 0.805 | 12 |
| Methylisobutyl ketone (MIBK) | 0.8 | 46 |
| Dispersing agent | 1.08 | 8 |
| Wetting agent | 1.03 | 1 |
| $TiO_2$ | 4.1 | 47 |
| $BaSO_4$ | 4.5 | 42 |
| Blue pigment | 1.65 | 1 |
| Inhibitor pigment | 1.34 | 16 |
| Ancamine hardener | 1.01 | 45 |

Table 7.2 Coatings formulations as a function of Beckopox resin (phr=parts per hundred epoxy resin in weight).

| No. | Inhibitor pigments | Inhibitor pigments (phr) | Dry weight Percent of inhibitor (wt%) | PVC of inhibitor pigments | Inactive pigments (phr) | Other components (phr) | Coating thickness (μm) |
|---|---|---|---|---|---|---|---|
| 1 | HDMTD/$TiO_x$ | 8 | 2.2 | 3% | 98 | 154 | 65-80 |
| 2 | HDMTD/$TiO_x$ | 16 | 4.3 | 6% | 90 | 154 | 68-95 |
| 3 | HDMTD/$TiO_x$ | 27 | 7.4 | 10% | 79 | 154 | 70-105 |

*7.2.3 Corrosion testing*

Three exposure tests were used to evaluate the corrosion protection effectiveness of the coatings containing HDMTD/$TiO_x$ particles in three different simulated corrosive environments.

The first test involved monitoring the damaged coatings (1mm diameter, 0.25 mm deep damage made by a Roland EGX-350 engraver equipped with a 1 mm diameter end mill) immersed in 0.5M NaCl solution for one day using an in-situ reflected microscopy set up, as described in previous studies. The optical analysis was conducted in ImageJ, based on a pixel-by-pixel analysis following the same protocol as in our previous works. [4, 10, 12-15] A static thresholding limit of 10 was used to analyze the metallic surface. After exposure, the scribes were analyzed with the help of a JEOL SJM-840 SEM with EDS. The concentration of inhibitors released into the electrolyte was measured with a PerkinElmer LAMBDA 35 UV/VIS spectrometer.

The second method used is the so-called droplet test to simulate environmental degradation at high humidity with condensation. Scribes of 1 mm wide, 20 mm long, 0.35 mm deep were made on the coatings and 105 μl of 0.5M NaCl solution was dropped on the scribes. The samples were

kept in a closed box with wetted towels under the metal plates to maintain humidity. Optical images of the drops were taken daily over one week exposure with the help of a Keyence VHX 1000 optical microscope. After 7-days exposure, the damaged coatings were analyzed using a Keyence Laser Scanning Confocal microscope and a JEOL SJM-840 SEM with EDS at 15kV. The concentration of inhibitors in the droplets was measured at the end of the exposure with a PerkinElmer LAMBDA 35 UV/VIS spectrometer.

For salt fog spray tests, 1 mm wide, 60 mm long, and 0.35 mm deep crossed scratches were made on 10x10 cm coated panels. Samples were exposed to a 5 wt% NaCl solution at 35°C for 1000 h according to ISO 9227, with photographs at intervals of 0, 168, 336, 500, 750, and 1000 h. Corrosion performance was assessed by examining the appearance and growth of pits, corrosion products, and creepage from the damage.

# 7.3 Results and discussion

*7.3.1 Anti-corrosion performance during immersion in 0.5M NaCl*

Figure 7.1 shows the time-evolution of the quantified global activity area coverage at the exposed metal surface (Figure 7.1.a) and the intensity maps with optical images (Figure 7.1b-d) for the HDMTD/$TiO_x$ coatings with PVCs of 3%, 6%, and 10%. The 3% PVC coating exhibited rapid surface activity, with surface changes reaching 25% area coverage at the damage site within 2 h of immersion. Notably, this activity was primarily located in the second quadrant (top left quadrant in images in Fig 1b), shown as several black spots in the optical image and a high degree of activity (dark purple) in the colored activity map (Figure 7.1b). Following this initial surface activity, the activity extended on the metal surface and increased intensity gradually, plateauing at 35% surface coverage at around 8 h immersion. These surface activities were proof as pits at intermetallic particles, as observed in the confocal microscope image of the damage sites after immersion, as shown in Figure 7.2a. This result suggests an inefficient corrosion inhibition by the coating with 3% PVC HDMTD/$TiO_x$ particles. However, the corrosion activity stopped at 8 h, hence suggesting that either the amount of HDMTD initially released was insufficient, and/or that the release rate of HDMTD was too slow to effectively prevent corrosion attack on the whole exposed areas.

In contrast, both the 6% and 10% PVC coatings provided significant levels of protection, showing near-zero surface activity at the damage for the first 2 h (note lack of activity in the activity maps in Figure 1c and 1d at 2h). This finding is consistent with the results shown in Chapter 6 [4] using a two component coating with 10% PVC inhibiting particles. After the initial full inhibition period, the coating with 6% PVC inhibitor (Figure 7.1c) displayed a relatively rapid increase in surface activity coverage until reaching a plateau at around 6 h immersion with 25% surface area coverage, yet at low intensity levels (i.e. small optically detectable surface changes related to minimal surface attack as confirmed by confocal microscope image in Figure 7.2b and SEM-EDS in Figure 7.3a). Furthermore, the intermetallic particles on the damage of the 6% PVC coating were clearly visible (shown as brown) under the confocal microscope (Figure 7.2b), and most of the intermetallic particles were intact under SEM (Figure 7.3a). Low Mg and about 4 at% S detected at locations 2 and 3 (Figure 7.3a) suggest that the surface activities are related to either dealloying and/or the deposition of HDMTD on the intermetallic particles.

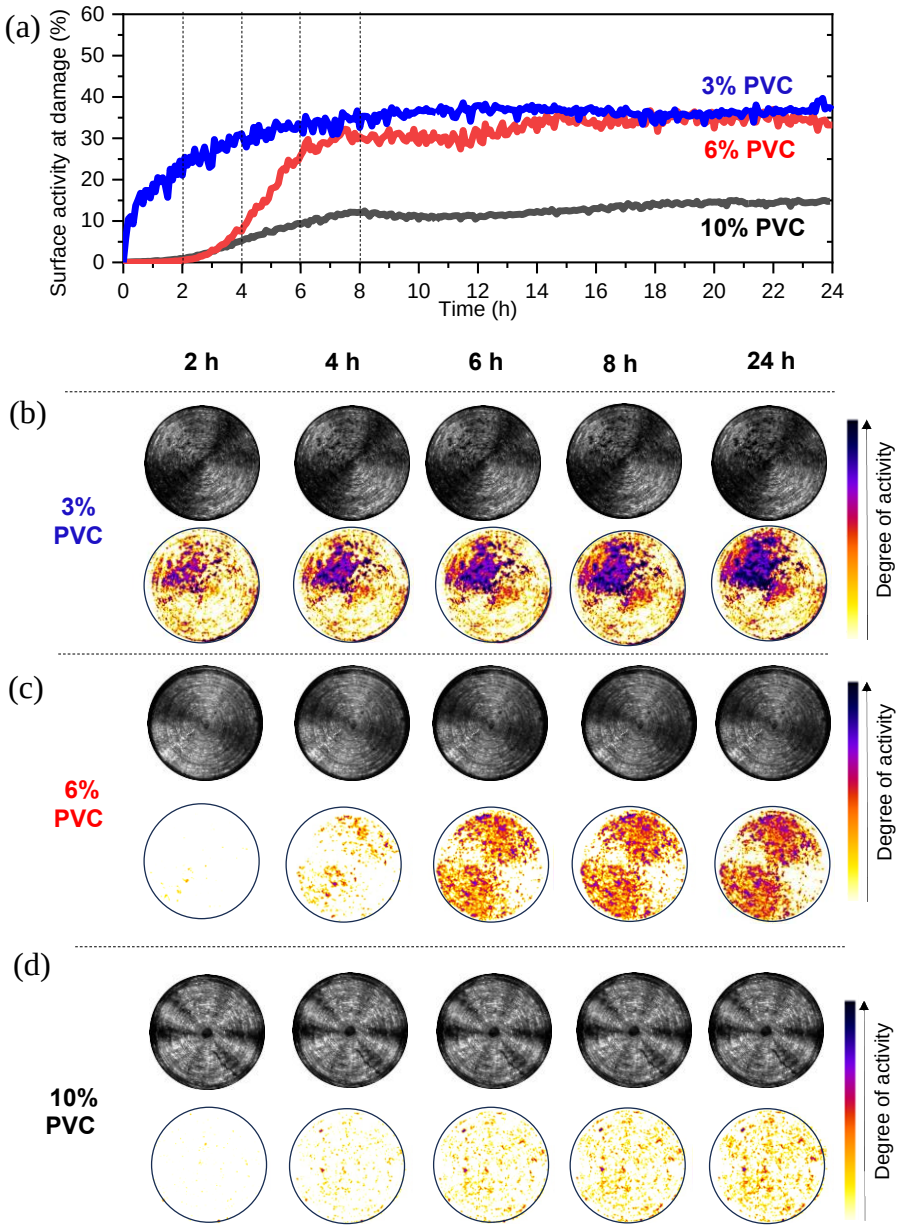


Figure 7.1 Figure 7.1a shows the global surface activity coverage (in %) at metal damage for the three studied coatings with HDMTD/$TiO_x$ particles immersed in 0.5M NaCl over a period of 24 hours. Figures b-d show the optical images during immersion and the activity intensity maps of the three coatings at 3% PVC (b), 6% PVC (c) and 10% PVC (d). The color intensity bar represents the degree (intensity) of the changes at a given location with pixel resolution.

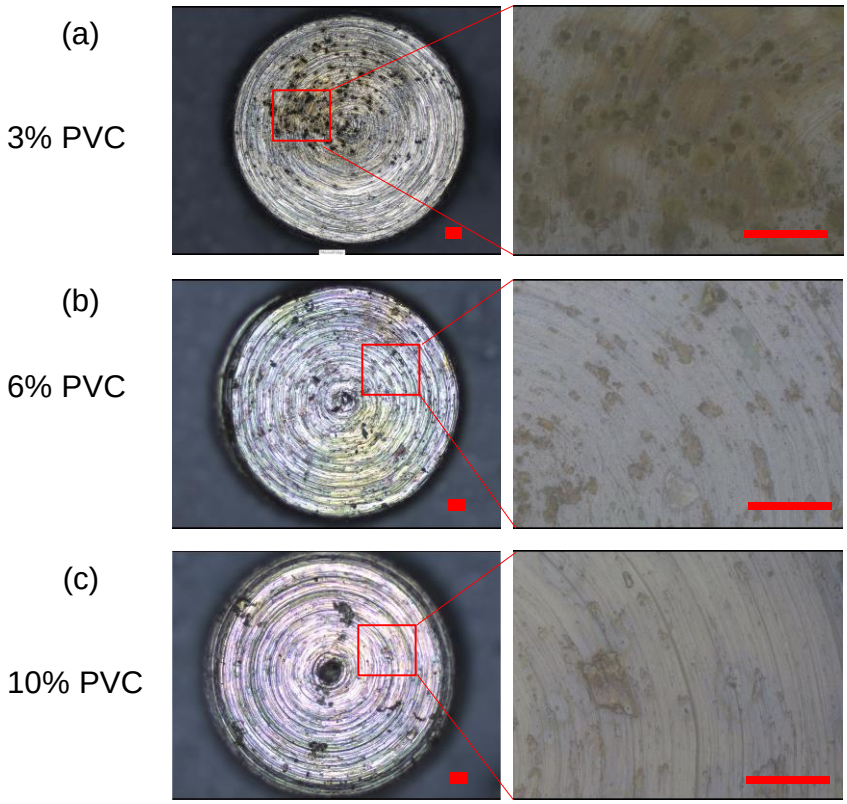


Figure 7.2 Confocal microscope analysis of the damages on the coatings contain (a) 3%; (b) 6% and (c) 10% PVC HDMTD/$TiO_x$ inhibitor pigments at the end of the 24 h immersion in 0.5M NaCl solution. Scale bar: 100 μm.

Meanwhile, the 10% PVC coating (Figure 7.1d) showed only a slow growth in surface activity area coverage plateauing at around 8% after 6 h immersion and at very low intensity (see yellow-orange color maps in Figure 7.1d) of the surface changes. The 10% PVC coating exhibits a uniform brownish color under the confocal microscope (Figure 7.2c), and SEM (Figure 7.3b) reveals trenching at some intermetallic particles however without any further corrosion activities like the oxide deposition. This aligns with our earlier findings [8] in Chapter 3 regarding the corrosion inhibition and stability of HDMTD on the AA2024-T3 surface. The trenching stopped due to the deposition of HDMTD on Cu-rich intermetallic particles (i.e., stable on the surface).

Overall, both 6% and 10% PVC coatings provided a significant level of protection. The minimal activity detected by operando optics was limited to the IMs and associated to inhibitor deposition and/or oxide removal as no significant local corrosion attack (dealloying or trenching) was revealed in SEM-EDS while IMs showed clear presence of Sulphur indicates the deposition of HDMTD.

SEM

(a)

6% PVC

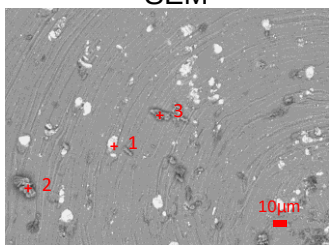


EDS

| At% | Spectrum 1 | Spectrum 2 | Spectrum 3 |
|---|---|---|---|
| O | 21.0 | 17.3 | 26.8 |
| Mg | 17.4 | 1.3 | 1.6 |
| Al | 40.7 | 71.9 | 63.0 |
| S | 0.9 | 4.3 | 4.4 |
| Cu | 20.0 | 2.5 | 4.1 |
| Si | 0.0 | 2.7 | 0.0 |
| Total | 100 | 100 | 100 |

(b)

10% PVC

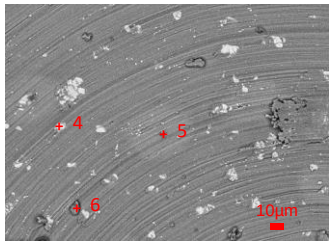


| At% | Spectrum 4 | Spectrum 5 | Spectrum 6 |
|---|---|---|---|
| O | 8.0 | 61.0 | 30.6 |
| Mg | 4.4 | 0.0 | 0.8 |
| Al | 82.0 | 35.6 | 66.2 |
| S | 0.0 | 1.5 | 1.1 |
| Cu | 5.7 | 1.1 | 1.3 |
| Total | 100 | 100 | 100 |

Figure 7.3 SEM/EDS analysis of the damages on (a) 6% PVC and (b) 10% PVC HDMTD/$TiO_x$ coatings at the end of the 24 h immersion in 0.5M NaCl solution.

Figure 7.4 displays the UV absorbance profiles of the electrolytes at the end of the immersion period for the three damaged coatings. The peak maximum at 328 nm was used to calculate the HDMTD content in the solutions using the calibration curve of HDMTD in 0.05M NaCl solution. As noted in the plot, the 3% PVC coating released the smallest amount of HDMTD (0.14 mM) which aligns with the optical activity maps indicating insufficient corrosion protection attributed to a relatively low initial release of HDMTD. Previous study [4] in Chapter 6 have demonstrated that the coating with HDMTD/$TiO_x$ particles exhibits an initial rapid release within 6 h, followed by a prolonged release over 3 days. As shown in Figure 7.1b, corrosion stopped at this point, suggesting that while the initial release may be insufficient, a sufficient amount of HDMTD may be released over time.

The 6% and 10% PVC coatings show twice as much HDMTD content in the electrolyte (2.8 mM and 3.1 mM respectively). Protection at these concentrations in bare AA2024 is complete [8, 14] and indicates a major initial release at the early stages of immersion sustained by further release form the coating, as expected for higher concentration of HDMTD in the coating and based on the cyclic immersion tests shown in chapter 6. [4] Overall, the low surface activity observed in optical measurements, the absence of local corrosion attack in SEM images, and the high levels of corrosion inhibitor measured in solution all correlate with the superior performance of the coatings containing 6% and 10% PVC HDMTD/$TiO_x$ particles.

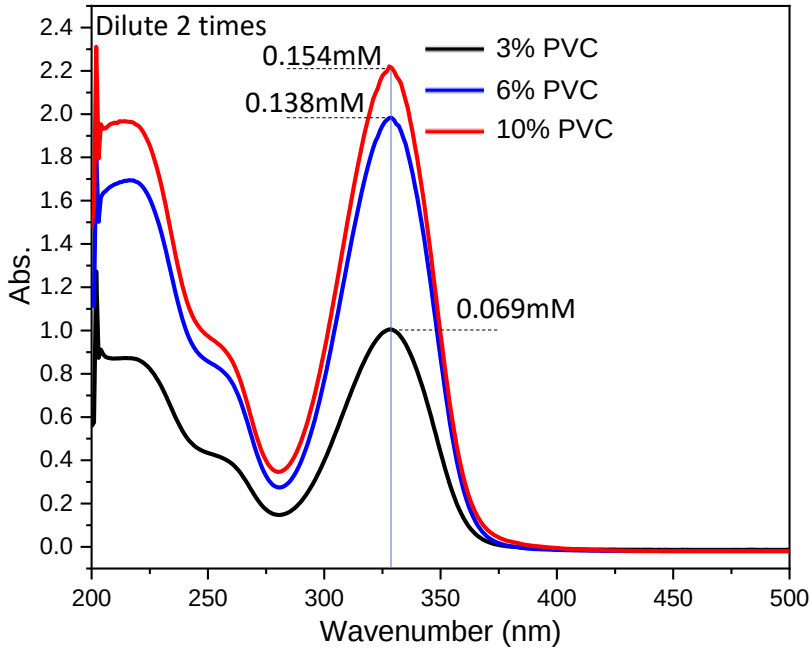


Figure 7.4 Concentrations of HDMTD released into 4.5mL 0.5M NaCl solution from damaged coatings with 3%, 6% and 10% PVC HDMTD/$TiO_x$ pigments. Note that these solutions were diluted 2 times, resulting in actual concentrations of 0.14 mM, 0.28 mM, and 0.31 mM for the 3%, 6%, and 10% PVC coatings, respectively.

*7.3.2 Droplet tests*

Figure 7.5 presents the optical micrographs and the close-up images under confocal microscope from 7-day droplet tests on three coatings with different PVC values. All the damaged areas across the coatings shared some common characteristics: they displayed full protection, remained shiny throughout the exposure with very low to no pitting observed.

The 3% and 6% PVC coatings did not show any coloring under the droplet area. However, the 3% PVC coating showed some minimal trenching, and under the confocal microscope (Figure 7.5a), black dots were visible, indicating activity. In contrast, the 6% PVC coating (Figure 7.5b) showed no such activity and maintained a perfectly shiny scribe with no yellowing, comparable to the DE/Ce coating (the best-performing DE system tested in Chapter 2). The 10% PVC coating (Figure 7.5c), however, exhibited a yellowish color within the droplet area, indicating a substantial release of HDMTD from the scribe. Close-up images revealed no trenching, but there was a noticeable deposit in line with the yellowing observed. At the edges of the scribes, the 3% PVC coating showed yellowing over time, while the 6% PVC coating remained shiny with no yellowing. The 10% PVC coating also showed yellowing at the edges of the scribes.

To reveal the reason of the coloring and detect the degree of local corrosion attack, SEM/EDX was performed at the end of the exposure to the droplet test, as shown in Figure 7.6. The 3% PVC coating (Figure 7.6a) exhibited trenching on some of the S-phase intermetallic particles (e.g., locations 1 and 2) with a high amount of sulfur deposition, indicating a substantial presence of

the inhibitor. This finding is consistent with the results presented in Chapter 3, [8] which indicate that HDMTD tends to precipitate and remain stable on S-phase particles. Additionally, some areas displayed a cracked oxide morphology compatible with aluminum oxide/hydroxide cracking (location 4), indicating a lack of protection. Figure 7.7 explains this local corrosion attack by showing that the 3% PVC coating released a measurable amount of HDMTD (2 mM), but significantly less compared to higher PVC coatings, suggesting that the local attack could be due to the slow and/or insufficient initial release of the inhibitor.

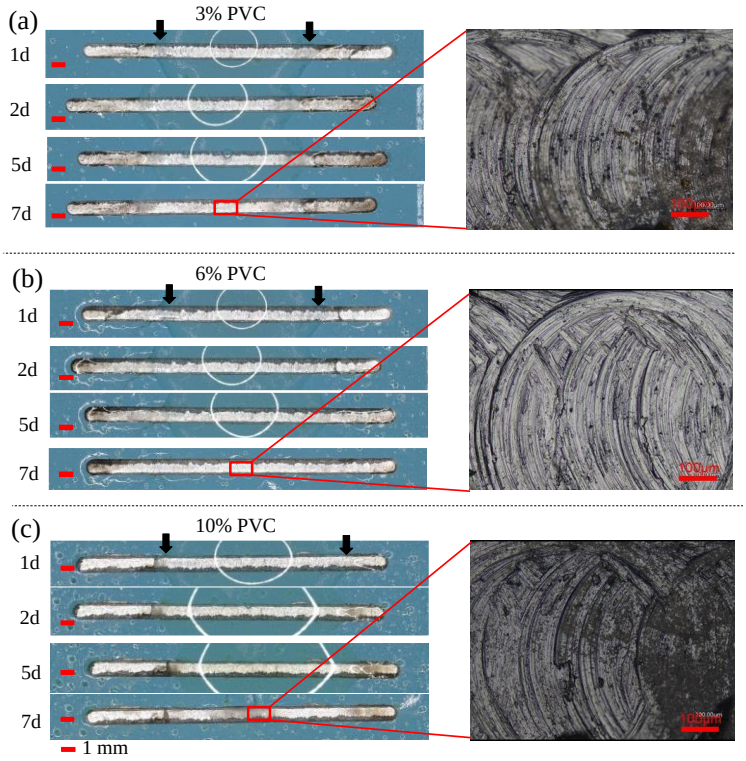


Figure 7.5 Optical images and confocal microscope images of three scratched coatings exposed to 105 µL droplet at 3 wt% (i.e., 0.5M) NaCl solution droplets, captured at intervals of 1 day, 2 days, 5 days, and 7 days. Note: The white lines in the center of the scribes are a visual reflection effect induced by the curvature of the droplet. The edges of the droplet can be seen as dark lines at the left and right of the center of the scribe (marked by two black arrows). The small white circles on the coatings are water condensation droplets.

In contrast, the 6% PVC coating (Figure 7.6b) showed a super clean metallic surface, with most intermetallic particles (e.g., location 6, 7, and 8 indicating S phases and Al-Cu-Fe-Mn phase) remaining intact. The 6% PVC coating released nearly twice the amount of HDMTD (3.8 mM) compared to the 3% PVC coating, as illustrated in Figure 7.7, highlighting its superior performance in sustaining inhibitor release and providing corrosion protection.

Furthermore, a large amount of oxide (both on the metallic surface and the edge of the scratch) was observed on the 10% PVC sample (Figure 7.6c). Interestingly, most of the intermetallic particles in this sample were also intact (e.g., location 9 and 10 indicating S phases) with sulfur

deposition, indicating a high level of inhibition for these intermetallic particles. No blistering or delamination was observed on this coating. Therefore, we attributed the oxide formation to the dissolution of the aluminum matrix due to the high concentration of acidic HDMTD released. This observation is consistent with the yellowish droplet seen on this sample and the high amounts of HDMTD measured by UV-Vis. Figure 7.7 confirms that the 10% PVC coating released a significant amount of HDMTD (8.7 mM), likely due to local agglomeration at the damage site. This supports the earlier discussion that the 10% PVC coating releases an excessive amount of HDMTD.

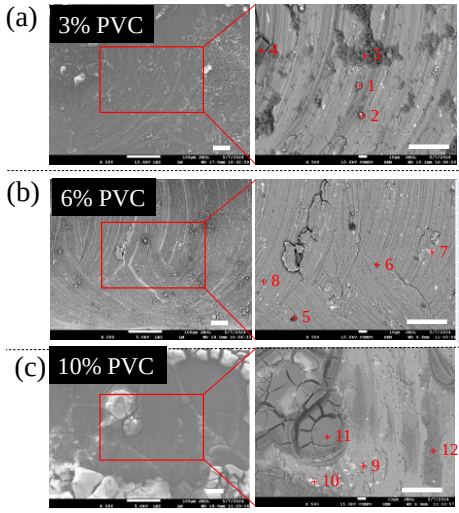


| At% | Spectrum 1 | Spectrum 2 | Spectrum 3 | Spectrum 4 |
|---|---|---|---|---|
| O | 62.41 | 56.9 | 53.66 | 59.26 |
| Mg | 2.88 | | | |
| Al | 16.2 | 16.81 | 46.34 | 40.74 |
| S | 5.47 | 10.07 | | |
| Cu | 13.03 | 16.23 | | |
| Total | 100 | 100 | 100 | 100 |
| Type | S phase | S phase | oxide | oxide |

| At% | Spectrum 5 | Spectrum 6 | Spectrum 7 | Spectrum 8 |
|---|---|---|---|---|
| O | 37.63 | 66.6 | 9.94 | 25.64 |
| Mg | | | | 1.76 |
| Al | 60.65 | 26.49 | 65.29 | 70.26 |
| S | 1.73 | 1.72 | | |
| Mn | | | 3.36 | |
| Fe | | | 5.23 | |
| Cu | | 5.19 | 16.17 | 2.34 |
| Total | 100 | 100 | 100 | 100 |
| Type | oxide | S phase | Al-Cu-Fe-Mn | S phase |

| At% | Spectrum 9 | Spectrum 10 | Spectrum 11 | Spectrum 12 |
|---|---|---|---|---|
| O | 40.09 | 45.56 | 65.39 | 59.63 |
| Mg | 11.25 | | | |
| Al | 24.61 | 7.32 | 33.53 | 40.23 |
| S | 3.99 | 4.84 | 1.08 | 0.14 |
| Cu | 20.06 | 42.29 | | |
| Total | 100 | 100 | 100 | 100 |
| Type | S phase | S phase | oxide | oxide |

Figure 7.6 SEM/EDS analysis of the coatings after exposure for 7 days to the droplet tests. Scale bar: 50 µm.

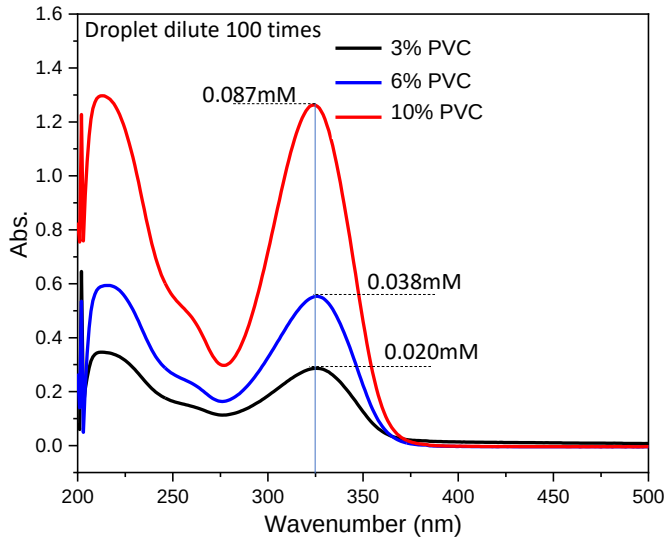


Figure 7.7 UV-Vis spectroscopy of the droplets used in the droplet test at the end of the test (7 days). Note that the droplets were diluted 100 times, resulting in actual concentrations of 2 mM, 3.8 mM, and 8.7 mM for the 3%, 6%, and 10% PVC coatings, respectively.

*7.3.3 Neutral salt fog spray (NSS) tests on bare AA2024-T3*

Figure 7.8 presents the results of neutral salt fog spray (NSS) tests for three coatings with different PVC levels of HDMTD/$TiO_x$ pigments applied on bare AA2024-T3. Overall, no significant amount of white corrosion products and pits were observed on the scratches of all three coatings over the 1000-hour exposure. However, creepage and blisters appeared very early (before 168 h). Interestingly, only the 3% PVC sample exhibited 2 pits at 336 h and an additional 3 pits by the end of the test. The pits were surrounded by white corrosion products, as seen in the close-up images in Figure 7.9a. Nevertheless, most of the scratch areas remained darkened and shown only a minimal amount of corrosion products as shown in the confocal microscope image in Figure 7.10 a. In contrast, the other two samples showed only darkening at the scratches without any pits or white corrosion products throughout the 1000-hour exposure. As confirmed by confocal microscope, these two samples also shown fewer corrosion products in the darkening areas (Figure 7.10a). These results are comparable to and even better than the best inorganic inhibitor systems (DE-Ce) previously tested in Chapter 2. Across the literature, NSS tests are usually performed on AA2024 with intact coatings. [16, 17] When applied on scratched coating, the exposure time are limited. For example, it was reported that a scratched coating with Li salts under 168 h NSS tests did not show any significant amount of corrosion products. [18] However, longer tests have not been done so far.

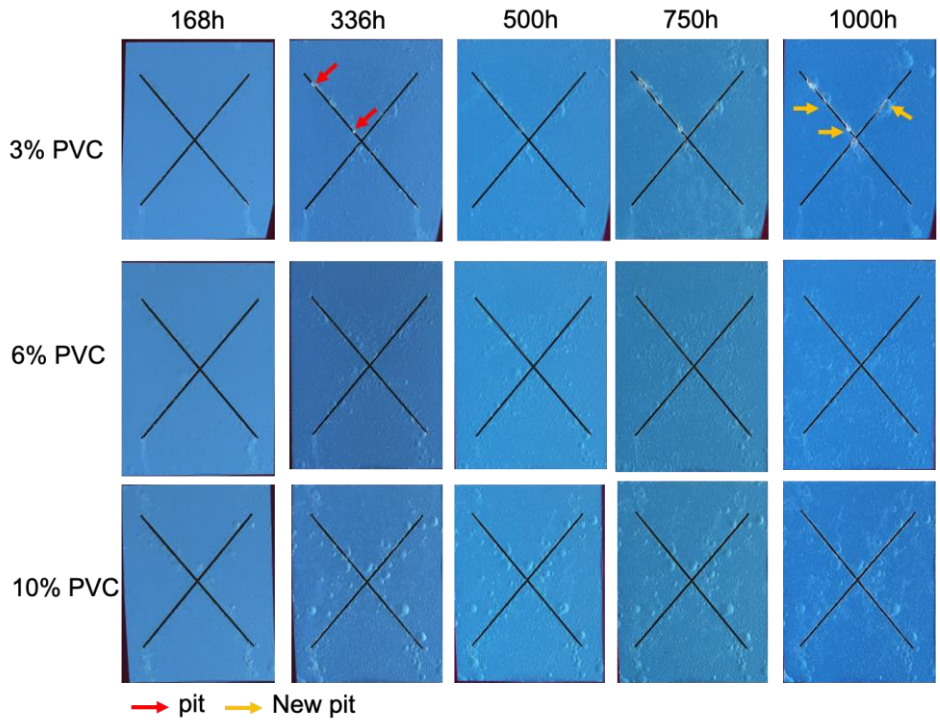


Figure 7.8 Results of salt fog spray (NSS) tests on the three coating systems applied to bare AA2024-T3. The red arrows mark the onset of two pits observed at 336 h, while the yellow arrows indicate the appearance of new pits at 1000 h.

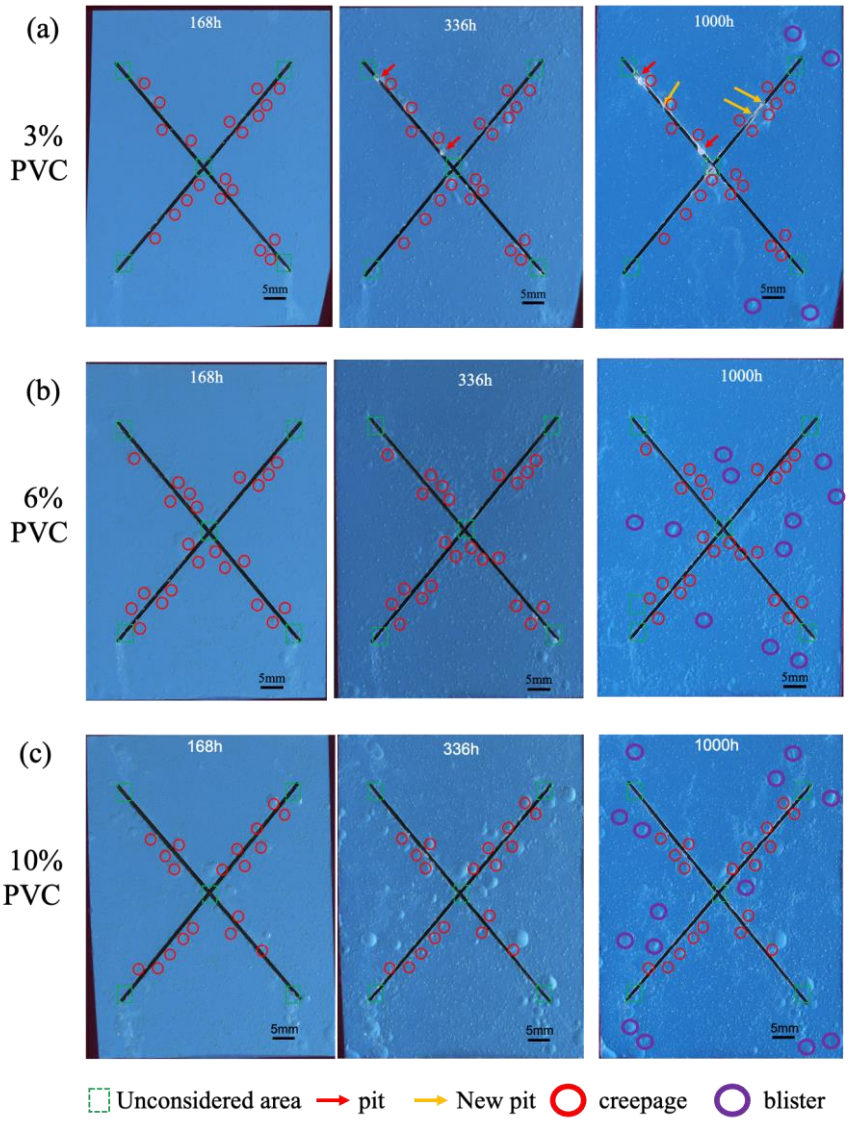


Figure 7.9 NSS results analysis of (a) 3%, (b) 6% and (c) 10% PVC HDMTD/$TiO_x$ coatings. Note that not all blisters are marked; only representative ones have been highlighted.

On the other hand, large amounts of creepage and blistering were observed in these three coatings, as seen in Figure 7.9. The amount of blistering increased with the PVC values, as seen in the 10% PVC sample in Figure 7.9c, which shows the largest creepage and blisters. This can be explained by the high solubility of HDMTD and agglomerated particles leading to high water uptake. These results are consistent with the DE-KDMTD samples in Chapter 2, which also show high creepage due to the high solubility of KDMTD. However, the level of blistering in the gas-phase deposited samples in this chapter is very high. By removing the polymer on top, the area underneath the blisters was found to be full of white corrosion products, as seen in Figure 7.10b, indicating that electrolyte accumulated under the blisters and led to corrosion.

Overall, these results confirm the significant benefits of using the gas-phase deposition strategy, specifically the ability to release a large amount of soluble inhibitors. They also highlight the need for more dedicated studies on the gas-phase deposition process to prevent water uptake and the agglomeration of gas-phase deposited particles within the coating matrix.

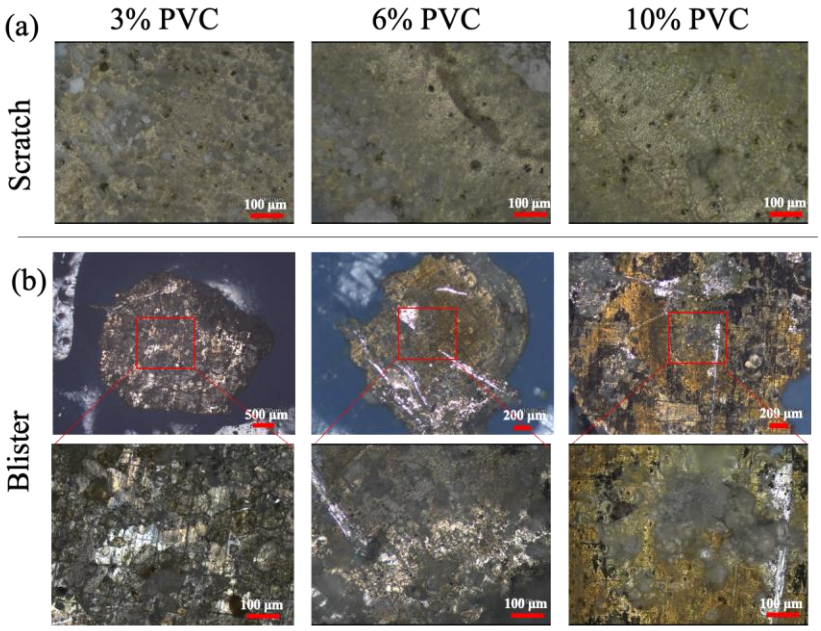


Figure 7.10 Confocal microscope images of the three coatings taken on (a) scratch area and (b) under blister. Note that the images on scratches were taken on the darkening areas. The blisters were broken with a needle to expose the area beneath.

# 7.4 Conclusions

This study evaluated lab-scale aircraft primers containing HDMTD/$TiO_x$ pigments with PVC levels of 3%, 6%, and 10% for their corrosion inhibition performance across three different tests.

When damaged coatings were exposed to 0.5M NaCl solution for 1 day, the 3% PVC coating exhibited rapid corrosion activity. In contrast, the 6% and 10% PVC coatings provided better protection, with only minor changes at intermetallic particles owing to the high release of HDMTD from the damage sites. After 7 days in the droplet test, the 3% and 6% PVC coatings remained shiny, with minimal activity in the 3% PVC coating. The 10% PVC coating showed significantly higher HDMTD release, indicated by a yellowish color and inhibitor deposition under the droplet. In the salt fog spray test, the 3% PVC coating showed a few pits, while the 6% and 10% PVC coatings exhibited darkening at scratches without pits or white corrosion products. These results were comparable to the best inorganic inhibitor systems discussed in Chapter 2. However, increased creepage and blistering were observed with higher PVC levels, suggesting issues with water uptake and particle agglomeration in the coatings.

These findings confirm the advantages of the gas-phase deposition strategy for HDMTD/$TiO_x$ coatings, particularly in isolating the inhibitors from reacting with the polymer matrix, which allows the inhibitors to remain active and soluble for effective release. The study of coatings with different PVC levels suggests that it is important to balance the amount of inhibitors in the coating, as excessive amounts are not necessary. Furthermore, the results also emphasize the need for further optimization to reduce water uptake, possibly by using lower solubility inhibitors, and to prevent particle agglomeration, potentially by modifying the surface chemistry or coverage of the gas-phase deposited layer, to enhance overall performance.

# 7.5 References

(1) Al-Sabbagh, A.; Osman, M.; Omar, A.; El-Gamal, I. Organic corrosion inhibitors for steel pipelines in oilfields. *Anti-corrosion methods and materials* **1996**, *43* (6), 11-16.
(2) Olajire, A. A. Corrosion inhibition of offshore oil and gas production facilities using organic compound inhibitors-A review. *Journal of Molecular Liquids* **2017**, *248*, 775-808.
(3) Yasakau, K.; Zheludkevich, M.; Karavai, O.; Ferreira, M. Influence of inhibitor addition on the corrosion protection performance of sol–gel coatings on AA2024. *Progress in organic coatings* **2008**, *63* (3), 352-361.
(4) Zhao, J.; van Ommen, J. R.; Garcia, S. J. Gas-phase deposited nanolayers guard organic microparticles in polymer matrices for active corrosion protection at damages. *Progress in Organic Coatings* **2024**, *192*, 108522.
(5) Haddadi, S.; Ramazani, S.; Mahdavian, M.; Taheri, P.; Mol, J. Fabrication and characterization of graphene-based carbon hollow spheres for encapsulation of organic corrosion inhibitors. *Chemical Engineering Journal* **2018**, *352*, 909-922.
(6) Maia, F.; Yasakau, K.; Carneiro, J.; Kallip, S.; Tedim, J.; Henriques, T.; Cabral, A.; Venâncio, J.; Zheludkevich, M.; Ferreira, M. Corrosion protection of AA2024 by sol–gel coatings modified with MBT-loaded polyurea microcapsules. *Chemical Engineering Journal* **2016**, *283*, 1108-1117.
(7) Denissen, P. J.; Shkirskiy, V.; Volovitch, P.; Garcia, S. J. Corrosion inhibition at scribed locations in coated AA2024-T3 by cerium-and DMTD-loaded natural silica microparticles under continuous immersion and wet/dry cyclic exposure. *ACS applied materials & interfaces* **2020**, *12* (20), 23417-23431.
(8) Zhao, J.; Santoso, A.; Garcia, S. J. Small concentrations of NaCl help building stable inhibiting layers from 2, 5-dimercapto-1, 3, 4-thiadiazole (DMTD) on AA2024-T3. *Corrosion Science* **2023**, *225*, 111562.
(9) Konuray, A. O.; Fernández-Francos, X.; Ramis, X. Analysis of the reaction mechanism of the thiol–epoxy addition initiated by nucleophilic tertiary amines. *Polymer chemistry* **2017**, *8* (38), 5934-5947.
(10) Denissen, P. J.; Garcia, S. J. Cerium-loaded algae exoskeletons for active corrosion protection of coated AA2024-T3. *Corrosion Science* **2017**, *128*, 164-175. DOI: 10.1016/j.corsci.2017.09.019.
(11) Kim, M. S.; Jeon, J. B.; Chang, J. Y. Selectively functionalized mesoporous silica particles with the PEGylated outer surface and the doxorubicin-grafted inner surface: Improvement of loading content and solubility. *Microporous and mesoporous materials* **2013**, *172*, 118-124.
(12) Denissen, P. J.; Homborg, A. M.; Garcia, S. J. Requirements for corrosion inhibitor release from damaged primers for stable protection: A simulation and experimental approach using cerium loaded carriers. *Surface and Coatings Technology* **2022**, *430*. DOI: 10.1016/j.surfcoat.2021.127966.
(13) Denissen, P. J.; Shkirskiy, V.; Volovitch, P.; Garcia, S. J. Corrosion Inhibition at Scribed Locations in Coated AA2024-T3 by Cerium- and DMTD-Loaded Natural Silica Microparticles under Continuous Immersion and Wet/Dry Cyclic Exposure. *ACS Appl Mater Interfaces* **2020**, *12* (20), 23417-23431. DOI: 10.1021/acsami.0c03368 From NLM PubMed-not-MEDLINE.
(14) Denissen, P. J.; Garcia, S. J. Reducing subjectivity in EIS interpretation of corrosion and corrosion inhibition processes by in-situ optical analysis. *Electrochimica Acta* **2019**, *293*, 514-524.
(15) Denissen, P. J.; Homborg, A. M.; Garcia, S. J. Interpreting electrochemical noise and monitoring local corrosion by means of highly resolved spatiotemporal real-time optics. *Journal of The Electrochemical Society* **2019**, *166* (11), C3275.
(16) Shruthi, T.; Walton, J.; McFall-Boegeman, S.; Westre, S.; Swain, G. M. Investigation of the trivalent chromium process conversion coating as a sealant for anodized AA2024-T3. *Journal of The Electrochemical Society* **2020**, *167* (11), 111504.
(17) Gad, S. M.; Zhou, X.; Lyon, S. B.; Emad, S. Inhibition mechanism of anticorrosion pigments leached from organic coatings: Comparison between salt spray and immersion testing. *Progress in Organic Coatings* **2023**, *174*, 107266.
(18) Visser, P.; Liu, Y.; Zhou, X.; Hashimoto, T.; Thompson, G. E.; Lyon, S. B.; van der Ven, L. G.; Mol, A. J.; Terryn, H. A. The corrosion protection of AA2024-T3 aluminium alloy by leaching of lithium-containing salts from organic coatings. *Faraday Discussions* **2015**, *180*, 511-526.

# Acknowledgements

I kept waiting for the right moment to complete this part. Now it is midnight, and I've just returned from our "Corridor" Sinterklaas party. Suddenly, it feels so real that I am about to finish my PhD and farewell to so many wonderful people. My tears are uncontrollably flowing, and yes—this is the moment to express my gratitude to everyone who accompanied me on this incredible 4-year journey.

**To my supervisors - 致导师**

Who should I start with? **Dr. Santiago J. Gracia**, of course! You are the best supervisor anyone could ask for—always available, friendly, critical, and maintaining the highest standards. Talking with you, whether about research or life, has always been inspiring. I was deeply touched when you said that, as a supervisor, your greatest achievement is your student. Your passion for education is remarkable, and I've seen how much I've grown under your guidance. For me, you are not just a supervisor but also a close friend who offered valuable suggestions and ideas to help me overcome challenges. We've shared so many great moments together, and I'll always cherish them. Thank you, **Prof. Ruud van Ommen**! Talking with you has always been insightful, and your expertise helped me navigate many challenges. I am truly grateful for the opportunity to use the ALD setup in your lab and to work with the wonderful colleagues I met there. I also want to express my heartfelt thanks to **Dr. Markus Jordan** from Airbus. I could not have done this without your valuable industry insights and continuous support. It was an amazing experience to visit Airbus in Bremen, conduct experiments, and discuss ideas with the colleagues there. Thank you for making that possible.

**Starting was not easy- 万事开头难**

Four and a half years ago, I arrived in Delft during the height of the Covid pandemic. I was filled with excitement for this new chapter but also a little worried. Yes, it was a unique time when the world was in panic, and I chose to leave my family to come to a land eight thousands of kilometers away from everything familiar. Thank you so much, **Shanta**! You are such a lovely person who helped me settle into the new environment so quickly. Thank you for organizing group activities, assisting me with processes, and even helping me learn Dutch. I would love to keep coming to our food truck Tuesdays 😊. At the same time, I joined our old group, NovAM, during a special period when **Prof. Sybrand van der Zwaag** was about to retire. Thank you, **Sybrand**, for the inspiring discussions during my first year of PhD. Your wisdom and expertise guided me greatly, and your tips on cycling and kayaking encouraged me to take up kayaking myself! Many thanks to **Yifan**, the first person from NovAM I met in person. Thank you for your tips while I was still in China, for picking me up on my first day, and for "feeding" me with your delicious food. Your cooking skills and energy are truly impressive! Thank you, **Paul**, for your guidance on diatoms and electrochemistry during the early stages of my PhD. I wish you all the best and will keep

following your world trip adventures! Thanks to my first office mate, **Dimos**! You taught me the spirit of NovAM, and we shared so many fun moments together. I wish you all the best for the future. Speaking of the spirit of NovAM, I want to thank all the old NovAM members: **Vincenzo, Hugo, Anton, Gawel, Vincent, Tadhg, Satya**—you created so many wonderful Friday evenings and unforgettable memories. Thank you for all your help in both research and life in the Netherlands!

**It's Getting Better - 渐入佳境**

The beginning wasn't easy, but at some point, I saw the light. To my lovely office mate, **Miisa**, I am so happy we moved into the same office together! I admire your artistic sense, your dedication to making things perfect, and your clever tips. **Tinashe**, you are such a reliable and kind friend. Thank you for accompanying me during Airbus meetings and trips, for always bringing snacks, and for buying me my favorite game, Mahjong! **Marlon**, the life of the party, you made our corrosion topic so cool that everyone wants you to stay in the Netherlands. Thank you for arranging my bachelor party! Thank you, **Elif**, for being so kind and helpful. I'm thrilled you came back to the group, and I will always treasure the wonderful days we spent in Spain and the gatherings at your place. **Lakshmi**, you are such a sweet person with an eye for detail. I wish you a productive and joyful PhD journey. **Riccardo**, a young and talented corrosion scientist, I wish you all the best in your space exploration journey. **Edward**, I am so proud of your creativity, hard work, and intelligence. It was a pleasure working with you on diatomite. I also want to thank all the master's, bachelor's students and visiting researchers who worked in the group: **Silvio, Matthias, Apurva, Tommaso, Laura, Ronan, Kato, Jaylan, Bernadine, Serena, Adria, Willem, Sera, Casper, Yang**. The structural changes in the department brought new connections, forming the "Corridor Group". We shared so many fun activities: Kingsday, Sinterklaas, sports days, potlucks, Chinese restaurants, birthday parties, and more. Thank you, **Leith**, my third office mate, and **Farah**, for your energy. Thank you to **Alejandro, Denize, Mirko, Tingyu, Theo, Zhibin, Zhiyuan**—you all filled the corridor with happiness.

To the scientists, technicians, and colleagues I worked with: **Durga**, thank you for your support in the chemical lab—you were always kind and available. **Caitlin**, thank you for your efforts to improve the lab environment. **Marlies, Jorhan, Roy, Pietro, Mohamond**, thank you for your guidance in the lab. **Albert, Rens, Bert**, thank you for your help with the ALD setup and XPS. To **Yinglu**, thank you for hosting me during my first Christmas and for our coffee chats in the city center. To **Xi Li** and **Nan Yue**, I miss our shopping trips, meals, and deep conversations. You are both wise and wonderful friends. To **Yuqian**, I am so grateful for our friendship. I will never forget our trip to Dubrovnik or all the things you taught me—ballet, bodypower, kayaking. You are brave, beautiful, and powerful. I hope you never change! To **Nan Tao, Ran Tao, Lubin, Jingyi**, thank you for your support and the lovely moments we shared. I also want to express my special thanks to my friends in Delft—you made my PhD life so colorful. Thank you, **Qingru**, my lovely friend and the first person I got to know here. We came on the same airplane and shared so many fun moments together. Wishing you all the best with **Xiaoming**! **Yueer**, you're such a cool neutron girl. Despite our struggles with Dutch, we managed to get through it! Thank you for always hosting us with **Sulian**. **Ziying**, I'm so happy we lived close to each other—we shopped, played sports, and enjoyed so many meals together. Wishing you a wonderful life with **Fengqi**!

A heartfelt thanks to **Tingting, Xingxing, Xueqing, Xinmin, Shan Qu, Wenxiu, Shangguan, Kaiqiao, Ming, Qinghe,** and **Keer** for all the great times we spent hanging out together!

**The End - 有始有终**

Finally, I want to express my heartfelt gratitude to all the friends, mentors, and loved ones who supported me throughout this journey. As the saying goes, "海内存知己，天涯若比邻"—though we may be separated by great distances, true friendship makes us feel as close as neighbours.

I also want to thank my parents. 感谢你们赋予我生命，保护我长大，支持我的每个决定，我爱你们. To my husband, **Xingyu (吴星宇)**: you have been my rock and my inspiration. Your unwavering support and belief in me carried me through my toughest moments. From long hours in the lab to everyday life, you were there every step of the way. Thank you for your love, patience, and faith in our shared future.

# List of publications

Journal publications

1. Zhao, J.; Garcia, S. J.
   *When Ionic State is More Important than Inhibitor Concentration: A Comparison of Epoxy-Amine Coatings with 2,5-Dimercapto-1,3,4-thiadiazole (DMTD) Salts Loaded in Diatom Exoskeletons*
   To be submitted, **2024**

2. Zhao, J.; Na, D.H. Garcia, S. J.
   *Surface Modification of Natural Porous Silica Microparticles to Control the Loading and Release of Organic Corrosion Inhibitors*
   Under review, **2024**

3. Zhao, J.; Garcia, S. J.
   *Assessment of the Corrosion Protection Power of Inhibitor-Loaded Diatomite Particles in Lab-Scale Model Primers: Salt Fog Spray and Droplet Test Analysis*
   To be submitted, **2024**

4. Zhao, J.; Garcia, S. J.
   *Corrosion Inhibition Power of Novel Gas-Phase Deposited Organic Inhibitors in Lab-Scale Model Aircraft Primers*
   To be submitted, **2024**

5. Zhao, J.; van Ommen, J. R.; Garcia, S. J.
   Gas-phase deposited nanolayers guard organic microparticles in polymer matrices for active corrosion protection at damages.
   *Progress in Organic Coatings* **2024**, *192*, 108522.

6. Zhao, J.; Santoso, A.; Garcia, S. J.
   Small concentrations of NaCl help building stable inhibiting layers from 2, 5-dimercapto-1, 3, 4-thiadiazole (DMTD) on AA2024-T3.
   *Corrosion Science* **2023**, *225*, 111562.

Conference contributions

1. Zhao, J.; Garcia, S. J.
   *Oral presentation: Organic corrosion inhibitor-loaded algae exoskeletons for aircraft coating design*
   European Corrosion Congress, Paris, France, September **2024**

2. Zhao, J.; van Ommen, J. R.; Garcia, S. J.
   *Oral presentation: Making possible the use of organic inhibitors in organic coatings for active corrosion protection*
   9th International Conference on Self-Healing Materials, Madrid, Spain, June **2024**

3. Zhao, J.; Na, D.H. Garcia, S. J.
   *Poster presentation:Protecting metals with algae exoskeletons*
   Materialen NL Conference, The Netherlands, December **2023**

4. Zhao, J.; Na, D.H. Garcia, S. J.
   *Poster presentation: Effect of diatomite surface modification on the loading and release of organic corrosion inhibitors from anti-corrosive coatings*
   European Corrosion Congress, Brussel, Belgium, September **2023**

5. Zhao, J.; van Ommen, J. R.; Garcia, S. J.
   *Oral presentation: Making possible the use of organic inhibitors in organic coatings via gas-phase deposition*
   European Corrosion Congress, Brussel, Belgium, September **2023**

6. Zhao, J.; Garcia, S. J.
   *Oral presentation: Stability of 2,5-Dimercapto-1,3,4-thiadiazole (DMTD) protective layers on AA2024-T3*
   European Corrosion Congress, Berlin, Germany, September **2022**

7. Zhao, J.; van Ommen, J. R.; Garcia, S. J.
   *Poster presentation: Effect of ALD coatings on organic inhibitor release*
   Coatings Science International Conference-CoSI 2022, The Netherlands, June **2022**

Poster prize award for the poster "Effect of diatomite surface modification on the loading and release of organic corrosion inhibitors from anti-corrosive coatings", European Corrosion Congress, Brussel, Belgium, September 2023.

# About the Author

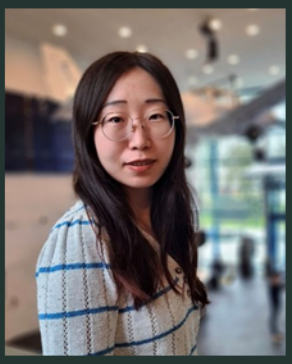

Jingjing Zhao was born and raised in Tianjin, a coastal city in northern China, where she completed her BSc and MSc degrees in the Faculty of Chemical Engineering at Tianjin University (TJU). Following her studies, she worked as an environmental engineer at the Institute of Environmental Protection Science in Tianjin from July 2018.

In June 2020, Jingjing began her PhD at the Faculty of Aerospace Engineering at Delft University of Technology, funded by Airbus. Under the guidance of Dr. Santiago J. Garcia Espallargas and Prof. dr. ir. J. Ruud van Ommen, her research centered on developing new aerospace anticorrosion coatings. Her work specifically explored organic corrosion inhibitors and innovative applications for these in aircraft primers, advancing the field of aerospace materials engineering.